

Critical Magnetic Fluctuations in Strongly Electron-Correlated Systems

Von der Fakultät Mathematik und Physik der Universität Stuttgart zur Erlangung
der Würde eines Doktors der Naturwissenschaften (Dr. rer. nat.) genehmigte
Abhandlung

Vorgelegt von

Heiko Trepka

aus Memmingen, Deutschland

Hauptberichter: Prof. Dr. Bernhard Keimer

Mitberichter: Prof. Dr. Sebastian Loth

Prüfungsvorsitzender: Prof. Dr. Maria Daghofer

Tag der mündlichen Prüfung: 27.06.2022

Max-Planck-Institut für Festkörperforschung

Stuttgart, 2022

Contents

Abbreviations	1
Abstract	3
Deutsche Zusammenfassung (kurz)	5
1. Introduction	7
2. Critical Magnetic Phenomena	12
2.1. Introduction	12
2.2. Universality, critical exponents and scaling	14
2.3. Exceptions and crossover	19
2.4. Dynamic critical scaling	24
2.5. Quantum phase transitions	29
3. Layered ruthenates	32
3.1. Introduction to Transition Metal Oxides	32
3.2. Layered ruthenates	35
4. Heavy-fermion system $\text{CeCu}_{6-x}\text{Au}_x$	50
5. Experimental Techniques	55
5.1. Neutron scattering	55
5.2. Triple-axis spectroscopy	60
5.3. Neutron spin-echo spectroscopy	65
5.4. Larmor diffraction	75
6. Critical magnetic fluctuations in layered ruthenates	79
6.1. Single-layer Ca_2RuO_4	79

6.2. Bilayer $\text{Ca}_3\text{Ru}_2\text{O}_7$	118
6.3. Ti-doped bilayer $\text{Ca}_3(\text{Ru}_{0.99}\text{Ti}_{0.01})_2\text{O}_7$	128
6.4. Discussion and Conclusion	133
7. Critical magnetic fluctuations in $\text{CeCu}_{6-x}\text{Au}_x$ ($x = 0.1, 0.2$)	138
7.1. $\text{CeCu}_{5.8}\text{Au}_{0.2}$	138
7.2. $\text{CeCu}_{5.9}\text{Au}_{0.1}$	149
7.3. Discussion and Conclusion	150
A. 1D and 2D spin-flip scattering	153
Deutsche Zusammenfassung	156
Bibliography	167
Acknowledgements	193

Abbreviations

AFM	antiferromagnet
BER II	Forschungsreaktor Berlin II
BG	background
BKT	Berezinkii-Kosterlitz-Thouless
CP	critical point
DE	double-exchange
FM	ferromagnet
FRM II	Forschungsreaktor München II
FWHM	full-width at half-maximum
HWHM	half-width at half-maximum
ILL	Institut Laue-Langevin
INS	Inelastic Neutron Scattering
KT	Kosterlitz-Thouless
LD	Larmor Diffraction
MC	Monte-Carlo
MF	mean-field
MIT	metal-to-insulator transition
MLZ	Heinz Maier-Leibnitz Zentrum
NRSE	Neutron Resonance Spin-Echo
NSE	Neutron Spin-Echo
NSF	non-spin-flip
PD	precession device
PL	power-law
QCP	quantum critical point
QPT	quantum phase transition
RF	radio-frequency

RIXS	Resonant Inelastic X-ray Scattering
RKKY	Ruderman-Kittel-Kasuya-Yoshida
RP	Ruddelston-Popper
RTS	ray-tracing simulation
SC	superconductivity
SE	superexchange
SF	spin-flip
SOC	spin-orbit coupling
TAS	Triple-Axis Spectroscopy
TMO	Transition Metal Oxides
2D-H	two-dimensional Heisenberg
3D-H	three-dimensional Heisenberg
2D-I	two-dimensional Ising
3D-I	three-dimensional Ising
2D-XY	two-dimensional XY
3D-XY	three-dimensional XY

Abstract

Critical Magnetic Fluctuations in Strongly Electron-Correlated Systems

In this work, we use high-resolution neutron Triple-Axis Spectroscopy (TAS) and Neutron Spin-Echo (NSE) spectroscopy to study the critical properties of the strongly electron-correlated $4d$ square-lattice antiferromagnets (AFMs) Ca_2RuO_4 , $\text{Ca}_3\text{Ru}_2\text{O}_7$, and Ti-doped $\text{Ca}_3(\text{Ru}_{0.99}\text{Ti}_{0.01})_2\text{O}_7$, as well as of the heavy-fermion system $\text{CeCu}_{6-x}\text{Au}_x$ ($x = 0.1, 0.2$) in vicinity and above the Néel-temperatures T_N . We extract static and dynamical critical exponents to determine the spin dimensionalities and relevant anisotropies. For the layered ruthenates with significant easy-plane anisotropy it was of particular interest whether or not a seldom two-dimensional XY (2D-XY) scaling can be observed and how the critical behavior is affected by the additional intra-bilayer exchange interactions and Ti-doping. For $\text{CeCu}_{6-x}\text{Au}_x$ ($x = 0.1, 0.2$), we aimed to resolve an expected quantum-to-classical crossover in the dynamical scaling behavior by taking advantage of the high energy-resolution of NSE.

While in the layered ruthenates we probe the temperature-dependence of the AFM Bragg-intensity, the Q -width, the amplitude and the energy-width of the magnetic diffuse scattering close to T_N to determine the critical behavior of the magnetic order parameter M , correlation length ξ , susceptibility χ , and the characteristic energy Γ with the corresponding critical exponents β , ν , γ , and z , respectively. We find that the critical behaviors of the single-layer compound Ca_2RuO_4 follow universal scaling laws that are compatible with predictions of the 2D-XY model. The bilayer compound $\text{Ca}_3\text{Ru}_2\text{O}_7$ is only partly consistent with the 2D-XY theory and best described by the three-dimensional Ising (3D-I) model, which is likely a consequence of the intra-bilayer exchange interactions in combination with an orthorhombic

single-ion anisotropy. In the Ti-doped bilayer compound $\text{Ca}_3(\text{Ru}_{0.99}\text{Ti}_{0.01})_2\text{O}_7$, we observe no evidence of critical scattering due to the first-order character of the magnetic transition. Our results imply that the layered ruthenates are potential solid-state platforms for research on the [2D-XY](#) model and the effects of 3D interactions and additional spin-space anisotropies on the magnetic fluctuations.

For the near quantum critical compound $\text{CeCu}_{5.8}\text{Au}_{0.2}$, we investigate the temperature-dependence of the [AFM](#) Bragg-intensity, the critical amplitudes and the energy-width of the magnetic diffuse scattering near T_N and determine the corresponding critical exponents β , γ , and z . For the dynamical critical behavior above T_N , we exploit the high energy resolution of [NSE](#) spectroscopy to complement previous [TAS](#) measurements by Stockert *et al.* [1] in the range $T_N < T < 1$ K. In close vicinity of T_N , we find a power-law behavior of the characteristic energy of the magnetic fluctuations that is compatible with classical [3D-I](#) scaling. Since the previous [TAS](#) data [1] are in reasonable agreement with quantum critical scaling at higher temperatures, our results indicate an expected, but hitherto not observed, quantum-to-classical crossover at $\Gamma \sim k_B T$. Furthermore, we find a scaling behavior of the order parameter compatible with the predictions of the mean-field model, which is consistent with prior works. The mean-field value is attributed to the presence of dominant [RKKY](#) long-ranged interactions in the heavy-fermion system $\text{CeCu}_{5.8}\text{Au}_{0.2}$. The extracted critical exponent of the critical amplitudes is not related to any universality class. In addition, we also performed [NSE](#) scans at the critically doped compound $\text{CeCu}_{5.9}\text{Au}_{0.1}$, but, contrary to previous [TAS](#) measurements [1], our data did not reveal a critical scaling behavior. Our results imply that the $\text{CeCu}_{6-x}\text{Au}_x$ series, especially the $\text{CeCu}_{5.8}\text{Au}_{0.2}$ compound, is a promising platform to investigate the transition from classical to quantum-critical scaling regimes. This can yield important insights on quantum critical points ([QCPs](#)) in general and, in the end, might also help for a better understanding of the unconventional superconductivity in heavy-fermions.

Deutsche Zusammenfassung (kurz)

Kritische magnetische Fluktuationen in stark korrelierten Elektronensystemen

In dieser Arbeit werden mittels hochauflösender Neutronenspektroskopie die kritischen magnetischen Eigenschaften in den geschichteten (*square-lattice*) Ruthenaten Ca_2RuO_4 , $\text{Ca}_3\text{Ru}_2\text{O}_7$ und in Ti-dotiertem $\text{Ca}_3(\text{Ru}_{0.99}\text{Ti}_{0.01})_2\text{O}_7$, sowie im schwere-Fermionensystem $\text{CeCu}_{6-x}\text{Au}_x$ ($x = 0.1, 0.2$) in der Nähe der Néel-Temperatur T_N bzw. des quantenkritischen Punkts untersucht. Experimentell werden statische und dynamische kritische Exponenten zur Bestimmung der Dimensionalität der magnetischen Ordnungsparameter und relevanter Anisotropien extrahiert. Speziell wird die Frage beantwortet, ob die kritischen Fluktuationen in geschichteten Ruthenaten dem **2D-XY**-Modell folgen und inwiefern zusätzliche Doppelschicht-Austauschwechselwirkungen das kritische Verhalten beeinflussen. Die Motivation zur Untersuchung des nahe quantenkritischen $\text{CeCu}_{5.8}\text{Au}_{0.2}$ bestand darin, den prognostizierten, aber bisher nicht beobachteten Übergang von quantenkritischen zu klassischem dynamischen Skalierungsverhalten zu bestimmen und die kritischen magnetischen Eigenschaften mit dem kritisch-dotierten $\text{CeCu}_{5.9}\text{Au}_{0.1}$ zu vergleichen.

Wir untersuchen in den geschichteten Ruthenaten die Temperaturabhängigkeit der antiferromagnetischen (**AFM**) Bragg-Intensität, sowie die Amplitude und Verteilung der kritischen Streuung im Impuls- und Energieraum mit Neutronen Dreiachsen- (*Triple-Axis Spectroscopy* (**TAS**)) und Spin-Echo (**NSE**)-Spektroskopie. Aus den Daten wird das kritische Verhalten des magnetischen Ordnungsparameters M , der Korrelationslänge ξ , der Suszeptibilität χ und der charakteristischen Energie Γ mit den entsprechenden kritischen Exponenten β, ν, γ und z bestimmt. Unsere Ergebnisse zeigen, dass das kritische Verhalten des einfach geschichteten Ca_2RuO_4

kompatibel mit dem **2D-XY**-Modell ist. Das Skalierungsverhalten des doppelt geschichteten $\text{Ca}_3\text{Ru}_2\text{O}_7$ ist dagegen nur teilweise konsistent mit dem **2D-XY**-Modell und wird besser durch das dreidimensionale Ising-Modell (**3D-I**) eingefangen. Dies resultiert wahrscheinlich aus der Kombination von Doppelschicht-Kopplung und orthorhombischer *single-ion* Anisotropie. In der Ti-dotierten Doppelschichtverbindung $\text{Ca}_3(\text{Ru}_{0.99}\text{Ti}_{0.01})_2\text{O}_7$ beobachten wir aufgrund des Übergangs erster Ordnung keine Anzeichen von kritischer Streuung. Damit veranschaulichen unsere Ergebnisse, dass die geschichteten Ruthenate potenzielle Festkörpersysteme sind, um das **2D-XY**-Modell zu erforschen, sowie die Auswirkungen von 3D-Wechselwirkungen und zusätzlichen Spin-Raum Anisotropien auf magnetische Fluktuationen zu untersuchen.

Bei $\text{CeCu}_{5.8}\text{Au}_{0.2}$ betrachten wir die Temperaturabhängigkeit der **AFM** Bragg-Intensität, der Amplitude und der Energiebreite der magnetischen diffusen Streuung in der Nähe von T_N und bestimmen die entsprechenden kritischen Exponenten β, γ und z . Für die Bestimmung des dynamischen kritischen Verhaltens benutzen wir die höhere Energieauflösung der **NSE**-Spektroskopie um frühere **TAS**-Messungen von Stockert *et al.* [1] im Bereich $T_N < T < 1$ K zu vervollständigen. Dabei finden wir unmittelbar oberhalb von T_N ein Skalierungsverhalten der charakteristischen Energie, welches durch ein klassisches 3D Potenzgesetz beschrieben werden kann. Da die **TAS**-Daten von Stockert *et al.* bei höheren Temperaturen mit einer quantenkritischen Skalierung kompatibel sind, deuten unsere Ergebnisse demnach den erwarteten Übergang vom quantenkritischen zum klassischen Skalierungsverhalten an. Das Skalierungsverhalten des Ordnungsparameters ist mit der Molekularfeldtheorie vereinbar, was auf die Präsenz von dominanten langreichweitigen **RKKY**-Wechselwirkungen zurückgeführt wird. Die Temperaturabhängigkeit der kritischen Amplitude oberhalb von T_N kann keiner Universalitätsklasse zugeordnet werden. Im quantenkritischen System $\text{CeCu}_{5.9}\text{Au}_{0.1}$ konnte mit unseren **NSE**-Messungen kein kritisches Verhalten beobachtet werden. Daher ist stattdessen geplant die Veränderung des kritischen Verhaltens bei Annäherung an den quantenkritischen Punkt in $\text{CeCu}_{5.8}\text{Au}_{0.2}$ durch Anwendung von hydrostatischem Druck zu untersuchen.

1. Introduction

Materials with strongly correlated electrons often show a wealth of physical ground states due to competing energy-scales of spin-orbit coupling (SOC), crystal field splitting, Hund's coupling, and inter-site exchange interactions. Apart from the extensively studied 3d-electron Transition Metal Oxides (TMO) [2], in recent years also TMO of other periods attracted much attention [3]. In particular, the group of layered ruthenates aroused interest by the discovery of unconventional superconductivity in Sr_2RuO_4 [4]. It turned out that the ruthenates exhibit a complex phase diagram and spin-excitations [5–7], which highly encourage to investigate the critical magnetic fluctuations close to the phase transitions. Such fluctuations can reveal important information on a system as they are inherently coupled to its ground state. In heavy-fermion systems the competition of interactions can suppress magnetic ordering and induce a quantum critical point (QCP). Here, the investigation of critical fluctuations is also of high interest as exotic physical phases such as superconductivity can occur close to QCPs [8–11].

One of the first studies of critical phenomena was related to the transition between the liquid and gaseous phases of carbon dioxide [12]. Due to the occurrence of density fluctuations near the critical point, enhanced light scattering (critical opalescence) was observed as soon as the correlation length of the density fluctuations coincided with the wavelength of visible light. The magnetic analogue of density fluctuations are critical fluctuations of the magnetic order parameter, that emerge in proximity to the magnetic transition temperature \tilde{T}_c (Curie- or Néel-temperature) of second order phase transitions. These fluctuations are characterized by a correlation length ξ and a response time τ , which both diverge at \tilde{T}_c [13–16]. In the critical regime, *i. e.* close to \tilde{T}_c , fundamental physical properties of a material, such as the magnetic susceptibility and the heat capacity, adopt critical behavior and can be described by power-laws $\propto |t|^\lambda$, with critical exponents λ and $t \equiv (T/\tilde{T}_c - 1)$ [14–18]. The

scaling behavior in the spatial and time domains are related via $\Gamma \propto \kappa^z \propto t^{z\nu}$ [15], with the critical exponents ν of the inverse correlation length $\kappa = \xi^{-1}$ and z of the characteristic energy $\Gamma \propto \tau^{-1}$. A hallmark of the corresponding scaling theory is the concept of universality [16, 19, 20], which predicts that the critical exponents are independent of microscopic details, and depend exclusively on the dimensionality of the interactions and the dimensionality of the order parameter as well as the range of the couplings. In magnetic systems, the scaling behavior of magnetic critical fluctuations thus encodes the spatial dimensionality of the system and possible magnetic anisotropies [16]. In particular the 2D-XY model has attracted significant attention, since it was employed as the model system for the unconventional vortex-unbinding transition proposed by Berezinskii, Kosterlitz, and Thouless (BKT) [21–23]. The fingerprints of BKT-transitions were observed in superfluid ^4He -films [24, 25] and proximity-coupled Josephson junction arrays [26, 27]. Yet, solid-state materials that realize the 2D-XY model are sparse [28–32].

Besides the classical second order phase transitions at finite temperatures, phase transitions at $T = 0$ can also occur [33–36]. The so-called quantum phase transitions (QPTs) are accompanied by quantum fluctuations and are driven by non-thermal tuning parameters, including pressure, doping, and magnetic field. In analogy to the critical point in classical phase transitions, the QPT takes place at the QCP. The QCP at $T = 0$ cannot be reached experimentally, but it can affect the critical behavior of the system at finite temperatures and support the emergence of intriguing physical phases such as superconductivity [8–11, 37].

A key experimental technique for the investigation of critical magnetic scattering is neutron TAS, which exploits the proportionality between the magnetic neutron scattering cross section and the dynamic scattering function $S(\mathbf{Q}, \omega)$, where the latter contains κ and Γ [38–40]. Γ can be derived from TAS energy-scans of the critical magnetic scattering, while κ corresponds to the energy-integrated width in momentum space (\mathbf{Q} -space). Pioneering studies investigated the critical magnetic fluctuations in classical magnetic systems, such as the 3D ferromagnet (FM) EuO [41–43] and the 3D AFM RbMnF₃ [44, 45]. Furthermore, TAS studies were carried out on systems with quasi-2D magnetic correlations, including the isotropic square-lattice AFMs Rb₂MnF₄ [46], Sr₂CuO₂Cl₂, and Sr₂Cu₃O₄Cl₂ [47], as well as the AFM parent compounds of the cuprate superconductors [48], which exhibit two-

dimensional Heisenberg (2D-H) scaling properties above their Néel temperatures. Complementary to TAS experiments, improved energy resolution was achieved with the NSE technique [49, 50], where groundbreaking works were on the critical dynamics in the isotropic FMs EuO and Fe [51, 52]. More recently, NSE helped to resolve controversies about the scaling behavior of heavy-fermion superconductors [53] and revealed a crossover in the dynamic scaling of the classical AFMs MnF₂ and Rb₂MnF₄ close to T_N [54].

Furthermore, critical magnetic fluctuations were investigated in 5d-electron TMO using X-ray scattering. In single-layer Sr₂IrO₄, which exhibits strong SOC [55, 56], nearly ideal 2D-H scaling was reported [57, 58]. On the other hand, in bilayer Sr₃Ir₂O₇ the scaling behavior close to the transition is consistent with the 3D-I universality class, but significant deviations were found and attributed to disorder [59].

In 4d-electron TMO, critical fluctuations have remained unexplored to date. Notably, ruthenates show a plethora of electronic ground states [3, 60–63] such as unconventional superconductivity in Sr₂RuO₄ [4] and excitonic AFM order in the Mott-insulator Ca₂RuO₄ [64, 65], arising from a delicate competition between the energy scales of SOC, crystal field splitting, Hund’s coupling, and inter-site exchange interactions. In the latter compound, spins are arranged in an AFM fashion within square-lattice RuO₂ planes and stacked along the *c*-axis in a G-type pattern with a Néel temperature $T_N \sim 110\text{K}$ [66–68]. The excitonic character is believed to result from excitonic transitions between non-magnetic singlet ($J_{\text{eff}}=0$) and magnetic triplet states ($J_{\text{eff}}=1$) [64, 65]. The nature of the excitonic magnetism was recently corroborated by Resonant Inelastic X-ray Scattering (RIXS) [69], Raman scattering [70], as well as Inelastic Neutron Scattering (INS), detecting a soft amplitude mode (‘Higgs-mode’) in the spin-wave spectrum [6].

The unquenched orbital angular momentum of the Ru magnetic moments in Ca₂RuO₄ further results in a highly unusual spectrum of transverse magnons in the AFM state [6]. The low-energy magnetic Hamiltonian derived from an analysis of this spectrum is dominated by an XY-type single-ion anisotropy, which is much larger than the nearest-neighbor exchange interaction and an Ising-type single-ion anisotropy resulting from an orthorhombic distortion of the crystal structure. At the same time, the INS experiments did not reveal any dispersion of the magnons

perpendicular to the RuO_2 layers, which implies that the interlayer interactions are much weaker than the interactions within the layers. The evidence for an approximate **2D-XY** symmetry of the magnetic Hamiltonian derived from the analysis of the magnon dispersions has motivated the present study.

In contrast to the Mott insulator Ca_2RuO_4 , the bilayer compound $\text{Ca}_3\text{Ru}_2\text{O}_7$ is metallic in the paramagnetic state and maintains considerable electrical conductivity below the Néel temperature $T_{\text{N},1} \sim 56 \text{ K}$ [71]. The magnetic structure is A-type **AFM** (*i. e.* **FM** bilayers with alternating orientation along the c-axis) [71, 72]. A second magnetic transition associated with a reorientation of the spins from the a- to the b-axis in the RuO_2 planes [73] and a greater reduction of the electrical conductivity occurs at $T_{\text{N},2} \sim 48 \text{ K}$ [71]. As the crystal structure of $\text{Ca}_3\text{Ru}_2\text{O}_7$ comprises two closely spaced RuO_2 layers within a unit cell, substantial interlayer interactions within a bilayer unit are expected and were indeed identified in **INS** studies of the magnon dispersions [7, 74]. As exchange interactions between bilayer units are weak, the dimensionality of the exchange-bond network is intermediate between 2D and 3D. The **INS** data also revealed an anisotropy gap, but were insufficient for a determination of the nature of the dominant anisotropy (Ising versus XY).

Additionally was found that only a marginal doping of the Ru-sites in $\text{Ca}_3\text{Ru}_2\text{O}_7$ with non-magnetic Ti-ions $\text{Ca}_3(\text{Ru}_{1-x}\text{Ti}_x)_2\text{O}_7$ is sufficient to reverse the **AFM** A-type state back to the G-type state that is realized in Ca_2RuO_4 [75–78]. In this regard, the two step-transition in $\text{Ca}_3\text{Ru}_2\text{O}_7$ turns into a sharp simultaneous magnetic, electronic, and structural transition with rather first-order character. The magnons in the spin-excitation spectrum of 1% Ti-doped $\text{Ca}_3\text{Ru}_2\text{O}_7$ could be described by a similar Hamiltonian as for Ca_2RuO_4 , but with an additional intra-bilayer coupling term [79].

From the spin-excitations in the ordered state, all three compounds can be considered as quasi-2D (bi-)layered square-lattice **AFMs**, with a significant easy-plane anisotropy, which are the essential requirements for the **2D-XY** model. Thus, a study of the critical behavior near T_{N} in Ca_2RuO_4 , $\text{Ca}_3\text{Ru}_2\text{O}_7$ and $\text{Ca}_3(\text{Ru}_{0.99}\text{Ti}_{0.01})_2\text{O}_7$ is of great interest.

The study of the critical magnetic fluctuations in $4f$ heavy-fermion systems is also very interesting, as these compounds are particularly suitable to investigate **QCPs**

due to a balanced interplay between Kondo screening and the **RKKY** interaction. In this context, the heavy-fermion series $\text{CeCu}_{6-x}\text{Au}_x$ with a quantum critical doping of $x_c \simeq 0.1$ and the possibility to prepare sufficiently large crystals for neutron scattering experiments aroused wide scientific interest. With respect to the dynamical critical behavior, a temperature dependence of the characteristic energy Γ was observed by **TAS** for the undoped ($x = 0$), the quantum critical ($x = 0.1$) and the nearly quantum critical ($x = 0.2$) systems, which is compatible with a quantum critical behavior ($\Gamma \propto k_B T$) at elevated temperatures [1]. However, at least for $\text{CeCu}_{5.8}\text{Au}_{0.2}$ with 3D **AFM** order below $T_N \sim 0.25$ K, one would expect a crossover to a classical scaling behavior near T_N . Yet, such a crossover may not have been observed because of the limited energy resolution of the **TAS** spectrometer.

In this work, we use high-resolution neutron **TAS** and **NSE** spectroscopy to examine the critical magnetic properties in the single-layer Ca_2RuO_4 , the bilayer $\text{Ca}_3\text{Ru}_2\text{O}_7$, and the Ti-doped bilayer $\text{Ca}_3(\text{Ru}_{0.99}\text{Ti}_{0.01})_2\text{O}_7$ as well as in the heavy-fermion compound $\text{CeCu}_{5.8}\text{Au}_{0.2}$. We extract static and dynamical critical exponents to determine the spin dimensionalities and relevant anisotropies. For the layered ruthenates it is of particular interest whether or not a **2D-XY** scaling can be observed and how the critical behavior is affected by the additional intra-bilayer exchange interactions and Ti-doping. For $\text{CeCu}_{5.8}\text{Au}_{0.2}$, we aim to resolve the expected quantum-to-classical crossover in the dynamical scaling behavior by taking advantage of the high energy-resolution of **NSE**.

2. Critical Magnetic Phenomena

We review critical phenomena in proximity to magnetic phase transitions. The study of the critical behavior can help to understand the nature of the magnetic ground state of complex systems by mapping them onto simple models (universality classes). Critical scaling can uncover magnetic anisotropies and dimensionality crossovers. We briefly discuss some basic aspects of quantum phase transitions.

2.1. Introduction

There are a number of comprehensive textbooks and review articles on critical phenomena. The most important for this work are Refs. [14–16, 80–83].

The first studies of critical phenomena were performed by Thomas Andrews in 1869 [12] on classical transitions between the gas-liquid phases of CO_2 . The p - T -diagram of such systems contains phase boundaries, which separate the single-phase regimes [Fig. 2.1a]. Right on top of such phase boundaries, the adjacent phases of both sides coexist. Tuning parameters such as temperature or pressure can be used to transfer one phase to the other across the phase boundaries. Since the two phases coexist at the boundaries, their Gibbs potential $G(p,T)$ is equal, but the partial derivatives may be discontinuous [14]. Depending on whether the first or second derivative of G is discontinuous, a distinction was historically made between first- and second-order phase transitions. Nowadays, instead of second-order phase transition, one rather uses the terms *continuous* or *critical* phase transition since G is actually non-analytic at the transition. In addition to the phase boundaries, Fig. 2.1a also shows a critical point (CP) at the end of the gas-liquid line at $T = \tilde{T}_c$. Beyond this CP the gaseous and liquid forms of matter are indistinguishable and can be transformed into each other by a process of continuous change [12].

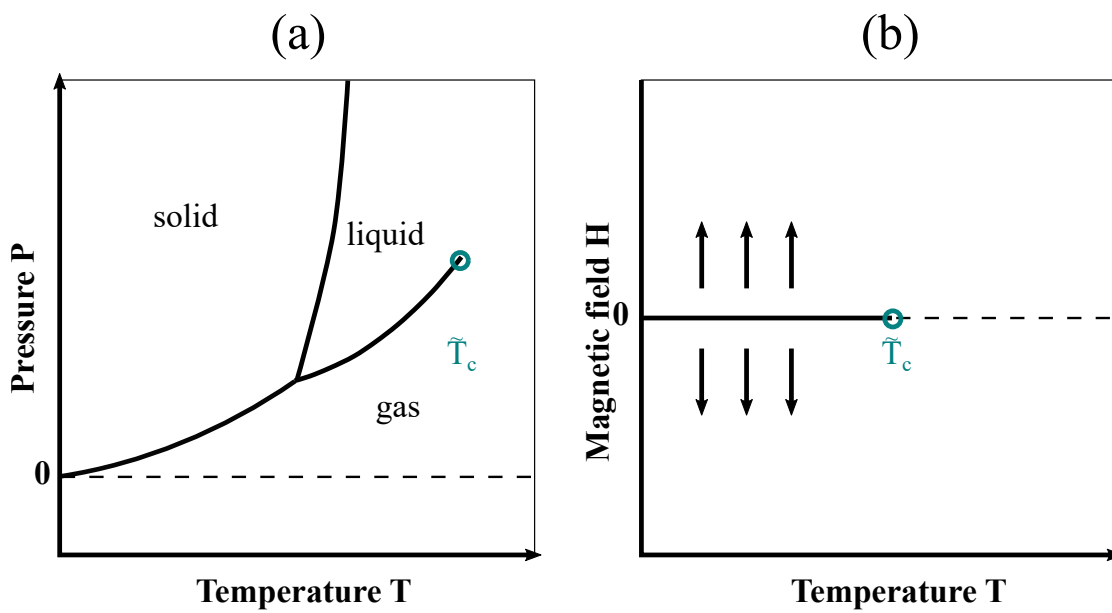


Fig. 2.1: (a) Generic p - T -diagram of a solid-liquid-gas system. The solid lines represent the phase boundaries where the two adjacent phases coexist. Beyond the CP at \tilde{T}_c the gaseous and liquid phases are indistinguishable. (b) Generic H - T -diagram of a magnetic system. Beyond the critical point at $T > \tilde{T}_c$, the order parameter is '0' (dashed line), while it is non-zero for $T < \tilde{T}_c$ (solid line). By applying a magnetic field the magnetization can be changed. Adapted from [14].

The magnetic analogue of the p - T -diagram for solid-liquid-gas systems is the H - T -diagram for magnetic systems [Fig. 2.1b]. Here the solid line corresponds to the magnetization, which can be changed by applying an external magnetic field or varying the temperature. In the H - T -diagram the CP is located at the transition temperature \tilde{T}_c , which is the Curie-temperature T_c for FMs and the Néel-temperature T_N for AFMs. The Gibbs potential for magnetic systems then turns to $G(T, H) = U - TS - MH$, with the internal energy U , the entropy S , and the external field H [82]. The relation between the specific heat at constant field C_H , the order parameter M_T , and the isothermal magnetic susceptibility χ_T is [14]

$$C_H = -T\left(\frac{\partial^2 G}{\partial T^2}\right)_H, \quad M_T = -\left(\frac{\partial G}{\partial H}\right)_T, \quad \chi_T = -\left(\frac{\partial^2 G}{\partial H^2}\right)_T. \quad (2.1)$$

Hence, for a continuous phase transition, M_T (first derivative of G) is a continuous function of T , whilst C_H and χ_T (second derivatives of G) are discontinuous at \tilde{T}_c [Fig. 2.2]. It has been found that in proximity to a CP three characteristics are often met [16]: (i) An order parameter M exists that is a continuous function of T and shows symmetry breaking while traversing the CP at \tilde{T}_c from $M > 0$ ($T < \tilde{T}_c$) to $M = 0$ ($T \geq \tilde{T}_c$). (ii) Fluctuating microregions emerge (magnetic moments), which diverge in size (correlation length ξ) as \tilde{T}_c is approached from both sides. (iii) The relaxation time $\tau = \omega_c^{-1}$ of the system diverges when \tilde{T}_c is approached (*critical slowing down*). Here ω_c denotes the characteristic energy of the fluctuating microregions.

2.2. Universality, critical exponents and scaling

The Ginzberg-Landau theory —also called mean-field (MF) theory— is the simplest approach to describe continuous phase transitions quantitatively [16]. The basic assumption is that the free energy $F(T, M) = U - TS$ can be expanded in power series as a function of the order parameter close to \tilde{T}_c [14]. Strictly speaking, this is not correct since the thermodynamic properties at \tilde{T}_c are non-analytic, but the model is solvable and holds for long-ranged correlations. It follows from the expansion that the magnetic order parameter M , the isothermal magnetic susceptibility χ , and the correlation length ξ can be described with simple power-

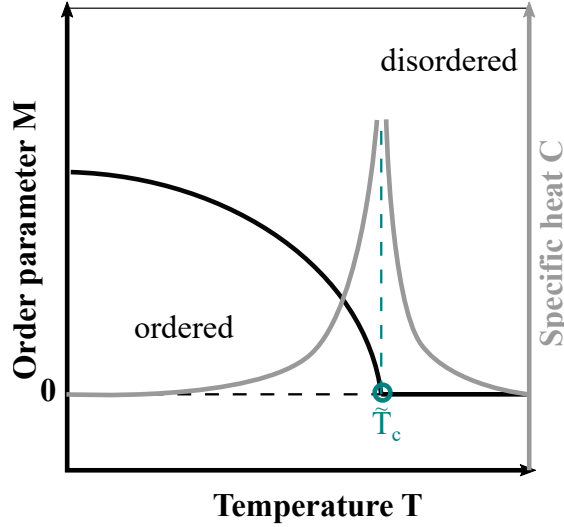


Fig. 2.2: Generic order parameter-temperature diagram of a continuous magnetic phase transition. Beyond the CP at $T > \tilde{T}_c$ the order parameter is 0, while it increases continuously for $T < \tilde{T}_c$. The grey solid line shows the heat capacity C_H with the corresponding discontinuity at $T = \tilde{T}_c$.

laws (PLs) $|t|^\lambda$ with the reduced temperature $t = (T - \tilde{T}_c)/\tilde{T}_c$ and the *critical exponents* λ (see Tab. 2.1). In general, the MF theory allows different critical exponents depending on whether the CP is approached either from above ($T > \tilde{T}_c$) or below ($T < \tilde{T}_c$). This is often indicated in literature by the use of λ or primed λ' , respectively. For the specific heat C a jump at \tilde{T}_c is predicted by MF theory. The correlation length ξ is mathematically defined as the mean distance r over that the equal-time spin pair correlation function decreases by $1/e$ [82]

$$G^{\alpha\beta}(\mathbf{r}, \xi) \equiv \langle s^\alpha(0) s^\beta(r) \rangle \approx |r|^{-1} \exp(-|r|/\xi) \quad . \quad (2.2)$$

$G^{\alpha\beta}(\mathbf{r}, \xi)$ is the probability of finding a spin at position \mathbf{r} pointing along the β direction, if a spin at the origin points along α . The Fourier transform of $G(\mathbf{r}, \xi)$ is the static scattering function $S(\mathbf{Q}, \kappa)$ with $\mathbf{Q} = \mathbf{G}_m + \mathbf{q}$, where \mathbf{G}_m is a magnetic reciprocal lattice vector, \mathbf{q} the relative momentum transfer, and $\kappa \equiv 1/\xi$ the inverse correlation length. $S(\mathbf{q})$ is proportional to the real part of the q -dependent susceptibility $\chi'(\mathbf{q}) \propto S(\mathbf{q})/T$ (see Eqn. (2.27) below) [38, 84]. $\chi'(\mathbf{q})$

was originally expressed in the Ornstein-Zernike form ($\eta = 0$) and later refined to [13, 16, 85]

$$\chi'(\mathbf{q}) = \frac{\chi'(\mathbf{0})}{[1 + q^2(1 - \eta/2)^{-1}/\kappa^2]^{1-\eta/2}} \quad , \quad (2.3)$$

with the critical exponent η and the staggered magnetic susceptibility $\chi'(\mathbf{0}) \equiv \chi_0$, which includes the out-factored term $\kappa^{-(2-\eta)}$. We will see in Chap. 5 that $\chi'(\mathbf{q})$ can be directly obtained from neutron scattering experiments [38, 82, 84].

Property	Exponent	PL	Conditions	MF value	Exp.
Susceptibility χ_T	γ	$t^{-\gamma}$	$T > \tilde{T}_c$	1	1.3-1.4
Magnetization M	β	$(-t)^\beta$	$T < \tilde{T}_c$	0.5	0.2-0.4
Magnetization M	δ	$H^{1/\delta}$	$T = \tilde{T}_c$	3	3-6
Specific heat C_H	α	$t^{-\alpha}$	$T > \tilde{T}_c$	jump	-0.3-0.3
Correlation length ξ	ν	$t^{-\nu}$	$T > \tilde{T}_c$	0.5	0.6-0.7

Tab. 2.1: Definitions of some magnetic critical exponents and comparison of the MF predictions with values found in experiments. From [16].

Although it is evident from Tab. 2.1 that the predictions of the MF theory deviate considerably from the experimentally observed critical exponents, the PL behavior of the physical properties close to \tilde{T}_c has been confirmed in a number of experiments, as discussed in Ref. [16] and exemplarily shown for RbMnF₃ in Fig. 2.3.

Another hallmark of critical phenomena is the concept of *universality* [16, 19, 20], dictating that λ depends exclusively on the long- or short-range nature of the interactions as well as the dimensionality of the system d and order parameter n . This is an important observation because it states that microscopic details such as the type of the elements or the sign of the interaction J are not relevant close to \tilde{T}_c . This enables to assign even complex systems to simple models (universality classes). In magnetic systems, the order parameter usually evolves according to an Ising ($n = 1$), XY ($n = 2$), or Heisenberg ($n = 3$) model with the general Hamiltonian [16]

$$\mathcal{H} = \sum_{\langle i,j \rangle} J_{ij}(S_i^x S_j^x + S_i^y S_j^y + S_i^z S_j^z) \quad , \quad (2.4)$$

where $J_{ij} > 0$ ($J_{ij} < 0$) couples the nearest neighbour spins on site i and j with pre-

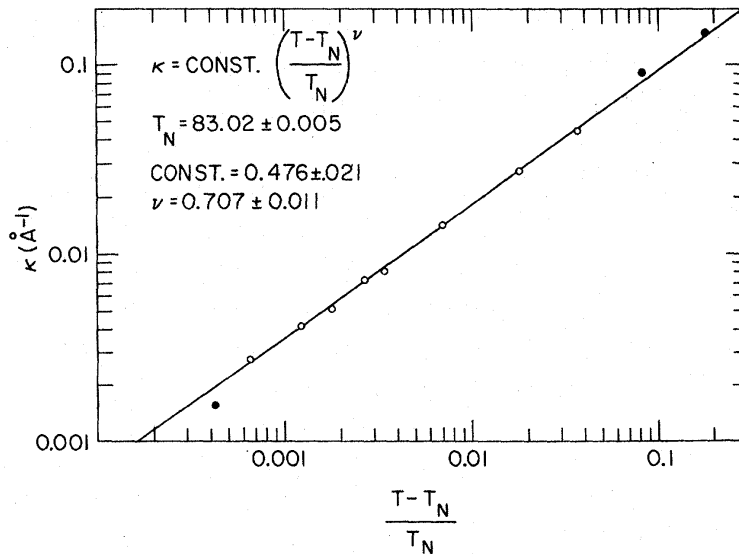


Fig. 2.3: Inverse correlation length $\kappa(T)$ in RbMnF₃. The critical exponent ν was obtained from the slope of a linear fit on double logarithmic scales. From [44].

ferred antiparallel (parallel) alignment. In particular, the **2D-XY** model attracted much interest in recent years due to the proposed unconventional topological phase transition (see below) [21–23].

In addition to the universality, the concept of *critical scaling* motivates the study of critical phenomena. The basic assumption of critical scaling is that only one fundamental length scale (ξ) is relevant [14, 86]. The static scattering function can be expressed by a product of $\kappa = \xi^{-1}$ and q with the scaling functions $f(x) = x^{-1}f'(x)$ where we define $x \equiv q/\kappa$

$$S(q, \kappa) = q^y f(x) \quad , \quad (2.5)$$

$$S(q, \kappa) = \kappa^y f'(x) \quad . \quad (2.6)$$

In the asymptotic limits $x \gg 1$ and $x \ll 1$ the scaling functions can be approximated by $\lim_{x \rightarrow \infty} f(x) \simeq 1$ and $\lim_{x \rightarrow 0} f'(x) \simeq 1$, respectively. If one then compares for instance (i) $S(q, 0) \propto q^{-2+\eta}$ [Eqn. (2.3)] and $S(q, 0) \sim q^y$ with (ii) $\chi_0 \propto S(0, \kappa) \propto t^{-\gamma} \propto \kappa^{-\gamma/\nu}$ [see Tab. 2.1] and $S(0, \kappa) \sim \kappa^y$ one gets the scaling

Model	MF [16]	2D-I [16]	3D-I [18]	2D-XY [23, 91]	3D-XY [92]	3D-H [93]
α	-	0	0.110(1)	-	-0.007(9)	-0.1336(15)
β	0.5	0.125	0.3265(3)	0.23	0.346(9)	0.3689(3)
γ	1	1.75	1.2375(2)	-	1.316(9)	1.3960(9)
δ	3	15	4.789(2)	15	4.81(8)	4.783(3)
η	0	0.25	0.0364(5)	0.25	0.03(2)	0.0375(5)
ν	0.5	1	0.6301(4)	-	0.669(3)	0.7112(5)

Tab. 2.2: Overview of (approximated) critical exponents of conventional universality classes. Besides the MF theory, only the 2D-I model is analytically solvable.

relation $\nu(2 - \eta) = \gamma$. Similarly, additional scaling relations between the critical exponents can be found, such as [14, 86, 87]:

$$2\beta + \gamma = 2 - \alpha \quad (2.7)$$

$$\beta(\delta + 1) = 2 - \alpha \quad (2.8)$$

$$\gamma(\delta + 1)/(\delta - 1) = 2 - \alpha \quad (2.9)$$

$$d\nu = 2 - \alpha \quad (2.10)$$

$$d\gamma/(2 - \eta) = 2 - \alpha \quad (2.11)$$

Consequently, knowledge of only two critical exponents may be sufficient to determine the remaining exponents as well. The scaling hypothesis also implies that the critical exponents λ and λ' , introduced in the MF theory for approaching \tilde{T}_c either from above or below, are the same.

To date only the two-dimensional Ising (2D-I) model could be solved analytically [88] and exact critical exponents were calculated, while the other values are approximated by different methods [18], mostly based on the renormalization group theory [89, 90]. In Tab. 2.2, the derived critical exponents for the conventional universality classes are listed in comparison with the MF values. The values can slightly vary depending on the underlying computation method, as described in [18].

2.3. Exceptions and crossover

Thus far, we only considered the critical behavior of models for which a magnetic ordering at finite temperatures is predicted. This is not the case, for instance, for the 2D-XY and 2D-H models [94]. Nevertheless, it has been shown experimentally that in systems with weak interlayer coupling J' , quasi-2D critical fluctuations can occur at temperatures above the 3D long-range ordering and affect the scaling behavior [48, 95, 96]. Above a crossover temperature $T_{co} > \tilde{T}_c$, the scaling may then be consistent with the predictions of quasi-2D models. Apart from that, the scaling behavior in these models can deviate from the simple PL scaling, as will be discussed below.

2D-Heisenberg model

Chakravarty, Halperin and Nelson [97, 98] described the 2D quantum Heisenberg model by a quantum non-linear σ model and derived, via renormalization group calculations, an expression for $\xi(T)$ and $S(\mathbf{0}, T)$. Subsequently Hasenfratz and Niedermayer [99] refined the expressions to

$$\xi \simeq \frac{e}{8} \frac{c}{2\pi\rho_s} \exp(2\pi\rho_s/T) \left(1 - 0.5 \frac{T}{2\pi\rho_s} \right) \quad , \quad (2.12)$$

with ρ_s and c denoting the $T = 0$ spin stiffness and the spin-wave velocity, respectively. These quantities depend on the nearest neighbour exchange coupling J and can be approached by using results from spin-wave approximation as described in Refs. [100, 101]. In Fig. 2.4, we exemplarily show 2D-H scaling of $\kappa(T)$ [Eqn. (2.12)] for the AFM parent compounds of the cuprate superconductors $\text{La}_{2-x}\text{Sr}_x\text{CuO}_4$. Keimer *et al.* [48] further proposed an expression accounting for the effects of 3D critical fluctuations

$$\xi_{\text{eff}} = \frac{\xi_0}{\sqrt{1 - \alpha_{\text{eff}}\xi_0^2}} \quad , \quad (2.13)$$

where ξ_0 denotes the correlation length of the unperturbed Heisenberg Hamiltonian and α_{eff} defines a suitable combination of perturbative terms. The T -dependence of $S(\mathbf{0}, T)$ was estimated as [98]

$$S(0) \propto T^2 \xi^2 \quad . \quad (2.14)$$

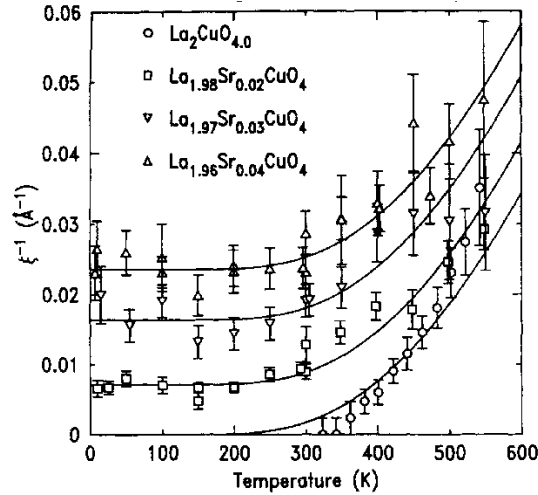


Fig. 2.4: Temperature-dependence of $\kappa(T)$ for pure, lightly doped, and weakly metallic $\text{La}_{2-x}\text{Sr}_x\text{CuO}_4$. The solid lines correspond to fits with the simple model $\kappa(x, T) = \kappa(x, 0) + \kappa(0, T)$ with the 2D-H scaling included in the T-dependent part $\kappa(0, T)$. From [48].

2D-XY model

The 2D-XY model described by Berezinkii, Kosterlitz, and Thouless (BKT-theory [21–23]). The basic concept of the BKT-theory is the existence of a topological phase transition at T_{KT} , with bound vortex-antivortex structures at $T < T_{KT}$ [Fig. 2.5a], that start to dissociate at $T > T_{KT}$ [Fig. 2.5b]. The correlation length in the 2D-XY model is defined as the distance between such vortices above T_{KT} . The vortices itself are characterized by the vorticity \tilde{v} , which denotes the phase change of the spins in multiples of 2π on a contour around the vortex. Regarding the critical behavior, the parameters of this model are the Kosterlitz-Thouless

temperature T_{KT} , $\eta = 0.25$ in $\chi'(q)$ [Eqn. (2.3)], and a dimensionless non-universal parameter b , which was previously determined to be approximately $b = 1.9$ [102]. The T -dependence of the correlation length was derived as [23]

$$\xi \propto \exp\left(\frac{b}{\sqrt{t_{KT}}}\right) \quad \text{with } t_{KT} \equiv (T/T_{KT} - 1) \quad . \quad (2.15)$$

The fingerprints of BKT-transitions were observed in superfluid ^4He films [24, 25] and proximity-coupled Josephson junction arrays [26, 27], whereas solid-state materials that realize the 2D-XY model are sparse [28–32]. BKT-transitions in real magnetic systems were only indirectly observed [103, 104] since the actual vortex unbinding is generally obscured by a 3D magnetic ordering due to finite interlayer coupling J' , as shown in Fig. 2.5c for K_2CuF_4 . For AFMs the relation between T_{KT} and T_N is proposed as [91, 102]

$$\frac{T_N - T_{KT}}{T_{KT}} = \frac{4b^2}{[\ln(J/J')]^2} \quad . \quad (2.16)$$

Moreover, by using the scaling relation $\chi_0 \propto \xi^{2-\eta}$ one gets [23]

$$\frac{S(0)}{T} \propto \exp\left(\frac{B}{\sqrt{t_{KT}}}\right) \quad , \quad (2.17)$$

with $B \equiv b(2 - \eta)$ and T_{KT} from above. Although the observation of the actual BKT-transition at T_{KT} is difficult, 2D-XY scaling may be suitable to describe the critical behavior of systems with even weak magnetic easy-plane anisotropy above T_N , as was theoretically derived in Refs. [105–107] and shown in a number of experiments [28, 29, 31, 102, 104, 108, 109]. Further study of the BKT-transition in solid-state systems therefore requires quasi-2D compounds with pronounced easy-plane anisotropy. In this respect, the square-lattice Ca-ruthenates Ca_2RuO_4 and $\text{Ca}_3\text{Ru}_2\text{O}_7$ are promising candidates, as they exhibit strong tetragonal (XY) single-ion anisotropy [6, 7] (see Chap. 3).

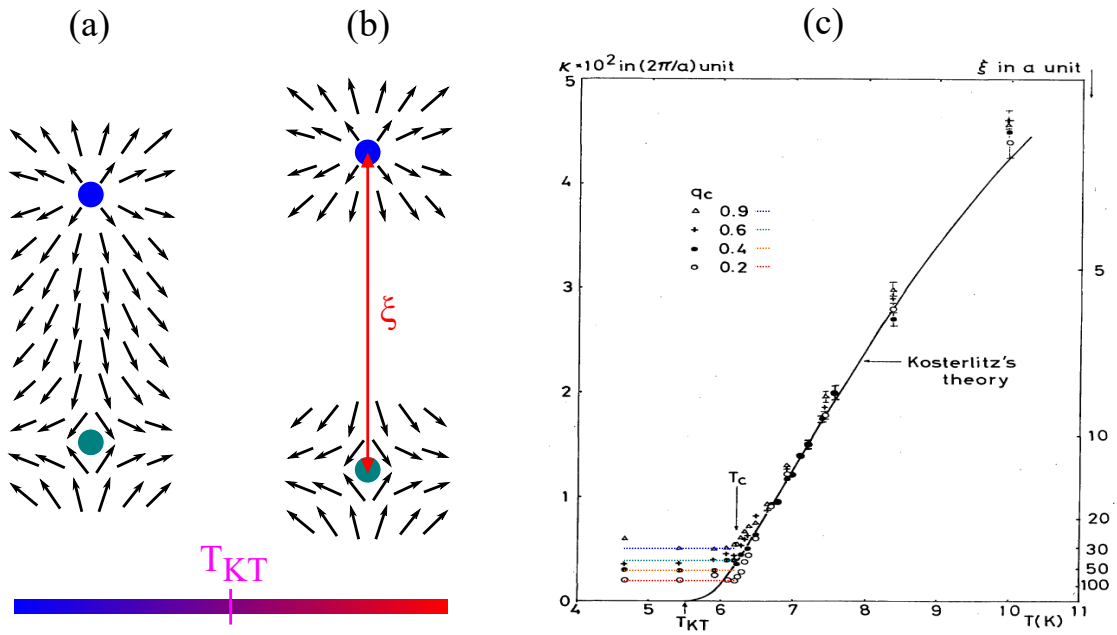


Fig. 2.5: (a,b) Illustration of the BKT-transition. (a) Vortex-antivortex pairs with vorticity $\tilde{v} = \pm 1$ dissociate at T_{KT} into (b) single vortices. ξ defines the correlation length between the isolated vortices above T_{KT} . The blue and green circles indicate the center of the vortices. Adapted from [110]. (c) Inverse correlation length $\kappa(T)$ for K_2CuF_4 with corresponding 2D-XY fit. It is assumed that the actual BKT-transition at T_{KT} is masked by the 3D FM ordering at $T_c > T_{KT}$. The saturation of $\kappa(T \leq T_c)$ at different nonzero values results from a q_c -dependence due to emerging 3D-couplings. From [29] (modified).

Crossover behavior

The critical exponents can indicate a crossover in the scaling behavior as \tilde{T}_c is approached, which is associated with a change in the spin or lattice dimensions. As an example for a crossover in the lattice dimensions from **2D-XY** to three-dimensional XY (**3D-XY**) near T_c , the temperature dependence of the magnetization of K_2CuF_4 is shown in Fig. 2.6. In general, the smallest term of the Hamiltonian is expected to eventually determine the critical behavior close to \tilde{T}_c [94]. For example, if we assume a magnetic Hamiltonian $\mathcal{H} = \mathcal{H}_0 + \mathcal{H}_1 + \mathcal{H}_2 + \mathcal{H}_3$ with the following terms

$$\mathcal{H}_0 = J \sum_{\langle i,j \rangle}^{(d)} \mathbf{S}_i \mathbf{S}_j \quad , \quad (2.18)$$

for an isotropic Heisenberg chain or layer system ($d = 1, 2$), with weak 3D interactions J'

$$\mathcal{H}_1 = J' \sum_{\langle i,j \rangle}^{(3-d)} \mathbf{S}_i \mathbf{S}_j \quad , \quad (2.19)$$

and additional easy-plane

$$\mathcal{H}_2 = E \sum_{\langle i \rangle} \mathbf{S}_i^{z^2} \quad , \quad (2.20)$$

and easy-axis anisotropies

$$\mathcal{H}_3 = \varepsilon \sum_{\langle i \rangle} \mathbf{S}_i^{x^2} \quad , \quad (2.21)$$

we would expect for the energy scales $|J| \gg |E| > |\varepsilon| > |J'|$, that the critical behavior changes from **2D-H** at $T \gg \tilde{T}_c$ upon cooling to **2D-XY**, **2D-I**, and eventually to **3D-I** at $T \geq \tilde{T}_c$. By following the T -dependence of the critical scaling, such crossovers can be detected, revealing important information on the underlying correlations in the system. Besides the empirical determination of the crossover regions, there are simple models for estimating the spin-lattice crossovers. For example, in Ref. [29] it is suggested that the crossover from 2D to 3D or Heisenberg to XY scaling behavior occurs at sufficiently large correlation lengths

$$\xi \geq \sqrt{J/J_A} \quad , \quad (2.22)$$

where J_A denotes an exchange anisotropy term such as J' or J_{XY} and ξ is in units of the corresponding lattice parameter. On the other hand, in Ref. [111], a crossover temperature from Heisenberg (XY) to Ising scaling was derived as

$$T_{\text{co}} = (J_A/J)^{1/\tilde{\delta}} T_N + T_N \quad , \quad (2.23)$$

with $\tilde{\delta} = 1.25$ (1.175).

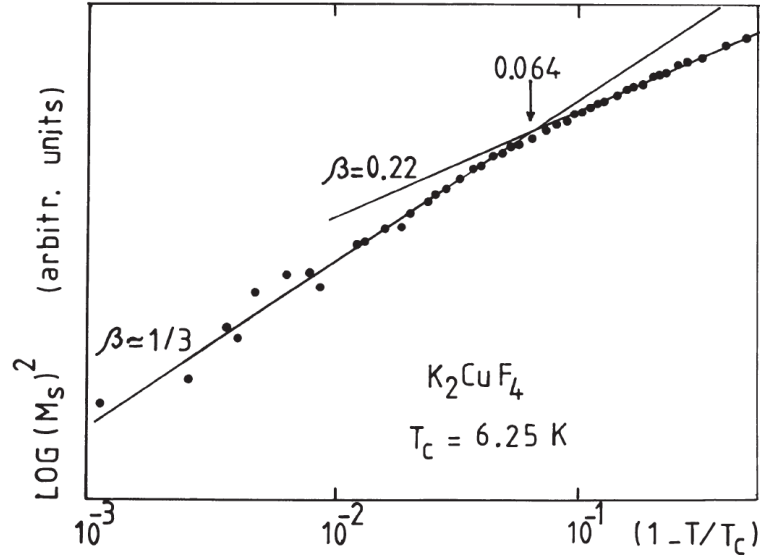


Fig. 2.6: Exemplary crossover in the lattice dimensions of K_2CuF_4 indicated by a change in the critical scaling of the magnetization M at $T_{\text{co}} < T_c$ from **2D-XY** ($\beta = 0.22$) to **3D-XY** ($\beta = 0.33$) upon heating. From [94].

2.4. Dynamic critical scaling

In the following, the dynamic properties of the critical fluctuations are discussed. Analogous to the static scattering function $S(\mathbf{q})$, we consider now the dynamic scattering function $S(\mathbf{q}, \omega)$, which is the Fourier transform of the time-dependent correlation function [84]. We will see in Chap. 5, that the cross section in neutron scattering is proportional to the dynamic scattering function $S(\mathbf{q}, \omega)$ with $\mathbf{Q} = \mathbf{G}_m + \mathbf{q} = \mathbf{k}_i - \mathbf{k}_f$ and $\omega = \hbar(k_i^2 - k_f^2)/(2m)$, where $\mathbf{k}_{i,f}$ are the incident and final

neutron wave vectors [38, 84]. The scattering function $S(\mathbf{q}, \omega)$ is related to the imaginary part of the generalized magnetic susceptibility via

$$S(\mathbf{q}, \omega) = \frac{\chi''(\mathbf{q}, \omega)}{1 - \exp(-\hbar\omega/k_{\text{B}}T)} \quad . \quad (2.24)$$

The denominator in Eqn. (2.24) is also known as the *detailed balance factor* according to the *detailed balance* principle [84]:

$$S(-\mathbf{q}, -\omega) = \exp(-\hbar\omega/k_{\text{B}}T)S(\mathbf{q}, \omega) \quad , \quad (2.25)$$

which accounts for the probability of a transition in the sample, that will be lower for excitation annihilation than for excitation creation [38]. The detailed balance factor is only relevant for relatively low sample temperatures, as used *e. g.* in our CeCu_{5.8}Au_{0.2} study (*cf.* Chap. 7).

The real and imaginary parts of the generalized susceptibility $\chi(\mathbf{q}, \omega)$ are Kramers–Kronig related. A general form of $\chi''(\mathbf{q}, \omega)$ is given by $\chi''(\mathbf{q}, \omega) = \chi'(\mathbf{q})F(\omega)\omega$, where $\chi'(\mathbf{q})$ is the real part of the static susceptibility (see Eqn. (2.3)) and $F(\omega)$ the spectral weight function, which is an even function of ω and satisfies the normalization condition $\int_{-\infty}^{\infty} F(\omega)d\omega = 1$. Above the ordering temperature, spin fluctuations at small \mathbf{q} are strongly damped and the spectral-weight function takes on a Lorentzian shape [38]:

$$F(\omega) = \frac{1}{\pi} \frac{\Gamma}{\Gamma^2 + \omega^2} \quad . \quad (2.26)$$

In this case, the characteristic energy of the critical fluctuations ω_c , that is defined as $\int_{-\omega_c}^{\omega_c} F(\omega)d\omega = 0.5$ equals the half-width at half-maximum (HWHM) Γ of the Lorentzian-function.

The Kramers-Kronig relation connects $\chi'(\mathbf{q})$ and $S(\mathbf{q}, \omega)$ via

$$\begin{aligned} k_{\text{B}}T\chi'(\mathbf{q}) &= \int_{-\infty}^{\infty} \frac{1 - \exp(-\hbar\omega/k_{\text{B}}T)}{\hbar\omega/k_{\text{B}}T} S(\mathbf{q}, \omega) d(\hbar\omega) \\ &\simeq \int_{-\infty}^{\infty} S(\mathbf{q}, \omega) d(\hbar\omega) = S(\mathbf{q}) \quad , \end{aligned} \quad (2.27)$$

where $\hbar\omega \ll k_{\text{B}}T$ was assumed [38, 84]. From this follows $S(0) \propto \chi_0 T$ for the static

case at $\mathbf{q} = 0$. To determine $S(\mathbf{q})$, in principle, it would be required to measure the entire $S(\mathbf{q}, \omega)$ function and perform a numerical ω -integration. This can be avoided in 2D systems by using an energy integrating **TAS** configuration, as introduced by Birgeneau *et al.* [112] and described in Chap. 5.

In analogy to the static critical scaling, the dynamic scaling hypothesis [15, 17, 82] states that the characteristic energy ω_c can be expressed as a product of κ or q and a scaling function $\Omega(q/\kappa) = (q/\kappa)^z \Omega'(q/\kappa)$

$$\omega_c(\mathbf{q}, \kappa) = \kappa^z \Omega(q/\kappa) \quad , \quad (2.28)$$

$$\omega_c(\mathbf{q}, \kappa) = q^z \Omega'(q/\kappa) \quad , \quad (2.29)$$

with the dynamical critical exponent z . In consequence, the concept of dynamic scaling links the spatial and frequency domain of a system. In the asymptotic limits, ω_c is related to the correlation length by $\lim_{q \rightarrow 0} \omega_c(\mathbf{q}, \kappa) \sim \kappa^z$, and thus the relaxation time $\tau = 1/\omega_c$ diverges as \tilde{T}_c is approached (*critical slowing down*). On the other hand, for the q -dependence of ω_c at \tilde{T}_c , it follows $\lim_{\kappa \rightarrow 0} \omega_c(\mathbf{q}, \kappa) \sim q^z$. In the following, we refer ω_c to Γ as we always assume a Lorentzian-shaped spectral weight function $F(\omega)$ for the description of critical fluctuations [Eqn.(2.26)]. An experimental example of the dynamic scaling for Rb_2CoF_4 is shown in Fig. 2.7.

In contrast to the universality of the static critical behavior (d , n , range of correlations), the dynamic critical exponents depend also on the conservation laws of the system [114, 115]. Thus, the dynamic critical exponents of systems belonging to the same static universality class can differ. This is the case, for instance, for 3D isotropic magnets, where the order parameter commutes with the Hamiltonian of the three-dimensional Heisenberg (**3D-H FM**), while it does not commute with that of the **3D-H AFM** [16]. We have listed in Tab. 2.3 the approximated dynamic critical exponents for various universality classes. The value of z for the **2D-I** model is still under debate and varies between 1.4 and 2.2 depending on the underlying computation method, as discussed in Ref. [116]. The chosen value $z = 1.75$ follows from a conventional theory $z = 2 - \eta$ and has been approved experimentally, for example, for Rb_2CoF_4 [Fig. 2.7]. Similar to the static critical behavior, the dynamic critical properties are also affected by changes in the spin-lattice dimensions, and

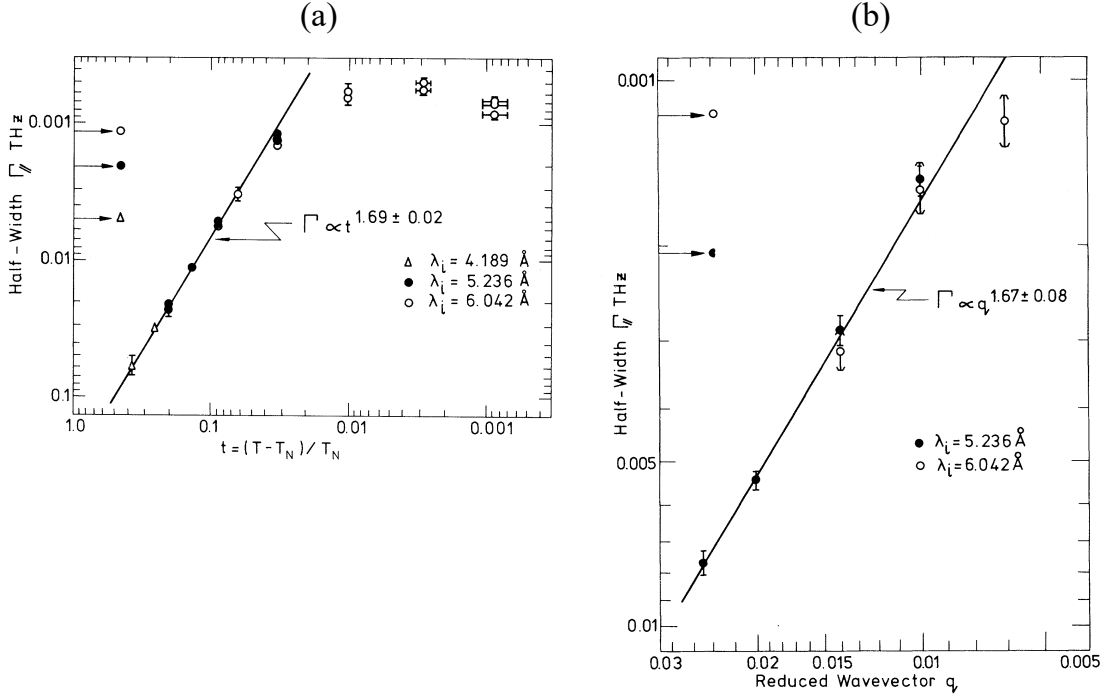


Fig. 2.7: Dynamic scaling of the characteristic energy $\Gamma(T, q)$ of the 2D-I system Rb_2CoF_4 . (a) T -dependence of $\Gamma(T)$ with corresponding scaling fit $\Gamma \propto \kappa^z \propto t^{z\nu}$. (b) Q -dependence of $\Gamma(q)$ with scaling fit $\Gamma \propto q^z$. The horizontal arrows indicate the energy resolution for the corresponding neutron wavelengths. From [113].

Models	Formula	Approx. z	ν	$z\nu$
3D-H FM [15]	$(d + 2 - \eta)/2$	2.5	0.7112	1.778
3D-H AFM [15]	$d/2$	1.5	0.7112	1.067
3D-XY [117]	$d/2$	1.5	0.669	1.004
3D-I [15, 118]	$2 + \alpha/\nu$	2	0.6301	1.260
2D-H AFM [15, 98]	$d/2$	1	-	-
2D-I [116]*	$2 - \eta$	1.75	1	1.75

Tab. 2.3: Dynamical critical exponents. d denotes the dimensionality of the system and η, α, ν correspond to the static critical exponents listed in Tab. 2.2. (*) The values for 2D-I systems are still under debate, but 1.75 has been experimentally approved for Rb_2CoF_4 [113]. Adapted from [15].

thus can show crossovers. Such crossovers have been studied, for example, by Tseng *et al.* [54] in the classical systems MnF_2 and Rb_2MnF_4 , as shown in Fig. 2.8.

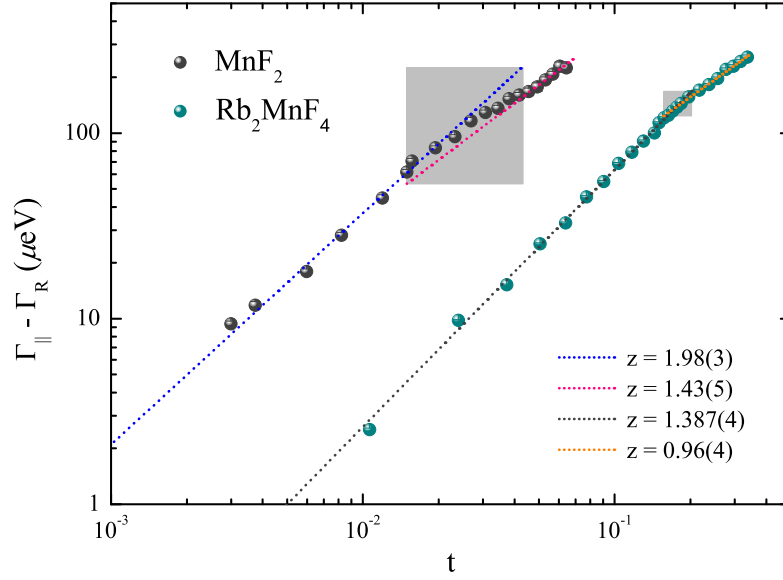


Fig. 2.8: Dynamic scaling of the characteristic energy $\Gamma(T)$ of the classical compounds MnF_2 and Rb_2MnF_4 , with scaling fit $\Gamma \propto t^{z\nu}$. The grey shaded areas indicate the crossover regions and Γ_R corresponds to the residual linewidth at T_N . From [54].

In summary, the investigation of the critical behavior of a system can reveal important information about the spin-lattice dimensions or the ranges of relevant forces. Moreover, because of the hypothesis of universality, one can find simple models to describe complex compounds, as the microscopic details are averaged out by the large and diverging correlation length ξ near \tilde{T}_c . This motivates us to study the critical behavior in the layered Ca-ruthenates, which are strongly correlated $4d$ electron systems with a plethora of ground states (see Chap. 3). We take advantage of neutron scattering (see Chap. 5) as an effective tool to determine critical phenomena, including the directly accessible dynamic scattering function $S(\mathbf{q}, \omega)$, the magnetic order parameter M , the correlation length ξ , the magnetic susceptibility $\chi(\mathbf{0})$, and the characteristic energy Γ of the fluctuations.

2.5. Quantum phase transitions

Classical continuous phase transitions are driven by thermal fluctuations at nonzero temperatures. However, phase transitions can also occur at $T = 0$, where thermal fluctuations are negligible. Such transitions are accompanied by quantum fluctuations, which emerge due to the Heisenberg uncertainty principle, and are therefore referred to as QPTs. While in the classical case the temperature difference $|T - \tilde{T}_c|$ to the critical point at \tilde{T}_c is crucial, for the QPT the deviation $|r - r_c|$ of a non-thermal tuning parameter r from a critical value r_c at the QCP is essential [119]. The tuning parameter r can be given by pressure, doping or an external magnetic field. To date, there are several systems with a proposed QCP studied by neutron spectroscopy, including heavy-fermion systems $\text{CeCu}_{6-x}\text{A}_x$ with $A = \text{Au}, \text{Ag}$ [120–123] and CeCu_2Si_2 [8], coupled-dimer AFMs XCuCl_3 [124–126] with $X = \text{Tl}, \text{K}$, as well as TMO with $3d$ (high- T_c cuprates, [11]), and $4d$ -electrons (Ca_2RuO_4 , [127]). In the following, we will discuss some basic aspects of QPTs based on Refs. [33–36].

A generic phase diagram with a QCP at r_c is shown in Fig. 2.9a, which contains characteristic regions: (i) Magnetic order at $r < r_c$ for $T < \tilde{T}_c$ with the corresponding classical critical regime (dark shaded area), and the thermally disordered phase for $T \gg \tilde{T}_c$. (ii) Quantum disorder at $r > r_c$ and low T . (iii) A fan-shaped quantum critical regime above the QCP at nonzero T separated from (i) and (ii) by phase boundaries (dashed lines), which are given by $T \propto |r - r_c|^{z\nu}$ with critical exponents z and ν . Although the QCP occurs at the experimentally inaccessible temperature $T = 0$, it affects the physical properties of the system in the quantum critical region at $T > 0$. In this respect, exotic physical phenomena such as superconductivity can appear close to a QCP due to an balanced competition of interactions favoring a magnetic or a nonmagnetic ground state [8, 9, 11, 37, 119]. An example of a QPT and the corresponding rich phase diagram [Fig. 2.9b] is given by the doping dependence of the high-temperature superconducting cuprates, as described in Ref. [11]. Here, the AFM phase in the pristine compound is destroyed at a certain level of hole-doping p_{\min} (tuning parameter) and an unconventional superconducting state occurs, which disappears at $p > p_{\max}$ and changes into a Fermi-liquid state. A pseudogap and strange-metal state emerge in proximity to the

QCP [11]. By analogy with the study of the critical behavior near T_c in classical phase-transitions, the study of the critical spin-fluctuations close to **QCP**s at $T > 0$ can help to understand the nature of the **QCP** and the underlying mechanisms for the occurrence of possible exotic phenomena.

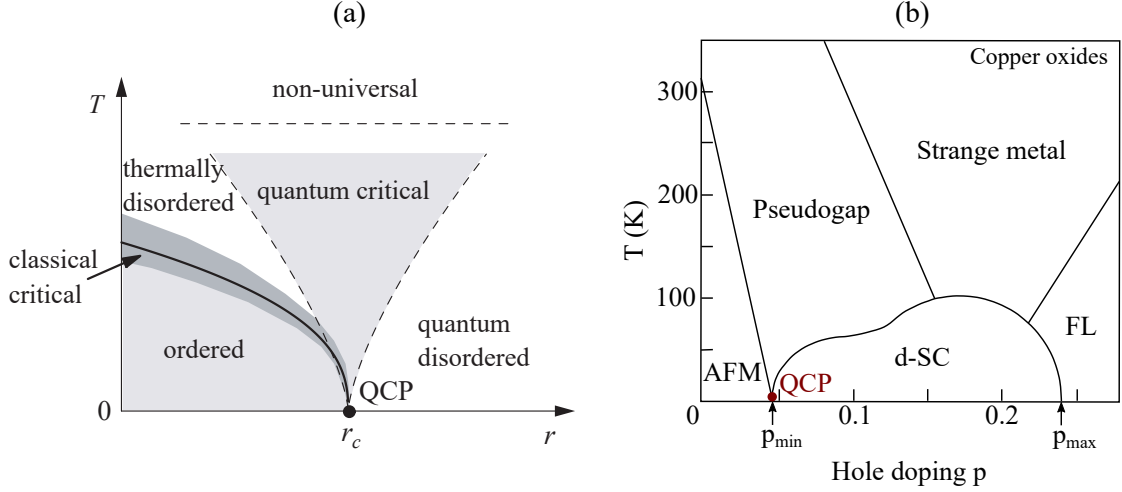


Fig. 2.9: (a) Generic phase diagram for **QPT**s. The dashed lines are given by $T \propto |r - r_c|^{z\nu}$ [119] and indicate the boundary of the quantum critical regime. Here r denotes a tuning parameter, such as pressure, doping, or an external magnetic field. From [33]. (b) Simplified phase diagram of high-temperature superconducting cuprates with a **QCP** at a critical hole doping level p_{min} separating the **AFM** phase from the unconventional superconductivity (**SC**) state. From [11] (modified).

In general, when approaching the **QCP** ($r \rightarrow r_c$), divergent time τ and length scales ξ are predicted. Similar to the classical case, the divergence can be described by **PL** scaling with the corresponding scaling relations $\tau \propto \xi^{-z} \propto |r - r_c|^{z\nu}$ and additionally a so-called ω/T -scaling of an observable $O(\omega, T)$ like, for example, the dynamic scattering function $S(\mathbf{q}, \omega)$ is expected [33]. It was further shown that a **QPT** in d space dimensions can be mapped onto a classical transition in effectively $(d + z)$ space dimensions [119], *i. e.* the critical behavior of a classical **3D-I** system, for example, can evolve to a **MF** behavior when the system is tuned towards the **QCP** [128–130]. This results from the fact that the deviations from **MF**-theory become the less the higher the space dimensionality is [33].

Moreover, when the magnetic fluctuations are responsible for the **QPT**, the relaxation time of the spin-fluctuations is expected to exhibit a critical slowing

down as $T = 0$ is approached, which is associated with a T -dependence of the energy-width $\Gamma(T)$ according to $\Gamma \propto k_B T$ [1].

In consequence, we expect different scaling behaviors in the classical ($\Gamma \ll k_B T$) and the quantum critical ($\Gamma \gg k_B T$) regime, with a crossover to the classical behavior at $\Gamma \sim k_B T$ near \tilde{T}_c [33, 131]. According to the generic diagram in Fig. 2.9a, such a crossover can be induced either by changing the tuning parameter r or by varying the temperature close to a QCP. In this work, we vary the temperature and determine $\Gamma(T)$ for the near quantum critical compound $\text{CeCu}_{5.8}\text{Au}_{0.2}$ and also examine the critical behavior in the quantum critically doped $\text{CeCu}_{5.9}\text{Au}_{0.1}$ (see Chap. 7).

3. Layered ruthenates

We give a brief overview of transition metal oxides in general, and discuss the Ca-doped compounds Ca_2RuO_4 and $\text{Ca}_3\text{Ru}_2\text{O}_7$ with the focus on their magnetic properties, and the influence of doping with nonmagnetic Ti-ions on the magnetism of bilayer $\text{Ca}_3\text{Ru}_2\text{O}_7$.

3.1. Introduction to Transition Metal Oxides

Transition metals are elements with either incomplete d sub-shells or which can form cations with incomplete d sub-shells [132]. The class of $3d$ -electron Transition Metal Oxides (TMO) has attracted much interest for many decades due to the discovery of high-temperature superconductivity (SC) in the layered cuprates $(\text{La,Ba})\text{CuO}_4$ [Fig. 3.1] by Bednorz and Müller [133]. Hitherto, the exact mechanism behind the unconventional d -wave SC in cuprates is still under debate [11], which has encouraged the investigation of structurally related systems. A plethora of electronic phases in the $3d$, $4d$, and $5d$ TMO [2, 3] has been uncovered, including Mott-Hubbard transitions in vanadates and titanates [134, 135], colossal magnetoresistance and multiferroicity in manganites [136, 137], unconventional SC in ruthenates [4], and Mott-physics in iridates [55, 56]. The wealth of physical ground states in the TMO results from a competition between the energy-scales of crystal field splitting, Hund's coupling, and inter-site exchange interactions. The Hund's coupling contains the energy-gain associated with Hund's semiempirical rules based on Coulomb-repulsion, Pauli's principle and spin-orbit coupling (SOC). The latter can be described with the exchange Hamiltonian [138]:

$$H_{\text{SO}} = \lambda_{\text{SO}} \mathbf{L} \mathbf{S} \quad , \quad (3.1)$$

where $\lambda_{\text{SO}} = \zeta_{\text{SO}}/(2S)$ is related to the single-electron SOC strength ζ_{SO} .

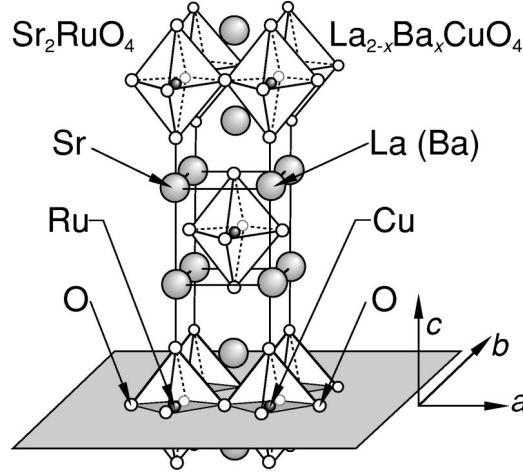


Fig. 3.1: Layered perovskite structure of cuprate (right) and ruthenate (left) superconductors. From [139].

As shown in Fig. 3.2, the cubic component of the crystal field (Δ_{CEF}), typically in the order of $\Delta_{\text{CEF}} = 2 - 4 \text{ eV}$ [2, 69, 140], lifts the degeneracy of the d -orbitals of a free d -ion. For an octahedral oxygen-environment, as realized *e. g.* in cuprates or ruthenates [Fig. 3.1], the splitting results in a lower-lying triplet state (t_{2g}) and a higher-lying doublet state (e_g) [141]. A further splitting of the t_{2g} and e_g states can be induced by the *Jahn-Teller effect* to avoid spin-frustration in systems with single electrons in degenerated energy-levels [2]. Typically, in the $3d$ TMO, the Hund's coupling is similar to Δ_{CEF} and thus a high-spin state occurs, whereas for $4d$ and $5d$ TMO, the Hund's coupling is smaller than the $e_g - t_{2g}$ splitting, which leads to a low-spin state [138]. In addition, the TMO differ significantly in terms of SOC strength, which increases as a rule of thumb with the fourth power of the atomic number $\zeta_{\text{SO}} \sim Z^4$ [142, 143]. In consequence, SOC in $3d$ TMO ($\zeta_{\text{SO}} \approx 20 \text{ meV}$ [2]) can be considered as a small perturbation and the spin-orbit degrees of freedom are quenched ($L = 0$), while SOC in $5d$ TMO is much stronger ($\zeta_{\text{SO}}^{5d} \approx 500 \text{ meV}$) and can no longer be considered as a small perturbation. Instead, it is more

appropriate to describe the physics with a total angular momentum $\mathbf{J} = |\mathbf{S} + \mathbf{L}|$. In the $4d$ TMO, the strength of SOC is placed in between that of the $3d$ and $5d$ analogues ($\zeta_{\text{SO}}^{4d} \approx 150 \text{ meV}$ [142, 143]), which can lead to exotic phenomena such as the excitonic magnetism in Ca_2RuO_4 (see below). Due to the balanced interplay of crystal field effects and moderate SOC, the $4d$ TMO are close to electronic and magnetic instabilities [Fig. 3.3b] [5] and thus only a weak perturbation induced by tuning parameters such as temperature, (chemical) pressure, or an external magnetic field, can affect a pronounced change of the physical properties and ground states [66, 75, 144].

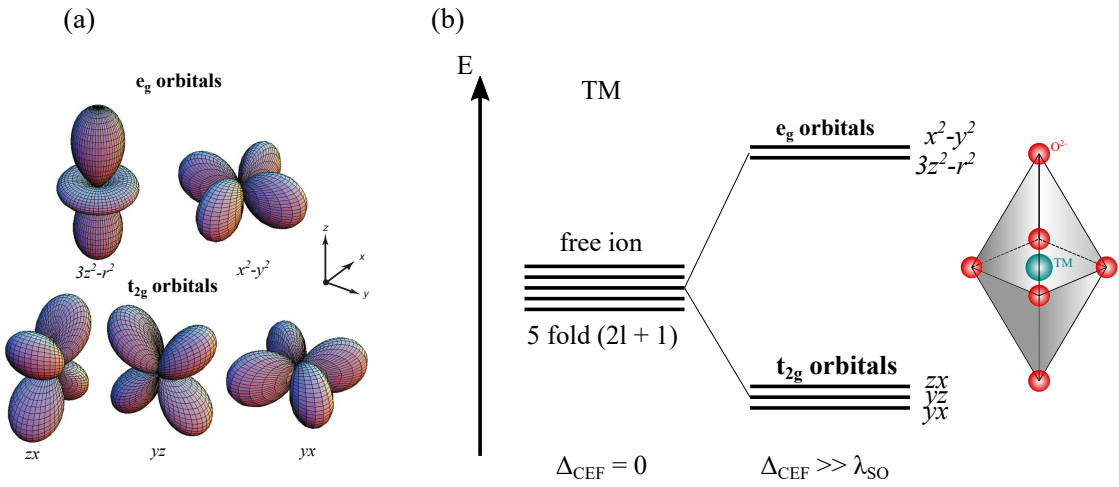


Fig. 3.2: (a) Spatial distribution of the electrons representing d -orbitals. From [141]. (b) The $2l + 1$ -fold degenerated d -orbitals of the free ion ($\Delta_{\text{CEF}} = 0$) split in a nonzero crystal electric field ($\Delta_{\text{CEF}} \neq 0$). Here, $l = 2$ denotes the quantum number of the d orbital angular momentum. Depending on the arrangement of the ligands (here octahedral symmetry) a splitting into e_g and t_{2g} manifolds occurs.

Apart from the intra-ionic SOC and the coulomb interaction with its ligands, the physics in TMO depend on the inter-site exchange with adjacent ions. The relevant interactions in TMO are the *direct exchange* between delocalized itinerant electrons (favors parallel spin-alignment) [145] and the indirect *superexchange* via nonmagnetic intermediate ions, where the spin-alignment depends on the symmetry of the orbitals involved [146]. Usually in TMO, the superexchange (SE) interaction outweighs the direct exchange [147]. The basic concept of SE is the (real or virtual) hopping of electrons between the lattice sites via ligand-ions and can be described

by the Hubbard model [148–151], which includes the Coulomb energy U for double orbital occupation and the hopping amplitude \tilde{t} , that is related to the bandwidth W via the coordination number \tilde{z} ($\tilde{t} = W/2\tilde{z}$).

In general, two extreme cases are distinguished: (i) $U \ll \tilde{t}$, *i. e.* the hopping of charge carriers is energetically supported corresponding to a metallic state. (ii) $U \gg \tilde{t}$, *i. e.* the significant on-site Coulomb repulsion prevents real electron hopping, and thus an insulating state is formed (*Mott-insulator*). Although real electron hopping through the solid is prevented in this case, virtual hopping between nearest neighbours is still possible. The associated energy gain by virtual hopping yields $J_{\text{SE}} = -2\tilde{t}^2/U$ [152]. According to Pauli’s principle, parallel spin-alignment of electrons within the same orbital is forbidden, and hence AFM order is preferred due to the virtual hopping between isovalent ions. In a solid, the sign and strength of the SE also depend on the symmetry of the electron orbitals involved (Goodenough-Kanamori-Anderson-rules [146, 153, 154]). The SE describes the exchange between isovalent ions, whereas the exchange between ions with different valences is called double-exchange (DE) [155]. In contrast to the SE, the DE enables real charge carrier hopping across the ligand orbitals and thus induces a FM alignment due to Hund’s coupling. This can be exploited to change the magnetic ground state from AFM to FM order using chemical doping, as was established for manganites [146] and recently proposed to explain the magnetic ground state in Ti-doped $\text{Ca}_3\text{Ru}_2\text{O}_7$ [77, 78].

3.2. Layered ruthenates

The layered ruthenates with Ru^{4+} -ions (electronic configuration $4d^4$) are members of a Ruddelsdon-Popper (RP) series [156], *i. e.* compounds that can be described by the sum formula $(\text{Sr}, \text{Ca})_{n+1}\text{Ru}_n\text{O}_{3n+1}$ with $n = [1, \infty]$. The index n indicates the number of oxygen-coupled layers of RuO_6 octahedra that are separated by non-magnetic layers of Sr- or Ca-ions [Fig. 3.3a]. The infinite layer complex ($n = \infty$), on the other hand, corresponds to a distorted perovskite structure.

As indicated in Fig. 3.3b, the class of layered ruthenates shows various physical phases such as the AFM Mott-insulator Ca_2RuO_4 [67, 159], the unconventional superconductor Sr_2RuO_4 [4], and the FM metals SrRuO_3 , $\text{Sr}_3\text{Ru}_2\text{O}_7$ and $\text{Sr}_4\text{Ru}_3\text{O}_{10}$,

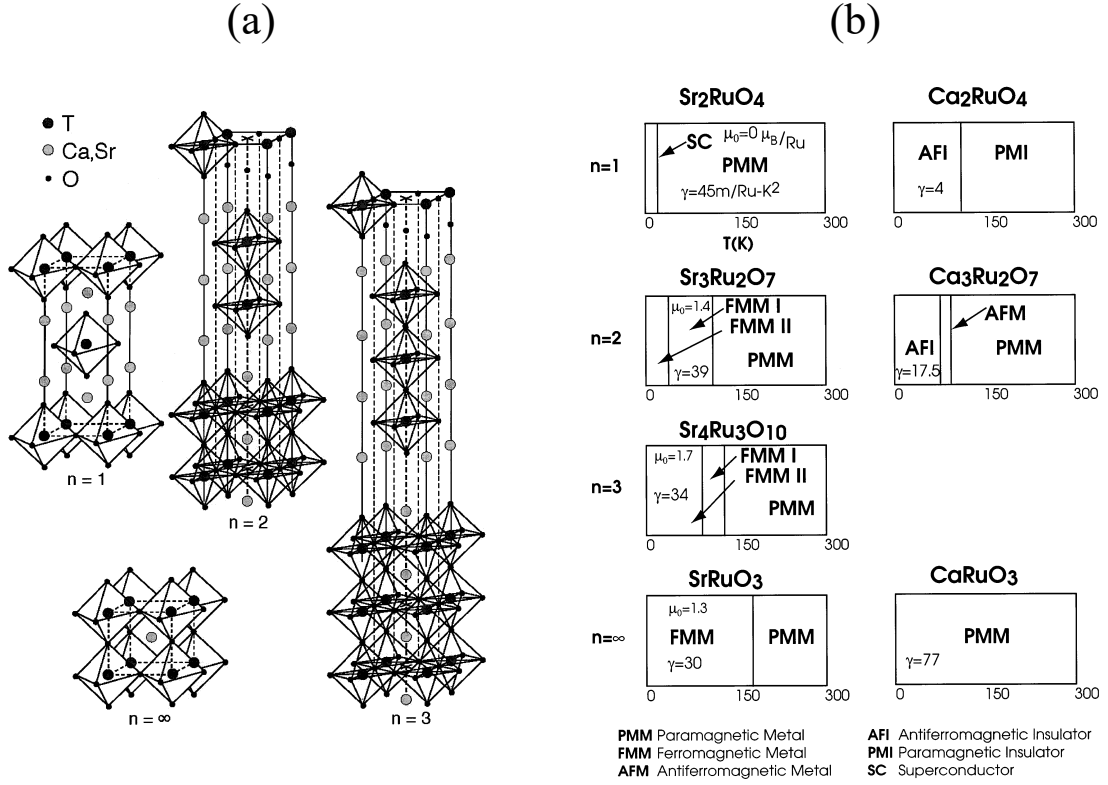


Fig. 3.3: (a) Crystal structure of the RP series $(\text{Sr}, \text{Ca})_{n+1}\text{T}_n\text{O}_{3n+1}$ with $n = 1, 2, 3, \infty$ denoting the number of oxygen-coupled TO_6 layers and $\text{T} = \text{Ti}, \text{Ru}, \text{Rh}, \text{etc.}$. (b) Overview of magnetic and electronic phases of selected layered ruthenates. γ (in units of $\text{mJ Ru}^{-1} \text{K}^{-2}$) and μ_0 (in units of $\mu_B \text{Ru}^{-1}$) denote the low-temperature electronic specific heat coefficient and the ordered magnetic moment. In the FMM II states a spin reorientation (canting) was proposed in [157, 158]. From [5].

respectively [157, 158, 160]. The enhanced electronic specific heat coefficients γ (see Fig. 3.3b) compared to conventional metals [161] signal the importance of electronic correlations in the layered ruthenates. The wealth of physical states results from (i) the different number of coupled layers n that is related to the number of Ru-Ru exchange interactions, which gradually decreases from six in the (distorted) perovskite structure ($n = \infty$), to five for bilayer compounds ($n = 2$), to four in case of single layer ruthenates ($n = 1$), and (ii) the distortions of the RuO_6 octahedron, which are more pronounced in the Ca-ruthenates [5] due to the

smaller ionic radii of the Ca-ions compared to the Sr-ions [162]. This distortion also amplifies the crystal field effects in the Ca-ruthenates.

Single-layer Ca_2RuO_4

Research on single-layer Ca_2RuO_4 was stimulated by the discovery of unconventional SC in Sr_2RuO_4 [4, 139, 163]. Sr_2RuO_4 is isostructural to the parent compound of the high- T_c cuprates (La,Ba) CuO_4 [Fig. 3.1], but is a good metal compared to the bad metallic cuprates [164, 165]. Hitherto the nature of the SC in Sr_2RuO_4 , *i. e.* the symmetry of the superconducting order parameter and the pairing mechanism, is still under debate [139, 163, 166, 167], which motivates the study of structurally related systems such as Ca_2RuO_4 .

The physical properties of the ruthenates are significantly affected by the structural distortions of the RuO_6 octahedron. Starting from the unconventional superconductor Sr_2RuO_4 [4], upon Ca-substitution $\text{Ca}_{2-x}\text{Sr}_x\text{RuO}_4$, the RuO_6 octahedra undergo a flattening, tilting, and rotation around the *c*-axis [168–171]. A rich phase diagram appears [Fig. 3.4] [172] with the AFM Mott-insulating end-member Ca_2RuO_4 [67, 68]. The proposed intermediate phases for $0.2 < x \leq 0.5$ in Fig. 3.4 are a magnetic-metal phase (M-M) with FM fluctuations [173, 174] and FM clusters that freeze out to a cluster-glass phase (C-G)[175]. This signals that Ca_2RuO_4 is in the vicinity of a magnetic instability. At low temperatures, Ca_2RuO_4 crystallizes in the orthorhombic space group *Pbca* with the lattice parameters $a = 5.39 \text{ \AA}$, $b = 5.63 \text{ \AA}$, and $c = 11.75 \text{ \AA}$ [66]. Ca_2RuO_4 can be synthesized in the two different phases 'short' or S-phase (orthorhombic) and 'long' or L-phase (tetragonal), which are classified by the value of the lattice constant *c* [66, 176]. In this work, we focus on the S-phase of Ca_2RuO_4 and thus refer to it in the following as Ca_2RuO_4 . Since the lattice parameters are temperature-dependent [66, 168][Fig. 3.5a-d], the distortions of the octahedron also change with temperature, which affects the physical properties. The lattice parameters show a discontinuity at the first-order metal-to-insulator transition (MIT) ($T_{\text{MIT}} = 360 \text{ K}$), that is accompanied by an abrupt jump in the in-plane resistivity [Fig. 3.5e] and heat capacity [67] [Fig. 3.6b].

In addition to the MIT, a magnetic transition occurs at $T_{\text{N}} = 110 \text{ K}$ [Fig. 3.6a] with a reduced staggered moment $M \approx 1.3 \mu_B$ compared to $2 \mu_B$ expected for Ru^{4+}

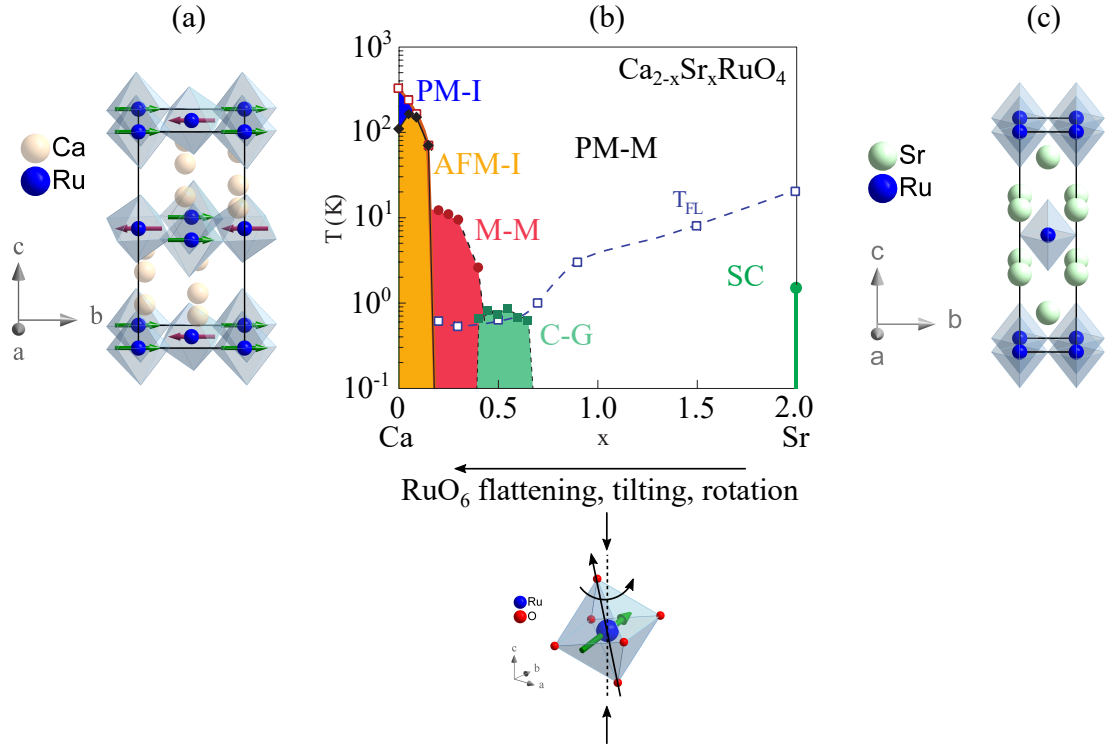


Fig. 3.4: (a) Crystal and magnetic structure of Ca_2RuO_4 . Oxygen-ions are omitted for clarity. (b) Phase diagram of $\text{Ca}_{2-x}\text{Sr}_x\text{RuO}_4$ with the abbreviations: unconventional superconductor (SC), cluster-glass (C-G), magnetic-metal (M-M). Below T_{FL} Fermi-liquid behavior was observed. From [172] (modified). The RuO_6 octahedron in the lower part of the panel indicates how the octahedra are quenched, tilted, and rotated around the c -axis with Ca-substitution. (c) Crystal structure of Sr_2RuO_4 . Oxygen-ions in (a) and (c) are omitted for clarity.

[66, 159, 176]. Here the spins are arranged in an AFM fashion within square-lattice RuO_2 planes pointing along the crystallographic b -axis and stacked along the c -axis in a G-type pattern [Fig. 3.4a]. Additionally a small canting in c -direction ($m_c \approx 0.1m_b$) was recently proposed [177]. The postulated quasi-2D nature of the spin fluctuations [176] due to the isolated single-layers in Ca_2RuO_4 was recently also derived from the magnon dispersion in the ordered phase (see below) [6].

Although magnetic ordering is confirmed by several experiments, one would expect a non-magnetic (Van Vleck-type) singlet ground state for the $4d^4$ Ru^{4+} -ion in a strong octahedral ligand field [178]. The reasons for the unexpected magnetic ground state are competing energy scales of the tetragonal component of the crystal

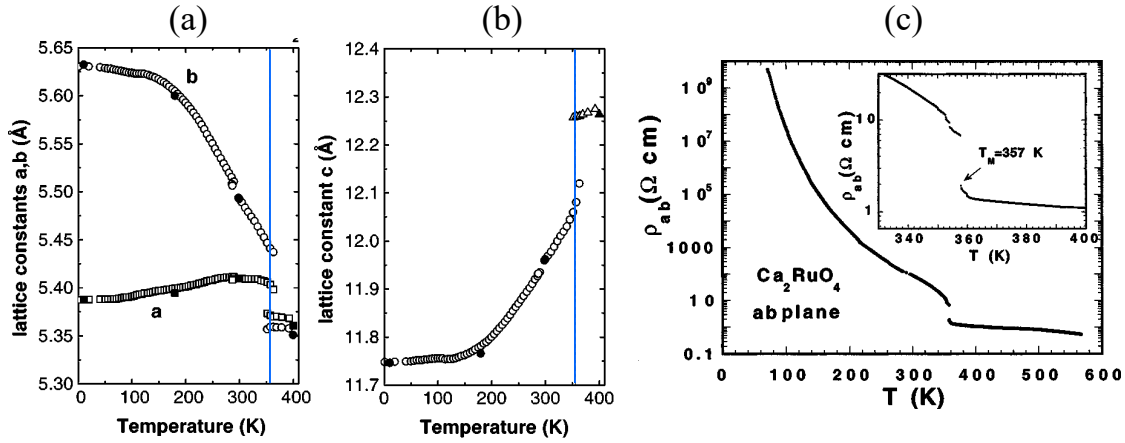


Fig. 3.5: (a,b) Temperature-dependence of the lattice parameter a, b , and c of Ca_2RuO_4 . The vertical blue lines indicate the metal-to-insulator transition at $T_{\text{MIT}} = 360$ K. From [168] (modified). (c) Electrical resistivity $\rho(T)$ vs. T for the (a, b) -plane. The inset shows the abrupt jump at T_{MIT} in more detail. From [67].

field splitting ($E_{x,y} \approx 0.25$ eV), spin-orbit coupling ($\lambda = \zeta_{\text{SO}}/2 = 0.07$ eV), and Hund's coupling ($J_H \approx 0.34$ eV) [69], as we will see below. The cubic component of the crystal field splitting in Ca_2RuO_4 dominates the Hund's coupling and thus leads to a splitting into e_g and t_{2g} states with all four electrons in the lower t_{2g} levels (low spin state) [179]. Taking into account SOC, we can distinguish two extreme cases as described in [6] and shown in Fig. 3.7: (i) $\lambda \ll E_{x,y}$, *i. e.* the crystal field splitting is much stronger than the SOC and thus the spin-orbit degree of freedom is quenched to $L = 0$. The crystal field (Jahn-Teller effect) would then further split the t_{2g} orbitals due to distortions of the RuO_6 octahedron in a lower lying orbital with xy , and higher lying orbitals with xz, yz symmetry [179]. The consequence would be a $S = 1$ Heisenberg magnet with a minimum at $Q = (0, 0)$ in the spin-wave spectrum. The Heisenberg character results from the isotropic nearest-neighbour exchange in absence of an orbital momentum [6]. (ii) For $\lambda \gg E_{x,y}$, a non-magnetic singlet ground state occurs [178], according to $\mathbf{J} = |\mathbf{S} + \mathbf{L}| = 0$ with $S = 1$ and an effective orbital momentum $L = 1$, as proposed for Sr_2IrO_4 [55].

In contrast to (i), the magnon dispersion in the ordered phase [Fig. 3.8] shows a global maximum at $Q = (0, 0)$ indicating significant SOC in Ca_2RuO_4 . Due to this contradiction, the appearance of an *excitonic magnetism* in Ca_2RuO_4 was

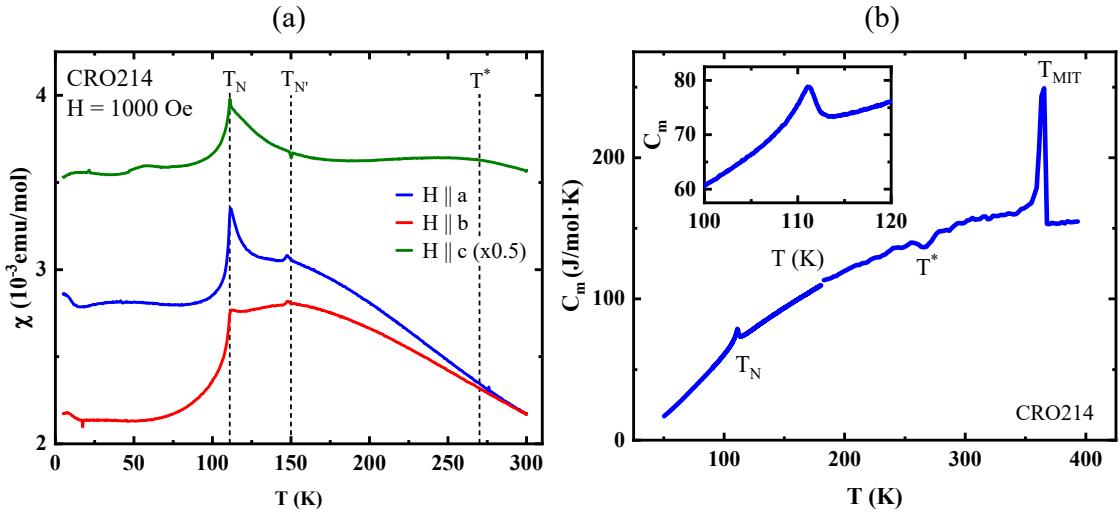


Fig. 3.6: (a) Magnetometry measurements of a Ca_2RuO_4 single crystal. We observe an AFM transition at $T_N = 111$ K and anomalies at (i) $T_{N'}$ = 150 K associated with the transition temperature of a 'B-centered' phase with a different magnetic ordering vector [66], and (ii) at $T^* = 270$ K associated with the proposed transition to orbital order. During the measurement with $H \parallel a$ we lost a small part of the crystal with an undefined mass, and thus we scaled the data for $H \parallel a$ on the 300 K value of $H \parallel b$. (b) Specific heat measurements on a different Ca_2RuO_4 single crystal obtained from M. Krautloher. We find a sharp feature corresponding to a first order transition at the MIT at $T_{\text{MIT}} = 370$ K, and a lambda anomaly at T_N related to a second order transition.

(‘Higgs’) mode in the spin-excitations, besides the two-fold degenerated transverse spin-waves (Goldstone modes), corresponding to the magnitude fluctuations of \mathbf{J} [65]. This Higgs-mode was recently corroborated in Ca_2RuO_4 by INS [Fig 3.8] [6], resonant x-ray scattering (RIXS) [69], and Raman scattering [70].

The dispersion of the transverse magnons obtained from INS could be well described by the following simplified Hamiltonian, where only nearest neighbour couplings were respected [6]:

$$\mathcal{H} = J \sum_{\langle i,j \rangle} (\mathbf{S}_i \mathbf{S}_j - \alpha S_i^z S_j^z) + E \sum_{\langle i \rangle} S_i^{z2} + \varepsilon \sum_{\langle i \rangle} S_i^{x2} \quad . \quad (3.2)$$

$J = 5.8 \text{ meV}$ denotes the in-plane nearest-neighbour SE coupling, $\alpha = 0.15$ the XY-type exchange anisotropy, $E = 25 \text{ meV}$ and $\varepsilon = 4.0 \text{ meV}$ the single-ion anisotropy terms of tetragonal (easy-plane) and orthorhombic (easy-axis) symmetries. \mathbf{S} is here considered as a pseudospin accounting for the spin-orbit entanglement. The weak interplane interaction J' [180] is neglected. Accordingly, Ca_2RuO_4 can be considered as a quasi-2D system with significant easy-plane anisotropy (E -term) and therefore a promising solid-state system to study the 2D-XY model [6] with potential vortex excitations (see Chap. 2). Moreover, it remains controversial to this day whether an additional phase in Ca_2RuO_4 at $T_N < T < T^*$ with $T^* \sim 270 \text{ K}$ exists [Fig. 3.6a], which could be associated with orbital ordering [177, 181–183], and/or a Jahn-Teller driven spin-nematic phase [184].

Ca_2RuO_4 exhibits further intriguing physical properties when pressure p or an electrical DC current is applied. More precisely, the Mott-insulator Ca_2RuO_4 can be tuned by hydrostatic pressure to a FM metal [185, 186] that shows SC below 0.4 K for $p > 90 \text{ kbar}$ [187]. Interestingly, the SC transition temperature in Ca_2RuO_4 thin films can be significantly increased up to $T_c = 64 \text{ K}$ [188]. On the other hand, an electric current of a few milliamperes is sufficient to induce a semimetallic behavior at room-temperature, suppress the AFM order in Ca_2RuO_4 , and cause a strong diamagnetic response below 50 K [189–191].

In summary, the AFM square-lattice Mott-insulator Ca_2RuO_4 exhibits unconventional excitonic magnetism due to an interplay of moderate SOC and crystal field effects. Therefore, it is an excellent candidate to investigate the magnetism in layered ruthenates. In addition, the spin-wave dispersion indicates that it is a

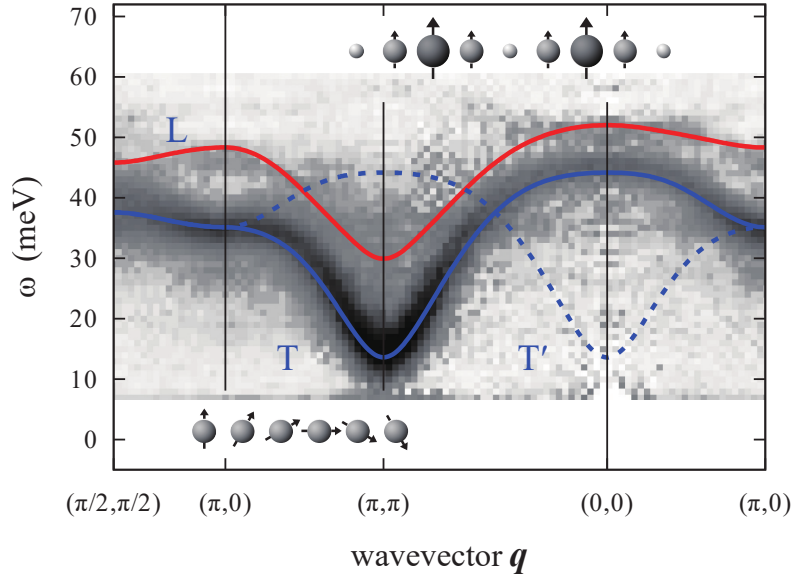


Fig. 3.8: Spin-excitations of Ca_2RuO_4 obtained from INS. The solid lines show model calculations derived in Ref. [6]. The red solid line denotes the longitudinal mode L according to the Higgs-mode, whereas the transverse in-plane magnon T and out-of-plane magnon T' are indicated by the blue solid and dotted lines, respectively. The magnon motions are depicted by the symbols. From [6, 138].

potential solid-state system to study the 2D-XY model. In consequence, a detailed investigation of the critical behavior in Ca_2RuO_4 close to the magnetic transition is of great interest, which could also provide information about the possible additional phase below T^* .

Bilayer $\text{Ca}_3\text{Ru}_2\text{O}_7$

The number n of oxygen-coupled RuO_6 layers determines the physical properties of the layered ruthenates. Therefore, we will compare in this work the critical behaviors of Ca_2RuO_4 with its bilayer analogue $\text{Ca}_3\text{Ru}_2\text{O}_7$ ($n = 2$).

$\text{Ca}_3\text{Ru}_2\text{O}_7$ crystallizes in orthorhombic structure ($Bb2_1m$). The lattice parameters are (50 K) $a = 5.36 \text{ \AA}$, $b = 5.53 \text{ \AA}$, and $c = 19.54 \text{ \AA}$ [71, 72] [Fig. 3.9a]. The octahedral distortions are less pronounced compared to Ca_2RuO_4 [7]. Figure 3.9b shows the T -dependence of a and c . The abrupt change at $T \sim 48 \text{ K}$ is assigned to a structural transition that also affects the magnetic structure, as discussed below.

Parallel to the structural changes the electrical properties vary in a complex manner. In Fig. 3.9c, we show the in-plane (ρ_a) and out-of-plane (ρ_c) electrical resistivity *vs.* T with the following features [192]: (i) ρ exhibits significant anisotropy with metallic character in the planes and insulating character perpendicular to the planes. (ii) A small anomaly at $T_{N,1} = 56$ K occurs that is followed by a discontinuity at $T_{N,2} = 48$ K with an increase of $\rho_{a,c}$ by a factor of 2. (iii) Below $T_{N,2}$, ρ_c increases by an order of magnitude, while ρ_a stays roughly constant with metallic character [193]. This behavior of ρ is suggested to result from a gapping of the Fermi-surface through a Fermi-surface reconstruction with remaining ungapped metallic pockets [60, 62, 194].

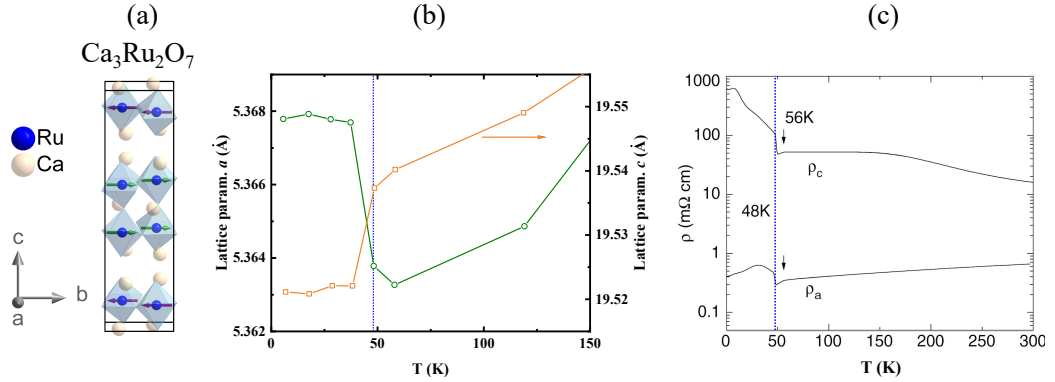


Fig. 3.9: (a) Crystal and magnetic structure of $\text{Ca}_3\text{Ru}_2\text{O}_7$. Oxygen-ions are omitted for clarity. (b) T -dependence of the lattice parameter a and c . Data from [72]. (c) T -dependence of in-plane ρ_a and out-of-plane ρ_c electrical resistivity. From [71] (modified). The vertical blue dotted line indicates a structural transition at $T = 48$ K that is accompanied by an increase of ρ .

The features in the electrical resistivity are similarly reflected in the heat capacity C [Fig. 3.10a], which has a small anomaly at $T_{N,1}$ and a sharp peak at $T_{N,2}$ [71]. While the former is associated with a second-order magnetic transition, the sharp peak was assigned to a first-order transition [195].

Both transitions were also observed in the magnetic susceptibility χ [Fig. 3.10b] [192]. From X-ray [73] and neutron scattering [72] experiments, it was derived that the magnetic structure of $\text{Ca}_3\text{Ru}_2\text{O}_7$ below $T_{N,1}$ contains FM bilayers that are antiferromagnetically stacked along c (A-type AFM), with the moments within the planes pointing along a . The second transition at $T_{N,2}$ was found to be accompanied

by a reorientation of the magnetic moments from $m \parallel a$ to $m \parallel b$ [Fig. 3.9a]. In this context, it was recently proposed that the spin-reorientation at $T_{N,2}$ is a gradual process starting at $T_{N,2} + 2$ K by formation of a cycloidal structure [196]. Moreover, a giant magnetoresistance in $\text{Ca}_3\text{Ru}_2\text{O}_7$ was found as a result of the spin-valve effect, which describes the decrease of resistance from an antiparallel to a parallel alignment of adjacent FM bilayers [197–200].

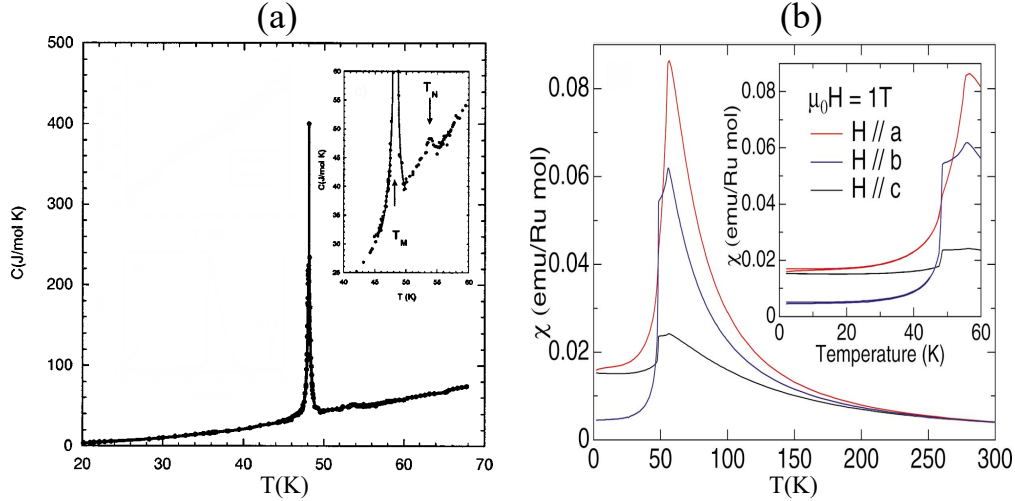


Fig. 3.10: T -dependence of the (a) specific heat and (b) magnetic susceptibility. (a) Shows the first- and second-order characteristics of the magnetic transitions at $T_{N,2} = 48$ K and $T_{N,1} = 56$ K, indicated by a sharp peak and a lambda anomaly, respectively. The inset shows a zoom on the transitions. From [71] (modified). (b) Shows a two-step like magnetic transition signalling a reorientation of the easy axis from $m \parallel a$ below $T_{N,1}$ to $m \parallel b$ at $T_{N,2}$. From [192] (modified).

Analogous to Ca_2RuO_4 , the magnon dispersion of $\text{Ca}_3\text{Ru}_2\text{O}_7$ in the ordered phase could be described by the following Hamiltonian [Fig. 3.11] [7]:

$$\mathcal{H} = J \sum_{\langle i,j \rangle} \mathbf{S}_i \mathbf{S}_j + J_c \sum_{\langle i,j \rangle} \mathbf{S}_i \mathbf{S}_j + E \sum_{\langle i \rangle} S_i^z{}^2 + \varepsilon \sum_{\langle i \rangle} S_i^x{}^2 \quad , \quad (3.3)$$

with the FM nearest neighbour Heisenberg coupling term $J = -3.75$ meV, the intra-bilayer interaction $J_c = -6.5$ meV, and the single-ion anisotropy terms $E = 5.5$ meV, $\varepsilon = 2.5$ meV. The weak inter-bilayer interaction J' was neglected. Strikingly, no magnon dispersion was found perpendicular to the bilayers, *i. e.* along the c -axis [74]

indicating a 2D nature of the magnetic interactions. Hence, the strong intra-bilayer coupling together with the weak inter-bilayer coupling in $\text{Ca}_3\text{Ru}_2\text{O}_7$ implies that the dimensionality of the exchange-bond network is intermediate between 2D and 3D. On the other hand, if the strongly coupled bilayers in $\text{Ca}_3\text{Ru}_2\text{O}_7$ behave like quasi-2D structures, as previously discussed in [75], then the significant easy-plane anisotropy term E suggests that $\text{Ca}_3\text{Ru}_2\text{O}_7$ may also be a potential solid-state system to study the 2D-XY model. Therefore, an investigation of the critical behavior in $\text{Ca}_3\text{Ru}_2\text{O}_7$ is of high interest.

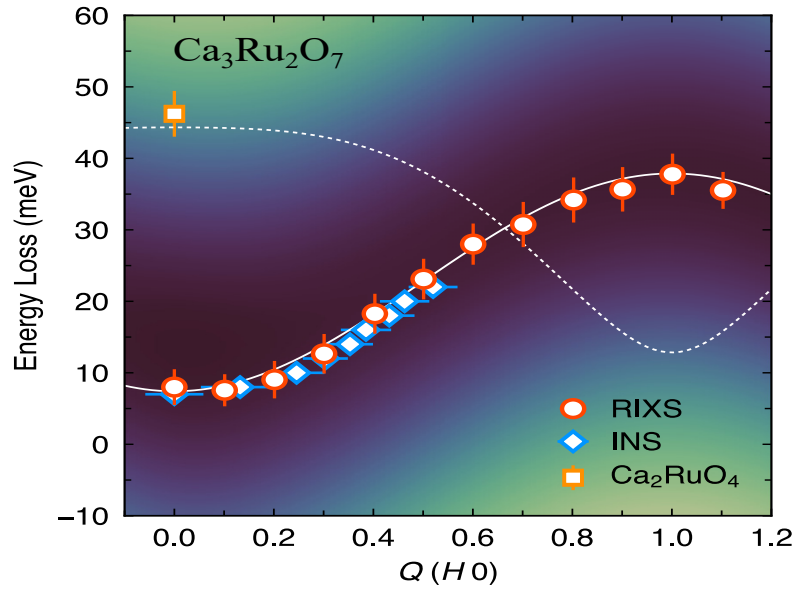


Fig. 3.11: Spin-wave excitations of $\text{Ca}_3\text{Ru}_2\text{O}_7$ obtained from RIXS and INS. The white solid line corresponds to the fitted magnon dispersion according to Eqn. (3.3). For comparison, the distinct INS results on Ca_2RuO_4 are shown with the global maximum at $Q = (0,0)$. From [7] (modified). No magnon dispersion was observed along the c -axis [74].

Ti-doped bilayer $\text{Ca}_3(\text{Ru}_{1-x}\text{Ti}_x)_2\text{O}_7$

The complex behavior of the electrical resistivity ρ [Fig. 3.9c] and the reorientation of the magnetic moments [Fig. 3.10b] indicate that $\text{Ca}_3\text{Ru}_2\text{O}_7$ is close to an electronic and magnetic instability [194, 200]. Accordingly, only a marginal perturbation such as chemical doping of the Ru-sites with non-magnetic Ti^{4+} -ions $\text{Ca}_3(\text{Ru}_{1-x}\text{Ti}_x)_2\text{O}_7$

is sufficient to significantly alter the physical properties of pristine $\text{Ca}_3\text{Ru}_2\text{O}_7$ [75–78].

In this work, we therefore also investigate the critical behavior of the 1% Ti-doped bilayer compound $\text{Ca}_3(\text{Ru}_{0.99}\text{Ti}_{0.01})_2\text{O}_7$, which crystallizes in orthorhombic structure ($Bb21m$) with the lattice parameters $a = 5.370 \text{ \AA}$, $b = 5.601 \text{ \AA}$, and $c = 19.351 \text{ \AA}$ [79]. The Ti-doping (electronic configuration $3d^0$) weakens the structural distortions in the lattice due to the smaller ionic-radii of the Ti-ions. This can be seen in the smaller tilting and rotation angles of the RuO_6 octahedron or the orthorhombicity $(a - b)/(a + b)$ of the lattice [3.12a,b] [162]. Accordingly, a bandwidth reduction is proposed, that increases the U/W ratio and thus induces a MIT [76], which contrasts with the metallic ground state in pristine $\text{Ca}_3\text{Ru}_2\text{O}_7$.

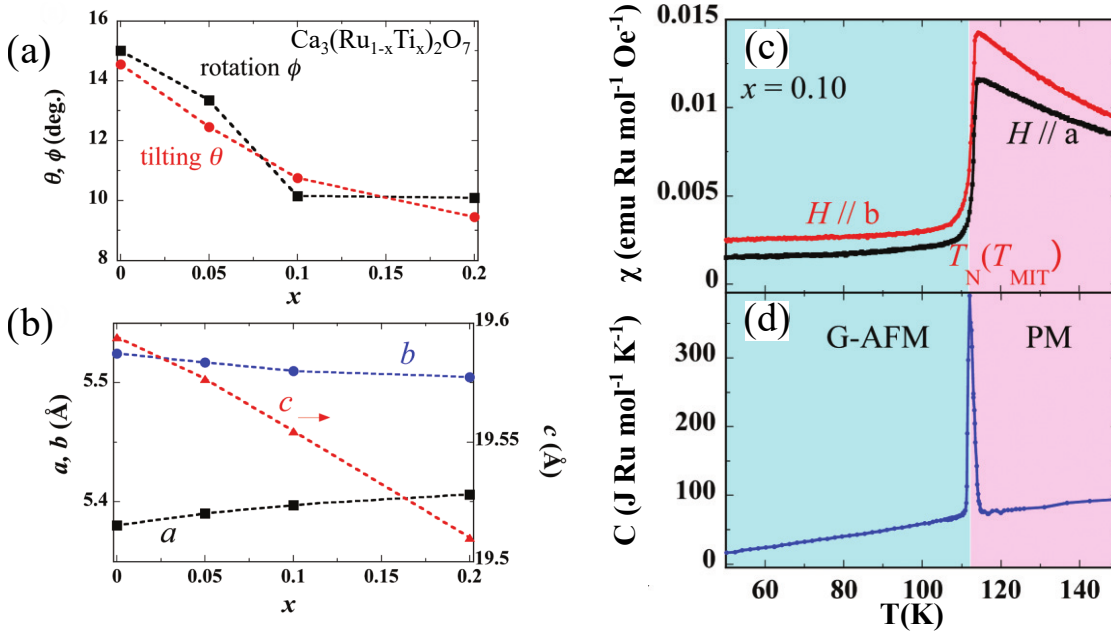


Fig. 3.12: (a) Rotation and tilting angles of RuO_6 octahedron, and (b) lattice parameter *vs.* Ti-doping in $\text{Ca}_3(\text{Ru}_{1-x}\text{Ti}_x)_2\text{O}_7$. (c) Magnetic susceptibility and (d) specific heat *vs.* temperature for a Ti-content of $x = 0.1$. From [77].

Moreover, the magnetic susceptibility and specific heat for 10% Ti-content ($x = 0.1$) indicate a drastic change in the magnetic properties [Fig. 3.12c,d]. The two-step transition in the A-type AFM $\text{Ca}_3\text{Ru}_2\text{O}_7$ (at $T_{N,1}$ and $T_{N,2}$) changes to a sharp single-step transition with G-type AFM ground state for $x \geq 0.05$ [77], that

resembles the ground state of Ca_2RuO_4 [66]. Between the doping-levels with the pure A-type or G-type AFM ground states, the appearance of an intermediate phase and thus a three-step transition has also been proposed [78]. This complex behavior is summarized in the magnetic phase diagram [Fig. 3.13] and was explained by a gradual suppression of the FM double-exchange between the Ru-ions due to the presence of non-magnetic Ti-ions. As a result, the AFM superexchange dominates the double-exchange [77, 78], which is reminiscent to the transition from an AFM to a FM state in manganites induced by chemical (hole)-doping [146].

No intermediate phase was observed in the crystals provided for our measurements and the onset of the pure G-type AFM state was found for lower substitution-levels ($x \geq 0.005$) [201]. Both features have been assigned to possible distribution inhomogeneities of the Ti-dopants in the bulk crystals.

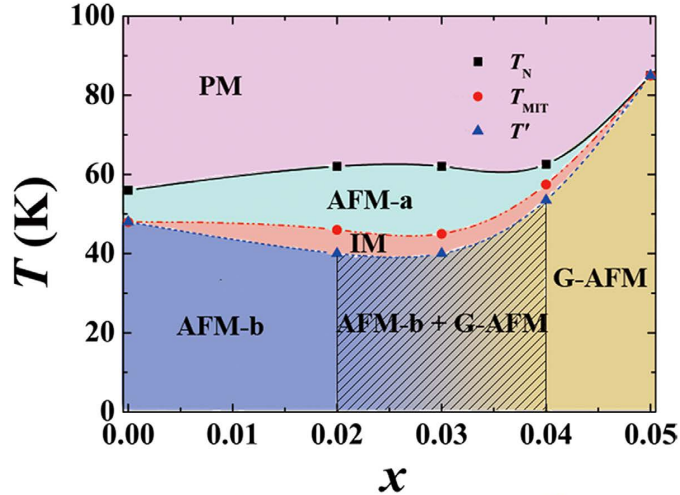


Fig. 3.13: Magnetic phase diagram of $\text{Ca}_3(\text{Ru}_{1-x}\text{Ti}_x)_2\text{O}_7$. We would like to note, that the onset of the pure G-type AFM phase may vary depending on the homogeneous distribution of the Ti-ions. From [78].

The spin-excitations in Ti-doped $\text{Ca}_3\text{Ru}_2\text{O}_7$ investigated by INS [79] show an unusual collective mode associated with the non-magnetic Ti-impurities in addition to the regular AFM magnons (Goldstone modes). The amplitude of the former mode was found to be comparable to the regular magnons, but the mode itself is localized in both energy and momentum space. This feature was explained by a non-local impurity-induced reduction of the orbital moment at the Ru-sites

near a Ti-impurity, which is due to a suppression of the orthorhombicity. Apart from that, the regular magnons could be described by the Hamiltonian used for single-layer Ca_2RuO_4 , but with an additional intra-bilayer coupling-term J_c . The resulting parameters are $J = 4.5$ meV, $J_c = 3.0$ meV and $E = 18.0$ meV, $\varepsilon = 4.5$ meV accounting for inter-ionic couplings and the single-ion anisotropy. Analogous to Ca_2RuO_4 , a global maximum was found at the Γ -point indicating a discrepancy from the pure $S = 1$ Heisenberg-model.

In summary, from the G-type AFM ground state in $\text{Ca}_3(\text{Ru}_{0.99}\text{Ti}_{0.01})_2\text{O}_7$ and the quasi-2D magnon dispersion with a significant easy-plane anisotropy, in principle, a similar critical behavior as for Ca_2RuO_4 or $\text{Ca}_3\text{Ru}_2\text{O}_7$ would be expected. On the other hand, however, the question arises of how the Ti-impurities affect the critical fluctuations since the second-order magnetic transition in pristine $\text{Ca}_3\text{Ru}_2\text{O}_7$ turns into a sharp transition with first-order character. In this respect, the critical fluctuations could be suppressed. Nevertheless, a study of the critical behavior in $\text{Ca}_3(\text{Ru}_{0.99}\text{Ti}_{0.01})_2\text{O}_7$ is crucial for comparison with the other two compounds.

4. Heavy-fermion system

CeCu_{6-x}Au_x

We give an overview of the heavy-fermion series CeCu_{6-x}Au_x, which exhibits a QCP for $x_c \simeq 0.1$. We focus on the properties of the near-critical doped compound CeCu_{5.8}Au_{0.2}, which we studied by NSE spectroscopy.

Heavy-fermion systems, *i. e.* intermetallic compounds containing $4f$ and $5f$ elements with high effective masses [202] such as Ce(Cu,Ru)₂Si₂ [203, 204], CeCu₆ [10], CeIn₃ [9], and UGa₃ [205] are model compounds to investigate QPTs. This arises from a balanced competition between the Kondo-effect [202, 206] and the RKKY-interaction (see Chap. 3) in these systems [207]. The Kondo-effect describes the screening of a local impurity/moment by the conduction electrons below a crossover temperature T_K , associated with an energy gain of $k_B T_K \propto e^{-\frac{1}{JN(E_F)}}$, and thus suppresses magnetic long-range order. Here, J and $N(E_F)$ denote the AFM coupling constant and the electronic density of states at the Fermi-level E_F . Conversely, the RKKY-interaction, which occurs between local magnetic moments mediated by the conduction electrons, supports magnetic order with an associated energy-gain of $k_B T_{\text{RKKY}} \propto J^2 N(E_F)$ [207]. In this work, we specifically investigate the critical behavior of CeCu_{5.8}Au_{0.2} belonging to the $4f$ heavy-fermion series CeCu_{6-x}Au_x to study QPTs.

Pristine CeCu₆ (electronic configuration Ce³⁺) is metallic and crystallizes in an orthorhombic $Pnma$ structure at room temperature (*cf.* Fig. 4.1a), that changes upon cooling into a monoclinic $P21/c$ structure at $T < 230$ K [208]. Below $T_{FL} \approx 0.2$ K [Fig. 4.1b] Fermi-liquid behaviour is indicated by an almost constant Sommerfeld coefficient of the electronic specific heat ($\gamma = C/T \approx \text{const.}$) and a quadratic dependence of the electrical resistivity ($\Delta\rho \propto T^2$) [10, 209–212]. It was proposed

that the deviation from $C/T = \text{const.}$ may result from the effects of magnetic order at $T \approx 2 \text{ mK}$ [213]. The suppression of the magnetic ordering down to very low temperatures is attributed to a predominant Kondo-screening with $T_K \sim 6 \text{ K}$ [211].

The situation changes when the Cu(2)-sites [214] in CeCu_6 are doped by Au-ions with bigger ionic radii [162] [Fig. 4.1a]. The unit-cell volume increases gradually and negative (chemical) pressure is induced [215]. This in turn leads to a weakening of the hybridization of the local $4f$ moments with the conduction electrons (Kondo-screening) [212] and eventually to the emergence of an AFM ground state above a critical Au-content of $x_c \sim 0.1$ [Fig. 4.1b]. It was found that the doping dependence of the transition temperature T_N at $x > x_c$ can be described as $T_N(x) \propto |x - x_c|^{z\nu}$ with $z\nu = 1$ [34, 211]. According to the generic phase diagram [Fig. 2.9a] the $\text{CeCu}_{6-x}\text{Au}_x$ system therefore undergoes a QPT with a QCP located at $x = x_c$ separating the quantum disordered ($x < x_c$) and magnetically ordered ($x > x_c$) regime. The QPT is accompanied by a structural transition from the low- T monoclinic symmetry in CeCu_6 to orthorhombic $Pnma$ symmetry that is realized in CeCu_6 at room-temperature [208], and it can be reversed by applying either hydrostatic pressure or an external magnetic field [121, 216].

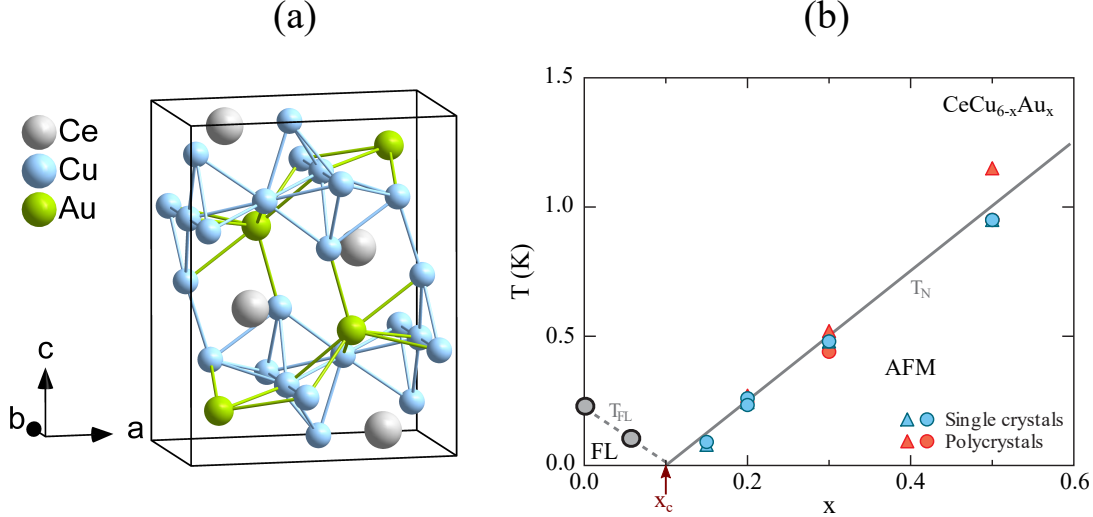


Fig. 4.1: (a) Crystal structure of stoichiometric CeCu_5Au with orthorhombic $Pnma$ symmetry. The position of the doped Au-ions correspond to the Cu(2)-site of the parent CeCu_6 [217]. (b) Phase diagram of $\text{CeCu}_{6-x}\text{Au}_x$ in dependence of Au-doping with the QCP at $x_c = 0.1$. From [10] (modified).

The QPT is accompanied by a significant variation of the heat capacity and electrical resistivity as shown in Fig. 4.2. A more detailed analysis in Ref. [212] revealed for the critically doped compound ($x = 0.1$) non-Fermi-liquid behavior [10, 211, 218], *i. e.* $C/T \propto -\ln(T)$ and $\Delta\rho \propto T$. Together with the dependence of the transition temperature from the tuning parameter $T_N(x) \propto |x - x_c|$ [34] a coupling of 3D conduction electrons with 2D critical fluctuations near the QCP [219] was proposed for $\text{CeCu}_{5.9}\text{Au}_{0.1}$.

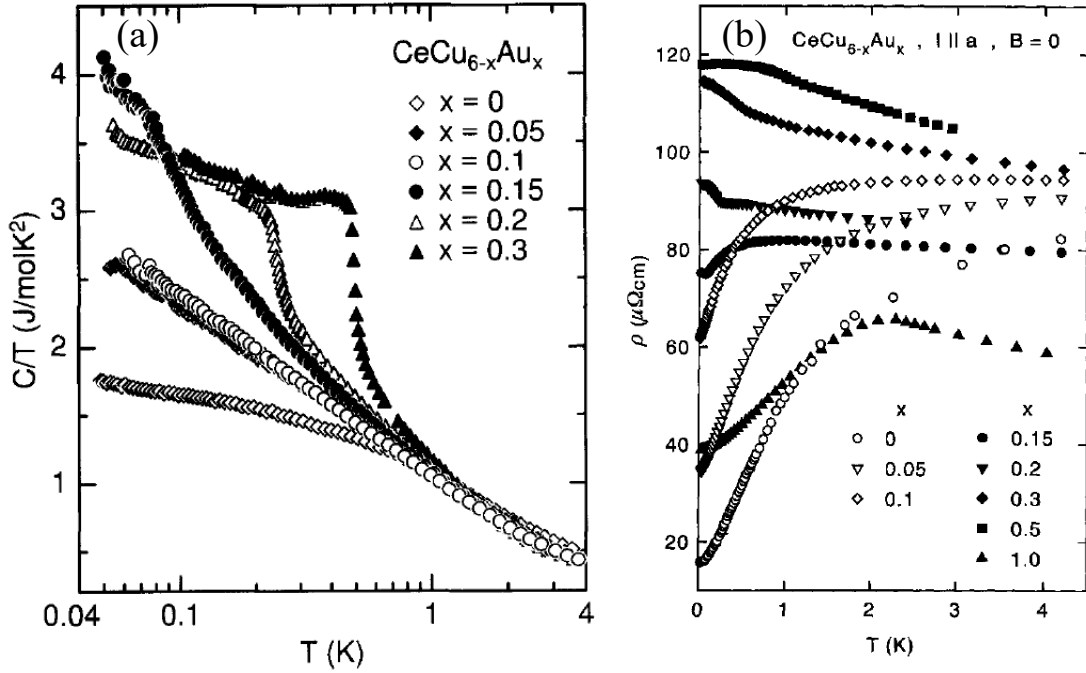


Fig. 4.2: (a) Heat capacity, and (b) electrical resistivity of $\text{CeCu}_{6-x}\text{Au}_x$ single-crystals for various Au-dopings x . The Fermi-liquid behaviour of pristine CeCu_6 , *i. e.* $C/T \approx \text{const.}$ and $\Delta\rho \propto T^2$ changes to a non-Fermi-liquid behaviour in the quantum critically doped compound ($x = 0.1$), *i. e.* $C/T \propto -\ln(T)$ and $\Delta\rho \propto T$. From [211, 212].

The 2D nature of the critical fluctuations was corroborated by comprehensive neutron experiments described in Refs. [219–224]. They found that the incommensurate positions of the enhanced diffuse critical scattering intensity for $x = 0.1$ ($\hbar\omega = 0.1$ meV), and the elastic magnetic Bragg-peaks for $0.1 < x < 0.5$ could be captured by four 1D rods in the reciprocal a,c -plane [Fig. 4.3a]. Such 1D rods in reciprocal space indicate quasi-2D correlations between the Ce-ions in real space.

Furthermore, there is no indication that for $x = 0.1$ the critical fluctuations act like 3D precursors, *i. e.* there is no particularly enhanced diffuse scattering only at the Bragg-position for $x = 0.2$. Both observations go along with the interpretation of the specific heat and electrical resistivity data, which suggest that 2D fluctuations couple with 3D fermionic quasiparticles [219]. The 'X' shape of the two rods in Fig. 4.3a results from the orthorhombic symmetry [222]. The displacement of the magnetic Bragg-peak positions for $x \geq 0.5$ is due to a reorientation of the magnetic ordering vector, which is not understood so far [220, 224, 225].

To check for a critical slowing down upon approaching the QCP ($\Gamma \rightarrow 0$), the characteristic energy $\Gamma(T)$ of the fluctuations for the doping levels $x = 0, 0.1, 0.2$ was determined with TAS by Stockert *et al.* [1]. As shown in Fig. 4.3b, $\Gamma(T)$ increases almost linearly for all doping levels at elevated temperatures, *i. e.* the temperature itself is the only relevant scale in the system. This changes at low- T , however, where CeCu₆ and CeCu_{5.9}Au_{0.1} show a nonzero offset, whilst CeCu_{5.8}Au_{0.2} becomes critical at $T = T_N$. The offset of the potential (quantum) critically doped compound CeCu_{5.9}Au_{0.1} emerges at lower T and is less pronounced than for CeCu₆, which indicates that the actual critical doping is at slightly higher $x_c > 0.1$. Overall a critical slowing down upon approaching the QCP was established.

An expected quantum-to-classical crossover in the scaling behavior (see Chap. 2) for the $x = 0.2$ compound close to the AFM transition was not reported so far. To be exact one would even expect a dimensionality crossover within the classical critical regime from 2D to 3D critical scaling as T_N is approached [226]. One possible reason for the lack of such crossovers could be the limited energy-resolution of the used TAS spectrometers [inset Fig. 4.3a] consistent with a recent NSE study on the dynamical scaling in the classical AFMs MnF₂ and Rb₂MnF₄ [54]. This highly encourage our NSE experiments on CeCu_{5.8}Au_{0.2} with significant higher energy-resolution than TAS at moderate neutron flux.

CeCu_{5.8}Au_{0.2}

CeCu_{5.8}Au_{0.2} crystallizes in orthorhombic $Pnma$ structure with lattice parameters $a = 8.105$, $b = 5.100$, and $c = 10.171$ and undergoes an AFM transition at $T_N \sim 0.25$ K [211]. The proposed magnetic structure contains a sinusoidal modulation of the

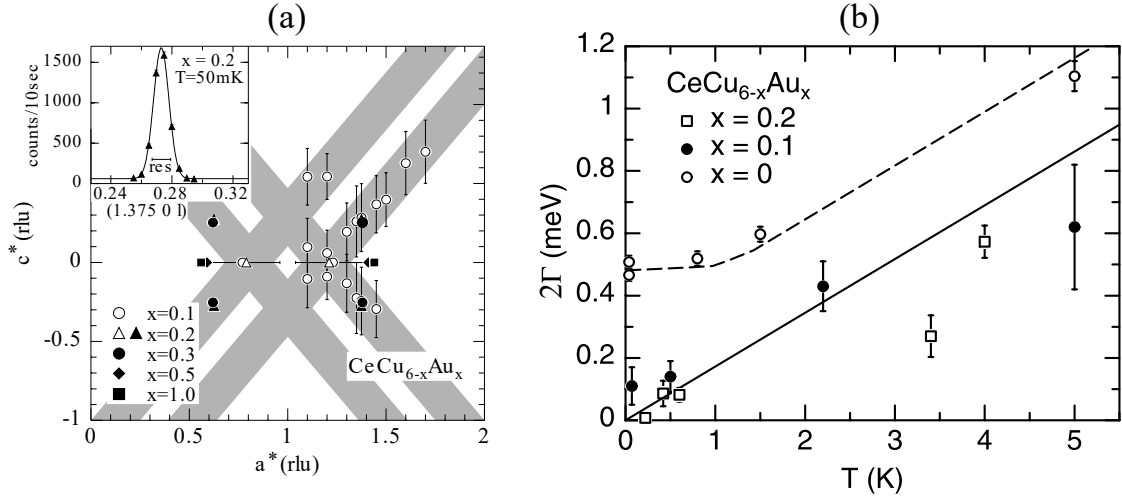


Fig. 4.3: (a) Positions of critical scattering intensity ($x = 0.1$, $\hbar\omega = 0.1$ meV) and magnetic Bragg-peaks ($0.2 < x < 1.0$) in $\text{CeCu}_{6-x}\text{Au}_x$. The errorbars indicate the linewidth of the diffuse scattering peak for $x = 0.1$. The four rods are attributed to the orthorhombic $Pnma$ symmetry. The open symbols for $x = 0.2$ correspond to short-range ordering peaks [219, 223]. The inset shows a resolution limited magnetic Bragg-peak. From [220] (b) T-dependence of the characteristic energy 2Γ at $Q = Q_{3D}$ for various doping. The solid line corresponds to $\Gamma = k_B T$, and the dashed line denotes $\Gamma = \Gamma_0 + k_B T$. From [1] (modified).

Ce-moments along the a -axis with the moments pointing along the c -axis [223, 224]. The derived effective moment is with $0.02 \mu_B \sim 1\%$ of the free Ce^{3+} value $2.54 \mu_B$. $\text{CeCu}_{5.8}\text{Au}_{0.2}$ can be tuned to quantum criticality by either applying a hydrostatic pressure of $p_c = 5$ kbar or an external magnetic field of $B_c = 0.4$ T [121].

5. Experimental Techniques

We review the main experimental techniques used in this work, namely neutron scattering on triple-axis and spin-echo spectrometers. We begin with a short summary of the basics concepts of neutron scattering and then focus on the concepts of the specific methods with a detailed discussion of the data analysis.

5.1. Neutron scattering

The experiments in this work were conducted at the research reactors [FRM II](#) (Munich), [BER II](#) (Berlin), and [ILL](#) (Grenoble), where nuclear fission of ^{235}U is used to generate neutrons. This concept differs from spallation sources, where neutrons are produced by bombarding a neutron-rich material with a pulse of accelerated protons [84]. The fission-neutrons with energies in the 100 meV range are then thermalized in a D_2O moderator and guided to the instruments in beam tubes. For some experimental techniques such as [NSE](#) spectroscopy (see below), a spin-polarized neutron beam is required. This can be achieved, for instance, by implementation of additional polarizing magnetic multi-layer guide-elements (supermirrors), which reflect only spin-up neutrons. At the instrument, the monochromator then defines the momentum $\hbar\mathbf{k}_i$ and energy $E_i = (\hbar\mathbf{k}_i)^2/(2m_n)$ of the incident neutrons impinging on the sample. In the scattering process, *i. e.* the interaction with matter, the momentum $\hbar\mathbf{k}_f$ and energy E_f of the scattered neutrons can change [Fig. 5.1a]. The basic concept of all neutron scattering techniques is then to determine the transfer of momentum $\hbar\mathbf{Q} = \hbar(\mathbf{k}_i - \mathbf{k}_f)$ and/or energy $\Delta E = \hbar\omega = \hbar^2(k_i^2 - k_f^2)/(2m_n)$, where \mathbf{Q} is the scattering vector. This provides important information about the microscopic static (*e. g.* atomic positions) and dynamic properties (*e. g.* phonons,

magnons) of the sample. Usually $\hbar = 1$ is assumed, and \mathbf{Q} and ω are named momentum and energy-transfer, respectively.

The actual quantity measured in a neutron scattering experiment is the rate of neutrons scattered to $\hat{\mathbf{k}}_f(\theta, \varphi)$ in a solid angle $d\Omega$ with a final energy $E_f \pm dE_f$ [Fig. 5.1b]. This quantity is called the double differential cross-section $\frac{d^2\sigma}{d\Omega dE}$, which contains contributions from coherent and incoherent scattering [38, 84]. Coherent scattering results from interference effects between the scattering from different atoms or magnetic moments, such as elastic Bragg-scattering or inelastic scattering from magnons. The incoherent part includes spin- and isotope incoherent scattering. Spin-incoherence results from scattering of a neutron on a single nucleus where the neutron spin and the nuclear spin simultaneously undergo a spin-flip. This leads to the localization of the scattering event to this single nucleus and results in a isotropic s-wave scattering amplitude. Isotope-incoherence does not involve spin-flips, and results from a variance of scattering lengths [227] of different isotopes.

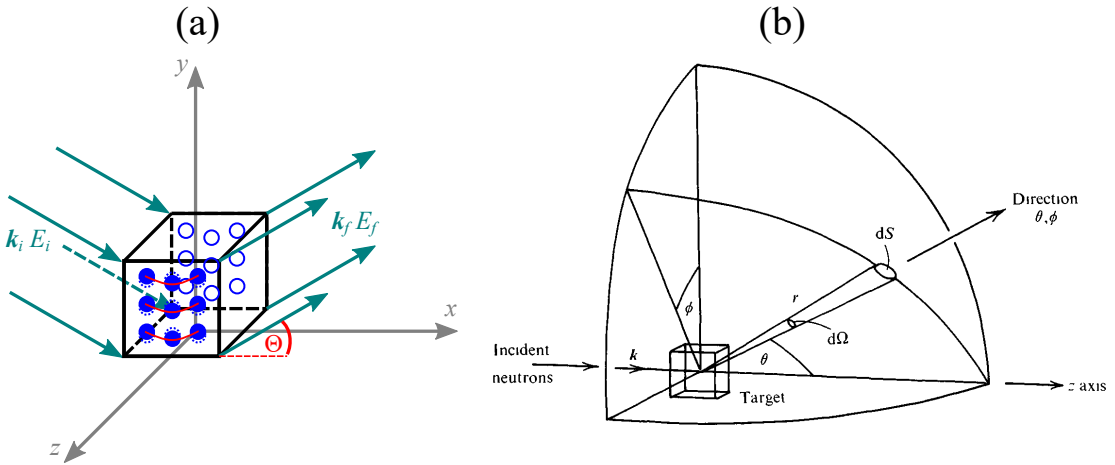


Fig. 5.1: (a) Illustration of the neutron-interaction with matter. By determining the transfer of momentum $\hbar\mathbf{Q} = \hbar(\mathbf{k}_i - \mathbf{k}_f)$ and energy $\Delta E = E_i - E_f$, one obtains information on the microscopic static (*e. g.* atomic positions) and dynamic (*e. g.* phonons) properties of the sample. (b) Definition of double differential cross-section $\frac{d^2\sigma}{d\Omega dE}$. From [40].

For nuclear scattering, the separation of $\frac{d^2\sigma}{d\Omega dE}$ reads [36]:

$$\begin{aligned} \left(\frac{d^2\sigma}{d\Omega dE}\right)_{\text{nuc}} &= \left(\frac{d^2\sigma}{d\Omega dE}\right)_{\text{coh}} + \left(\frac{d^2\sigma}{d\Omega dE}\right)_{\text{inc}} \\ &= N \frac{k_f}{k_i} \left(b_{\text{coh}}^2 S_{\text{coh}}(\mathbf{Q}, \omega) + b_{\text{inc}}^2 S_{\text{inc}}(\mathbf{Q}, \omega)\right) \quad , \end{aligned} \quad (5.1)$$

where N denotes the number of nuclei (scattering centers) and b_{coh} and b_{inc} are the tabulated [227] coherent and incoherent scattering lengths [84]. $S(\mathbf{Q}, \omega)$ are the scattering functions:

$$S_{\text{coh}}(\mathbf{Q}, \omega) = \frac{1}{2\pi N} \frac{k_f}{k_i} b_{\text{coh}}^2 \sum_{l, l'}^{l \neq l'} \int_{-\infty}^{\infty} \langle e^{-i\mathbf{Q}\mathbf{r}_{l'}(0)} e^{i\mathbf{Q}\mathbf{r}_l(t)} \rangle e^{-i\omega t} dt \quad (5.2)$$

and

$$S_{\text{inc}}(\mathbf{Q}, \omega) = \frac{1}{2\pi N} \frac{k_f}{k_i} b_{\text{inc}}^2 \sum_l \int_{-\infty}^{\infty} \langle e^{-i\mathbf{Q}\mathbf{r}_l(0)} e^{i\mathbf{Q}\mathbf{r}_l(t)} \rangle e^{-i\omega t} dt \quad . \quad (5.3)$$

Here $\mathbf{r}_{l'}(0)$ and $\mathbf{r}_l(t)$ denote the position vectors of the l' -th and l -th nuclei at time 0 and t , respectively. The brackets $\langle \dots \rangle$ describe the thermal average. The double-sum is missing in $S_{\text{inc}}(\mathbf{Q}, \omega)$, because incoherent scattering does not result from interference effects with other atoms. The incoherent part is not relevant for the critical scattering and not further discussed here. $S(\mathbf{Q}, \omega)$ is connected by Fourier-transforms to the real-space correlation function $G(\mathbf{r}, t)$, which describes the probability of finding a particle at time t and position \mathbf{r}_l when another particle was at position $\mathbf{r}_{l'}$ at $t = 0$ [84, 228]. Thus, $S(\mathbf{Q}, \omega)$ contains the information neutrons can provide about condensed matter: (i) Where do atoms sit (\mathbf{Q} -dependence), and (ii) how do they move (t -dependence).

For elastic Bragg scattering at a Bravais-lattice, the t -dependence vanishes and $S(\mathbf{Q}, \omega)$ can be written as [84]

$$S_{\text{nuc}}(\mathbf{Q}, \omega) \propto \delta(\hbar\omega) \sum_{\mathbf{G}} \delta(\mathbf{Q} - \mathbf{G}) \quad , \quad (5.4)$$

with the reciprocal lattice vectors \mathbf{G} . The corresponding nuclear cross-section is then

$$\left(\frac{d\sigma}{d\Omega}\right)_{\text{nuc}} \propto \sum_{\mathbf{G}} \delta(\mathbf{Q} - \mathbf{G}) |F_N(\mathbf{G})|^2, \quad (5.5)$$

where the nuclear structure factor $F_N(\mathbf{G})$ accounts for more than one atom per unit cell and also contains fluctuations of the atoms about their equilibrium positions. The latter are included in the *Debye-Waller* factor e^{-2W} with $W = 1/2\langle(\mathbf{Q} \cdot \mathbf{u})^2\rangle$ and \mathbf{u} as the thermal displacement of an atom from its equilibrium position \mathbf{r} [38]. Hence, the resulting differential cross-section, *i. e.* the experimental neutron scattering intensity, is proportional to $|F_N(\mathbf{G})|^2$. Due to the short range strong interaction between neutron and nucleus, the nuclear structure factor for a single atom is constant.

Magnetic scattering arises from interactions of the neutron spins with unpaired electrons. The cross section depends on the polarization (orientation) of the neutron spins as well as on the direction of the magnetic moments of the unpaired electrons in the sample. More specifically, the magnetic moments of the neutrons $\boldsymbol{\mu}_n = -\gamma_n \mu_N \boldsymbol{\sigma}$ ($\gamma_n = 1.9132$ [39]) interacts with the magnetic field \mathbf{B} generated by the dipole moment of the electron $\boldsymbol{\mu}_e = -2\mu_B \mathbf{s}$ and its orbital motion [39]. Here μ_N and μ_B denote the nuclear and Bohr-magneton and $\boldsymbol{\sigma}$ describes the Pauli spin operator with its components

$$\sigma_x = \begin{pmatrix} 0 & 1 \\ 1 & 0 \end{pmatrix} \quad \sigma_y = \begin{pmatrix} 0 & -i \\ i & 0 \end{pmatrix} \quad \sigma_z = \begin{pmatrix} 1 & 0 \\ 0 & -1 \end{pmatrix}. \quad (5.6)$$

Analogous to Eqn. (5.1) for nuclear scattering, the magnetic cross-section is also proportional to the (magnetic) scattering function $S(\mathbf{Q}, \omega)$ and can be written as [84]

$$\left(\frac{d^2\sigma}{d\Omega dE}\right)_{\text{mag}} = \frac{k_f}{k_i} \left(\frac{\gamma_n r_0}{2\mu_B}\right)^2 S(\mathbf{Q}, \omega), \quad (5.7)$$

with $r_0 = \mu_0 e^2 / (4\pi m_e)$. However, a general expression of $S(\mathbf{Q}, \omega)$, *i. e.* taking into account polarized neutrons, spin and orbital momentum of the electrons, is lengthy, especially for atoms with two or more unpaired electrons [84]. Thus, for simplicity, we consider here only the case of unpolarized neutrons, neglect the

orbital momentum, and assume just one type of magnetic ion. The magnetic scattering function is then [84]:

$$S(\mathbf{Q}, \omega) = |f(\mathbf{Q})|^2 e^{-2W} \underbrace{\sum_{\alpha, \beta} (\delta_{\alpha, \beta} - \hat{Q}_\alpha \hat{Q}_\beta)}_{P\text{-factor}} S_{\text{mag}}^{\alpha, \beta}(\mathbf{Q}, \omega) \quad , \quad (5.8)$$

with

$$S_{\text{mag}}^{\alpha, \beta}(\mathbf{Q}, \omega) = g^2 \mu_B^2 \frac{N}{2\pi} \sum_{\mathbf{l}} e^{i\mathbf{Q}\mathbf{l}} \int_{-\infty}^{\infty} \langle s_0^\alpha(0) s_l^\beta(t) \rangle e^{-i\omega t} dt \quad , \quad (5.9)$$

where α, β stand for the x, y, z components, and the sum is over the lattice vectors $\mathbf{l} = \mathbf{r}_l - \mathbf{r}_{l'}$. $N, f(\mathbf{Q})$, and $S_{\text{mag}}^{\alpha, \beta}(\mathbf{Q}, \omega)$ denote the number of magnetic atoms, the magnetic form factor and the *partial magnetic scattering function*. The latter is the space-time Fourier-transform of the spin pair correlation function [41, 84, 112], which yields the probability of finding the β -component $s_l^\beta(t)$ of a spin at position \mathbf{r}_l and time t if the α -component of a spin was $s_0^\alpha(0)$ at the origin and time $t = 0$ [41, 229]. The polarization factor (P -factor) in Eqn. (5.8) is only nonzero for magnetic components \mathbf{M}_\perp perpendicular to the momentum transfer \mathbf{Q} : $\mathbf{M}_\perp = \mathbf{Q} \times (\mathbf{M} \times \mathbf{Q})$ and thus neutrons can only probe \mathbf{M}_\perp [84].

The magnetic form factor $f(\mathbf{Q})$ [Eqn. (5.8)] corresponds to the Fourier transform of the spin density of unpaired electrons in real-space, which is in the order of several angstroms. This results in a non-constant \mathbf{Q} -dependence, which is typically described by spherical Bessel-functions [84]. Both the magnetic form factor and the P -factor can be exploited to separate nuclear and magnetic scattering.

In addition, magnetic scattering may induce neutron spin-flips, which can be addressed by a polarization analysis of an initially polarized neutron beam. Moon, Riste, and Köhler [230] introduced the so-called 1D polarization-analysis where the neutron spins are defined with respect to the magnetic guide field, which serves as a quantization axis. With spin-flippers up- and down-stream the sample, the four scattering channels $++$, $--$ (non-spin-flip) and $+-$, $-+$ (spin-flip) can be probed, where the symbols '+' and '-' define the orientation of the neutron spins and indicate the state before and after the scattering process (*cf.* App.A). In case of pure nuclear scattering, this can help to separate coherent or isotopic incoherent scattering, which do not affect the neutron spin state, from the spin incoherent

scattering, which affects a spin-flip (SF) of two-thirds of the neutron spins [84]. Moreover, magnetic contributions can be unambiguously distinguished from the coherent nuclear signal since the magnetic scattering shows pure SF scattering.

In NSE spectroscopy, as used in this work, the precession of neutron spins is used to measure energy-transfers. Thus, spin-flips from magnetic scattering disturb the spin-echo signals. However, by the analysis method discussed below and shown in [54], it is possible to exploit these spin-flips to separate signals from in-plane and out-of-plane magnetic scattering.

5.2. Triple-axis spectroscopy

The Triple-Axis Spectroscopy (TAS) technique was invented by Brockhouse more than 60 years ago [231] and has always been an important spectroscopy method. This results mainly from the ability to measure $S(\mathbf{Q}, \omega)$ at essentially any point in momentum $\hbar\mathbf{Q}$ and energy $\hbar\omega$ space [38]. The basic setup includes three rotation axes defining the monochromator-sample (MS), sample-analyzer (SA), and analyzer-detector (AD) angles, respectively [Fig. 5.2]. The monochromator, sample, and analyzer angles define k_i , k_f , $\mathbf{Q} = \mathbf{k}_i - \mathbf{k}_f$, and $\omega \propto k_i^2 - k_f^2$. Conventionally, $\omega > 0$ ($k_f < k_i$) is named energy-loss scattering.

The energy- and momentum-resolution of TAS is given by the monochromaticity and collimation of the neutron beam. Since the neutron flux is rather limited, both parameters are set to relaxed values by choosing a modest collimation in the order of 1° and by using mosaic monochromator and analyzer crystals [Fig. 5.2], which reflect a band of neutron wave vectors $\mathbf{k}_0 \pm \mathbf{k}$ around the mean value \mathbf{k}_0 . Accordingly, a distribution of momentum and energy transfers arises ($\mathbf{Q}_0 \pm \mathbf{Q}, \omega_0 \pm \omega$). To account for this resolution effect and extract the intrinsic scattering function $S(\mathbf{Q}, \omega)$, deconvolution of the experimental data with the instrumental resolution function $\mathbf{R}(\mathbf{Q}, \omega)$ is required.

The resolution function of a TAS instrument was first analytically described by Cooper and Nathans [233]. They developed a second-order matrix formalism to map the six components of $\mathbf{k}_i, \mathbf{k}_f$ onto the physically interesting four components

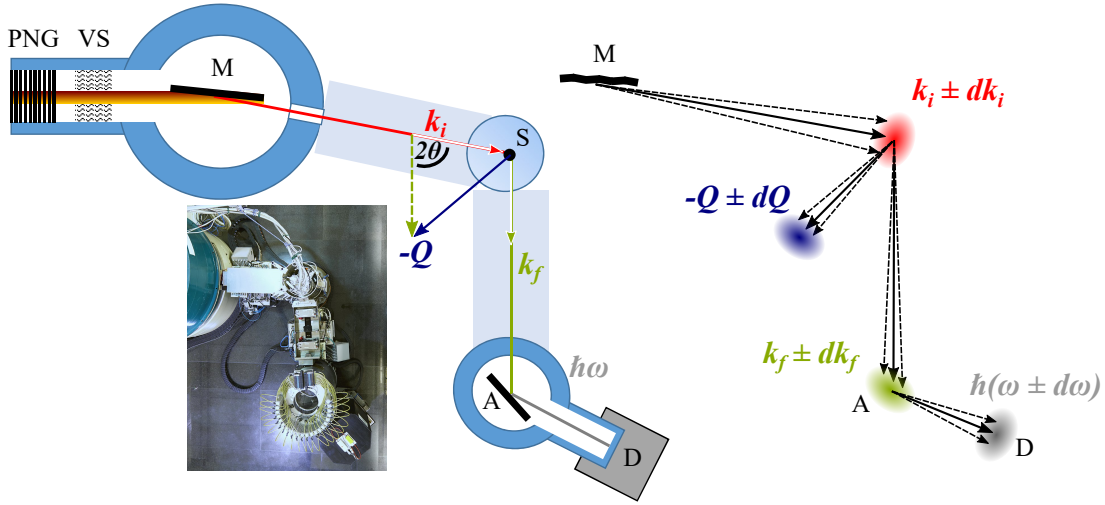


Fig. 5.2: Left: Schematic drawing and picture of the spin-echo TAS instrument TRISP at the FRM II [232]. For completeness, the polarizing neutron guide (PNG) and velocity selector (VS) are included. Right: Illustration of the limited instrumental TAS resolution due to mosaicity of monochromator and analyzer crystals.

of \mathbf{Q} and ω . The resolution function describes an ellipsoid in the four-dimensional (\mathbf{Q}, ω) -space:

$$R(\mathbf{Q}_0 - \mathbf{Q}, \omega_0 - \omega) = R_0 \exp \left(-\frac{1}{2} \sum_{i=1}^4 \sum_{j=1}^4 \tilde{M}_{i,j} X_i X_j \right) \quad , \quad (5.10)$$

where $\mathbf{X} = (\mathbf{Q}_0 - \mathbf{Q}, \omega_0 - \omega)$, and \tilde{M} denotes the 4×4 -resolution matrix. The signal I at the detector for a specific (\mathbf{Q}_0, ω_0) -position is given by the convolution of the resolution function with the sample-intrinsic $S(\mathbf{Q}, \omega)$:

$$I(\mathbf{Q}_0, \omega_0) \propto \int R(\mathbf{Q}_0 - \mathbf{Q}, \omega_0 - \omega) S(\mathbf{Q}, \omega) d\mathbf{Q} d\omega \quad . \quad (5.11)$$

Later Popovici [234] refined the elements of \tilde{M} to include spatial effects such as the curvature of focusing monochromators and analyzer, as well as the sample size. To simulate the corresponding resolution functions for the analysis of the data in this work, we use the RESLIB [235] and TAKIN [236] softwares and found the best agreements for our relatively large samples with the Popovici-model. In 1D, *i. e.* for a cut through the resolution ellipsoid in a certain direction, the TAS resolution

function is described by a Gaussian-function. Moreover, the resolution function and the corresponding slope of the ellipsoid in (\mathbf{Q}, ω) depend on the instrumental configuration, which has to be adjusted to the studied excitations to obtain optimal \mathbf{Q} - and ω -resolution [38].

Considering the energy-resolution ΔE of TAS instruments, typical values are 20-200 μeV for cold TAS instruments such as the IN12 at the ILL [237]. The best energy-resolution to date, however, can be achieved using NSE spectroscopy with $\Delta E \approx 1 \text{ neV}$ (IN15 at the ILL [238]). The NSE technique takes advantage of a completely different approach than TAS (see below), where beam monochromatization is the limiting factor due to the limited neutron flux. In this work, we use a combination of TAS and NSE spectroscopy at the TRISP spectrometer, which achieves an energy-resolution better than 1 μeV .

For the study of critical magnetic scattering both the width in Q and ω of $S(\mathbf{Q}, \omega)$ are essential parameters. For a proper determination of the static scattering function $S(\mathbf{Q})$, it would be necessary to measure the entire $S(\mathbf{Q}, \omega)$ function and perform a numerical ω -integration (see Eqn. (2.27)). This can be circumvented in quasi-2D systems by using an energy integrating TAS configuration as described by Birgeneau *et al.* [112]. In this configuration, the TAS analyzer is removed (two-axis mode) and k_f is aligned perpendicular to the 2D-layers [Fig. 5.3], corresponding to the ab -plane in Ca_2RuO_4 . The magnitude of k_f varies with ω , but the relevant components of \mathbf{q}_{2D} in the 2D planes are constant and independent of ω . In consequence, the detector signal corresponds to an energy integration according to Eqn. (5.12), where the lower integration limit (energy-gain scattering) is given by the thermal energy of the fluctuations, and the upper limit (energy-loss scattering) is given by the energy E_i of the incident neutrons:

$$S(\mathbf{Q}) = \int_{-\infty}^{\infty} S(\mathbf{Q}, \omega) d(\hbar\omega) \approx \int_{-k_B T}^{E_i} S(\mathbf{Q}, \omega) d(\hbar\omega) \quad . \quad (5.12)$$

In the case of Ca_2RuO_4 , we achieved this energy-integrating configuration with $k_f \parallel c$ by choosing $Q = (1 \ 0 \ 0.83)$ for $k_i = 1.75 \text{ \AA}^{-1}$.

For materials with more 3D character of the magnetic order, like $\text{Ca}_3\text{Ru}_2\text{O}_7$ [7], all components of \mathbf{q} are relevant and Q_L cannot be chosen arbitrarily. Thus, the aforementioned integration-technique, which depends on the integration along the

and $\kappa_0 = 0.2 \text{ \AA}^{-1}$. This choice of parameters is close to experimental values extracted from power-law fitting (see Chap. 6). Furthermore, we assume a Lorentzian $S(\omega) = \Gamma_q / [\Gamma_q^2 + \omega^2]$ with a q -dependent energy width $\Gamma_q = \Gamma(T)[1 + (q/\kappa_{\text{in}}(T))^2]$ [44, 239, 240]. Here, the T -dependent energy-width is $\Gamma(T) = \Gamma_0 t^{z\nu}$, with $\Gamma_0 = 1 \text{ meV}$ and $z\nu = 1$. We then calculate the integral [Eqn. (5.12)] in the limits between $-k_{\text{B}}T$ and E_i for each q_i in the Q_{H} -scan and fit the resulting intensity with a Lorentzian with HWHM κ_{out} . The results of this simulation are shown in Fig. 5.4. For the two-axis mode, the difference of the measured κ_{out} compared to the intrinsic κ_{in} is only of the order of a few percent. Such a change in the scaling behavior lies within our statistical error of the critical exponent ν . Hence, we did not correct the two-axis data of $\text{Ca}_3\text{Ru}_2\text{O}_7$ in Chap. 6 for the integration effect.

For comparison, we also conducted the same simulation for the triple-axis case [Fig. 5.4], where we added a Gaussian-distribution with the instrumental energy-resolution ($\pm 0.04 \text{ meV}$ for $k_i = 1.3 \text{ \AA}^{-1}$) as full-width at half-maximum (FWHM). For the latter case the difference between κ_{in} and κ_{out} is much larger.

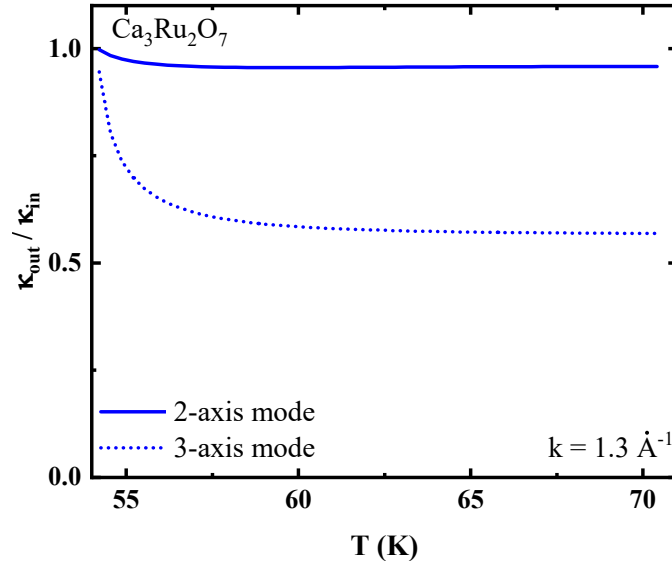


Fig. 5.4: Simulated ratios of $\kappa_{\text{out}}/\kappa_{\text{in}}$ vs. T in the two- and three-axis mode, respectively (see details in text).

5.3. Neutron spin-echo spectroscopy

The essential property of Neutron Spin-Echo (NSE) is that the energy-resolution is decoupled from the monochromatization [49, 241, 242]. This is achieved by using the neutron spin as an internal clock to measure the difference in flight-time in two magnetic field regions up- and down-stream the sample. The difference in flight-time corresponds to the energy-transfer and is monitored by a difference in the Larmor precession angle of the neutron spin in the two field regions. In this way, high energy-resolution is achieved without limiting the neutron flux by monochromatization. NSE directly measures the real part of the intermediate scattering function $\tilde{I}(\mathbf{Q}, t)$ [50], which corresponds to the time Fourier-transformation of $S(\mathbf{Q}, \omega)$. This intrinsic Fourier-transform property also facilitates the treatment of the resolution-function, because the usual convolution of the resolution function with $S(\mathbf{Q}, \omega)$ in conventional spectrometry (see Eqn. (5.11)) is converted to a product in NSE [242].

There are two main types of spin-echo techniques in use [50]: (i) The original NSE spectrometer invented by Mezei [49, 241, 242] uses static magnetic fields generated by large solenoid coils. These spectrometers provide very high energy-resolution for small momentum transfers \mathbf{Q} and quasi-elastic scattering (the mean energy-transfer is zero) [50]. (ii) For the spectroscopy of excitations at higher momentum- and energy-transfers the Neutron Resonance Spin-Echo (NRSE) technique has proven useful [243–247]. The Larmor-precession is induced by small radio-frequency coils. These compact devices are inserted into a TAS [Fig. 5.8]. The TAS provides the momentum-resolution and a coarse energy-resolution to suppress background, the NRSE then boosts the energy-resolution by two orders of magnitude to the sub- μeV range. The same setup can be used for the high-resolution Larmor Diffraction (LD) technique (see below) [248, 249]. In this work, measurements were performed at the hybrid thermal neutron triple-axis NRSE spectrometer TRISP at the FRM II [232].

Prior to the discussion of the NRSE approach used at TRISP, we describe the general concept of the spin-echo technique based on the original setup suggested by Mezei [Fig. 5.5] [49, 241].

We first assume a z -polarized neutron beam propagating along the y -axis ($\mathbf{v}_1 \parallel y$)

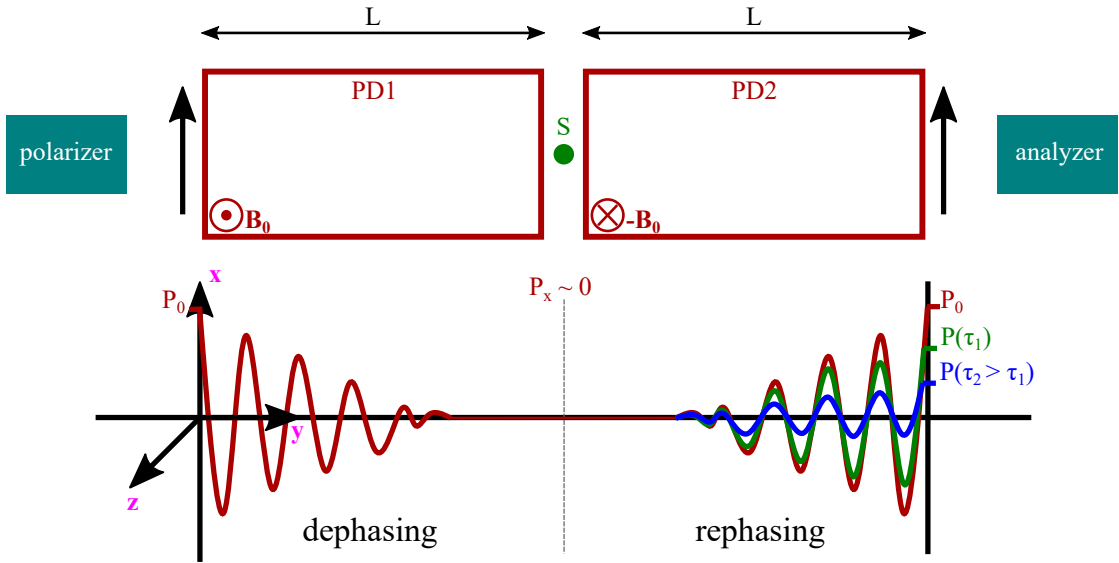


Fig. 5.5: Schematic drawing of the conventional NSE spectrometer as proposed by Mezei [241]. The neutrons enter the first PD1 ($\mathbf{B}_0 \parallel z$) with spins oriented perpendicular to \mathbf{B}_0 . While traversing PD1, the neutron spins precess around the initial beam polarization $P_0 \parallel x$ vanishes due to a slight variation in the Larmor phases φ_i of the neutron spins resulting from a variance of the neutron velocities. After the scattering process in the sample, the neutrons enter a second precession device PD2 with an opposite magnetic field ($\mathbf{B}_0 \parallel -z$), which reverses the precession phases accumulated in precession device (PD)1 and affects recovery of the neutron beam polarization. For excitations in the sample with $\Gamma = 0$, P_0 is reproduced (echoed) after PD2 ($P = P_0$). However, for excitations with $\Gamma > 0$, an additional variance in the neutron phase is induced and P_f is lowered ($P < P_0$). The dependence of P vs. the spin-echo time τ (the magnetic field B_0) is proportional to the Fourier-transform of $S(\mathbf{Q}, \omega)$.

[Fig. 5.5]. In a $\pi/2$ -flipper the spins of the neutrons with velocity v_1 are rotated parallel to the x -axis ($\boldsymbol{\sigma} \parallel x$), which is perpendicular to the direction of the static magnetic fields in the precession devices (PDs) ($\mathbf{B}_0 \parallel z$). Hence, upon entering the first PD, the neutron spins start precessing around \mathbf{B}_0 with a Larmor frequency of

$$\omega_L = \gamma_n \mathbf{B}_0 \quad , \quad (5.13)$$

where $\gamma_n = 2.916 \text{ kHz/Oe}$ denotes the gyromagnetic ratio of a neutron. The total spin precession after traversing both PDs takes [242]

$$\Phi = \varphi_1 + \varphi_2 = \omega_L \left(\frac{1}{v_1} - \frac{1}{v_2} \right) L \approx \omega_L \frac{\delta v}{v_1^2} L \quad , \quad (5.14)$$

where we used the approximation $v_2 = v_1 + \delta v$ with $\delta v \ll v_1$, *i. e.* we assumed very small velocity changes. For small energy transfers, we can use the following approximation

$$\hbar\omega = \frac{m}{2}(v_2^2 - v_1^2) \approx mv_1\delta v \quad (5.15)$$

and Eqn. (5.14), to relate Φ and the energy transfer $\hbar\omega$ in the scattering process within the sample

$$\Phi = \omega \left(\frac{\hbar\omega_L L}{mv_1^3} \right) \equiv \omega\tau_{\text{NSE}} \quad . \quad (5.16)$$

The so-called *spin-echo time* τ_{NSE} is a measure for the energy resolution of a **NSE** instrument. Accordingly, instead of measuring the energy of in- and outgoing neutrons independently as in **TAS**, **NSE** spectroscopy directly probes the energy transfer of each neutron. Thus, the resolution is not limited by the monochromatization of the incoming neutrons [244].

In the experiment, the polarization $P \hat{=} P_x$ [Fig. 5.5] given by the average $\langle \cos(\Phi) \rangle$ is monitored. With the scattering function $S(\mathbf{Q}, \omega)$ as the probability of a neutron being scattered with an energy transfer $\hbar\omega$, this average is [49, 241]:

$$P(\mathbf{Q}, \tau_{\text{NSE}}) = \langle \cos(\Phi) \rangle = \int S(\mathbf{Q}, \omega) \cos(\omega\tau_{\text{NSE}}) d\omega \quad . \quad (5.17)$$

Accordingly, **NSE** spectroscopy effectively measures the cosine Fourier transform of $S(\mathbf{Q}, \omega)$, which corresponds to the real part of the intermediate scattering function $\tilde{I}(\mathbf{Q}, \tau_{\text{NSE}})$ [242]. In the following we refer to τ as the spin-echo time τ_{NSE} . It follows from Eqn. (5.17) that the final polarization P decays exponentially with τ if we assume a simple Lorentzian profile for the spectral weight function $F(\omega)$ with **HWHM** Γ in $S(\mathbf{Q}, \omega)$ [Eqn. (2.26)], as expected *e. g.* for critical magnetic scattering

$$P(\tau) = P_0 \exp(-\Gamma\tau) \quad . \quad (5.18)$$

To determine $\Gamma(T)$ one measures the decrease of P vs. τ at different temperatures T . The polarization for a certain value of τ can be extracted from scanning the precession phase accumulated in the second PD by a small phase offset $\Delta\varphi(x) = 2\pi(x - x_0)/dL$ with the period dL . The resulting sinusoidal count rates $I(\Delta\varphi)$ are then given by the expression

$$I(\Delta\varphi) = \frac{I_0}{2}(1 + P \cos(\Delta\varphi)) \quad , \quad (5.19)$$

where $I_0/2$ is the mean intensity corresponding to $P = 0$. Experimentally, such a scan of $\Delta\varphi$ can be achieved either by changing the magnitude of the magnetic field B_0 or the length L of the second PD. Accordingly, the parameters of a spin-echo scan are the polarization P , the intensity I_0 , and the phase shift x_0 .

NRSE spectroscopy

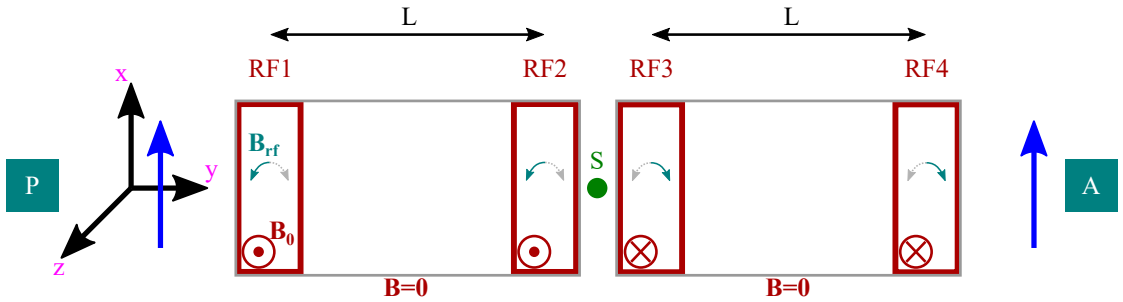


Fig. 5.6: Schematic design of a NRSE spectrometer as proposed in [243, 244, 246, 247]. The large solenoid coils of the conventional NSE, indicated by the grey boxes, are replaced by four or eight (bootstrap [245]) π -flipper coils. The π -flipper coils utilize a combination of an oscillating radio-frequency (RF) field B_{rf} , that consists of two counter-rotating components, and a static magnetic field B_0 . Depending on the direction of B_0 , only one rotating component affects the spin (green arrow), while the other is averaged out (grey arrow).

In the following, we describe the NRSE method and explain the main differences to NSE based on the works [243–247, 250]. The design of a NRSE spectrometer is schematically shown in Fig. 5.6. We first describe the RF spin-flipper. Each RF spin-flipper coil consists of a static magnetic field B_0 (here $\parallel \pm z$) and an radio-frequency field B_{rf} ($\parallel \pm x$) oscillating with the frequency ω_{rf} of the Larmor-precession

($\omega_{\text{rf}} = \gamma_n B_0 = \omega_L$). The linear RF field can be decomposed in two counter-rotating components where only the component rotating in the same direction as the neutron spin is effective [250]. Depending on the direction of \mathbf{B}_0 , either the clockwise or counter-clockwise component affects the neutron spin. Inside the coil, the neutron spin sees this rotating component as a static field B_{rf} and performs a π -rotation around this field [Fig. 5.7].

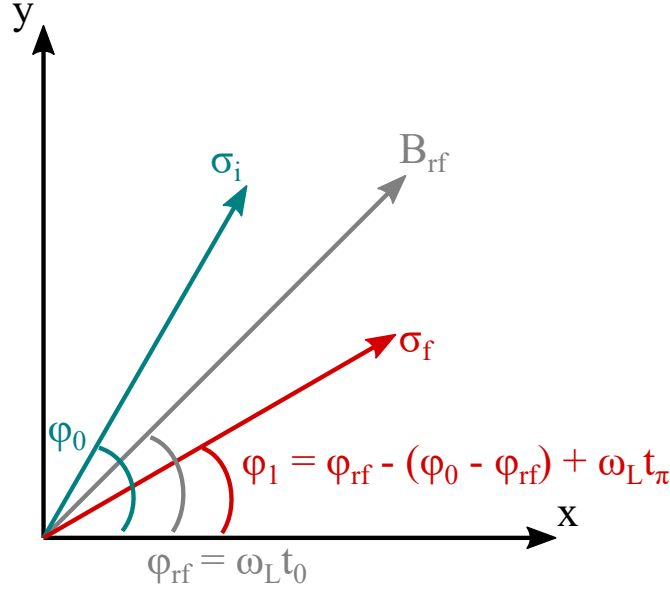


Fig. 5.7: Principle of a RF spin flipper coil as implemented in the NRSE spectrometer. We assume an incoming neutron whose spin σ_i and the x -axis form an angle φ_0 at time t_0 . Upon entering the RF-flipper, the spin will be π -flipped around a rotating field B_{rf} ending up in the state σ_f with an angle φ_1 . The rotation of B_{rf} during the π -flip ($\varphi_\pi = \omega_L t_\pi$) is neglected in the drawing. Adapted from [250].

We assume in Fig. 5.7 an incoming neutron at time t_0 whose spin takes the angles φ_0 and $\varphi_{\text{rf}} = \omega_L t_0$ with respect to the x -axis and B_{rf} , respectively. While the neutron spin performs the π -flip around B_{rf} , the magnetic field also rotates by $\omega_L t_\pi$, where $t_\pi = d/v$ is the time the neutron with velocity v spends in the coil of width d . The precession angle of the neutron spin after traversing one RF spin-flipper coil (C1) writes [250]

$$\varphi_1 = 2\omega_L t_0 - \varphi_0 + \omega_L t_\pi \quad . \quad (5.20)$$

As shown in Fig. 5.6, one precession arm in the NRSE spectrometer consists of two identical RF coils, *i. e.* after travelling a field-free distance L , the neutron will enter a second RF flipper-coil (C2) at time $t_1 = L/v$. The total precession angle after C2 becomes

$$\Phi_{C1-C2} = 2\omega_L t_1 - \varphi_1 + \omega_L t_\pi = 2\omega_L(t_1 - t_0) + \varphi_0 = 2\omega_L \frac{L}{v} + \varphi_0 \quad . \quad (5.21)$$

If we now compare Φ_{C1-C2} after two RF spin-flipper coils separated by a zero-field region of length L , with the precession angle Φ_{PD1} after one PD with length L in the conventional NSE spectrometer [Eqn. (5.14)], we obtain $\Phi_{C1-C2} = 2\Phi_{PD1}$. Thus, the resolution of NRSE is equivalent to that of conventional NSE spectrometer consisting of solenoids of length L containing a field B_0 twice the static field in the flipper coils.

The second precession region with negative B_0 is formed by the coils C3, C4. The RF coils work efficiently at higher frequencies, but at lower frequencies (typically < 40 kHz) the field-component rotating opposite to the neutron spin disturbs the spin-flip. To bridge the gap between this minimum RF and zero, additional DC spin-echo coils are inserted in between the RF flippers [Fig. 5.8]. The RF-coils at TRISP provide spin-echo times in the range $\tau_{\min} \leq \tau \leq 15\tau_{\min}$ with $\tau_{\min} = 4.087$ ps (3.43 ps) for $k_i = 2.51 \text{ \AA}^{-1}$ (2.66 \AA^{-1}). The additional DC-coils cover the smaller τ -range $0 \leq \tau \leq 1.8\tau_{\min}$.

In a spin-echo scan the polarization at each τ is measured by a small variation $\Delta\varphi$ in the interval $\pm\pi$ of the precession phase in PD2 (see Eqn. (5.19)). This is realized either by scanning the electrical current I02 in coil DC2 (change of B_0) or by scanning the translational position TC4 of C4 (change of L). $\Delta\varphi$ is much smaller than the total Larmor-phase and the variation of τ is negligible. The corresponding $\Delta\varphi$ are

$$\Delta\varphi(I02) = 2\pi(I02 - I01)/\Delta I02 \quad , \quad (5.22)$$

$$\Delta\varphi(TC4) = 2\pi(TC4)/\Delta TC4 \quad , \quad (5.23)$$

with the periods $\Delta I02 = 2\pi k_f / C_{\text{coil}}$ and $\Delta TC4 = 2\pi \hbar k_f / (m\omega_L)$, where $C_{\text{coil}} = 50.074 \text{ \AA}^{-1} \text{ A}^{-1}$ is a parameter of the DC coils used at TRISP.

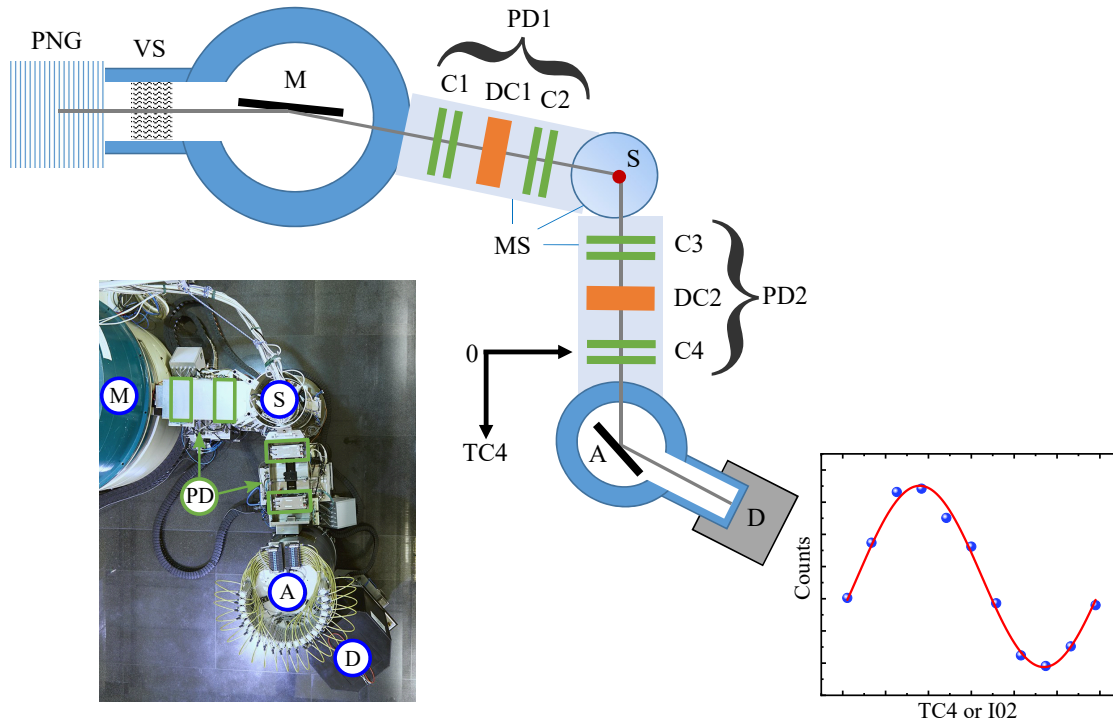


Fig. 5.8: Schematic drawing and picture of the NRSE instrument TRISP at FRM II. Before entering the first PD, the neutron beam is spin-polarized by a polarizing neutron guide (PNG) and monochromatized by both a velocity selector (VS) and a monochromator (M). The sample is positioned in between the PDs, which include the DC-coils ($DC_{1,2}$) as well as the RF spin-flipper coils (C_{1-4}). The earth magnetic field is shielded by μ -metal shields (MS) around the PDs and the sample region. After the PDs, the final polarization P_f and the energy of the scattered neutron beam is determined by an analyzer and detector, respectively. The inset shows an example of a spin-echo scan. The polarization P is measured either by scanning the current I_{02} in DC_2 or by linear translation TC_4 of C_4 .

Spin-flip scattering

So far, we have considered only non-spin-flip (NSF) scattering in the sample. For magnetic scattering, however, SF processes act on incoming neutron spins and thereby affect the precession angle [Fig. 5.9]. Adjusting the sign of the static magnetic fields in the PDs can be exploited not only to differentiate between nuclear and magnetic scattering, as described above, but also to separate the contributions from in-plane ($M_{\perp,y}$) and out-of-plane ($M_{\perp,z}$) magnetic fluctuations [54]. The (\perp)-symbol indicates that only magnetic components perpendicular to \mathbf{Q} can be observed. In Fig. 5.9, we assume an incoming neutron with a spin phase φ_i after the first PD. We use the conventional coordinate system with $x \parallel \mathbf{Q}$, y perpendicular to the \mathbf{Q} in the scattering plane, and z perpendicular to the scattering plane. According to [54], the neutron can then be π -flip scattered at either $M_{\perp,y}$ or $M_{\perp,z}$ with the corresponding spin-phase φ_f after scattering (*cf.* App. A)

$$\varphi_{f_y} = \pi - \varphi_i \quad , \quad (5.24)$$

$$\varphi_{f_z} = \pi + \varphi_i \quad . \quad (5.25)$$

Scattering on in-plane fluctuations $M_{\perp,y}$ reverses the sign of φ_i , effectively inverting the field of \mathbf{B}_0 in the first PD, whilst from scattering on the out-of-plane fluctuations $M_{\perp,z}$ the sign remains unaffected. Thus, depending on the field directions of \mathbf{B}_0 in the PDs, *i. e.* parallel ($\uparrow\uparrow$) or anti-parallel ($\uparrow\downarrow$) to each other, either the scattering on M_y ($\uparrow\uparrow$) or M_z ($\uparrow\downarrow$) fulfills the echo-condition, whereas the other component will be depolarized. To determine the contributions from in-plane $M_{\perp,y}$ and out-of-plane $M_{\perp,z}$ magnetic fluctuations in the signal, we therefore measure spin-echo scans for both directions of the magnetic field \mathbf{B}_0 in PD2 [54].

The component not fulfilling the echo-condition has a nonzero polarization at small $\tau < \tau_{\text{dep}}$ and interferes with the other component leading to a fast oscillation of the polarization. For $\tau > \tau_{\text{dep}}$, this component is depolarized and the oscillations disappear. According to [251], the period of these oscillations in units of the current[Amps] in coil DC2 is

$$T_{\text{osc}} = \frac{k_i}{2C'_{\text{coil}}} \quad (5.26)$$

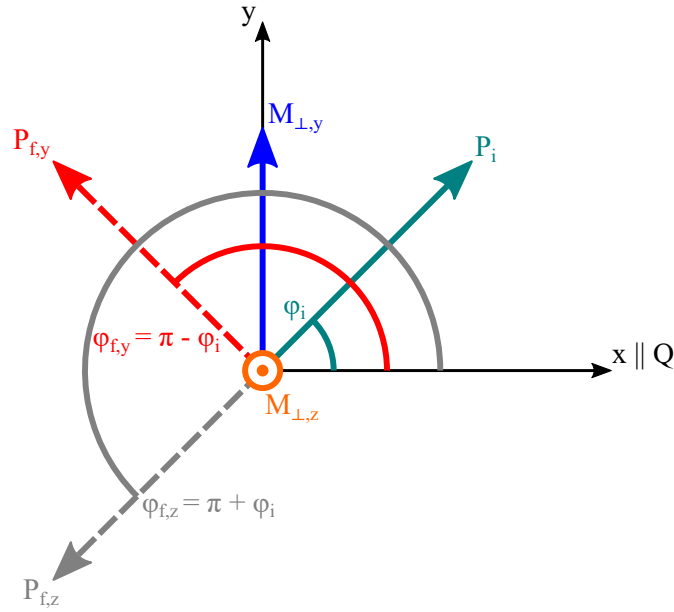


Fig. 5.9: Model of magnetic spin-flip processes from scattering at in-plane ($M_{\perp,y}$) and out-of-plane ($M_{\perp,z}$) fluctuations. Depending on the direction of the static magnetic field \mathbf{B}_0 in the second PD, either the neutrons scattered on $M_{\perp,y}$ ($\uparrow\uparrow$) or on $M_{\perp,z}$ ($\uparrow\downarrow$) fulfill the echo-condition (5.14), whereas the other component will be depolarized at sufficiently high τ . The two arrows denote parallel ($\uparrow\uparrow$) or antiparallel ($\uparrow\downarrow$) magnetic fields in the PDs. Adapted from [54].

with an instrumental parameter $C'_{\text{coil}} = 50.074/(2\pi) \text{ \AA}^{-1} \text{ A}^{-1}$ for the coils used at TRISP. To determine τ_{dep} for the experiments in this work, we assume a Gaussian distribution of wave vectors with FWHM Δk_i around the nominal k_i . The corresponding distribution of the Larmor-phase $\Delta\varphi_1$ around φ_1 due to Δk_i is $\Delta\varphi_1 = \Delta k_i/k_i \varphi_1$ [54]. We get a beam depolarization $\Delta\varphi_1 = 2\pi$ after passing two PDs for $\tau_{\text{dep}} > 10$ ps for $k_i = 2.66 \text{ \AA}^{-1}$ and $\Delta k_i = 0.034 \text{ \AA}^{-1}$.

Data analysis based on ray-tracing model

As mentioned above, in-plane and out-of-plane magnetic scattering channels can interfere with each other and lead to a complex spin-echo signal with a fast oscillating

polarization. A simple analytical analysis of this complex signal containing linewidth information of both M_y and M_z is not possible. We therefore describe both the Larmor-precession and the spin-flip processes in the sample in a numerical model, which is included in the fit-function. This approach was implemented in MATLAB and first used to analyse critical scattering in the classical model systems MnF_2 and Rb_2MnF_4 [54], and in the heavy-fermion system UGe_2 [53]. It was possible to separate the contributions of M_y and M_z . This is a clear advantage of NRSE over TAS, where separation of transverse and longitudinal signals requires measurement at different Q -positions, as described in [252].

The numerical simulation is similar to a Monte-Carlo (MC) simulation where the parameters are selected by random numbers. It turned out that MC does not work inside the fitting function due to the statistical noise. We therefore use discrete distributions instead of random numbers. The main steps of the simulation (ray-tracing simulation (RTS)) are [251]:

1. Definition of an incoming spin-polarized neutron band ($k_i \pm dk_i, \varphi_i$) with a Gaussian velocity distribution p_k with FWHM Δk_i
2. Simulation of the accumulated precession angle φ_1 of each defined neutron after the first PD
3. Simulation of the scattering process on (i) in-plane ($M_{\perp,y}$) and (ii) out-of-plane ($M_{\perp,z}$) fluctuations with the corresponding spin-flips in the precession angle $\varphi_S = \pi \mp \varphi_1$ weighted with the probability $p_\omega = S(\mathbf{Q}, \omega)d\omega$ of being scattered with an energy transfer ω . We assume $S(\mathbf{Q}, \omega) \sim S(\omega)$, *i. e.* that $S(\mathbf{Q}, \omega)$ is independent of \mathbf{Q} within the Q -resolution of the TAS. $S(\omega)$ further includes the intensities I of the involved scattering components. For Ca_2RuO_4 at $Q = (1\ 0\ 0)$, we observe two signals denoted as '1' and '2', which each can consist of in-plane (ip) and out-of-plane (op) components:

$$S(\omega) = \frac{I_1}{I_1 + I_2} \cdot \left[\frac{I_{1,\text{ip}}}{I_{1,\text{ip}} + I_{1,\text{op}}} \cdot L(\omega, \Gamma_{1,\text{ip}}) + \frac{I_{1,\text{op}}}{I_{1,\text{ip}} + I_{1,\text{op}}} \cdot L(\omega, \Gamma_{1,\text{op}}) \right] + \frac{I_2}{I_1 + I_2} \cdot \left[\frac{I_{2,\text{ip}}}{I_{2,\text{ip}} + I_{2,\text{op}}} \cdot L(\omega, \Gamma_{2,\text{ip}}) + \frac{I_{2,\text{op}}}{I_{2,\text{ip}} + I_{2,\text{op}}} \cdot L(\omega, \Gamma_{2,\text{op}}) \right] \quad (5.27)$$

with $L(\omega, \Gamma) = \Gamma / (\omega^2 + \Gamma^2)$.

4. Inclusion of the Gaussian energy resolution $R(\omega)$ of the background **TAS** as $p_\omega = S(\omega)R(\omega)d\omega$.
5. Calculation of the precession angles φ_f while traversing the second **PD**
6. Summation over the contributions of each neutron spin to the final polarization P_f

Some exemplary **RTS** for different parameters are shown in Fig. 5.10. The fast oscillations appear only when the intensity of the in-plane scattering is nonzero [Fig. 5.10a-c], as observed for $\text{CeCu}_{5.8}\text{Au}_{0.2}$ (see Chap. 7). On the other hand, we will see in Chap. 6, that panel (d) describes the situation in Ca_2RuO_4 at $Q = (1\ 0\ 0)$ best, where a saturation of the polarization is observed for $\tau > 20$ ps.

5.4. Larmor diffraction

Larmor Diffraction (**LD**) was invented by Rekveldt [248, 249] and is closely related to the neutron spin-echo technique. In the following, we briefly discuss the principle of **LD** based on Refs. [248, 249, 253–256]. Similar to **TAS**, the resolution in conventional neutron diffraction techniques depends on the monochromatization and divergence of the neutron beam, which is limited by the finite neutron flux. In **LD** the Larmor-phase is used to determine the lattice spacings $d_{hkl} \equiv d$, and the resolution is decoupled from the beam-collimation and monochromatization. With this approach, small changes in the lattice spacings and its spread Δd can be resolved with a resolution better than $\Delta d/d \sim 10^{-5}$, as shown in [255]. This corresponds to at least one order of magnitude higher resolution compared to conventional neutron diffraction instruments. The development of new designs for Larmor-diffractometers is an ongoing procedure [50], but for simplicity we focus in the following on the conventional design proposed by Rekveldt [Fig. 5.11].

LD requires an initially polarized neutron beam and a precession region with an applied magnetic field \mathbf{B} perpendicular to the polarization direction. At the entrance of the magnetic field region, the neutron spins perform Larmor precessions with precession angle $\varphi_{LD} = \omega_L t_L$ before and after the diffraction process with the precession time $t_L = L^*/v_\perp$ [Fig. 5.11]. Here L^* denotes the length of the precession

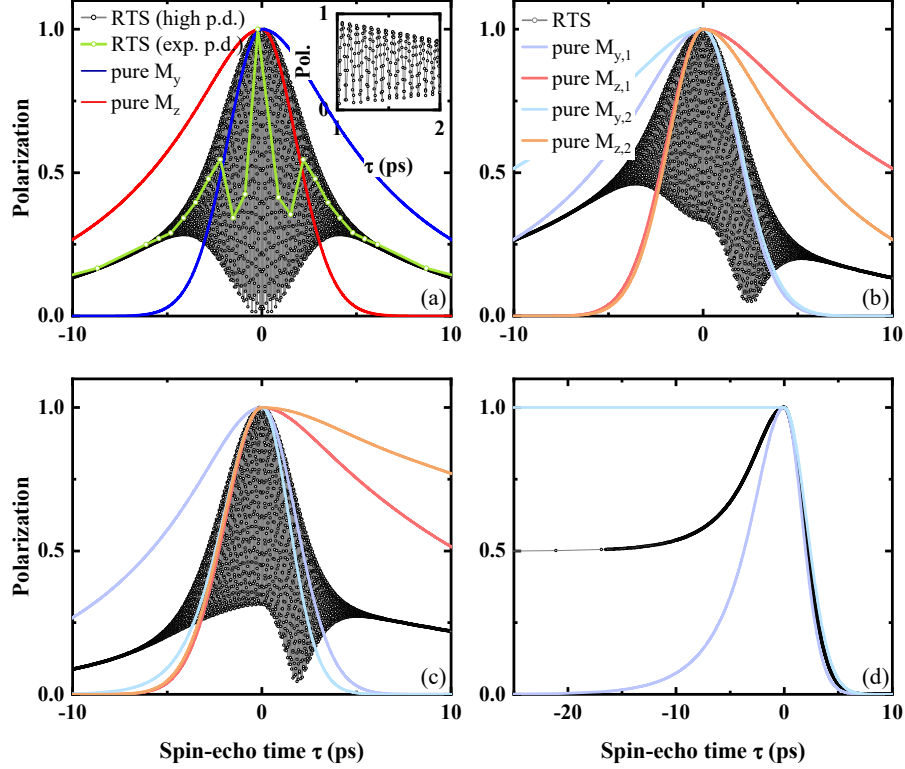


Fig. 5.10: Illustration of the neutron ray-tracing simulation. In (a) only one signal component with identical Γ for in-plane (M_y) and out-of-plane (M_z) scattering was assumed, whereas in (b-d) two signal components (1,2) with different Γ were considered, each with contributions from M_y and M_z . The grey shaded part corresponds to the high-frequency polarization oscillations resulting from the interference of M_y and M_z (resolved in the inset of panel (a)). In most of our experiments this oscillation was not resolved and sampled with a low point-density (p.d.) shown by the green curve in panel (a). For the examples different parameters were used: (a) $\Gamma_y = \Gamma_z = 100 \mu\text{eV}$, $I_y/I_z = 1$. The inset shows the oscillating behavior due to the interference of M_y and M_z . (b) $\Gamma_{z,1} = \Gamma_{y,2} = \Gamma_{y,1}/2 = \Gamma_{z,2}/2 = 50 \mu\text{eV}$, $I_1/I_2 = 1$, $I_y/I_z = 1/2$. (c) $\Gamma_{y,1} = 100 \mu\text{eV}$, $\Gamma_{z,1} = 50 \mu\text{eV}$, $\Gamma_{y,2} = 500 \mu\text{eV}$, $\Gamma_{z,2} = 20 \mu\text{eV}$, $I_1/I_2 = 1$, $I_y/I_z = 1/2$. (d) $\Gamma_{y,1} = 200 \mu\text{eV}$, $\Gamma_{y,2} = 1 \text{ neV}$, $I_y/I_z \sim 0$, $I_1/I_2 = 1$. For details regarding the scattering function see text. We assumed $k_f = 2.66 \text{ \AA}^{-1}$ and the velocity distribution $\Delta k = 0.034 \text{ FWHM}$.

region and v_{\perp} defines the velocity component perpendicular to the magnetic field boundaries. The velocity $v_{\perp} = (\hbar/m) k_{\perp} = (\hbar/m) G/2$ is proportional to the lattice spacing d via the reciprocal lattice vector $G = 2\pi/d$ and is independent of k and the Bragg-angle, if the field boundaries are aligned parallel to the lattice planes. After running through both precession-regions the phase is:

$$\varphi_{LD} = \frac{2\omega_L L^* m}{\hbar\pi} d \quad . \quad (5.28)$$

φ_{LD} is a measure for the lattice spacing d .

A variation of the d spacing by thermal expansion effects, for instance, induces a shift of the total precession angle

$$\Delta\Phi = \Phi \frac{\Delta d}{d} \quad . \quad (5.29)$$

At TRISP, $\Delta\Phi$ is measured by scanning the length of the precession region L^* by translational variation *TC4* of the fourth coil position [Fig. 5.11b]. $\Delta\Phi$ is then obtained by fitting the sinusoidal intensity $I(\Phi + \Delta\Phi)$ with Eqn. (5.19). For an orthorhombic system like Ca_2RuO_4 , the lattice spacing is related to the lattice parameter by $d(h,k,l) = (h^2/a^2 + k^2/b^2 + l^2/c^2)^{-0.5}$. Hence, with a proper choice of nuclear Bragg-peaks, the temperature dependence of the lattice parameter itself can be measured directly.

From the depolarization of the neutron beam *vs.* Φ , the **FWHM** ε_{FW} of a normalized Gaussian distribution function $f(\Delta d/d)$ of the lattice spacing variations around the mean value d can be extracted. This is similar to **NSE** spectroscopy, where the energy width Γ of the scattering function $S(\omega)$ can be determined from the depolarization of the neutron beam *vs.* τ (see Eqn. (5.18)). The corresponding expression for **LD** is:

$$P(\Phi) = P_0 \exp\left(-\frac{\Phi^2 \varepsilon_{FW}^2}{16 \ln 2}\right) \quad . \quad (5.30)$$

At TRISP, $P(\Phi)$ can be obtained by varying the frequency applied in the RF-coils ($\Phi = \omega\tau$) [Fig. 5.11c].

In summary, **LD** is a powerful method to study the thermal expansion of lattice spacings (parameter) and to determine the distribution function $f(\Delta d/d)$ of the lattice spacings to reveal structural changes.

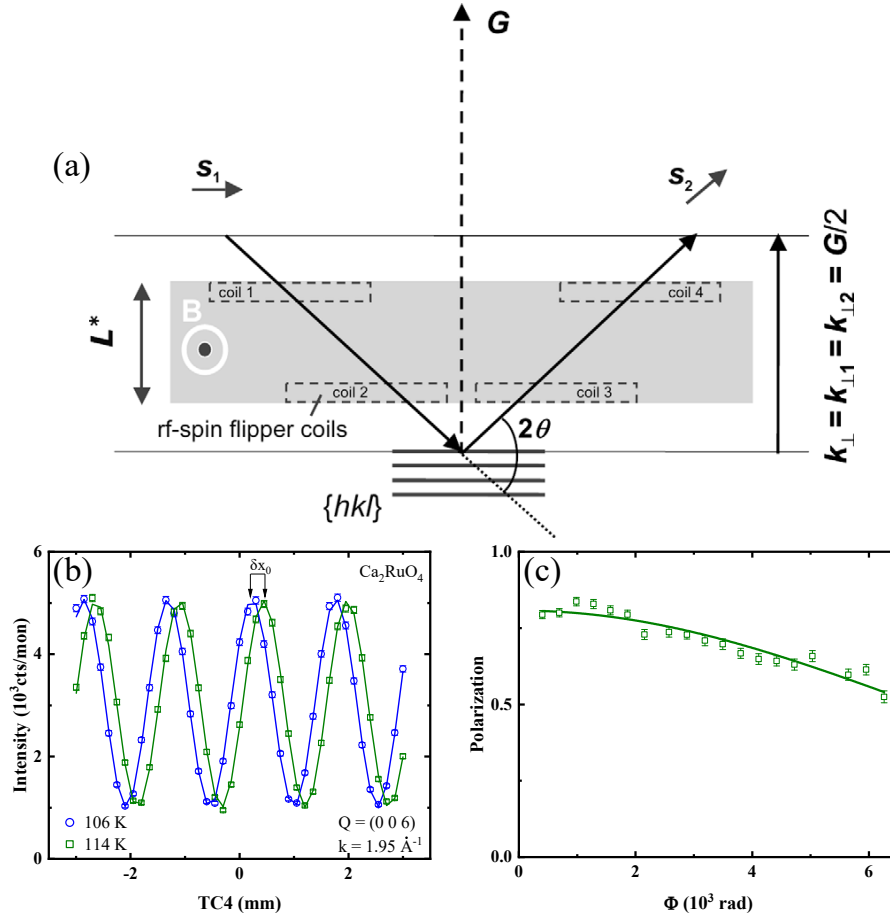


Fig. 5.11: (a) Concept of LD. The neutron spins S of a polarized neutron beam undergo Larmor precessions in the precession region with a perpendicular magnetic field (grey box). The precession of each neutron spin depends solely on the component of k_{\perp} perpendicular to the field boundaries, which is proportional to the lattice spacing d . At TRISP, the precession region is defined by four RF-spin flipper coils, as indicated by the boxes with broken lines. From [255]. (b) Example for a LD scan performed on a Ca_2RuO_4 single-crystal at the nuclear Bragg-peak $(0\ 0\ 6)$. From the phase-shift δx_0 between two temperatures, the relative change of lattice spacings $\Delta d/d$ can be obtained. (c) Example for a $P(\Phi)$ curve to determine FWHM ε_{FW} of the variance of lattice spacings $f(\Delta d/d)$.

6. Critical magnetic fluctuations in layered ruthenates

We present **TAS** and **NSE** studies on the critical behavior in the layered ruthenates Ca_2RuO_4 , $\text{Ca}_3\text{Ru}_2\text{O}_7$, and $\text{Ca}_3(\text{Ru}_{0.99}\text{Ti}_{0.01})_2\text{O}_7$ in the vicinity of the Néel-temperatures. We find that the critical behavior of single-layer Ca_2RuO_4 is compatible with predictions of the **2D-XY** model. The bilayer compound $\text{Ca}_3\text{Ru}_2\text{O}_7$ is only partly consistent with the **2D-XY** theory and best described by the **3D-I** model, likely due to the intra-bilayer exchange interactions in combination with an orthorhombic single-ion anisotropy. No critical behavior is observed in $\text{Ca}_3(\text{Ru}_{0.99}\text{Ti}_{0.01})_2\text{O}_7$, because of the to first-order character of the magnetic transition.

6.1. Single-layer Ca_2RuO_4

Characterization and experimental details

High-quality single crystals of Ca_2RuO_4 , $\text{Ca}_3\text{Ru}_2\text{O}_7$, and $\text{Ca}_3(\text{Ru}_{0.99}\text{Ti}_{0.01})_2\text{O}_7$ were grown by the optical floating zone method [68], as described in Refs. [6, 7, 79]. The lattice parameters of Ca_2RuO_4 are $a = 5.39 \text{ \AA}$, $b = 5.63 \text{ \AA}$, and $c = 11.75 \text{ \AA}$ [66]. In addition to the magnetic characterization of a particular Ca_2RuO_4 single-crystal [Fig. 6.1], we measured a number of various other crystals with a SQUID magnetometer to check their uniformity. Figure 6.1a displays an overview of the corresponding normalized c -axis susceptibilities ($H \parallel c$) of selected crystals. The extracted variance of the maximum positions $T_{\text{max},i}$ is small ($\pm 0.5 \text{ K}$) [Fig. 6.1b], whereas the widths of the curves around T_{max} are significantly broad (**FWHM** $\approx 8 \text{ K}$). This signals that T_N is not sharply defined in our Ca_2RuO_4 samples, but

that an intrinsic distribution of Néel-temperatures is present. Such a variance of T_N can *e.g.* result from microstrains within the crystal, which can be expected in Ca_2RuO_4 below the simultaneous structural and metal-to-insulator transition at 360 K [67].

As described in Chap. 5, neutron Larmor Diffraction is specialized to study not only the T -dependence of the lattice spacings d , but also the Gaussian distribution of the lattice spacings $f(\Delta d/d)$ with FWHM ε_{FW} . In particular, the latter contains information on the microstrains within the sample. We therefore took advantage of the LD capability at TRISP and performed LD scans on a selected Ca_2RuO_4 single-crystal (≈ 2.5 mg) at various nuclear Bragg-peaks (4 0 0), (0 4 0), and (0 0 6). This was used to determine the thermal expansion $\Delta L = L(T) - L(4K)$ of the lattice parameter $L = a, b, c$ and ε_{FW} [Fig. 6.2]. The obtained T -dependence of the lattice parameters [Fig. 6.2a-c] is in good agreement with previous neutron measurements [66]. The distribution of the lattice spacings is in the order of $\sim 10^{-4}$ and approximately doubles upon cooling from 200 K [Fig. 6.2d-f]. Above 200 K, the distribution enhances slightly as the structural MIT at 370 K is approached. Additionally, small anomalies were found at T_N [Fig. 6.2e,f]. These observations are consistent with the appearance of microstrains within our samples and support our conjecture of a strain-dependence of T_N in Ca_2RuO_4 , which is reminiscent of the (pseudo)spin-lattice coupling in Sr_2IrO_4 [257, 258]. In the following analysis, we take this distribution of T_N into account, which allows us to extract the critical properties of Ca_2RuO_4 similar to the case of a sharply defined T_N .

Now we proceed with the experimental details of the following neutron experiments. To enhance the intensity of neutron scattering, about 100 single-crystals containing orthorhombic (a, b)-twins with a total mass of 1.5 g were co-aligned on three Si-plates with thicknesses of 0.5 mm and placed in Al-sample holders [Fig. 6.3a]. The mosaicity of the sample array obtained from rocking-scans was between 2-3° [Fig. 6.3b] in line with [6]. Due to the (a, b)-twinning, the scattering planes were (H 0 L)/(0 K L).

The energy integrating TAS experiments (two-axis mode) on Ca_2RuO_4 were carried out at the thermal neutron spectrometer TRISP [232, 259] at the FRM II neutron source. The instrument was operated with clockwise scattering sense at the monochromator and sample ($SM = -1$, $SS = -1$) at $k_i = 1.75 \text{ \AA}^{-1}$. The dynamic

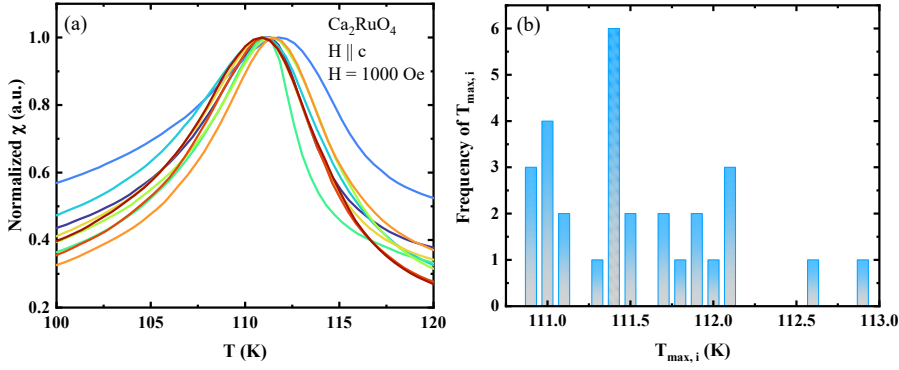


Fig. 6.1: (a) Overview of the normalized c -axis magnetic susceptibility on selected Ca_2RuO_4 single-crystals. (b) Shows the variance of the maximum positions $T_{\text{max},i}$ for the crystals i . Although the variance of $T_{\text{max},i}$ is small ($\pm 0.5 \text{ K}$), the width of the transitions is relatively large.

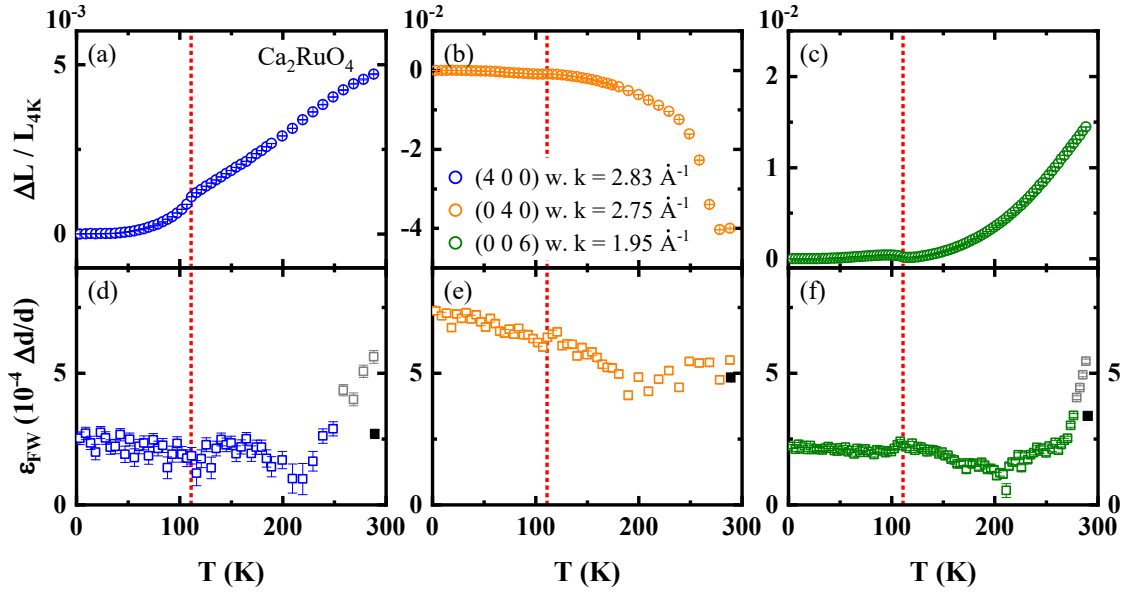


Fig. 6.2: (a-c) Thermal expansion of the lattice parameter $L = a, b, c$ with $\Delta L = L(T) - L(4K)$ obtained from LD measurements at the nuclear Bragg-peaks $(4\ 0\ 0)$, $(0\ 4\ 0)$, and $(0\ 0\ 6)$. (d-f) T -dependence of the FWHM ε_{FW} of the corresponding lattice spacing distribution $f(\Delta d/d)$. The full black squares are from a temperature stable frequency scan, while the grey points are likely artefacts of a reduced polarization due to thermal drifts. The red dotted lines indicate T_N .

properties were determined from measurements at (i) the cold neutron TAS FLEXX [260] at the BER II neutron source and at (ii) TRISP by using the NSE capability. For the TAS measurements, an instrumental configuration $SM = -1$, $SS = 1$, $SA = -1$, open collimation, and a neutron wave vector $k_f = 1.3 \text{ \AA}^{-1}$ (TAS energy resolution/vanadium width $\approx 0.15 \text{ meV}$) were used. In addition to a velocity selector, a Be-filter in the primary spectrometer was used to suppress higher monochromator orders. The NSE measurements were conducted at $Q = (1 \ 0 \ 0)$ with $k_i = 2.66 \text{ \AA}^{-1}$ (TAS energy resolution $\approx 1 \text{ meV}$) and $Q = (1 \ 0 \ 0.53)$ with $k_i = 2.51 \text{ \AA}^{-1}$ (TAS energy resolution $\approx 0.9 \text{ meV}$) with the same instrumental configurations $SM = -1$, $SS = -1$, and $SA = -1$. A small offset in the thermometry between TRISP and FLEXX was corrected by comparing the $(1 \ 0 \ 0)$ peak intensities.

Static critical properties of Ca_2RuO_4

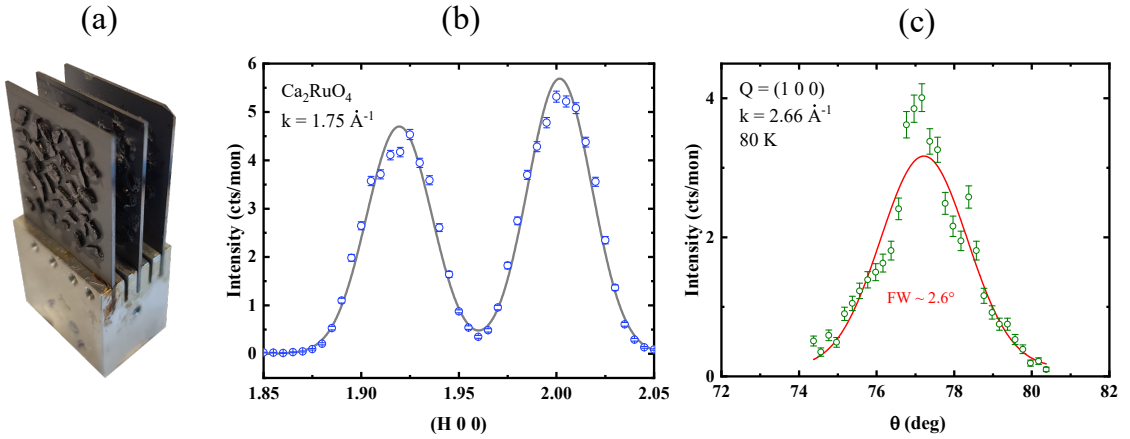


Fig. 6.3: (a) Picture of the Ca_2RuO_4 array. (b) $(H \ 0 \ 0)$ scan shows the $(2 \ 0 \ 0)$ and $(0 \ 2 \ 0)$ peaks due to (a,b) -twinning of the Ca_2RuO_4 crystals. The grey solid line is a fit with two Gaussian-functions ($\text{FWHM} \approx 0.04 \text{ r.l.u.}$). (c) Rocking scans at the AFM $(1 \ 0 \ 0)$ peak at 80 K ($T \ll T_N$).

First, we like to determine the critical exponent β of the order parameter M (staggered magnetization). For an ideal second-order phase transition, the order parameter is $M \propto |t|^\beta$ and vanishes above T_N . Thus, the critical exponent β can be extracted from the measured nominal magnetic $(1 \ 0 \ 0)$ peak intensity $I_{100} \propto M^2 \propto |t|^{2\beta}$ in Fig. 6.4a. In general, β and the other critical exponents are

extracted from the slopes of linear fits in double-logarithmic plots (see $\text{Ca}_3\text{Ru}_2\text{O}_7$ below). However, the data in Fig. 6.4a cannot be described directly with a PL scaling function. Especially the intensity around the anticipated $T_N = 110$ K [66, 176] does not show the expected sharp drop, but is smeared out. In principle, there are two reasons for a rounding of the magnetic Bragg-intensity at T_N , namely critical scattering or a variance of transition temperatures. One way to distinguish between them is to measure the scattering intensity at a Q -position in distance to the magnetic Bragg-peak, where its contribution is suppressed. This can be especially useful in quasi-2D systems, where the critical scattering is expected to be independent along the direction perpendicular to the isolated 2D planes and can therefore be particularly pronounced [261].

Ca_2RuO_4 is considered as a good realization of a quasi-2D system with a magnetic rod perpendicular to the (a,b) -plane, *i. e.* along the c -direction. This was previously suggested by the magnetic susceptibility in the paramagnetic state [176], which contains a broad maximum for $H \parallel b$ (easy axis) [Fig. 3.6a], and recently established by the magnon dispersion in the ordered phase [6] (see Chap. 3). We therefore expect also the critical fluctuations in Ca_2RuO_4 to be quasi-2D like, *i. e.* independent of Q_L . Accordingly, we measure an enhancement of the scattered intensity at $Q = (1\ 0\ 0.83)$ [inset in Fig. 6.4a], *i. e.* in distance to the $(1\ 0\ 0)$ peak, for temperatures in vicinity to the anticipated T_N of approximately 110 K [66, 176]. More specifically, we observe that the critical scattering intensity peaks at a temperature slightly higher than 110 K. This behavior is likely related to the fact that T_N of our Ca_2RuO_4 sample is not sharply defined, but there is an intrinsic distribution of Néel temperatures around a rather uniform mean T_N of our crystals [see gray shaded area in Fig. 6.4a]. This observation is consistent with our results from magnetometry and LD measurements (see above).

As the rounding of the $(1\ 0\ 0)$ peak intensity cannot be attributed to critical scattering above T_N , since the data in the inset of Fig. 6.4a indicate that the contribution of critical scattering is two orders of magnitude smaller, we fit the $(1\ 0\ 0)$ data in the range 90 - 120 K ($-0.2 < t < 0.1$) instead with a convolution of the above mentioned PL and a Gaussian distribution of T_N with a FWHM ΔT_N [Fig. 6.4a]. The resulting fit parameters are $T_N = 112.20(1)$ K, $\Delta T_N = 4.84(1)$ K, and $\beta = 0.158(6)$. It can be found in Tab. 2.2, that the β -value lies in between the

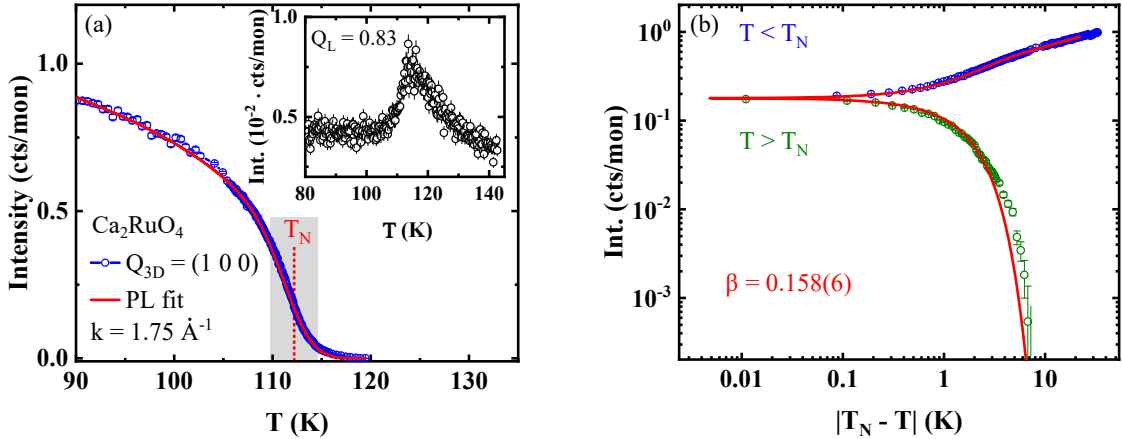


Fig. 6.4: Magnetic order parameter and critical scattering in Ca₂RuO₄. (a) Intensity of the magnetic (1 0 0) peak measured as a function of temperature. The red solid line is a PL fit $I \propto M^2 \propto |t|^{2\beta}$, with $\beta = 0.158(6)$ and $T_N = 112.20(1)$ K, convoluted with a Gaussian-distribution of Néel temperatures T_N with a FWHM of 4.84(1) K (grey shaded area). The inset shows the intensity measured at $Q = (1\ 0\ 0.83)$. The increase of intensity in vicinity to T_N indicates the presence of critical scattering from critical magnetic fluctuations. (b) Shows the same data as in (a) on a double-logarithmic scale. The data and fits are non-linear due to the distribution of T_N .

limits of the 2D-I ($\beta = 0.125$ [16]) and 2D-XY model ($\beta = 0.23$ [91]), as suggested for a XY system with fourfold crystal field anisotropy (XYh_4) [262]. Figure 6.4b shows I_{100} and the fit curve on a double-logarithmic scale, illustrating that the PL fit provides an adequate description of the data below T_N , and also for a range of temperatures above T_N . The strong deviation from a simple PL (straight line in double logarithmic plot) is due to the Gaussian distribution of T_N .

Next, we like to extract the inverse correlation length $\kappa(T)$ and the critical amplitude $S_0(T)$ from the static scattering function $S(\mathbf{q})$, which would in principle require an energy-integration of the dynamic scattering function $S(\mathbf{q}, \omega)$ (see Eqn. (2.27)). However, due to the 2D-character of the magnetism in Ca₂RuO₄, we can take advantage of the energy-integrating two-axis mode (see Chap. 5 and Ref. [112]) in the following TAS measurements. For this, we chose $Q = (1\ 0\ 0.83)$ for the Q_H -scans [Fig. 6.5], which lies on the rod of the 2D magnetic scattering intensity, and corresponds to the proper energy-integrating configuration with alignment of $k_f \parallel c$ at $Q = (1\ 0\ 0.83)$ for $k_i = 1.75 \text{ \AA}^{-1}$.

Prior to fitting of the scans with Voigt-profiles, we thoroughly determine the background (BG) contributions. Representative scans are shown in Fig. 6.5a-d. We identify several components of the BG: (i) A temperature-independent component, which is determined at 170 K [Fig. 6.5a], *i.e.* well above T_N . The obtained fit is employed as 'high-temperature' BG (H-T BG) in the analysis of the data measured at all other temperatures (see dashed-dotted lines in Fig. 6.5a-d). (ii) The scan at the lowest measured temperature $T = 80$ K [Fig. 6.5b] shows two incommensurate peaks besides the H-T BG. By comparing the T -dependent intensity of these resolution limited peaks with the intensities of the magnetic (1 0 0) [Fig. 6.4a] and (1 0 1) peaks [66], they can be assigned to the (1 0 1) peak of the main domain, and the (0 1 1) peak of the twin domain [177]. The (1 0 1) peak is likely associated with a minority 'B-centered' phase with a different propagation vector and transition temperature $T_{N,101} \approx 150$ K [66]. For our crystals the amount of the 'B-centered' phase was estimated to be less than 5% [6]. Finally, we subtract the H-T BG and the aforementioned two peaks with a proper T -scaling from the Q -scans, *i.e.* according to their T -dependence measured in Fig. 6.4a and [66], and obtain the corrected data shown in Fig. 6.5e. These data are well described by Voigt-profiles, which correspond to the convolution of the intrinsic Lorentzian ($\eta = 0$) with HWHM κ [Eqn. (2.3)] and the Gaussian instrumental resolution. The constant width of the instrumental Gaussian (FWHM ≈ 0.034 r.l.u.) was extracted from the 80 K scan in agreement with simulations carried out with the RESLIB [235] and TAKIN [236] softwares, respectively. Some models on critical scattering suggest a deviation of $\chi'(\mathbf{q})$ from the Lorentzian form, taking into account the critical exponent η (see Eqn. (2.3)). However, as we will see below, for our case a variation of η does not affect the results significant. Therefore, we used the simplest approach for $\chi'(\mathbf{q})$, which is the Lorentzian-function.

Prior to the discussion of the inverse correlation length $\kappa(T)$ extracted from Fig. 6.5e, we address the possible presence of concurrent longitudinal (parallel to the static ordering vector) and transverse fluctuations. In general, for the TAS configurations used in this work both components are expected to contribute to $S(\mathbf{Q}, \omega)$ and thus to the TAS signal. This results from the fact the neutrons are sensitive to the components of magnetic fluctuations perpendicular to \mathbf{Q} , which correspond for Ca_2RuO_4 to fluctuations along the b -axis and along the (a, c) -axes,

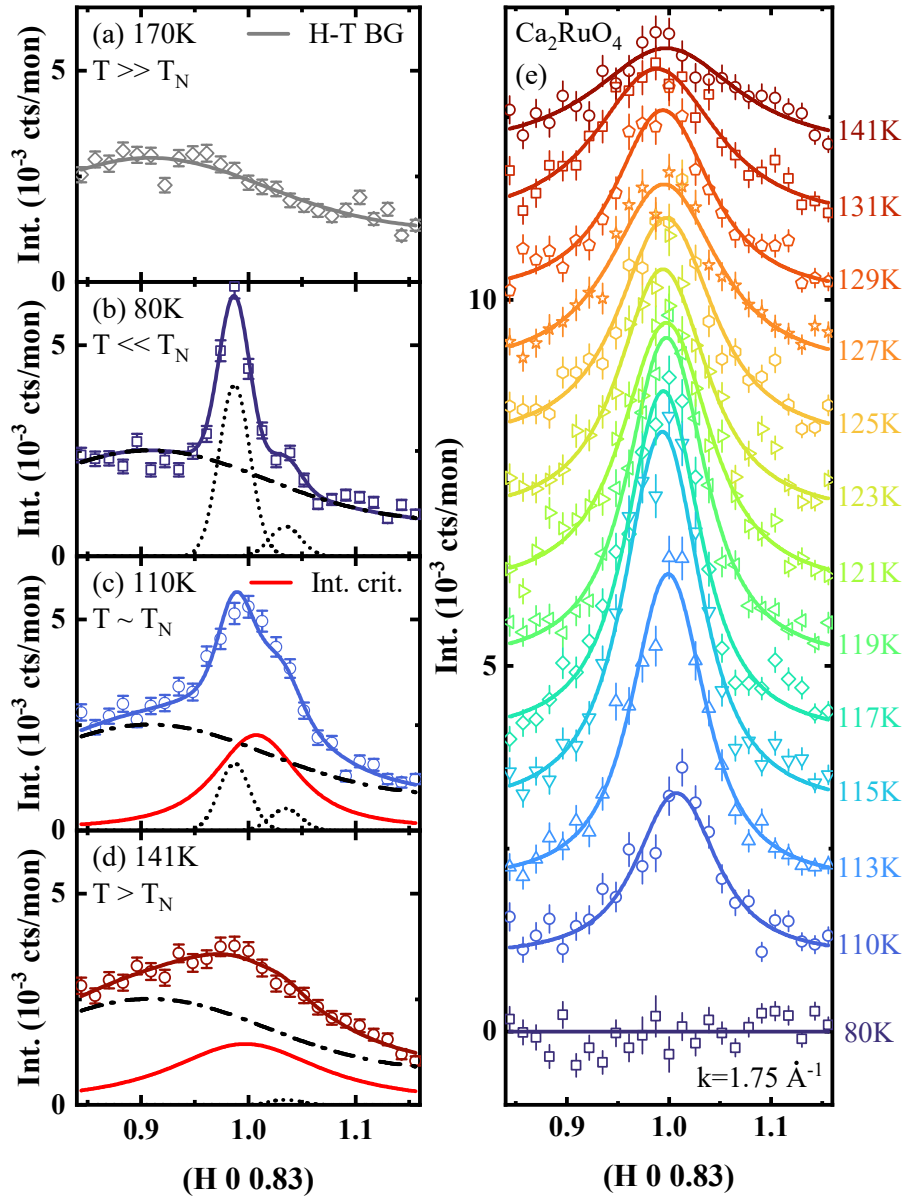


Fig. 6.5: Selected energy-integrated Q_H -scans around $(H\ 0\ 0.83)$ for Ca_2RuO_4 before (a-d) and after (e) BG subtraction. The data contain a T -independent constant BG, which was determined at $T = 170\text{ K}$ and labelled as 'high-temperature' (H-T) BG (a). Panels (b-d) show the H-T BG as a dashed-dotted line. At low- T , two small T -dependent resolution limited Gaussian-peaks (black dotted lines) appear (b-d), which are attributed to the magnetic $(1\ 0\ 1)$ peak of the main domain and the $(0\ 1\ 1)$ peak of the twin domain, respectively. The critical scattering component (Voigt-profile) is shown as a red line. (e) Selected Q_H -scans after BG subtraction with corresponding fit functions (solid lines). For clarity the data are plotted with a constant offset.

respectively. A separation of longitudinal and transverse contributions from **TAS** would require measurements at another Q -position, as described in [239, 252]. However, **NSE** spectroscopy [49–52] is capable to separate the two components [54] by solely measure at one Q -position (see Chap. 5). To this end, we carried out high-resolution **NSE** measurements on Ca₂RuO₄ at TRISP (see below) and obtained that transverse fluctuations along the c -axis are negligible or absent. Thus, we assume in the following that the fluctuations observed in the **TAS** experiments are also purely longitudinal. A possible explanation for this absence is that these fluctuations are gapped and not excited in the T -range of our study.

The inverse correlation length $\kappa(T)$ resulting from the fits in Fig. 6.5 is shown in Fig. 6.7. A temperature-dependent broadening above 116 K ($T_N + 4$ K) can be observed, while the Q -width is approximately constant for $T < 116$ K. This contrasts the conventional critical scaling theory where the correlation length ξ should diverge at T_N and thus $\kappa = \xi^{-1}$ should converge to zero. In the following, we will discuss several models to explain this saturation of κ at $T < 116$ K: (i) An obvious reason for such lower bound of the linewidth are crystallographic defects [263, 264]. One possible type of defect in Ca₂RuO₄ can be domain walls of the structural twins, which can disrupt the long-range magnetic ordering. However, from the Q -width (**FWHM**) of the resolution-limited (1 0 0) magnetic peak [$\Delta Q \approx 0.035$ r.l.u.] we can estimate a lower border of the domain size $d_s > 2\pi/\Delta Q \approx 150$ Å [40], which is much larger than the extracted correlation length of 20 Å at $Q = (1\ 0\ 0.83)$ and $T = 110$ K. Thus we exclude domain size effects as the origin of the observed linewidth saturation. (ii) At $T \simeq T_N$, *i. e.* close to the 3D ordering, one expects a crossover of the critical fluctuations from a 2D to a 3D character with an increasing influence of the Q_L component on κ .

To check a corresponding Q_L -dependence close to T_N , we measured Q_H -scans in the same configuration at the magnetic Bragg-peak position $Q = (1\ 0\ 0)$ at 80 K, 111 K and, 114 K [Fig. 6.6a-c]. At 80 K, where the contributions from critical fluctuations are small, we observe three resolution-limited (**FWHM** ≈ 0.035 r.l.u.) components in the signal: (i) The strong magnetic (1 0 0) peak from the main domain, (ii) the magnetic (0 1 0) peak of the minority 'B'-centered phase [66] at about $Q_H = 0.96$ from the twin domain, and (iii) a T -independent spurious peak at $Q_H = 0.9$. Yet, the origin of the last component is unclear. These three

components together with a constant offset are defined as the BG in the following. A high- T BG at $(1\ 0\ 0)$ was not measured. Analogous to above, we subtract the BG with the aforementioned two peaks (i) and (ii) with a proper T -scaling from the Q -scans, *i. e.* according to their temperature-dependence measured in Fig. 6.4a and [66]. By doing so, we could extract a critical component at 111 K and 114 K, which can be well described with a Voigt-function (red lines in Fig. 6.6b,c). The data after BG-subtraction are plotted in Fig. 6.6d and the corresponding Q -widths are included in Fig. 6.7. The latter are significantly smaller than the values obtained at $(1\ 0\ 0.83)$. However, the separation of the critical component at 111 K has to be taken with caution due to the high-intense $(1\ 0\ 0)$ peak. Moreover, the ideal energy-integration configuration ($k_f \parallel c$) is not fulfilled at this Q -position and $k_i = 1.75 \text{ \AA}^{-1}$. Nevertheless, with an analogous simulation as described for 3D-like systems in Chap.5, we could estimate that the fitted κ is in maximum 25% smaller than the intrinsic Q -width due to inelasticity effects. Even if we assume a 25% broader Q -width than the extracted $\kappa = 0.0075$ r.l.u. at 114 K, the Q -width is still significant smaller as the $\kappa = 0.035$ r.l.u. obtained at $(1\ 0\ 0.83)$.

This supports our conjecture of a Q_L -dependence arising from 3D couplings close to T_N . Such an effect was also described in Refs. [29, 102] (*cf.* Fig. 2.5c) and modelled by an effective κ with $\kappa_{\text{eff}}^2 = \kappa_{3D}^2 + \kappa_{\text{pow}}^2$, $\kappa_{3D}^2 \equiv Q_L^2 J'/J$, and $\kappa_{\text{pow}}^2 \equiv \kappa_0 t^{2\nu}$. A fit of our experimental $\kappa(T)$ with a convolution of κ_{eff} and the aforementioned Gaussian distribution of T_N results in an exponent $\nu = 1.0(1)$ and $\kappa_{3D} = 0.035(1)$, and describes the data over the entire measured T -range (green dashed-dotted line in Fig. 6.7). The exponent ν matches the universal value of the 2D-I model ($\nu_{2DI} = 1$ [16]). From $\kappa_{3D} = 0.035(1)$ we obtain the ratio $J'/J = 0.002$. This is in agreement with $J'/J = 0.004$ derived from INS on 1% Ti-doped Ca_2RuO_4 [180]. Assuming $J = 5.8$ meV [6], this corresponds to an interlayer coupling $J' \approx 0.01$ meV.

The red dashed line in Fig. 6.7 shows a PL fit $\kappa \propto |t|^\nu$ without a κ -offset at T_N , *i. e.* without a Q_L dependence due to 3D correlations, convoluted with the variance of T_N . Only the data for $T > 116$ K, *i. e.* beyond the saturation region, were included in the fit. The rounded shape of the red line towards T_N results from the T_N variance. The resulting $\nu = 0.42(4)$ is close to the MF value of $\nu_{\text{MF}} = 0.5$, but is at odds with $\nu = 1.0(1)$ obtained in the previous PL fit with the offset in κ , although both fits give a satisfactory description of the data for $T > 116$ K. Furthermore, a

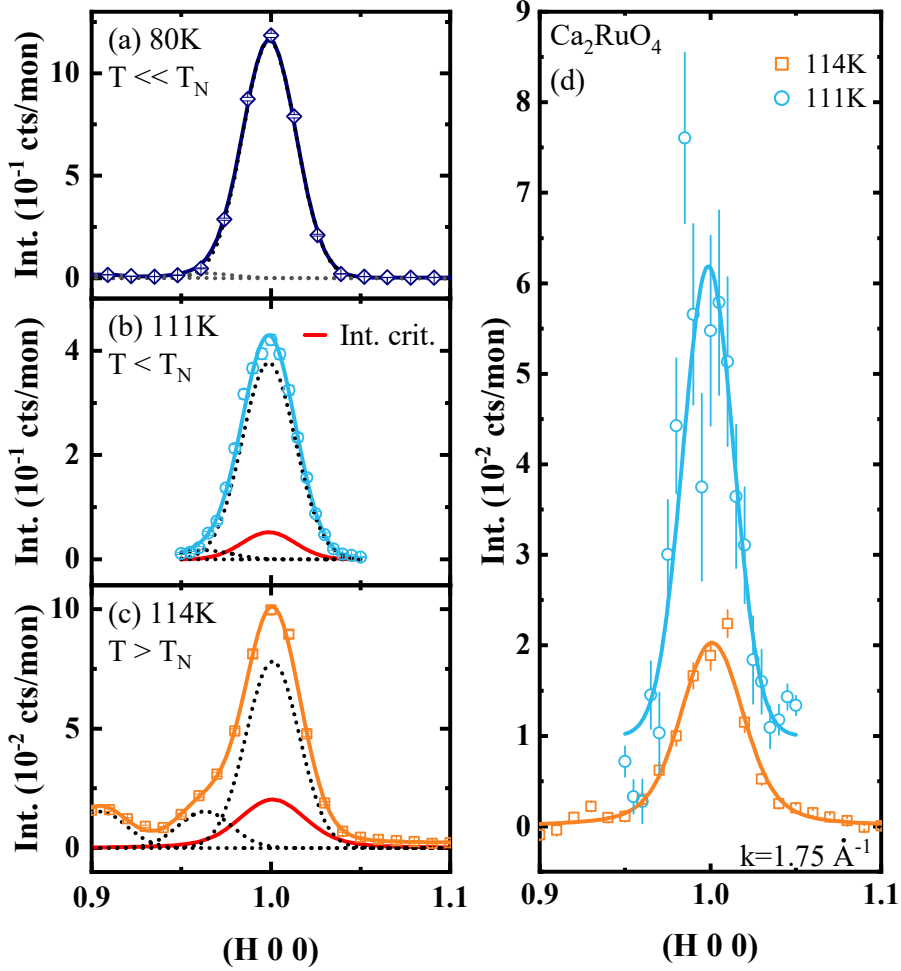


Fig. 6.6: Selected energy-integrated Q_H -scans around $(H\ 0\ 0)$ for Ca_2RuO_4 before (a-c) and after (d) BG subtraction. The BG, shown as a black dotted line in panels (a-c), consists of a T -independent offset and peak at $H = 0.9$, and two T -dependent resolution limited Gaussian-peaks, which are attributed to the magnetic $(1\ 0\ 0)$ peak of the main domain and the $(0\ 1\ 0)$ peak of the twin domain, respectively. The critical scattering component (Voigt-profile) is shown as a red line in panels (b,c). (d) Selected Q_H -scans after BG subtraction with corresponding fit functions (solid lines). For clarity the data are plotted with a constant offset.

fit of $\kappa(T)$ with a 2D quantum Heisenberg model described in Chap. 2 and Refs. [97–99], with an anisotropy parameter α_{eff} accounting for perturbations, such as 3D correlations, from the 2D-H model close to T_{N} [48], also gives a good agreement with the data (not shown here). However, we excluded this model because of two reasons: (i) The extracted effective perturbation term $\alpha_{\text{eff}} \approx 10^{-2}$ was two orders of magnitude higher than found in established 2D-H systems [48] and (ii) due to the large easy-plane anisotropy in Ca_2RuO_4 [6].

We now focus on the 2D-XY model (see Chap. 2), which was already suggested in the context of the magnon dispersion [6] and describes a topological phase transition accompanied by an unbinding of vortex/antivortex pairs [21–23]. The parameters of this model are the Kosterlitz-Thouless (KT)-temperature T_{KT} , a critical exponent $\eta = 0.25$, and a dimensionless non-universal parameter b [23, 265], which was previously determined to be approximately 1.9 [102]. According to Eqn. (2.15) and Ref. [23], the correlation length in this model is defined as

$$\xi \propto \exp\left(\frac{b}{\sqrt{t_{\text{KT}}}}\right), \quad \text{with } t_{\text{KT}} \equiv (T/T_{\text{KT}} - 1) \quad .$$

For systems with magnetic long-range order the actual KT-transition at $T_{\text{KT}} < T_{\text{N}}$ is usually obscured by the 3D ordering with nonzero interlayer couplings J' , which occur around T_{N} . The relation between T_{KT} and T_{N} is given by Eqn. (2.16) [91, 102]:

$$\frac{T_{\text{N}} - T_{\text{KT}}}{T_{\text{KT}}} = \frac{4b^2}{[\ln(J/J')]^2} \quad .$$

Assuming $J'/J = 0.002$, as derived from the above PL fit with Q_{L} -dependence to capture the κ -offset, we obtain $\tilde{T}_{\text{KT}} = 82$ K, with \tilde{T}_{KT} denoting the KT-temperature derived from Eqn. (2.16) and T_{KT} the KT-temperature extracted from fits to $\kappa(T)$ in Fig. 6.7 in the following. As expected for a system with $T_{\text{KT}} < T_{\text{N}}$, our data do not show any signatures of a transition around 82 K. Nonetheless, we use this model in the following to describe the scaling above T_{N} , as it was demonstrated [105–107] and experimentally confirmed [28, 29, 104], that even a XY anisotropy much weaker than in the case of Ca_2RuO_4 can result in 2D-XY scaling. Next, we fit Eqn. (2.15) to $\kappa(T)$ for $T > 116$ K. As T_{KT} is much lower than the lower limit of the fitting range, a possible distribution of T_{N} and T_{KT} temperatures in the sample

will not affect the result of the fit significantly and is therefore not considered here. The resulting fit (black solid line in Fig. 6.7) with $T_{\text{KT}} = 87(2)\text{K} \approx 0.8T_{\text{N}}$ provides an excellent description of the data, and is in reasonable agreement with $\tilde{T}_{\text{KT}} = 82\text{K}$ from Eqn. (2.16). A fit with b as a free parameter did not converge, since it couples strongly to T_{KT} . Thus, b was fixed to 1.9 [102].

In summary, the data in Fig. 6.7 are consistent with both, the 2D-XY (black solid line) and 2D-I (green dashed-dotted line) scaling behavior for $T > 116\text{K}$. Nevertheless, we rule out the latter scaling for the description of $\kappa(T)$, as the critical peak amplitudes $S_0(T)/T$ [Fig. 6.9] with the corresponding critical exponent γ (see below) are not compatible with the 2D-I model, although a crossover to 2D-I scaling close to T_{N} is expected due to the orthorhombic anisotropy ε [6]. While this crossover from 2D-XY to 2D-I scaling presumably occurs in a T -range very close to T_{N} and is not resolved in our data, we attribute the observed saturation for $T < 116\text{K}$ to a crossover to 3D coupling, which eventually drives the magnetic transition. An estimation of the crossover regions according to Eqns. (2.22) and (2.23) is not reliable for Ca_2RuO_4 due to the predominant tetragonal anisotropy term E , as the approximations were originally derived for systems with dominant Heisenberg-exchange and only small exchange anisotropies.

Prior to the discussion of the staggered susceptibility $\chi_0(T)$ obtained from Fig. 6.5e, we address the peak-shape of our Q -scans. As described above, for the analysis of the Q -scans, we fitted the data with a Voigt-profile, *i. e.* a convolution of a Gaussian (instrumental resolution) and a simple Lorentzian function. Beyond this approximation, which is commonly used to describe critical scattering [32, 58, 59], subtle deviations from the Lorentzian form were proposed, accounting for the critical exponent $\eta \neq 0$ (see Eqn. (2.3)). In this respect, for 3D and 2D universality classes $\eta \approx 0$ and $\eta = 0.25$ was predicted [16]. Hence, the peak-shape of the Q -scans also includes information on the critical behavior of the system. However, we find that for Ca_2RuO_4 fits with $\eta = 0$ and $\eta = 0.25$ yield peak shapes that are essentially the same within the experimental error of our data [Fig. 6.8, inset]. Nevertheless, we carried out the analysis of the full set of Q -scans not only for $\eta = 0$ (Ornstein-Zernike form, Eqn. (2.3)), but also for $\eta = 0.25$ (2D-XY model, [23]). As can be seen in Fig. 2.3, the effect of η on our Q -widths is small, and is negligible with respect to the corresponding scaling behavior of $\kappa(T)$. Specifically,

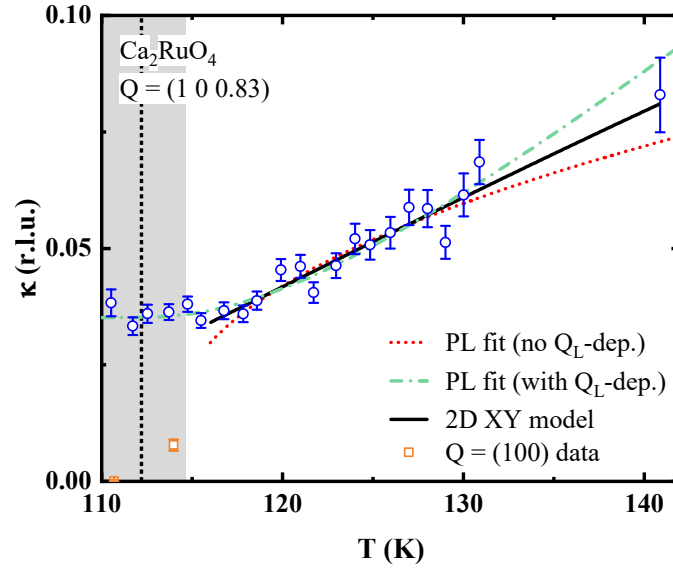


Fig. 6.7: Inverse correlation length $\kappa(T)$ of Ca_2RuO_4 with various fit functions: The green dashed-dotted line is a **PL** fit with $\nu = 1.0(1)$ and $\kappa_{3D} = Q_L \sqrt{J'/J} = 0.035(1)$. The red dashed line is a **PL** fit for $T > 116\text{K}$ and $\kappa(T \leq T_N) = 0$, with $\nu = 0.42(4)$. The black solid line corresponds to a **2D-XY** fit for $T > 116\text{K}$, with $T_{KT} = 87(2)\text{K}$ and $b = 1.9$. The smaller Q -width at the $(1\ 0\ 0)$ (orange points) indicate the emergence of 3D-couplings close to T_N . The vertical dashed line shows the average T_N and the grey bar the variance of T_N .

we obtain from **2D-XY** fits [Eqn. (2.15)] on the non-Lorentzian data ($\eta = 0.25$) for the KT-temperature $T_{\text{KT}} = 88(2)$ K for Ca_2RuO_4 , which coincides within the statistical errors with the value derived from the Ornstein-Zernike fits. In principle, a variety of other factors such as a non-Gaussian instrumental resolution and surface effects [266, 267] can also influence the peak-shape, which generally make the determination of η challenging.

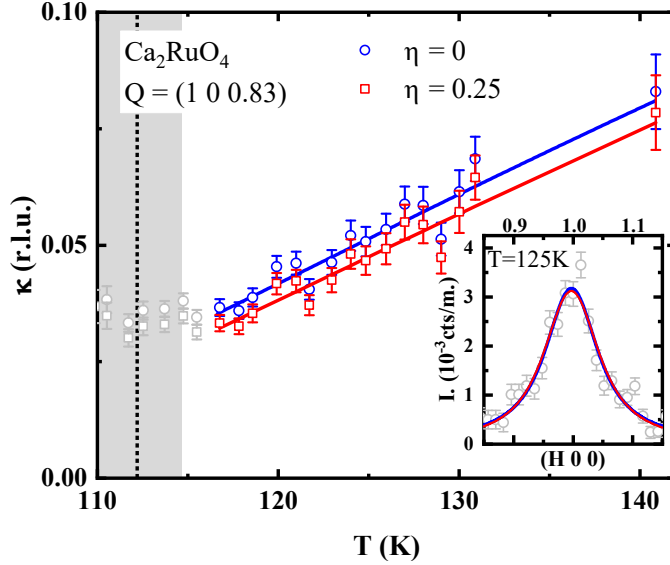


Fig. 6.8: Comparison of the Q -widths κ for a fitting of the Q -scans of Ca_2RuO_4 with $\eta = 0$ (blue points) and $\eta = 0.25$ (red points) [Eqn. (2.3)]. The grey points were not considered in the fits. The black vertical line indicates T_{N} and the grey bar the variance of T_{N} . The inset shows the corresponding fits at $T = 125$ K.

In addition to $\kappa(T)$, we analyzed the staggered susceptibility χ_0 , which also shows critical behavior close to T_{N} . Related via the Kramers-Kronig relation, χ_0 is proportional to $S(0) \propto \chi_0 T$ (see Eqn. (2.27)), *i. e.* the peak amplitude of the Lorentzian-profile $S(\mathbf{q})$. In the following, $S(0)$ will be denoted as S_0 . Figure 6.9 shows the temperature-dependence of the amplitude measured at $(1 0 0.83)$. First, we fit a **PL** $\propto |t|^{-\gamma}$ in the range $110\text{K} < T < 140\text{K}$, convoluted with the Gaussian T_{N} distribution by assuming $S_0 = 0$ for $T < T_{\text{N}}$. The agreement with the data is not convincing and the extracted critical exponent $\gamma = 0.47(2)$ does not match universal values [16], especially not the value predicted for the **2D-I** model $\gamma_{2\text{DI}} = 1.75$. Furthermore, since scaling theory predicts **PL** behavior for temperatures both

above and below T_N (see Chap. 2), we also carried out a **PL** fit in the entire T -range (95-140 K) where $A_-|t|^{-\gamma}$ and $A_+|t|^{-\gamma}$ for $T < T_N$ and $T > T_N$ was assumed (not shown here). Nevertheless, the resulting critical exponent $\gamma = 0.426(7)$ is similar to the value extracted from $A_+|t|^{-\gamma}$ in the range 110-140 K ($\gamma = 0.47(2)$). This corroborates that **PL** scaling is unsuited to capture the temperature-dependence of the amplitudes. Next, we fit the range $110\text{ K} < T < 140\text{ K}$ with the **2D-XY** model (see Eqn. (2.17)) by using the scaling relation $\chi_0 \propto \xi^{2-\eta}$ [23]:

$$\frac{S(0)}{T} \propto \exp\left(\frac{B}{\sqrt{t_{\text{KT}}}}\right),$$

with $B \equiv b(2 - \eta)$ and $T_{\text{KT}} = 87(2)$ from above. We fixed $\eta = 0.25$ as suggested for the 2D-XY model [23]. The model gives a good description of the data with only one free parameter in the fit, that is, the proportionality constant in Eqn. (2.17).

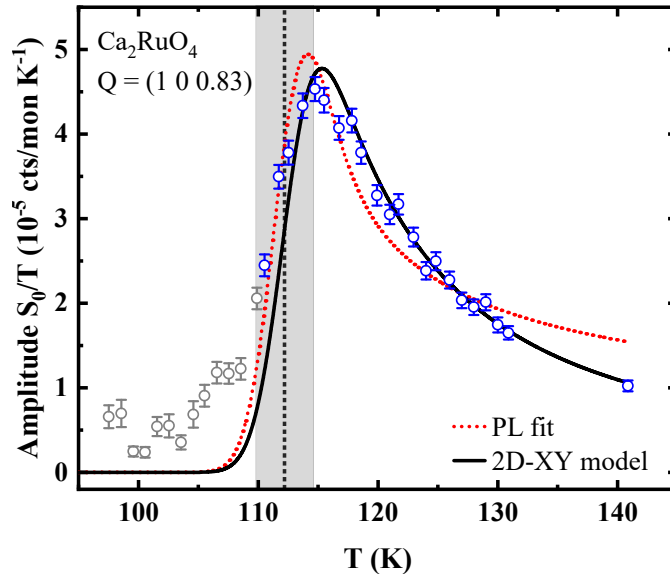


Fig. 6.9: Peak amplitude $S_0(T)/T$ of Ca_2RuO_4 . The red dotted line is a **PL** scaling fit ($\gamma = 0.47(2)$) and the black solid line corresponds to the **2D-XY** model. The grey data points were not included in the fit. The black vertical line indicates T_N and the grey bar the variance of T_N .

Dynamic critical properties

TAS measurements

Figures 6.10a-d show selected energy-scans at $(1\ 0\ 0)$ measured on the cold neutron TAS FLEXX with $k_f = 1.3\text{\AA}^{-1}$. A temperature-independent BG from elastic incoherent scattering recorded at 170 K was subtracted from the raw data. The BG corrected data are described by a fit with the sum of a resolution-limited Gaussian-peak ($\text{FWHM} \approx 0.12\text{ meV}$) and a Voigt-function for the critical scattering. The resolution was extracted from the width of the elastic magnetic scattering at 80 K, *i. e.* well-below T_N . The free parameters of the fits are the amplitude of the Gaussian-peak, and the amplitude and width of the Voigt-peak. As shown in Fig. 6.11, the T -dependence of the amplitudes of the Gaussian and the Voigt match the intensities of the $(1\ 0\ 0)$ peak [Fig. 6.4b] and the amplitude of the critical scattering at $(1\ 0\ 0.83)$ [Fig. 6.4b, inset], respectively. Thus we assign the former to elastic magnetic scattering from the $(1\ 0\ 0)$ still present above T_N due to the variance of T_N , which agrees with our NSE results discussed below. An overview of the energy-scans and the resulting fit curves at selected temperatures is shown in Fig. 6.10e. The noise in our data around $\Delta E = 0$ is attributed to the BG subtraction of the intense elastic $(1\ 0\ 0)$ peak. Nevertheless, the tails of the quasi-elastic scattering, which mainly contain the information on Γ , are well-captured by our Voigt-fits.

The resulting energy-width $\Gamma(T)$ of the critical component is plotted in Fig. 6.12a. Above 115 K, the data show a significant broadening, while below, no systematic trend was observed. For these data ($T \leq 115\text{ K}$) the intensity of the $(1\ 0\ 0)$ peak is much stronger than the critical scattering and extraction of $\Gamma(T)$ in the fit is not reliable. Therefore, we exclude this T -range in the following scaling analysis. We will see below, that even with the higher energy-resolution of NSE spectroscopy the separation of the two contributions at $Q = (1\ 0\ 0)$ is challenging. To determine the dynamic critical exponent z from $\Gamma(T)$ above 115 K, in analogy to $\kappa(T)$, we fit a convolution of the PL $\Gamma \propto |t|^{z\nu}$ with a Gaussian distribution of T_N (red dotted line). By assuming $\Gamma(T) = 0$ for $T \leq T_N$ as predicted by dynamic scaling theory [15], the PL fit yields $z\nu = 1.1(1)$. In spite of the good agreement with the data in Fig. 6.12a, the error margin is relatively large and only the 3D-H model

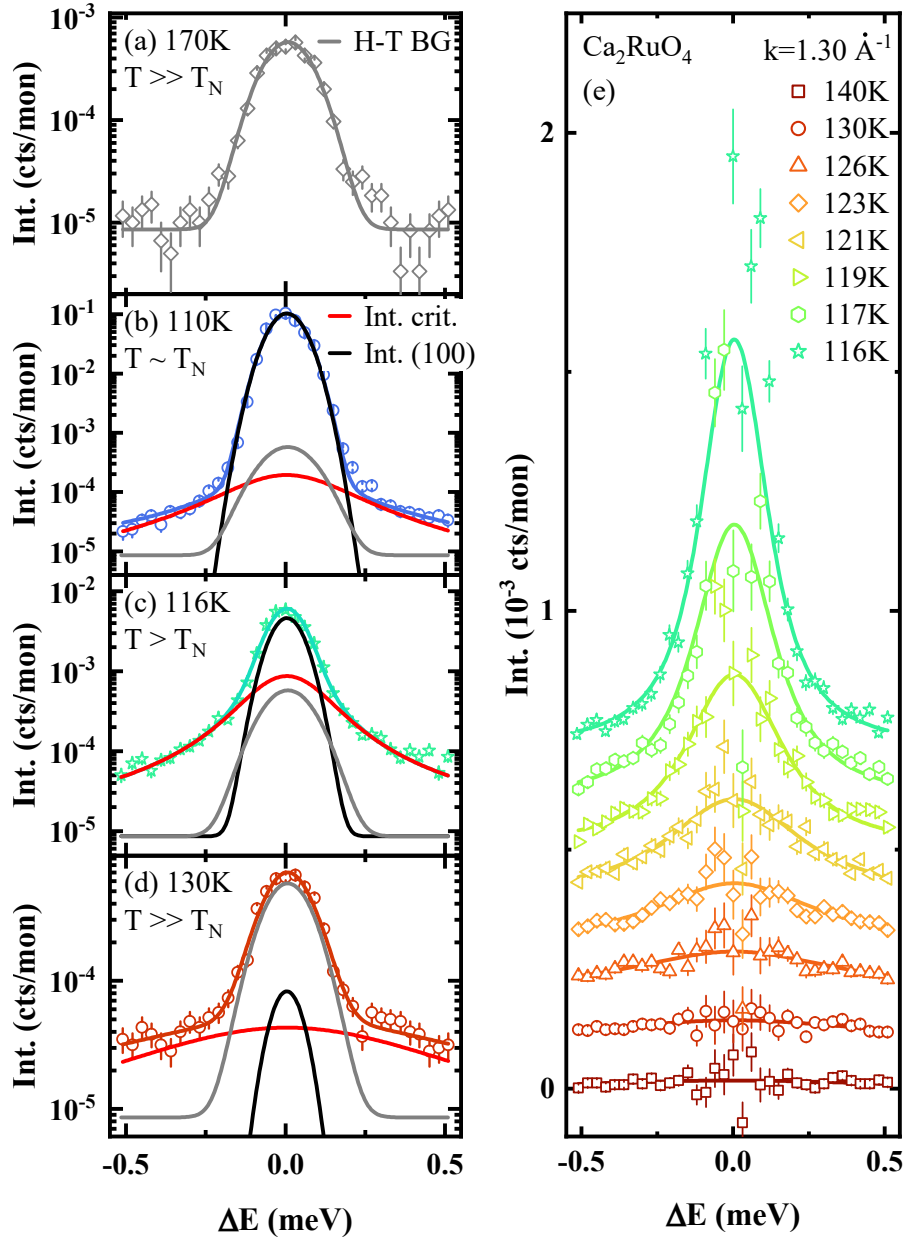


Fig. 6.10: Selected energy scans of Ca_2RuO_4 before (a-d) and after (e) BG subtraction. (a-d) Besides a constant high- T BG (170 K), we fitted a sum of a broad critical Voigt-profile and a resolution limited Gaussian-peak over the entire T -range. The latter is attributed to the magnetic (1 0 0) peak that shows the aforementioned distribution of T_N . (e) Selected energy scans after high- T BG and elastic (1 0 0) peak subtraction with corresponding fits (solid lines). For clarity the curves are plotted with a constant offset.

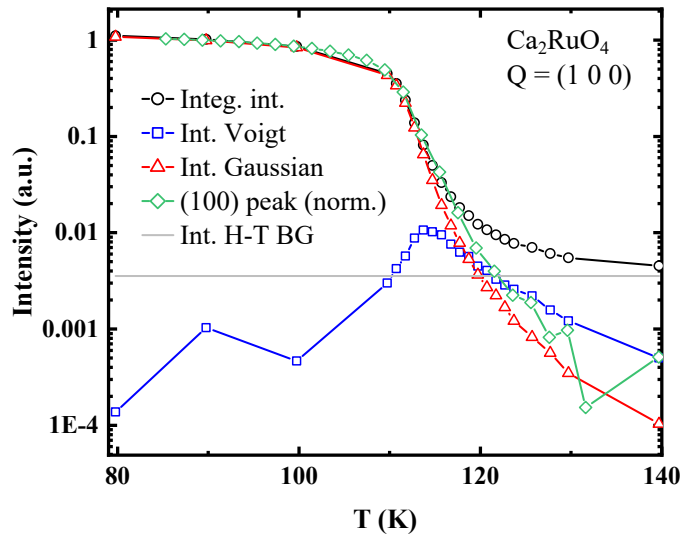


Fig. 6.11: Integrated intensities of the fit components in the energy-scans at $Q = (1\ 0\ 0)$ *vs.* T , including the overall integrated intensity (black), the Voigt-profile of the critical scattering (blue), and the resolution-limited Gaussian profile (red). For comparison, we also show the $(1\ 0\ 0)$ peak intensity (green), measured with $k_f = 1.5\ \text{\AA}^{-1}$ and normalized on the 80 K point of the overall integrated intensity (black). The horizontal gray line indicates the intensity level of the high-temperature (H-T) BG at 170 K.

($z\nu_{3\text{DH}} = 1.067$, [15, 93]) and the 3D-I model ($z\nu_{3\text{DI}} = 1.26$, [15, 18]) are reasonably close to the obtained exponent (see Tab. 2.3). However, 3D-scaling is not expected well above T_{N} for this quasi-2D system. Furthermore, $z\nu = 1.1(1)$ is far away from the 2D-I scaling ($z\nu_{2\text{DI}} = 1.75$, [16, 116]), which was discussed in the context of $\kappa(T)$ of Ca_2RuO_4 (green dashed-dotted line in Fig. 6.7).

Next, we also examine the critical dynamics of Ca_2RuO_4 in terms of the 2D-XY model. For the motion of vortices in a FM square-lattice a dynamic scattering function $S(\mathbf{q}, \omega)$ with a quadratic Lorentzian form (central peak) was derived [265, 268, 269], and also experimentally observed [28, 270, 271]. However, such a central peak is not present in our data [Fig. 6.10], which can be described by a simple Lorentzian function. Thus, we use instead the dynamic scaling relation $\Gamma \propto \kappa^z$ suggested to be appropriate for relaxational dynamics in the 2D-XY model [117] to check for 2D-XY scaling above 115 K. The black solid line in Fig. 6.12a shows the scaling for a critical exponent $z_{\text{XY}} = 2.0$, which was postulated for the 2D-XY model [117]. The agreement with the data is lower than for the PL fit. Nevertheless, the black solid line lies almost within the errorbars at high temperatures and deviations at low temperatures could be due to the variance of T_{N} or a crossover to a different scaling behavior. Using z as a free fit parameter increases the agreement with the data, but the obtained value of $z_{\text{XY}} = 3.04(6)$ (fit not shown here) is at odds with the 2D-XY universality class.

In addition, we determine z directly from plotting Γ vs. κ on double logarithmic scales [Fig. 6.12b]. In such a plot, the slope of a linear fit on the data corresponds to the critical exponent of the scaling relation $\Gamma = \kappa^z$. The resulting critical exponent $z = 2.9(2)$ (red dotted line) is not comparable to any known universal value. However, the plotted Γ vs. κ data points might be affected by uncertainties arising from the fact, that the Q - and energy-scans on Ca_2RuO_4 were performed at different instruments, Q -positions, and temperatures. In more detail, the data points in Fig. 6.12b were generated by interpolating $\kappa(T)$ to the temperatures at which $\Gamma(T)$ was measured and the same fitting range ($T > 115$ K) was included, where the impact on T_{N} distribution is negligible. We find that the 2D-XY model (solid black line) with the exponent $z_{\text{XY}} = 2.0$ [117] captures the Γ vs. κ data reasonable well. Nevertheless, we performed complementary NSE measurements with higher energy-resolution to confirm the TAS results.

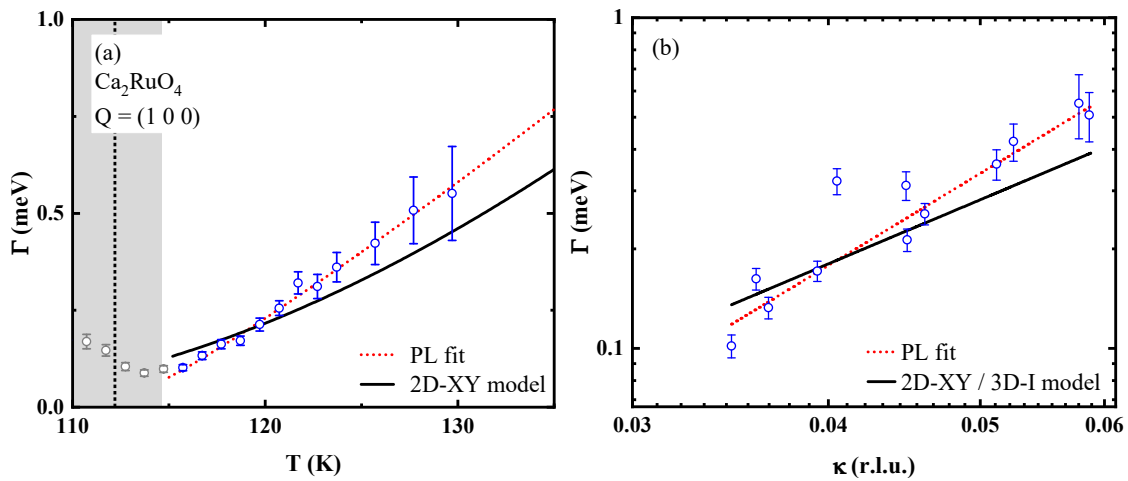


Fig. 6.12: (a) Energy-width Γ of Ca_2RuO_4 vs. temperature. The red dotted line is a PL scaling fit with exponent $z\nu = 1.1(1)$. The black solid line corresponds to a 2D-XY scaling fit with $z_{XY} = 2.0$ [117]. The grey data points are not included in the fits. The black vertical line indicates T_N and the grey bar the variance of T_N . (b) Energy-width Γ of Ca_2RuO_4 vs. the inverse correlation length κ on double-logarithmic scales. The red dotted line is a linear fit with the slope corresponding to the dynamical critical exponent $z = 2.9(2)$, according to the scaling relation $\Gamma \propto \kappa^z$. The black solid line corresponds to the 2D-XY model with $z_{XY} = 2.0$ [117]. This exponent is also proposed for the 3D-I model [15, 18], but the 2D-XY model is consistent with the static critical properties.

NSE measurements

At $Q = (1\ 0\ 0)$

Neutrons are sensitive to components of magnetic fluctuations perpendicular to Q . For the TAS configurations used in this work, both the critical longitudinal fluctuations (parallel to the static ordering vector) and the transverse fluctuations are expected to contribute to the same $S(Q, \omega)$ and so to the TAS signal. In case of Ca_2RuO_4 , the corresponding fluctuations are along the b -axis (longitudinal) and along the (a, c) -axes, respectively [Fig. 6.13]. A separation of the two components would therefore require additional TAS measurements at another Q -position [239, 252]. This can be circumvented by operating NSE with different magnetic field orientations (see Chap. 5 and Ref. [54]). In consequence, we performed complementary high-resolution measurements at the hybrid thermal neutron TAS and NRSE spectrometer TRISP. The measurements were conducted at the same array of co-aligned Ca_2RuO_4 single crystals described above [Fig. 6.3]. The data were collected from different experimental runs, which we refer in the following to exp. 1-3. In the first experimental run (exp. 1), the high- T BG was not measured in all configurations and the BG-scan from exp. 2, scaled by a factor close to one, was used instead. This scaling factor was extracted from a comparison of the scattering intensities at $T = 150$ K.

The spin-echo scans at TRISP are carried out either by scanning the electrical current I02 through the DC-coil (DC2) in the second PD or by scanning the translational position TC4 of the fourth RF-coil C4 [Chap. 5]. Depending on the alignment of the magnetic fields $B_{1,2}$ in the PDs ($\uparrow\downarrow$ or $\uparrow\uparrow$) either SF-scattering on the in-plane or out-of-plane magnetic fluctuations fulfill the echo condition and yield a polarized signal. To assign the measured signal to the corresponding fluctuations in Ca_2RuO_4 , we apply the general spin-flip model [Fig. 5.9] on the scattering plane and Q -position used in Ca_2RuO_4 [Fig. 6.13]. It follows that the scattering on the fluctuations along the c -axis satisfies the echo-condition for parallel ($\uparrow\uparrow$) fields due to the effective field inversion ($\varphi_{f,c} = \pi - \varphi_i$), whereas the echo-condition for scattering on the fluctuations along the twinned (a, b) -axis ($\varphi_{f,(a,b)} = \pi + \varphi_i$) is fulfilled for antiparallel ($\uparrow\downarrow$) fields. In this channel also contributions from both nuclear coherent and incoherent scattering can be expected.

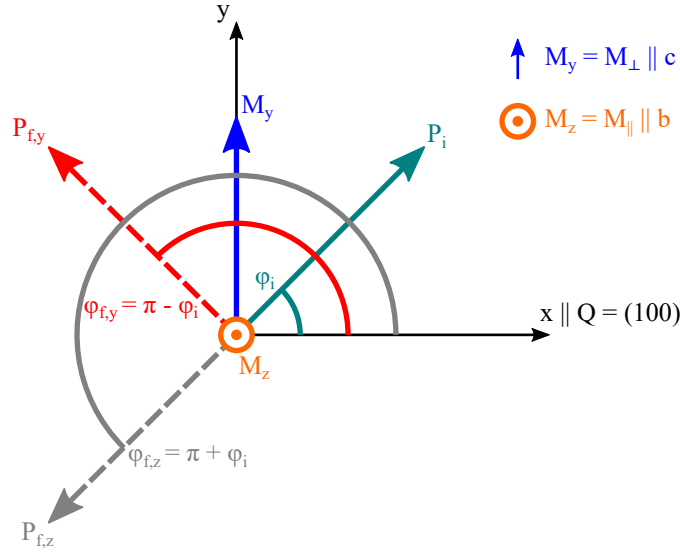


Fig. 6.13: The model of magnetic spin-flip scattering, shown in Fig. 5.9, applied on the scattering plane used in our sample (H 0 L). We assume that $Q_{\text{AFM}} = (100)$ is parallel to the x -axis and hence the intrinsic longitudinal M_{\parallel} and transverse M_{\perp} fluctuations correspond to M_z and M_y of the model.

In Fig. 6.14, we show exemplary spin-echo scans for $\tau = 2$ ps (DC-mode) and $\tau = 20$ ps (RF-mode) for parallel and antiparallel field alignments at various temperatures. We observe a phase-shift of $\sim \pi$ between the 80 K data ($T \ll T_N$) and the 150 K data ($T \gg T_N$), where magnetic scattering is weak [Fig. 6.4]. Since nuclear spin-incoherent scattering is negligible in Ca_2RuO_4 [227], which could affect spin-flip scattering, we assign the phase-shift instead to the magnetic spin-flip scattering. To extract the polarization from the spin-echo scans, we fitted the data with the sinusoidal relation [Eqn. (5.19)] and used the corresponding $\Delta\varphi$ for DC- and RF-mode [Eqn. (5.22)].

The resulting phase-offset of the raw-data relative to the high- T BG in units of π is plotted in Fig. 6.15. We observe for all three experiments a phase-shift of $\sim \pi$ at $T \leq 120$ K, which abruptly changes towards ~ 0 at 120 K. This indicates that magnetic spin-flip scattering becomes weak above 120 K. In addition, there is a phase-shift of $\sim \pi/4$ in the exp. 1 data (blue points) compared to the other experiments. Such a phase-shift can have two origins in our measurements: (i) Hysteresis effects due to a rapid change of the magnetic field alignments from

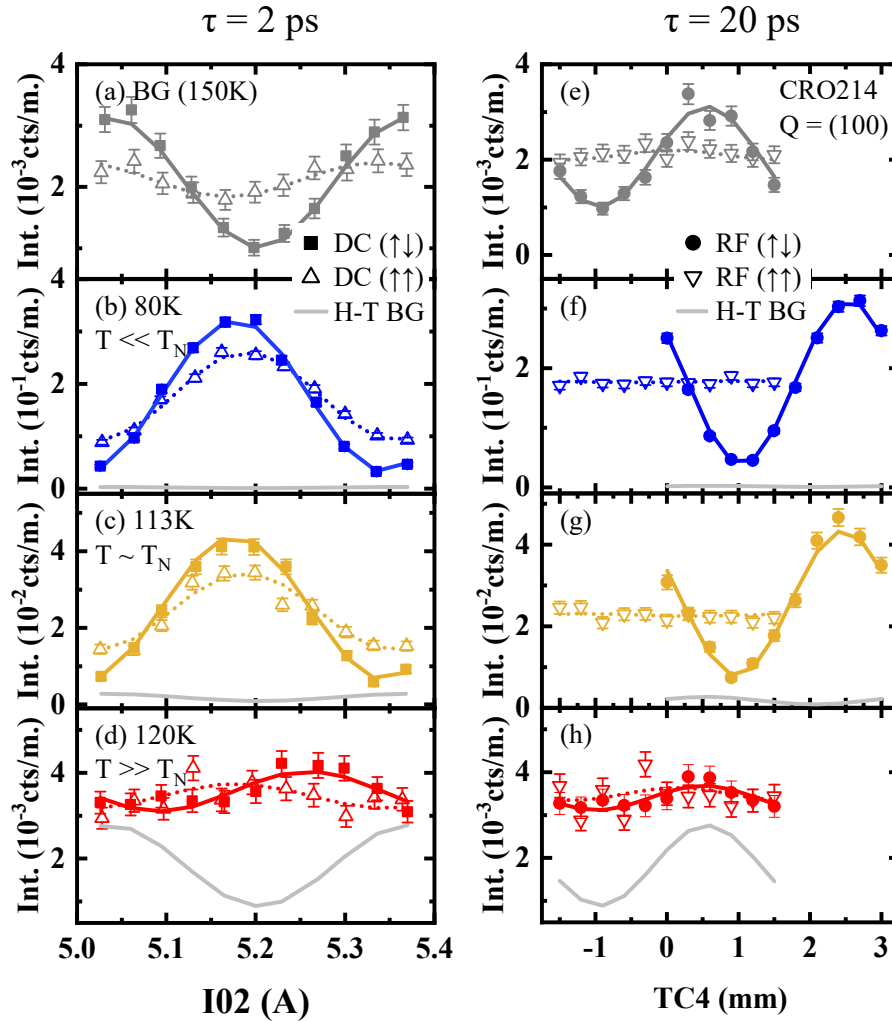


Fig. 6.14: Example NSE-scans for the parallel ($\uparrow\uparrow$) and anti-parallel ($\uparrow\downarrow$) magnetic field directions $\mathbf{B}_{1,2}$ at selected temperatures and spin-echo times τ . The echo-condition can be fulfilled either by scanning the current I02 (DC-mode, $\tau = 2$ ps, a-d) or the length of the second PD (RF-mode, $\tau = 20$ ps, e-h). The latter is realized by translation TC4 of the fourth NRSE-coil. The signal at 150 K (a,e), *i. e.* far above T_N , is associated with a non-magnetic high- T BG. The resulting cosine-fits [Eqn. (5.19)] are indicated by dashed and solid lines. For comparison the H-T BG in ($\uparrow\downarrow$) configuration is included by grey solid lines. Based on the phase-shift of the data compared to the H-T BG, we can infer magnetic spin-flip scattering.

($\uparrow\uparrow$) to ($\uparrow\downarrow$) or (ii) A general phase-shift of the exp. 1 scans relative to the other experiments and thus also to the used BG from exp. 2. As we measured at least the BG in DC-mode for antiparallel fields in exp. 1, we could determine the phase-shift of the exp. 1 data relative to this BG (not shown here). We found a smaller but still significant phase-shift compared to the other experiments. We therefore propose hysteresis effects as origin for the differing phase-shift in the exp. 1 measurements. However, a correction for hysteresis effects would be complex. Thus, we did not correct our exp. 1 data for these effects and used the scaled BG from exp. 2 for the analysis. We will see below, that at higher temperatures where the signal to BG ratio becomes low, the energy-widths of the exp. 1 series are no longer reliable due to this non-ideal BG treatment.

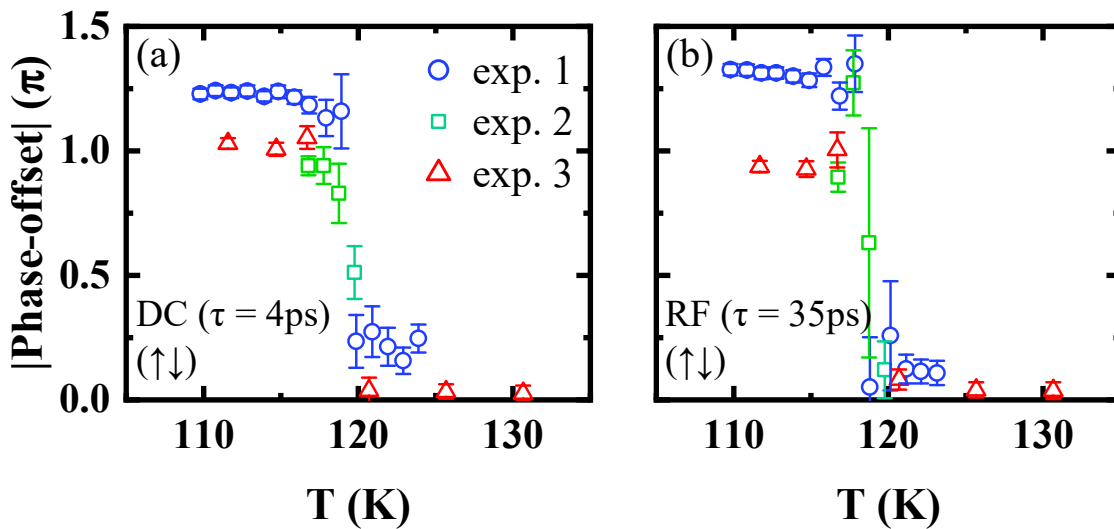


Fig. 6.15: Phase-offset of the NSE-scans for antiparallel fields (before BG subtraction) related to the high- T BG in units of π *vs.* temperature. The colors are assigned to the different experimental runs.

In Fig. 6.16a, the intensity I_0 of the raw data *vs.* temperature is plotted. The data show order parameter-like behavior over the entire T -range, that is smeared out in vicinity of T_N analogous to the (1 0 0) Bragg-peak intensity measured in TAS mode [Fig. 6.4].

The polarization of the raw data *vs.* τ for selected temperatures is shown in Fig. 6.17. Here the polarization was normalized for the instrumental depolarization,

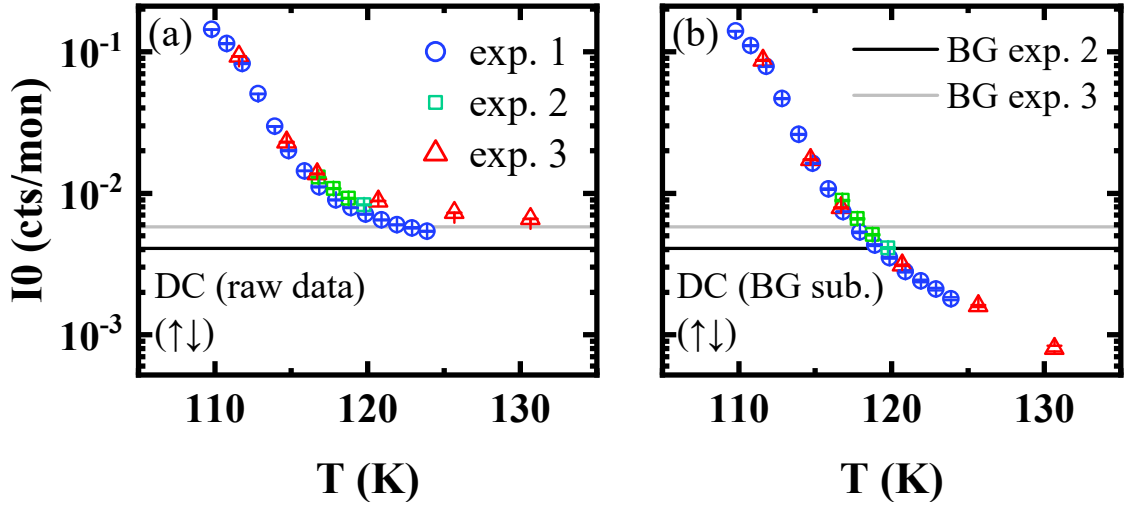


Fig. 6.16: Intensity of the NSE-scans in DC-mode and with antiparallel fields *vs.* temperature before (a) and after (b) BG subtraction. The colors are assigned to the different experimental runs.

i. e. the loss of beam polarization as it passes through the spin-echo coils. More precisely, we normalized the data on the polarization extracted from the 80 K scan with antiparallel fields, where strong elastic magnetic scattering is expected. The small fluctuations of the polarization around '1' at 80 K after normalization [Fig. 6.17a] arise from the fact, that the τ -dependence of the polarization at small spin-echo times was approximated by an exponential function according to Eqn. (5.18).

From the polarization of the raw data in Fig. 6.17, we can conclude: (i) The signal contains a small polarization for parallel magnetic fields ($\tau > 0$). (ii) For $\tau < 0$ ($\uparrow\downarrow$) and $T > T_N$, the polarization starts to decrease with $|\tau|$ and temperature [Fig. 6.17b], as expected for nonzero energy-widths $\Gamma(T)$. Interestingly, the polarization saturates at 117 K for $\tau < -10$ ps at a nonzero value [Fig. 6.17c]. This cannot be explained by accounting the critical scattering alone, but indicates an additional component. (iii) The polarization of the high- T BG is almost constant at 0.5 and thus higher than the 117 K data [Fig. 6.17d]. However, from the T -dependence of the phase-offset [Fig. 6.15a] and the critical fluctuations [Fig. 6.4a, inset], we can infer that the magnetic scattering is small or absent at 150 K. Hence, the polarization is

solely attributed to elastic ($\Gamma = 0$) NSF scattering [84, 230] without magnetic contributions.

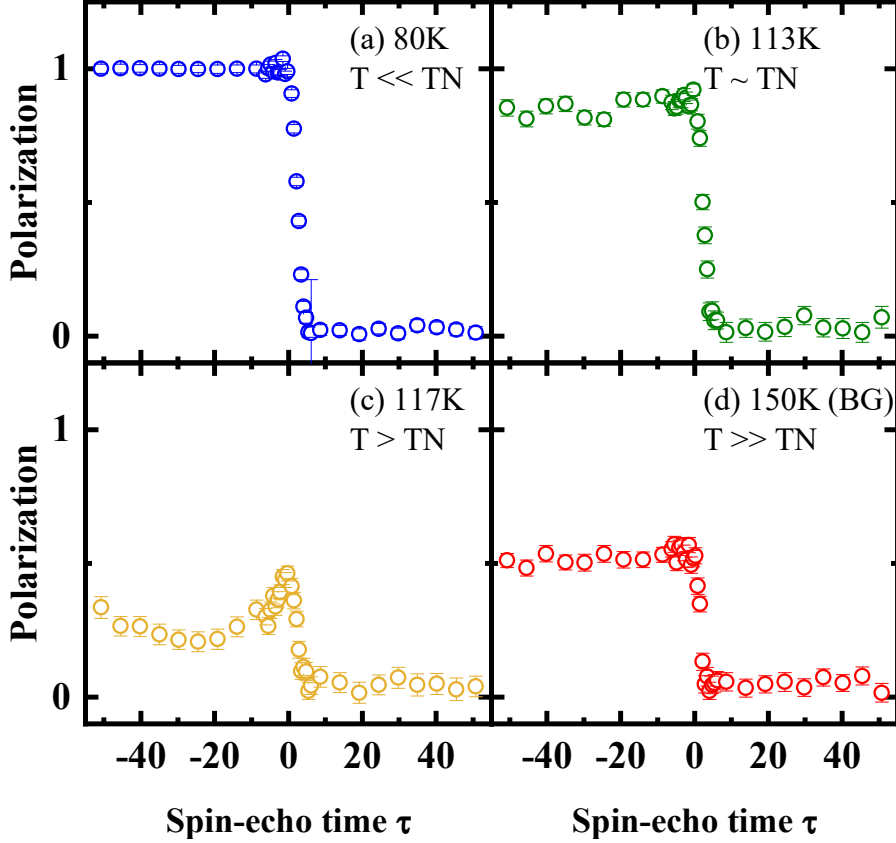


Fig. 6.17: Polarization *vs.* τ before BG subtraction for selected temperatures. While the τ and T -dependent depolarization is expected for critical scattering above T_N (b,c), there is no significant polarization at $\tau > 0$. The saturation of the polarization for $|\tau| > 10$ ps for antiparallel fields in panel (c) indicates an additional NSF component. The constant polarization of the 150 K data (BG) for $\tau < 0$ is assigned to elastic NSF scattering with energy linewidth $\Gamma = 0$.

Next, we discuss the data after subtracting a high- T BG. The BG-subtraction was performed as explained in the following: First, we fitted the 150 K scan (BG) with the sinusoidal function [Eqn. (5.19)] and then subtracted the BG-scan $I_{\text{BG}}(\Delta\varphi)$ from the data $I(T, \Delta\varphi) = I_{\text{raw}}(T, \Delta\varphi) - I_{\text{BG}}(150 \text{ K}, \Delta\varphi)$. The resulting BG-corrected data are then fitted again with Eqn. (5.19) to determine the polarization. In this procedure, we assume that the phases of the NSE scans are constant for each

τ , which is reasonable for Ca_2RuO_4 as the experimental set-up did not change in between the different runs. A more general BG treatment is shown below for $\text{CeCu}_{5.8}\text{Au}_{0.2}$ (see Chap. 7), where the BG is instead included in the fit function. In Fig. 6.16b, the mean NSE intensity I_0 vs. T is plotted after BG subtraction. I_0 still shows an order parameter-like behavior that is smeared out in vicinity of T_N , which is in line with the TAS experiments above [Fig. 6.4a].

Now, we discuss the spin-echo polarization P vs. τ and temperature. In Fig. 6.18, a number of $P(\tau)$ curves at selected temperatures are shown. For the parallel field alignment ($\tau > 0$), still no significant polarization is observed at $T \leq 121$ K. The small constant polarization found at $T > 121$ K is attributed to artefacts from the limited statistics of our data. Moreover, no fast oscillations of the polarization at small τ were found, which are a hallmark of interfering scattering from in-plane and out-of-plane fluctuations [54]. This signals that the in-plane fluctuations (along the c -axis) are weak or absent. A possible explanation for this is that the c -axis fluctuations might be gapped in our T -range for the quasi-2D system Ca_2RuO_4 . The black solid line in the overview plot [Fig. 6.18e] represents the depolarization due to the nonzero velocity-distribution of the neutrons. It indicates that $P(\tau > 0)$ results mainly from the depolarization of the out-of-plane scattering component, which does not fulfill the echo-condition for parallel fields.

For $\tau < 0$, on the other hand, we observe a T -dependent depolarization upon heating with a saturation at nonzero polarization for $\tau < -10$ ps. This resembles the observations made before BG correction and confirms that the second component with $\Gamma = 0$ does not result from the subtracted elastic nuclear NSF BG, but is attributed to elastic magnetic (1 0 0) scattering (elastic component). To finally extract $\Gamma(T)$, we fitted our data with a ray-tracing simulation (RTS) based on [54, 251] and described in Chap. 5 [Fig. 6.18]. The assumptions of our simulation are: (i) $P(\tau = 0) = P_0 = 1$. (ii) The detailed balance factor (*cf.* Eqn.(2.24)) in our T -range is 1. (iii) Fast oscillations of the polarization are absent in our data and therefore in-plane fluctuations (along c -axis) are neglected. (iv) The linewidth of the so-called elastic component at $\tau < 0$ is constant and 0. (v) The neutron velocity distribution Δk_i of the incident beam is constant. (vi) The intensity-ratio of the critical and elastic component is fixed to the ratio of the integrated intensities derived from the TAS energy-scans at FLEXX. Assumption (vi) was

made to reduce the total number of free parameters in the **RTS**. We also tried fitting the data without assumption (vi), *i. e.* with a free intensity-ratio, and found agreement with the ratio derived from the **TAS** experiment close to T_N , whereas at $T > 120$ K deviations emerged. These deviations, however, were assigned to the larger statistical errors of the **NSE** data at higher T .

The resulting $\Gamma(T)$ of the critical component, *i. e.* the longitudinal fluctuations along the magnetic easy axis (b -axis) is plotted in Fig. 6.19 (triangles). For comparison, we have also included the energy widths derived from the **TAS** measurements on FLEXX (blue circles). With the exception of the exp. 1 data at $T \geq 120$ K (light orange triangles), a continuous broadening of $\Gamma(T)$ is observed from T_N to 125 K, similar to the **TAS** measurements. Above 125 K, the signal-to-BG ratio is too small for a reliable extraction of $\Gamma(T)$. The deviation of the exp. 1 data above 120 K from the other experiments is assigned to the non-ideal subtraction of the scaled BG from exp. 2, which is only an approximation that deteriorates with a smaller signal-to-BG ratio. We therefore neglect these data and the 130 K point in the following analysis of the scaling behavior. Moreover, analogous to the **TAS** data, a reliable separation of the critical component and the strong elastic component in close vicinity to T_N was not possible.

Overall, the **NRSE** data show a similar temperature-scaling, as derived from the **TAS** experiments. This is also reflected in the extracted critical exponents from the **PL** fits (dotted lines). While the **TAS** data reveal an exponent of $z\nu = 1.1(1)$, the **PL** fit on the **NRSE** data in the range 112-126 K yields $z\nu = 0.90(3)$ (a fit in the same T -range as for **TAS** reveals $z\nu = 0.91(3)$). We attribute the deviation between the critical exponents to the rather broad signals for the high-energy resolution of **NRSE**. For $\Gamma > 0.2$ meV, for instance, the cut of the Lorentzian tails due to the resolution of the background triple-axis spectrometer (**FWHM** ≈ 1 meV for $k_i = 2.66 \text{ \AA}^{-1}$) can yield an effective experimental Γ that is about 20 % smaller than the intrinsic value. This was estimated by fitting the product of a Lorentzian-function $L(\Gamma_{\text{in}}, \omega)$ with an intrinsic width Γ_{in} and a Gaussian-function (**TAS** resolution), with a Lorentzian function $L(\Gamma_{\text{out}}, \omega)$ with width Γ_{out} (not shown here). Although we account for the energy-cut from the **TAS** resolution in the **RTS**, it might be underestimated due to the limited statistics of our data. We therefore conclude that the **NSE** results are broadly consistent with the dynamic

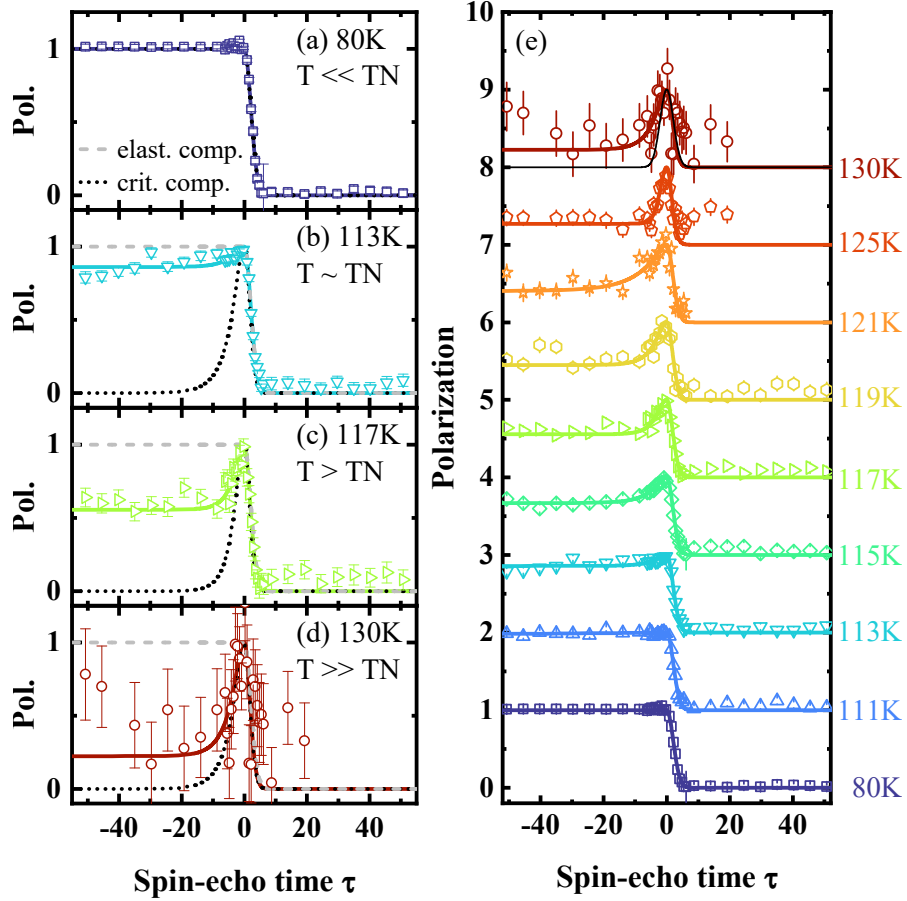


Fig. 6.18: (a-d) $P(\tau)$ curves after BG subtraction at representative temperatures. The solid lines correspond to fits from neutron ray-tracing simulations. We observe two components for $\tau < 0$: (i) A component (grey dashed line) with constant polarization according to a linewidth $\Gamma = 0$ (elastic component) and (ii) a component assigned to critical fluctuations (black dotted line) with a nonzero, T -dependent Γ (critical component). In the fit the two components are weighted with an intensity ratio according to the integrated intensities from the **TAS** measurements at **FLEX**. (e) Overview of $P(\tau)$ curves for selected temperatures with corresponding fits from ray-tracing simulations. The black solid line indicates the depolarization of an elastic component not fulfilling the echo-condition. For clarity, we plotted the curves with a constant offset.

scaling derived from our **TAS** measurements and furthermore, that our **TAS** data are more trustworthy for the broad energy-widths.

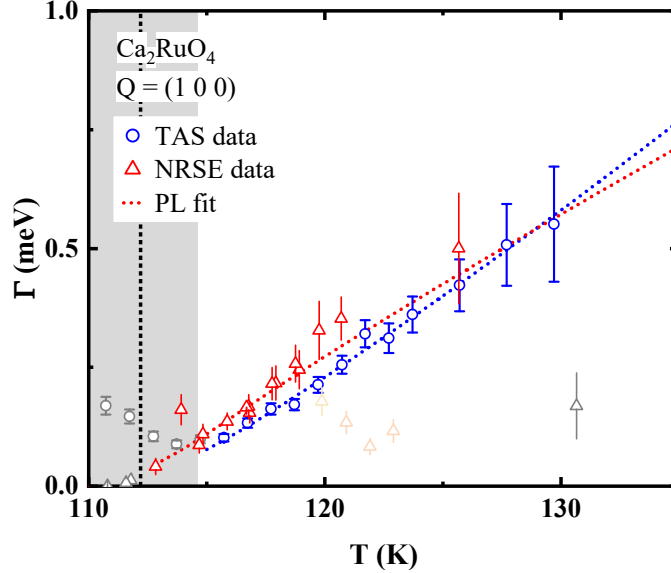


Fig. 6.19: Energy-width $\Gamma(T)$ of Ca_2RuO_4 derived from **TAS** (blue points) and **NRSE** (red triangles). The light orange triangles were obtained from the exp. 1 dataset, in which no high-T BG was measured. Although the **NRSE** data show a small y -offset, the scaling behavior is similar with an exponent of $z\nu = 0.90(3)$ from a **PL** fit in the range 112-126 K. For comparison we added the **PL** scaling fit on the **TAS** data with exponent $z\nu = 1.1(1)$ (blue dotted line). The grey and light orange data are not included in the fits and the grey bar indicates the variance of T_N .

At $Q = (1\ 0\ 0.53)$

In addition, we performed a series of **NRSE**-scans in distance to the magnetic Bragg-peak at $Q = (1\ 0\ 0.53)$ to suppress the elastic component and determine the energy-width close to T_N . We choose $Q_L = 0.53$ corresponding to an instrumental **TAS** configuration with $k_f \parallel c$ for the used neutron wave vector $2.51\ \text{\AA}^{-1}$.

According to the spin-flip model of Ca_2RuO_4 at $Q = (1\ 0\ 0)$ [Fig. 6.13] described above, we illustrate the corresponding spin-flip processes at $Q = (1\ 0\ 0.53)$ in Fig. 6.20. It appears that overall the echo-conditions are fulfilled for the same configurations, *i. e.* we mainly probe the scattering on fluctuations along the c -axis for parallel field alignment ($\tau > 0$), while we are sensitive to the scattering on the

fluctuations along the twinned (a,b) -axis for antiparallel fields ($\tau < 0$). However, since we study the magnetic components perpendicular to \mathbf{Q} with neutron scattering, strictly speaking we only detect the projection of $M_{\perp,c}$ on M_y . From the lattice parameter we can only estimate a marginal difference $M_y = 0.97M_{\perp,c}$ and thus assume $M_y \sim M_{\perp,c}$ in good approximation. In Fig. 6.21, we show exemplary spin-

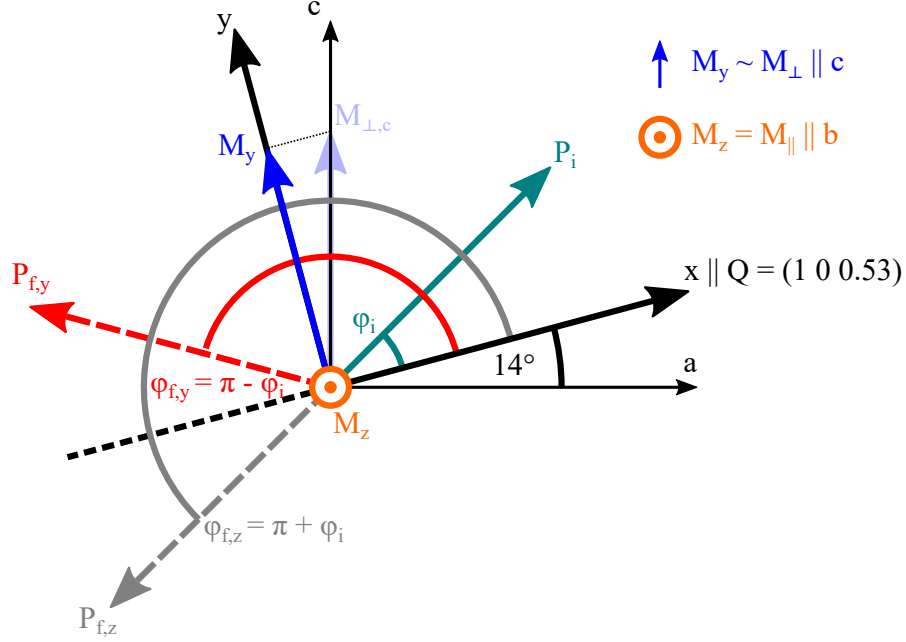


Fig. 6.20: Model of magnetic spin-flip scattering used for Ca_2RuO_4 at $(1\ 0\ 0)$ (cf. Fig. 6.13) adjusted for $\mathbf{Q} = (1\ 0\ 0.53)$. M_y is a projection of $M_{\perp,c}||c$ (light blue arrow) as neutrons probe only the magnetic components perpendicular to \mathbf{Q} . However, with the corresponding lattice parameter $M_{\perp} \sim M_y$ is assumed in good approximation.

echo scans for $\tau = 3$ ps (DC-mode) and $\tau = 30$ ps (RF-mode) in both operation modes at various temperatures. The scans at 80 K ($T \ll T_N$) and 170 K ($T \gg T_N$) are essentially the same in contrast to the measurements at $(1\ 0\ 0)$ [Fig. 6.14]. This unambiguously confirms that the contributions from the 3D magnetic $(1\ 0\ 0)$ Bragg-peak are negligible at $(1\ 0\ 0.53)$. On the other hand, the magnetic spin-flip scattering at 114 K ($T > T_N$), indicated by a phase-offset of π [Fig. 6.21c], signals the appearance of pure quasi-2D critical magnetic fluctuations. This is consistent with the peaked scattering intensity observed at $(1\ 0\ 0.83)$ [inset Fig. 6.4a].

The resulting phase-offset of the raw-data relative to the high- T BG in units of π

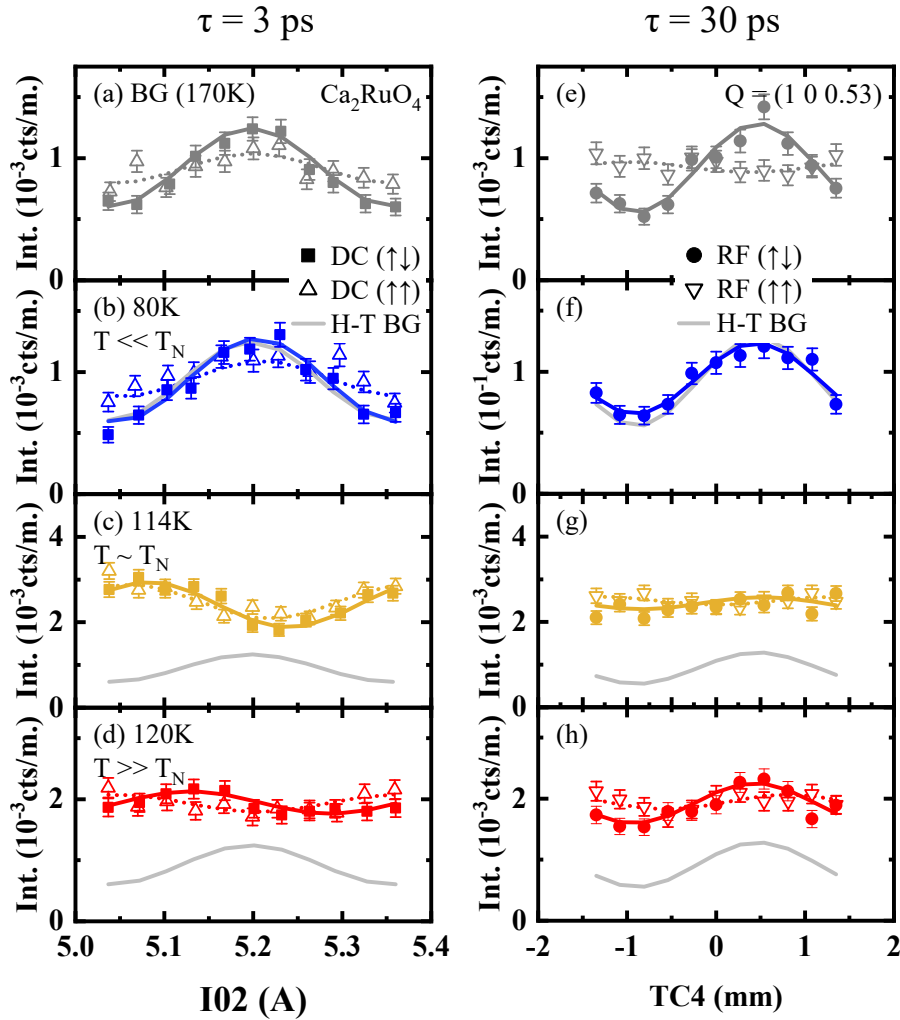


Fig. 6.21: Exemplary NSE scans for the parallel ($\uparrow\uparrow$) and antiparallel ($\uparrow\downarrow$) magnetic field alignments of $\mathbf{B}_{1,2}$ at selected temperatures and spin-echo times $\tau = 3$ ps (DC-mode, a-d) and 30 ps (RF-mode, e-h), respectively. The resulting cosine-fits [Eqn. (5.19)] are indicated by dashed and solid lines. For comparison the high- T BG in ($\uparrow\downarrow$) configuration is shown by grey solid lines.

is plotted in Fig. 6.22. For the DC-mode scans [Fig. 6.22a], the phase-offset shows a peaked structure with its maximum at π and 114 K. Whereas, the RF-mode scans show no phase-offset over the entire T -range.

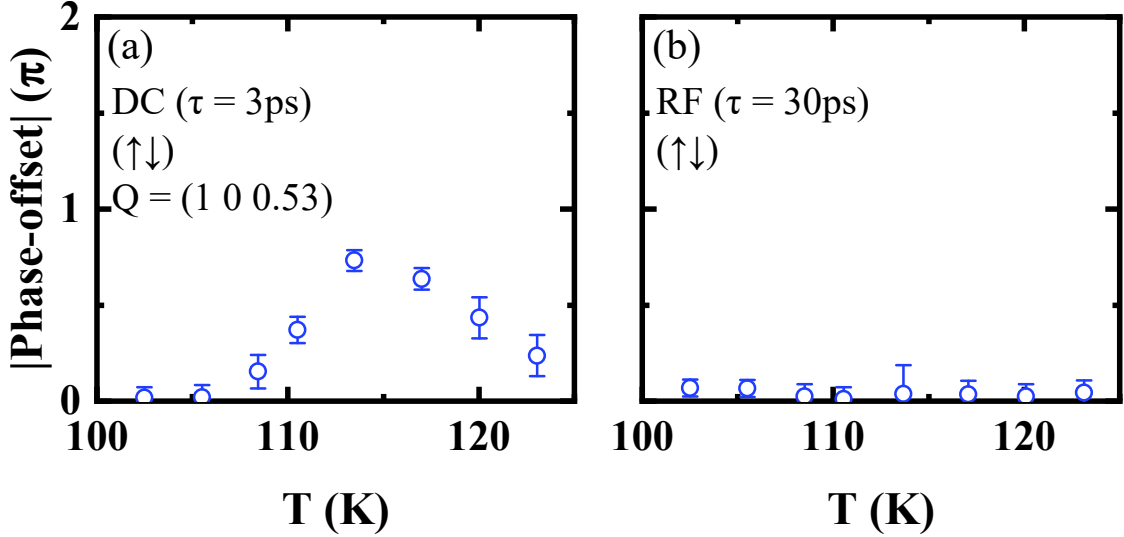


Fig. 6.22: Phase-offset of the NSE scans in SE-mode ($\uparrow\downarrow$) at $Q = (1\ 0\ 0.53)$ before BG subtraction relative to the high- T BG in units of π vs. temperature for two selected τ .

Figure 6.23a shows the corresponding mean intensity I_0 of the raw NSE data vs. temperature. The intensity exhibits a peaked T -dependence with the maximum at 114 K in agreement with the critical scattering intensity measured at $(1\ 0\ 0.83)$ [inset in Fig. 6.4a]. This allows us to interpret the phase-offsets shown in Fig. 6.21 as follows: (i) The peaked-shaped phase-offset at small τ [Fig. 6.21a] results from SF scattering on critical magnetic fluctuations, which becomes weaker as one moves away from T_N . Hence, the BG-to-signal ratio becomes more prominent at low and high temperatures and the phase-offset disappears. (ii) The absence of a phase-offset at higher τ [Fig. 6.21b] over the entire T -range indicates that the depolarization $P(\tau)$ of the critical component happens already at relatively small τ , *i. e.* the linewidth of the signal is significantly broad even at low temperatures.

The normalized polarization of the raw data vs. τ for selected temperatures is shown in Fig. 6.17. Since no elastic magnetic scattering was observed at $(1\ 0\ 0.53)$, we used the same normalization as for the $(1\ 0\ 0)$ data. Prior to the BG subtraction, we can already assume the following: (i) The polarization of the 80 K and 170 K

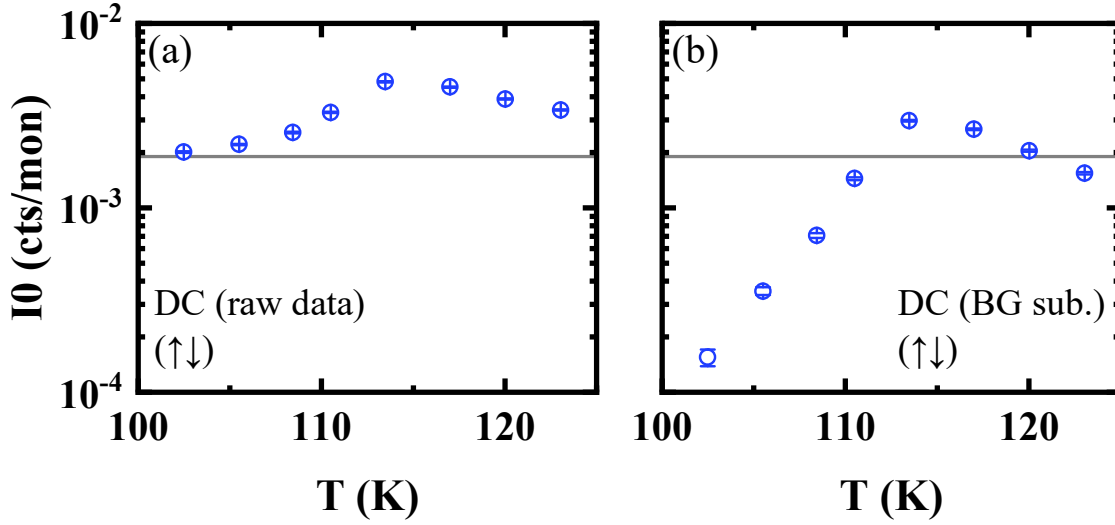


Fig. 6.23: Intensity of the NSE scans (DC mode) for antiparallel fields *vs.* temperature before (a) and after (b) BG subtraction.

(BG) data are essentially the same and describe an elastic NSF BG. (ii) For 114 K, the polarization shows a sudden drop at small τ and increases again for larger τ , indicating a mixture of critical fluctuations and the NSF BG. This is in line with the absence of a phase-offset at larger τ .

Next, we discuss the data after subtracting a high- T BG analogous to the $Q = (1\ 0\ 0)$ data. The intensity I_0 *vs.* T is shown in Fig. 6.23b. I_0 is still peaked at T_N , which is consistent with the TAS experiments above [Fig. 6.11]. Figure 6.25 shows several $P(\tau)$ curves at selected temperatures. No significant polarization is observed for the parallel field alignment ($\tau > 0$). Moreover, again no fast oscillations of the polarization at small τ were found, which are a hallmark of interfering scattering from in-plane and out-of-plane fluctuations [54]. This coincides with our results obtained at $(1\ 0\ 0)$ and signals that the in-plane fluctuations, *i. e.* along the c -axis are weak or absent and might be gapped in our T -range. The black solid line in Fig. 6.25 represents the depolarization due to the nonzero velocity-distribution of the neutrons. It indicates that $P(\tau > 0)$ mainly results from the depolarization of the out-of-plane scattering (longitudinal), which does not fulfill the echo-condition for parallel fields. For $\tau < 0$, we observe a fast τ -dependent depolarization. To extract $\Gamma(T)$, we fitted our data with a RTS based on [54, 251]

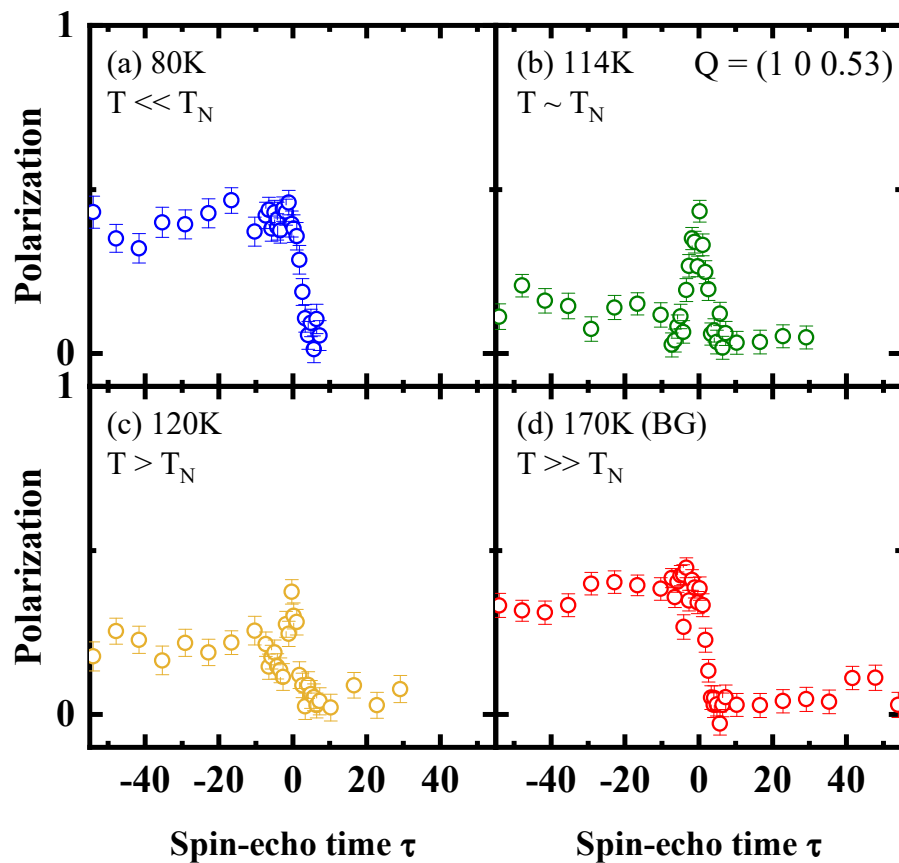


Fig. 6.24: Normalized polarization *vs.* τ before BG subtraction for selected temperatures. The polarization of the 80 K and 170 K data (BG) are essentially the same describing a NSF BG. For 114K the polarization shows a sudden drop at small τ and increases again for larger τ due to a mixture of critical fluctuations and the NSF BG.

and described in Chap. 5 [Fig. 6.25]. The assumptions of our simulation are: (i) $P(\tau = 0) = P_0 = 1$. (ii) Since fast oscillations of the polarization are absent at small τ , in-plane fluctuations (along c -axis) are neglected. (iii) The neutron velocity distribution Δk_i of the beam is constant.

The resulting $\Gamma(T)$ of the longitudinal critical component, *i. e.* the fluctuations along the magnetic easy axis (b -axis), is plotted in Fig. 6.26 (black squares). For comparison, we also included the energy widths derived from the TAS (blue circles) and the NRSE measurements at (1 0 0) (triangles). Below 120 K, the linewidths do not fit the data from the other two experiments. The deviation from the TAS data could, in principle, be explained by the quite broad signals for NSE, which are cut by the background TAS. However, this cannot explain the deviation from the NRSE data obtained at (1 0 0). We therefore attribute the offset in Γ close to T_N to the appearance of 3D-couplings, which is associated with a Q_L -dependence of Γ , reminiscent of what we observed previously for κ at (1 0 0.83) [Fig. 6.7]. This is also consistent with predictions of the dynamic scaling theory $\Gamma(T_N, q) \propto q^z$ (see Chap. 2). Furthermore, such a Q_L -dependence close to T_N would also explain the agreement of $\Gamma(T)$ with the other experiments at elevated temperatures, where the 3D-couplings become negligible. In this respect, it would be of major interest to determine z also from the q -dependence at $T \sim T_N$ and compare it with the non-universal value extracted from the temperature-scaling of Γ and κ [Fig. 6.12].

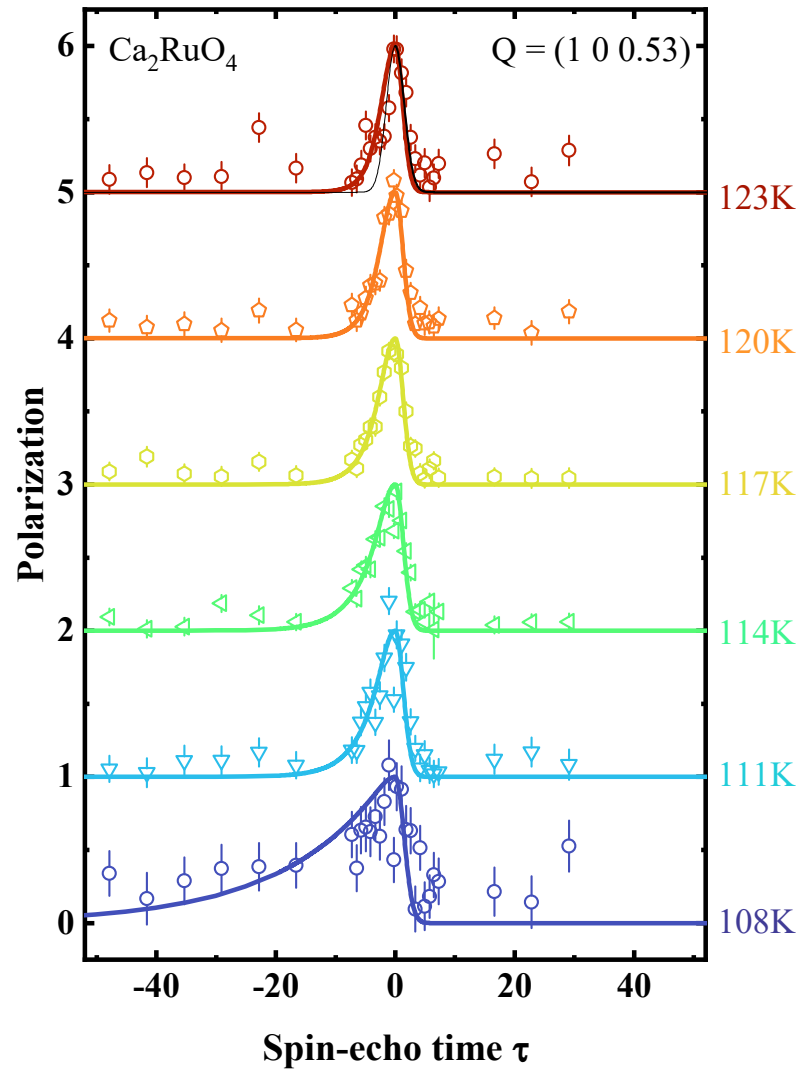


Fig. 6.25: Overview of $P(\tau)$ curves for selected temperatures with corresponding fits from ray-tracing simulations. The black solid line indicates the depolarization of an elastic component not fulfilling the echo-condition. For clarity we plotted the curves with a constant offset.

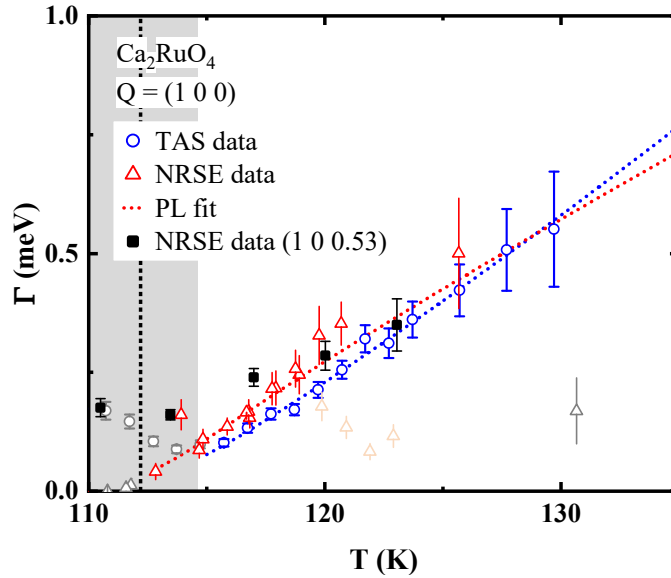


Fig. 6.26: Energy-width $\Gamma(T)$ of Ca_2RuO_4 derived from **TAS** (blue points), **NRSE** at $(1\ 0\ 0)$ (blue triangles), and **NRSE** at $(1\ 0\ 0.53)$ (black squares). For $T \sim T_N$, the $(1\ 0\ 0.53)$ data do not match the linewidths from the other experiments likely due to the appearance of 3D-couplings and thus a Q_L -dependence close to T_N . The light orange triangles were part of the exp. 1 dataset where no high- T BG was measured. Although the **NRSE** data at $(1\ 0\ 0)$ show a small y -offset, the scaling behavior is similar with an exponent of $z\nu = 0.90(3)$ from a **PL** fit in the range 112-126 K. For comparison, we added the **PL** scaling fit on the **TAS** data with exponent $z\nu = 1.1(1)$ (grey dotted line). The grey and light orange data are not included in the fits.

6.2. Bilayer $\text{Ca}_3\text{Ru}_2\text{O}_7$

We have seen so far that the critical scaling in single-layer Ca_2RuO_4 is consistent with the 2D-XY model. The following section on $\text{Ca}_3\text{Ru}_2\text{O}_7$ shows that the critical behavior changes to more 3D character due to the occurrence of intra-bilayer exchange interactions.

Experimental details

About 30 $\text{Ca}_3\text{Ru}_2\text{O}_7$ single-crystals with a total mass of 0.8g that included orthorhombic (a,b)-twins were co-aligned on Si-plates with thicknesses of 0.5 mm and arranged in Al-sample holders [Fig. 6.27a]. The lattice parameters are $a = 5.36 \text{ \AA}$, $b = 5.53 \text{ \AA}$, $c = 19.54 \text{ \AA}$ and the mosaicity of the sample array was about 3° . Due to the (a,b)-twinning, the scattering plane was (H 0 L)/(0 K L) as for Ca_2RuO_4 [Fig. 6.27a,b].

The experiments on $\text{Ca}_3\text{Ru}_2\text{O}_7$ [272] were carried out at ThALES [273], which is a cold neutron TAS at the ILL. For the Q - and energy-scans the instrument was operated (i) in two-axis mode with scattering sense $SM = 1$, $SS = -1$ and $k_i = 1.3 \text{ \AA}^{-1}$ and (ii) in three-axis mode with $SM = 1$, $SS = -1$, $SA = 1$ and $k_f = 1.3 \text{ \AA}^{-1}$ with double focusing monochromator and analyzer (energy resolution $\approx 0.08 \text{ meV}$). A Be-filter was used to suppress higher monochromator orders.

Static critical properties of $\text{Ca}_3\text{Ru}_2\text{O}_7$

Figure 6.28a shows the magnetic (0 0 1) peak intensity I_{001} measured upon warming, with a first-order transition at $T_{N,2} \approx 48 \text{ K}$ and a second-order transition at $T_{N,1} \approx 56 \text{ K}$, in good agreement with Ref. [195]. In contrast to the magnetic peak of Ca_2RuO_4 [Fig. 6.4a], I_{001} of $\text{Ca}_3\text{Ru}_2\text{O}_7$ drops sharply towards $T_{N,1}$, suggesting that possible distribution of Néel temperatures $\Delta T_{N,1}$ is negligible. We explain this observation with the appearance of less pronounced intrinsic crystal strains above the structural transition at $T_{N,2}$. Moreover, in comparison to Ca_2RuO_4 , the crystal-field distortions are expected to be weaker in $\text{Ca}_3\text{Ru}_2\text{O}_7$ [7]. In order to establish the presence of critical scattering, we measure the scattering intensity in distance to the (0 0 1) Bragg position at $Q = (0 0 1.3)$ as a function of temperature (see inset

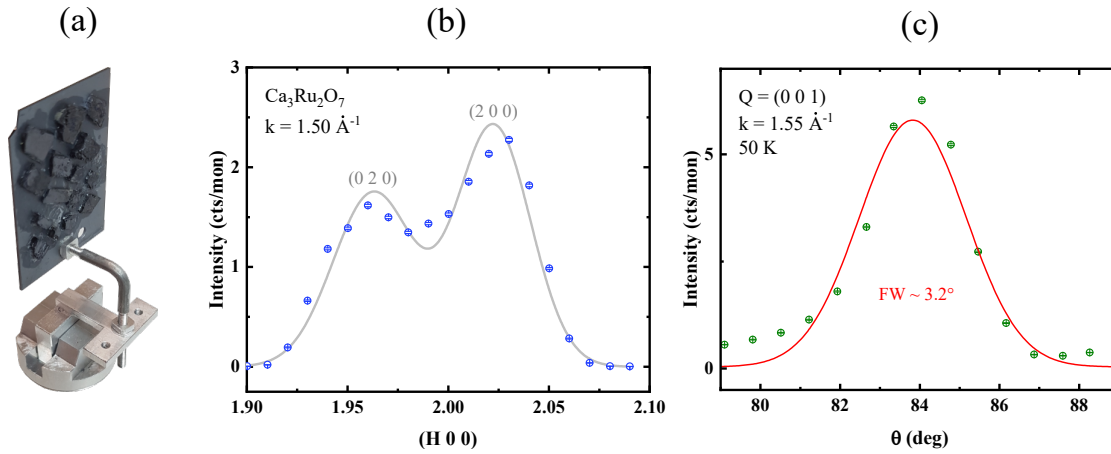


Fig. 6.27: (a) Picture of the used sample array of $\text{Ca}_3\text{Ru}_2\text{O}_7$ (b) $(H\ 0\ 0)$ scan shows $(2\ 0\ 0)$ and $(0\ 2\ 0)$ peaks due to twinning of the $\text{Ca}_3\text{Ru}_2\text{O}_7$ crystals in the (a,b) -plane. The peak positions are slightly shifted with respect to the nominal Q_H values because the lattice parameter were not yet adjusted. The grey solid line corresponds to a fit with two Gaussian-functions ($\text{FWHM} \approx 0.04$ r.l.u.). (c) Rocking (A_3) scans at the magnetic $(0\ 0\ 1)$ peak in the ordered regime at $50\ \text{K}$ ($T < T_N$).

Fig. 6.28a). The corresponding critical intensity in the inset in Fig. 6.28a peaks at $T_{N,1}$, and its magnitude is compatible with the remaining intensity for $T > T_{N,1}$ in Fig. 6.28a. A PL fit (without a $T_{N,1}$ distribution) in the range $49\ \text{K} < T < T_{N,1}$ ($0 < |t| < 0.1$), *i. e.* between $T_{N,1}$ and $T_{N,2}$, yields a critical exponent $\beta = 0.230(6)$ and $T_{N,1} = 54.16(2)\ \text{K}$ [Fig. 6.28]. Figure 6.28b shows I_{001} and the PL fit on a double-logarithmic scale, suggesting a purely linear evolution of I_{001} in such a plot for the measured temperatures. The obtained value of β matches the universal value of the 2D-XY model ($\beta = 0.23$ [91, 274]), although it should be taken with caution as the point density in close vicinity of $T_{N,1}$ is sparse. Moreover, the intrinsic scaling behavior could be obfuscated due to a contribution in the scattering intensity from an overlap with the second transition at $T_{N,2}$.

To extract $\kappa(T)$ and the amplitude of the critical scattering, we carried out Q_H -scans around $(H\ 0\ 1)$ in the two-axis mode. The ideal energy-integrating configuration used for Ca_2RuO_4 is not applicable for 3D systems (see Chap. 5). Therefore, we performed a numerical simulation to estimate the effects of inelasticity on the experimental Q -width and found that the integration according to Eqn. (5.12) is sufficiently satisfied for our two-axis configuration in $\text{Ca}_3\text{Ru}_2\text{O}_7$ (see Chap. 5).

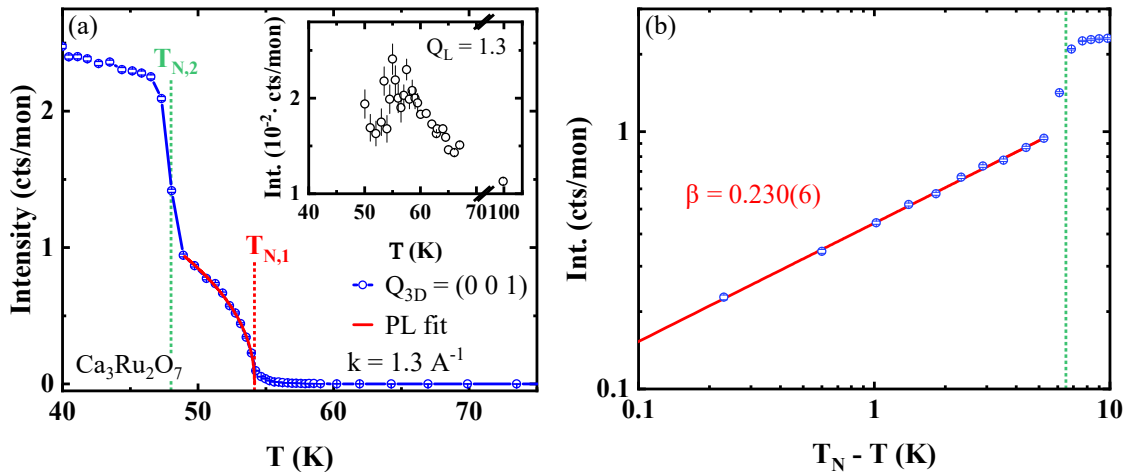


Fig. 6.28: Critical scattering and magnetic order parameter in $\text{Ca}_3\text{Ru}_2\text{O}_7$. (a) Intensity of the magnetic $(0\ 0\ 1)$ peak. Below $T_{N,2} = 48\text{K}$, the magnetic moments reorient from $m \parallel a$ to $m \parallel b$. The red solid line is a power-law fit, which yields $T_N = 54.16(2)\text{K}$ and $\beta = 0.230(6)$. The inset shows the intensity measured at $Q = (0\ 0\ 1.3)$, with the increase of intensity in vicinity to $T_N \sim 54\text{K}$ indicating the presence of critical scattering. (b) Shows the same data as in (a) for $T < T_N$ on a double-logarithmic scale. In contrast to Ca_2RuO_4 [Fig. 6.4b], no deviation from a straight line is visible, suggesting that a possible distribution of $T_{N,1}$ is negligible.

Moreover, for $\text{Ca}_3\text{Ru}_2\text{O}_7$, spin-echo experiments to discern longitudinal and transverse fluctuations are planned in future experiments, but have not been carried out yet. Nonetheless, from the fact that in the present study both, the static and dynamical critical fluctuations in $\text{Ca}_3\text{Ru}_2\text{O}_7$ are well-captured by power-laws (see below), we conclude that the non-critical transverse fluctuations do not contribute significant intensity around $T_{\text{N},1}$ [261].

From the Q_{H} -scans we subtracted two BG components: (i) A sharp peak at $H = 0$, which is clearly visible at high- T (150 K) [Fig. 6.30a]. In addition, we performed a scan around $(H\ 0\ 1.25)$ at 100 K and found that the sharp feature is independent of Q_{L} and T [Fig. 6.29]. Thus, we assign it to 2D diffuse nuclear scattering from disorder along the c -axis due to *e.g.* stacking faults. (ii) The sharp resolution-limited $(0\ 0\ 1)$ peak with Gaussian-width ≈ 0.01 r.l.u. [Fig. 6.30b], which rapidly vanishes above $T_{\text{N},1}$. The $(0\ 0\ 1)$ peak is intense at $T \leq 54.5$ K and the extraction of critical scattering is not reliable. The BG corrected Q_{H} -scans can be captured by a simple Voigt-profile (intrinsic Lorentzian critical scattering convoluted with instrumental Gaussian-profile) [Fig. 6.30e], as expected for 3D-like systems ($\eta \approx 0$). A critical scattering intensity can be clearly observed at least up to 70 K. There might also be a contribution from critical fluctuations even at 100 K, but since it is very weak we do not consider this temperature in the following analysis.

In order to extract the critical exponent ν , the resulting Q -width $\kappa(T)$ is plotted in Fig. 6.31a on double logarithmic scales. In the following analysis of $\text{Ca}_3\text{Ru}_2\text{O}_7$, we extract the critical exponents of the PLs from the slopes of linear fits in plots with double logarithmic scaling, whereas plots with linear scaling were employed in the above analysis of Ca_2RuO_4 , due to the variance of T_{N} in the latter material. The red dotted line shows a linear fit in the range $55\text{K} \leq T \leq 70\text{K}$ with the slope corresponding to the critical exponent in the scaling relation $\kappa \propto t^\nu$. The obtained $\nu = 0.550(4)$ lies between the 3D-I ($\nu_{3\text{DI}} = 0.630$, [18]) and the MF model ($\nu_{\text{MF}} = 0.5$). The MF model, however, is at odds with the modeling of the magnon dispersion of $\text{Ca}_3\text{Ru}_2\text{O}_7$ in Ref. [7], which used only nearest-neighbor couplings and no long-ranged interactions in the spin Hamiltonian [16]. Thus, we assign the critical scaling of $\kappa(T)$ rather to the 3D-I model. In analogy to Ca_2RuO_4 , we also fit $\kappa(T)$ of $\text{Ca}_3\text{Ru}_2\text{O}_7$ with the 2D-XY model, using Eqn. (2.15), $\eta = 0.25$, and $b = 1.9$.

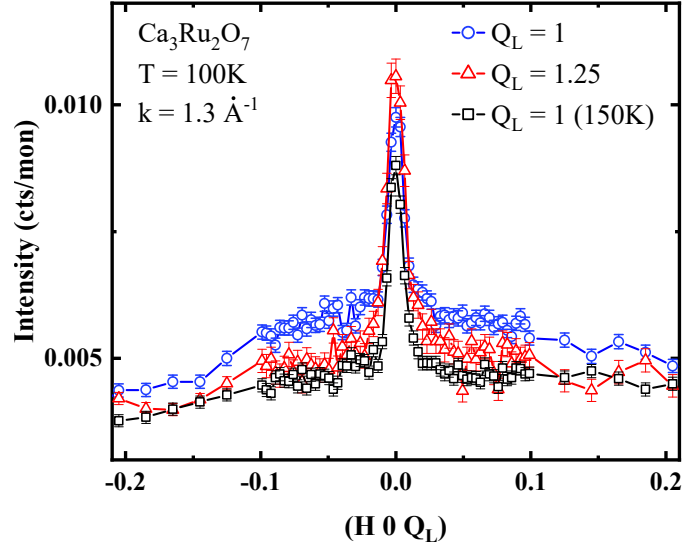


Fig. 6.29: $(H\ 0\ Q_L)$ scans in the two-axis mode at $Q_L = 1$ and 1.25 for $T = 100$ and 150 K. The corresponding TAS angles are: A_4 (A_3) = 13.8° (83.1°) and 17.3° (81.3°).

The obtained KT-temperature is $T_{KT} = 45.42(6)$ K, but the agreement between the fit (black dashed-dotted line) and the data is unsatisfactory for most temperatures [Fig. 6.31a]. We also test a fit with b as a free parameter, since lower values of b were reported in some experiments [109, 275] and derived in numerical calculations [265]. Such a fit (not shown here), with $b = 0.44(1)$ and $T_{KT} = 53.18(7)$, yields a better agreement with the $\kappa(T)$ data of $\text{Ca}_3\text{Ru}_2\text{O}_7$. However, using the latter values of b and T_{KT} as an input for the fit of the critical amplitudes (see below) results in a very strong deviation from the data (not shown here) and is therefore disregarded. In summary, we conclude that the 3D-I model is most appropriate to describe the critical behavior of $\kappa(T)$ above T_N .

Additionally, the data might indicate a deviation from the straight line at $T \geq T_N + 5$ K (~ 60 K), signalling a potential crossover in the scaling behavior. We therefore coarsely estimated the crossover to Ising scaling in $\text{Ca}_3\text{Ru}_2\text{O}_7$ from Eqns. (2.22) and (2.23) by assuming ε as the anisotropic exchange J_A . We derived Ising scaling for correlations lengths $\xi \geq \sqrt{J_c/\varepsilon} = 1.6$, which corresponds to

$$\kappa \leq 1/(2\pi \cdot 1.6) \approx 0.1 \text{ r.l.u.} \quad . \quad (6.1)$$

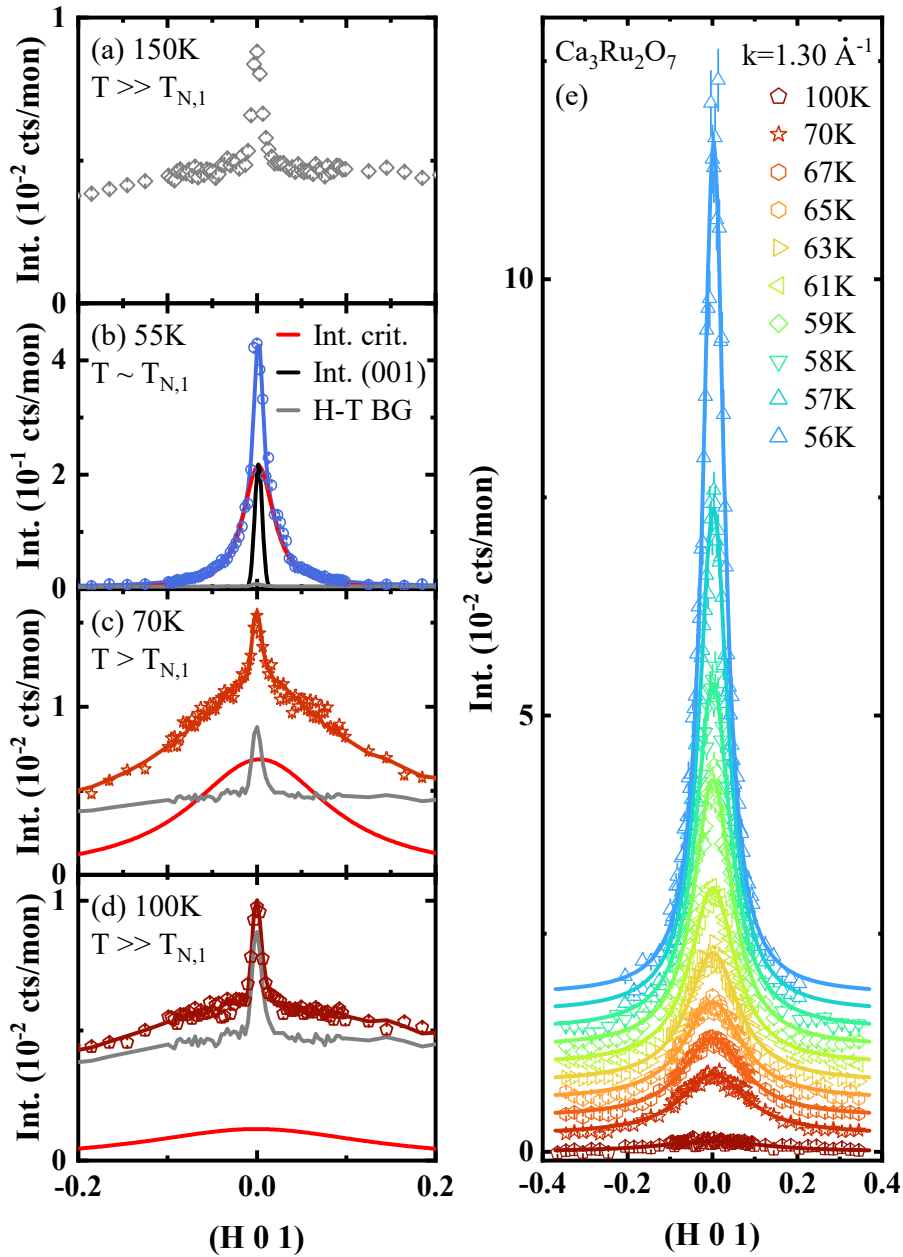


Fig. 6.30: Selected energy-integrated transverse Q_H -scans around $(H\ 0\ 1)$ for $\text{Ca}_3\text{Ru}_2\text{O}_7$ before (a-d) and after (e) BG subtraction. (a) The high- T BG contains a sharp peak that is independent of Q_L . (b) Close to $T_{N,1}$, a resolution limited Gaussian-component arising from the $(0\ 0\ 1)$ magnetic Bragg-peak is observed in addition to the Voigt-profile of the critical scattering. (c,d) Above $T_{N,1}$, the sharp peak and critical scattering are observed. (e) Selected Q_H -scans after BG subtraction with corresponding fits (solid lines). For clarity the data are plotted with a constant offset.

For the crossover temperature, we get

$$T_{\text{co}} = T_{\text{N}} + T_{\text{N}} \cdot (\varepsilon/J_c)^{\frac{1}{1.175}} \approx 80 \text{ K} \quad .$$

Thus, both estimations suggest that we are close to a XY to Ising crossover, albeit in our T -range we expect Ising scaling. This is consistent with $\kappa(T)$.

The critical exponent γ of the staggered susceptibility is obtained by fitting the corresponding peak amplitudes S_0/T with the PL scaling $\chi \propto t^{-\gamma}$ in the range $55 \text{ K} \leq T \leq 70 \text{ K}$. From the slope of the corresponding linear fit (red dotted line) in the double-logarithmic plot [Fig. 6.31b], we extract $\gamma = 1.290(4)$, which is close to the value predicted for the 3D-I model ($\gamma_{\text{3DI}} = 1.238$, [18]), as indicated by the green solid line in Fig. 6.31b. For the comparison with the 2D-XY model, we use Eqn. (2.17), with $\eta = 0.25$ and $b = 1.9$, as well as $T_{\text{KT}} = 45.42 \text{ K}$ determined from the fit of $\kappa(T)$ above. In spite of good agreement with the data at $T > T_{\text{N}} + 2 \text{ K}$ (see black dashed-dotted line), the PL fits are much more suitable to describe the scaling of the critical amplitudes closer to T_{N} .

Dynamic critical properties of $\text{Ca}_3\text{Ru}_2\text{O}_7$

Figures 6.32a-d display selected energy-scans at the (0 0 1) peak of $\text{Ca}_3\text{Ru}_2\text{O}_7$. A constant elastic incoherent high- T BG is subtracted from the energy-scans, which was measured at $T = 100 \text{ K}$, where the contribution of critical scattering is negligible [Fig. 6.30d]. Subsequently, a single Voigt-function (Gaussian-width $\approx 0.06 \text{ meV}$) is fitted to the scans. An overview of the energy-scans after BG subtraction with the corresponding fits is plotted in Fig. 6.32e for selected temperatures. The resulting energy-width $\Gamma(T)$ of $\text{Ca}_3\text{Ru}_2\text{O}_7$ is shown in Fig. 6.33a on double logarithmic scales. The data are well-captured by a linear fit (red dotted line) in the range $55 \text{ K} \leq T \leq 70 \text{ K}$ with a slope $z\nu = 1.186(8)$, corresponding to the critical exponent in the scaling relation $\Gamma \propto t^{z\nu}$. This exponent is close to the value predicted for the 3D-I model ($z\nu_{\text{3DI}} = 1.260$, [15, 18]) indicated by the green solid line in Fig. 6.33a, which is consistent with the static critical properties. In analogy to Ca_2RuO_4 , we also carry out a fit with the 2D-XY model, using the dynamic scaling relation $\Gamma \propto \kappa^z$ with $z_{\text{XY}} = 2.0$ [117]. The resulting fit (black dashed-dotted line in Fig. 6.33a) describes the data reasonably well at high temperatures, but deviates strongly in

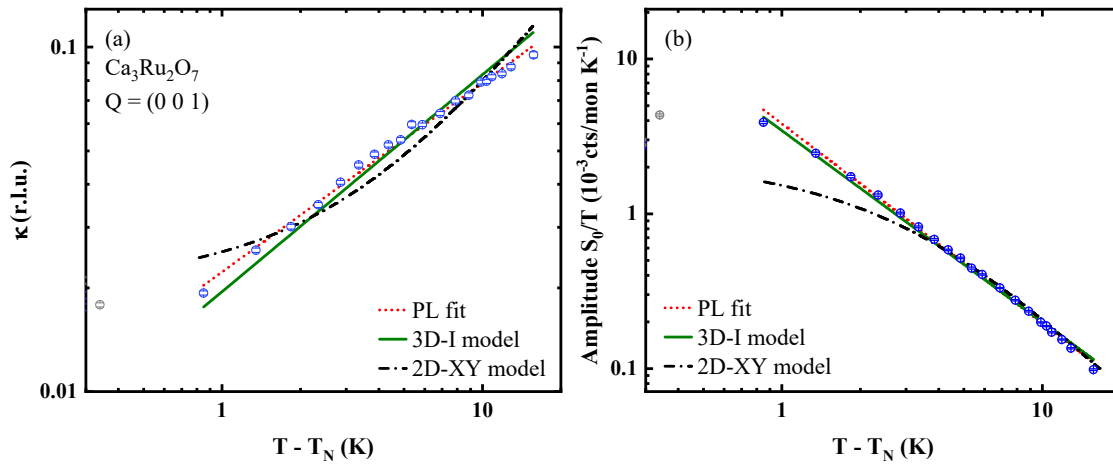


Fig. 6.31: Temperature-dependence of (a) inverse correlation length $\kappa(T)$ and (b) peak amplitude $S_0(T)/T$ of $\text{Ca}_3\text{Ru}_2\text{O}_7$ on double logarithmic scales. (a) The data are well-captured by a linear fit in the range $55\text{K} \leq T \leq 70\text{K}$ (red dotted line), with the slope corresponding to the critical exponent $\nu = 0.550(4)$ in the scaling relation $\kappa \propto t^\nu$. The green solid line indicates **3D-I** scaling. The black dashed-dotted line corresponds to the **2D-XY** model with $T_{\text{KT}} = 45.42(6)\text{K}$ and $b = 1.9$. (b) The red dotted line is a linear fit with the slope corresponding to the critical exponent $\gamma = 1.290(4)$, according to the scaling relation $\chi \propto t^{-\gamma}$. The green solid line indicates **3D-I** scaling. The black dashed-dotted line corresponds to the **2D-XY** model with $T_{\text{KT}} = 45.42(6)\text{K}$, $b = 1.9$, and $\eta = 0.25$. The grey data points were not included in the fits

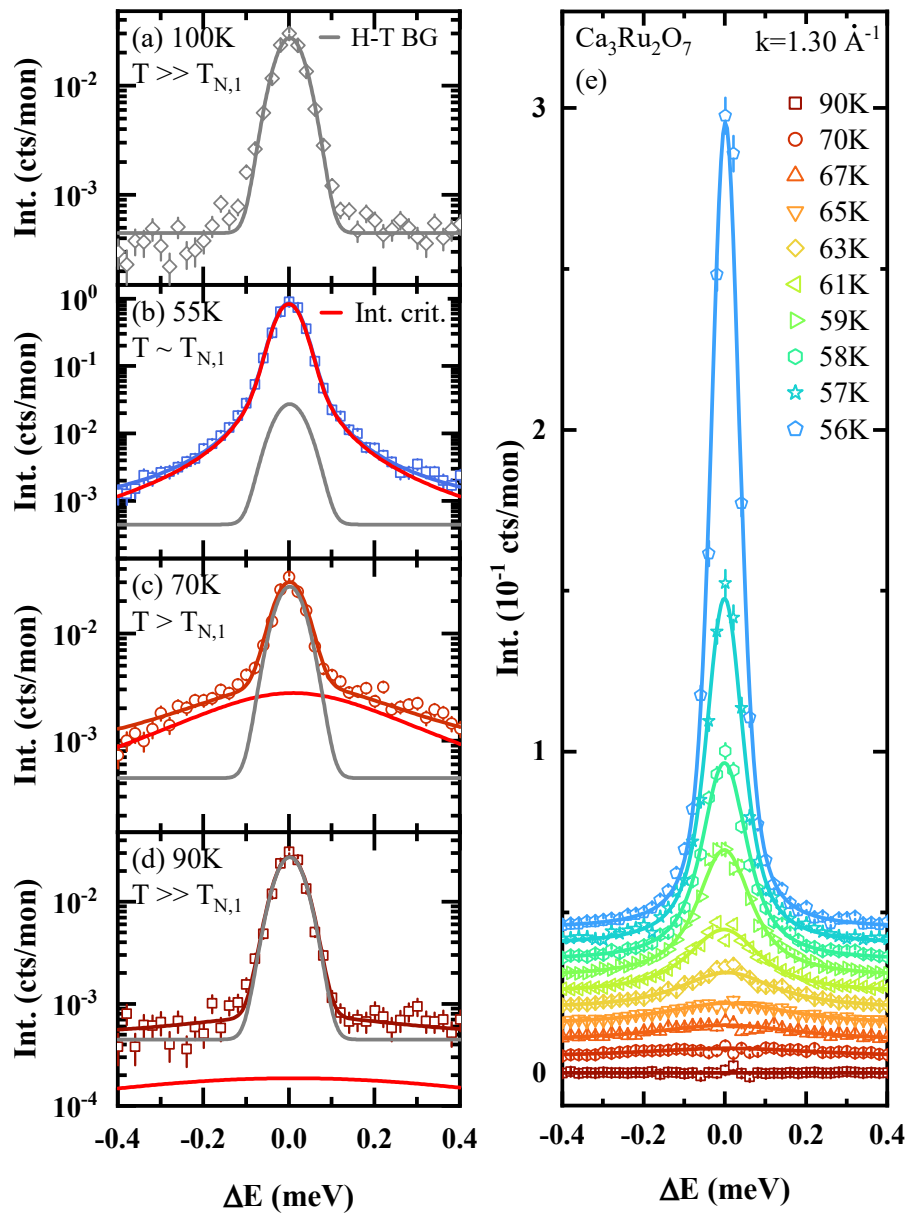


Fig. 6.32: Selected energy scans of $\text{Ca}_3\text{Ru}_2\text{O}_7$ before (a-d) and after (e) BG subtraction. (a-d) In contrast to Ca_2RuO_4 , the $\text{Ca}_3\text{Ru}_2\text{O}_7$ data could be well fitted by a single Voigt-profile and a constant elastic high-T BG measured at 100 K. (d) Selected energy scans after BG subtraction with corresponding fit functions (solid lines). For clarity the curves are plotted with a constant offset.

proximity to T_N . Figure 6.33b shows a plot of Γ vs. κ on double logarithmic scales, which allows to determine z directly. From the slope of a linear fit (red dotted line), we derive $z = 2.14(2)$ as the critical exponent, which is close to $z = 2.0$ proposed for the 3D-I model [15, 118] and consistent with the $\Gamma(T)$ scaling above. Note that $z = 2.0$ also corresponds to the 2D-XY model [117]. However, since the 3D-I scaling is also compatible with the temperature-dependence of the Q -width and critical amplitudes at $T > T_N$ of $\text{Ca}_3\text{Ru}_2\text{O}_7$, we consider this model as most appropriate.

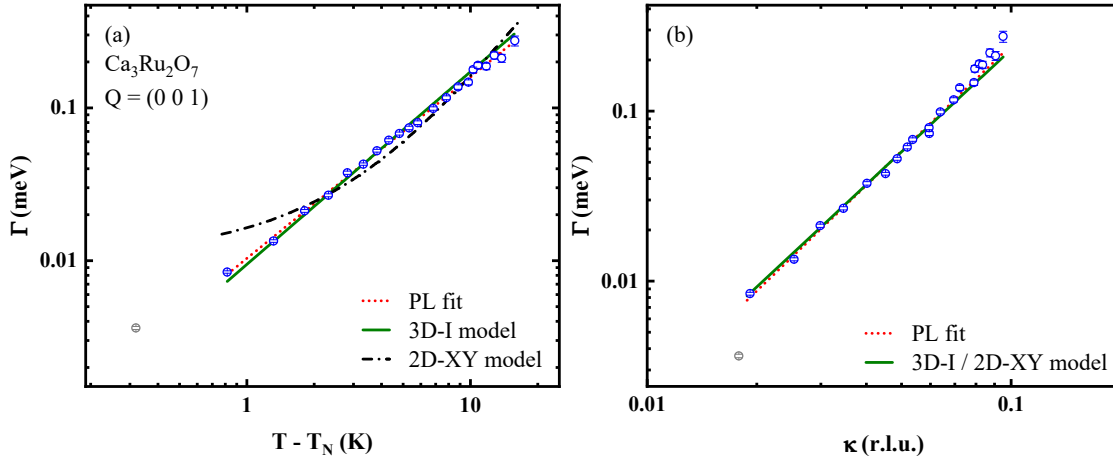


Fig. 6.33: Energy-width Γ of $\text{Ca}_3\text{Ru}_2\text{O}_7$ vs. temperature (a) and the inverse correlation length (b) on double-logarithmic scales. (a) The red dotted line is a linear fit with the slope corresponding to the critical exponent $z\nu = 1.186(8)$, according to the scaling relation $\Gamma \propto t^{z\nu}$. The green solid line indicates 3D-I scaling with $z\nu_{3\text{DI}} = 1.260$ [15, 18]. The black dashed-dotted line corresponds to the 2D-XY model with the exponent $z = 2.0$ [117]. (b) The red dotted line is a linear fit with the slope corresponding to the critical exponent $z = 2.14(2)$, according to the scaling relation $\Gamma \propto \kappa^z$. The green solid line corresponds to 3D-I scaling and the 2D-XY model, which both exhibit the exponent $z = 2.0$ [15, 117]. However, the 3D-I model is also consistent with the static critical properties of $\text{Ca}_3\text{Ru}_2\text{O}_7$. The grey data points were not included in the fits.

6.3. Ti-doped bilayer $\text{Ca}_3(\text{Ru}_{0.99}\text{Ti}_{0.01})_2\text{O}_7$

$\text{Ca}_3\text{Ru}_2\text{O}_7$ is close to electronic and magnetic instabilities, as outlined in Chap. 3. In consequence, only a marginal doping with Ti-ions is sufficient to tune the ground state of the A-type AFM correlated metal $\text{Ca}_3\text{Ru}_2\text{O}_7$ to a G-type AFM Mott-insulator, similar to what is realized in Ca_2RuO_4 . It is therefore of great interest to study how the critical behavior in $\text{Ca}_3(\text{Ru}_{1-x}\text{Ti}_x)_2\text{O}_7$ changes in vicinity to the G-type magnetic transition. According to [201], for our crystals a sharp single-step transition to a pure G-type AFM ground state is expected from 1%-Ti doping ($x \geq 0.01$). We see below, that this sharp-transition has first-order character and thus critical magnetic fluctuations are suppressed in $\text{Ca}_3(\text{Ru}_{0.99}\text{Ti}_{0.01})_2\text{O}_7$.

Experimental details

About 30 $\text{Ca}_3(\text{Ru}_{0.99}\text{Ti}_{0.01})_2\text{O}_7$ single-crystals with a total mass of 1 g that included orthorhombic (a,b)-twins were co-aligned on Si-plates with thicknesses of 0.5 mm and arranged in Al-sample holders [Fig. 6.34a]. The lattice parameters are $a = 5.370 \text{ \AA}$, $b = 5.601 \text{ \AA}$, $c = 19.351 \text{ \AA}$ [79] and the mosaicity of the sample array was about 3° . Due to the (a,b)-twinning, the scattering plane was (H 0 L)/(0 K L) [Fig. 6.34a,b].

The experiments on $\text{Ca}_3(\text{Ru}_{0.99}\text{Ti}_{0.01})_2\text{O}_7$ [276] were carried out at the cold neutron TAS IN12 [237] at the ILL. The instrument was operated in three-axis mode with scattering sense $SM = -1$, $SS = 1$, $SA = -1$ and $k_f = 1.3 \text{ \AA}^{-1}$ with double focusing monochromator and analyzer (energy resolution $\approx 0.07 \text{ meV}$). In addition, a Be-filter was used to suppress higher monochromator orders.

Neutron scattering on $\text{Ca}_3(\text{Ru}_{0.99}\text{Ti}_{0.01})_2\text{O}_7$

Before discussing the neutron scattering results, we consider the heat capacity of a selected $\text{Ca}_3(\text{Ru}_{0.99}\text{Ti}_{0.01})_2\text{O}_7$ single-crystal [Fig. 6.35a]. On cooling, the curve shows a small anomaly at $T_{N,1} = 56 \text{ K}$ and a divergence at $T_{N,2} = 55 \text{ K}$ indicating a first-order transition. According to Fig. 3.12 and [201], we assign the latter to the sharp G-type AFM transition, whereas the small anomaly at $T_{N,1}$ signals also the occurrence of an A-type AFM phase in our crystals. Such a mixed ground state of A- and G-type phases is consistent with the phase diagram shown in Fig. 3.12,

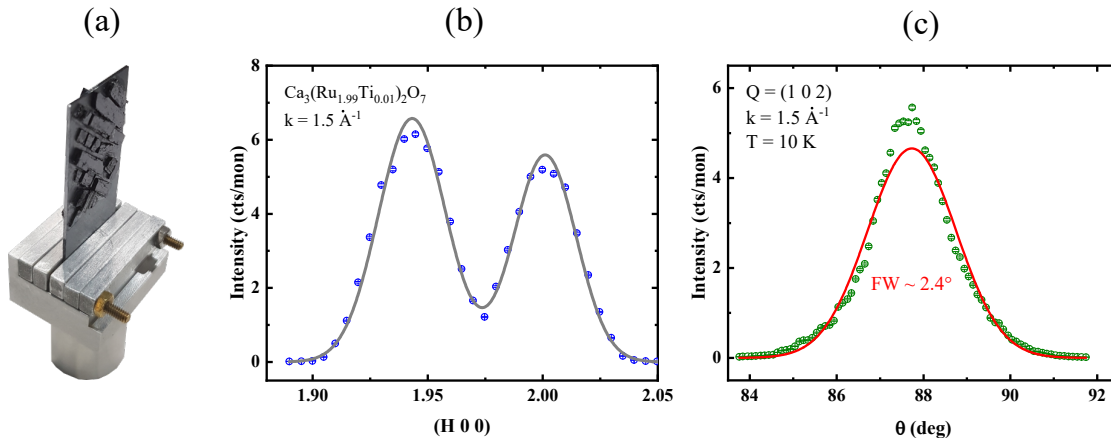


Fig. 6.34: (a) Picture of the $\text{Ca}_3(\text{Ru}_{0.99}\text{Ti}_{0.01})_2\text{O}_7$ sample array. (b) $(H\ 0\ 0)$ scan shows $(2\ 0\ 0)$ and $(0\ 2\ 0)$ peaks due to twinning of the $\text{Ca}_3(\text{Ru}_{0.99}\text{Ti}_{0.01})_2\text{O}_7$ crystals in the (a,b) -plane. The grey solid line corresponds to a fit with two Gaussian-functions (FWHM ≈ 0.03 r.l.u.). (c) Rocking (A3) scan at the AFM $(1\ 0\ 2)$ peak of the G-type phase at 10 K ($T \ll T_N$). The $(1\ 0\ 2)$ peak is forbidden in pure $\text{Ca}_3\text{Ru}_2\text{O}_7$.

and further supported by our neutron scattering experiments, where the magnetic Bragg-peaks of both phases occur: (i) The $(0\ 0\ 1)$ peak associated with the A-type phase (not shown here) and (ii) the $(1\ 0\ 2)$ peak associated with the G-type phase [Fig. 6.34c] [75].

In this work, we aim to clarify whether critical magnetic fluctuations occur in vicinity of the sharp G-type transition with supposed first-order character. Thus, we focus on the temperature-dependence of the magnetic Bragg-intensity at $Q = (1\ 0\ 2)$ as well as the Q -width of the diffuse scattering above $T_{N,2}$. The T -dependence of the $(1\ 0\ 2)$ peak intensity was measured upon heating and is shown in Fig. 6.35b. In contrast to the continuous behavior of the $(0\ 0\ 1)$ peak in pure $\text{Ca}_3\text{Ru}_2\text{O}_7$ at $T_{N,2} < T < T_{N,1}$ [Fig. 6.28], the intensity of the $(1\ 0\ 2)$ peak in $\text{Ca}_3(\text{Ru}_{0.99}\text{Ti}_{0.01})_2\text{O}_7$ abruptly drops at $T_{N,2} \approx 55$ K. This is a clear evidence of a first-order transition consistent with the heat capacity measurement on one selected single-crystal [Fig. 6.35a]. We note that the sharp drop of the $(1\ 0\ 2)$ peak is 0.25 K above the discontinuity detected in the heat capacity, which might result from a different thermometry at IN12. The typical peaked structure of the critical scattering intensity around T_N , detected in Ca_2RuO_4 and $\text{Ca}_3\text{Ru}_2\text{O}_7$ in small distance to the nominal magnetic Bragg-position [see insets of Figs. 6.4a and 6.28a],

was not visible in $\text{Ca}_3(\text{Ru}_{0.99}\text{Ti}_{0.01})_2\text{O}_7$. This suggests that the critical fluctuations associated with the G-type AFM ground state are absent in $\text{Ca}_3(\text{Ru}_{0.99}\text{Ti}_{0.01})_2\text{O}_7$ due to the first-order transition.

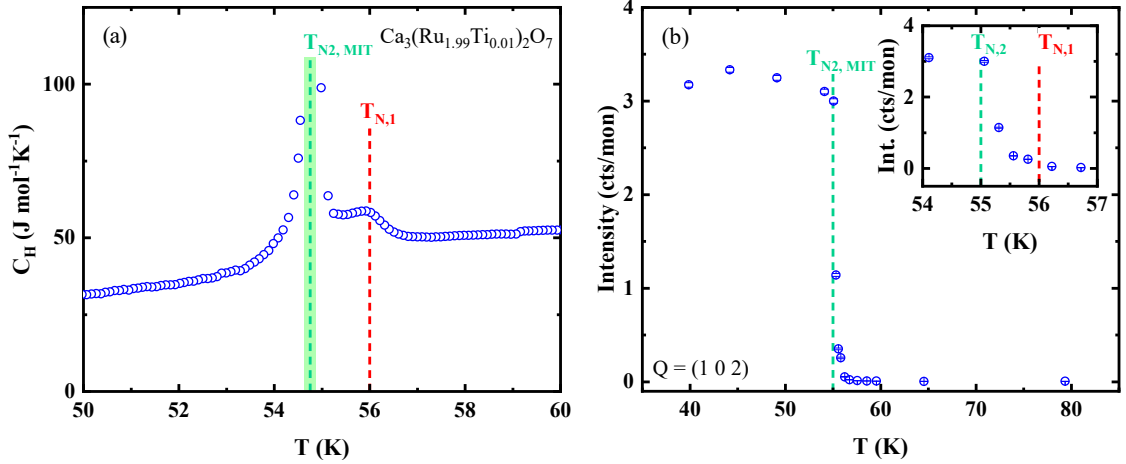


Fig. 6.35: (a) Heat capacity of a selected $\text{Ca}_3(\text{Ru}_{0.99}\text{Ti}_{0.01})_2\text{O}_7$ single-crystal. On cooling, the heat capacity shows a small anomaly at $T_{N,1} = 56 \text{ K}$ and a discontinuity at $T_{N,2} \sim 55 \text{ K}$. The former indicates a transition to the A-type AFM phase and the latter a first-order transition to the G-type AFM phase, which is accompanied by a MIT. (b) Magnetic (1 0 2) Bragg intensity of the G-type phase *vs.* T . The sharp intensity-drop corresponds to the first-order transition at $T_{N,2}$ in panel (a). The small anomaly in the heat capacity at $T_{N,1}$ (red dashed line) is not visible since $Q = (1\ 0\ 2)$ is a forbidden peak-position for the A-type AFM phase. The inset shows a zoom on the data.

The T -dependence of the Q -width and amplitude obtained from (H 0 2)-scans further supports this assumption. In Fig. 6.36a-d, we present the corresponding Q_H -scans at selected temperatures before BG subtraction. The BG is derived from a scan at $T = 150 \text{ K}$ [Fig. 6.36a], where magnetic scattering is negligible, and is indicated by a grey solid line in the other panels. In Fig. 6.36e, we show an overview of selected Q_H -scans after BG subtraction with corresponding Voigt-fits. The instrumental resolution of the TAS spectrometer ($\text{FWHM} \approx 0.035$) was experimentally determined from the elastic magnetic Bragg-peak consistent with TAKIN simulations. The resulting Q -width $\kappa(T)$ is plotted in Fig. 6.37a. Except for the two data points between $T_{N,1}$ and $T_{N,2}$, $\kappa(T)$ is close to the instrumental resolution in the entire T -range. We therefore assign the broadening between $T_{N,1}$ and $T_{N,2}$ to a variance in the lattice parameter in proximity to the structural transition at

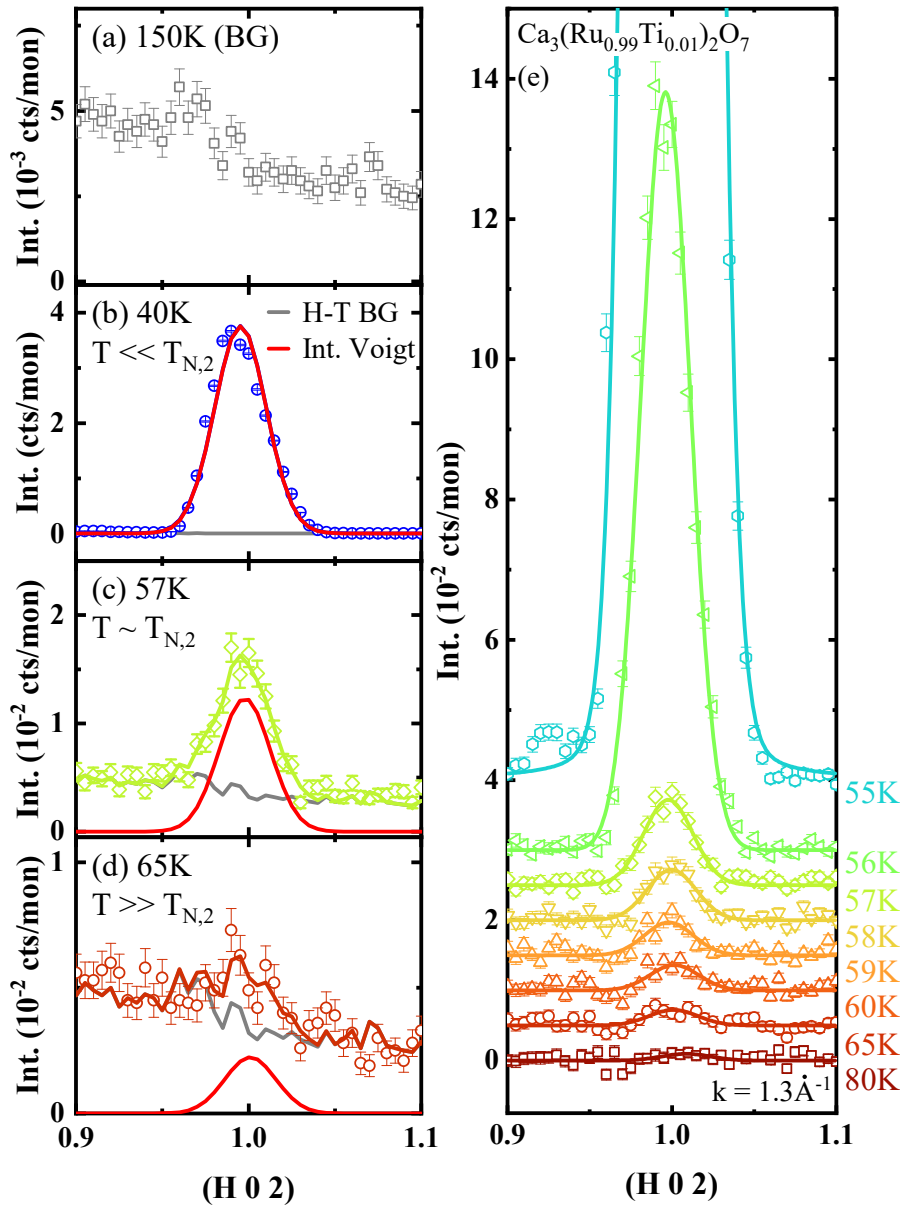


Fig. 6.36: Selected Q_H -scans around $(H\ 0\ 2)$ for $\text{Ca}_3(\text{Ru}_{0.99}\text{Ti}_{0.01})_2\text{O}_7$ before (a-d) and after (e) BG subtraction. (a) Constant 'high-temperature' (H-T) BG determined at $T = 150\text{K}$ and indicated in panels (b-d) as a dashed grey line. A Voigt-fit is shown as a red solid line. (e) Selected Q_H -scans after BG subtraction with corresponding fit functions (solid lines). For clarity the data are plotted with a constant offset.

$T_{N,2}$. This is similarly reflected in the T -dependence of the lattice parameters and the Q -widths of the nuclear $(2\ 0\ 0)$, $(0\ 2\ 0)$, and $(0\ 0\ 2)$ peaks [Fig. 6.38]. Here, the lattice parameters were determined from the peak positions of the corresponding nuclear peaks. From these observations, we conclude that the critical fluctuations associated with the G-type phase are suppressed in $\text{Ca}_3(\text{Ru}_{0.99}\text{Ti}_{0.01})_2\text{O}_7$ due to the first-order character of the transition at $T_{N,2}$.

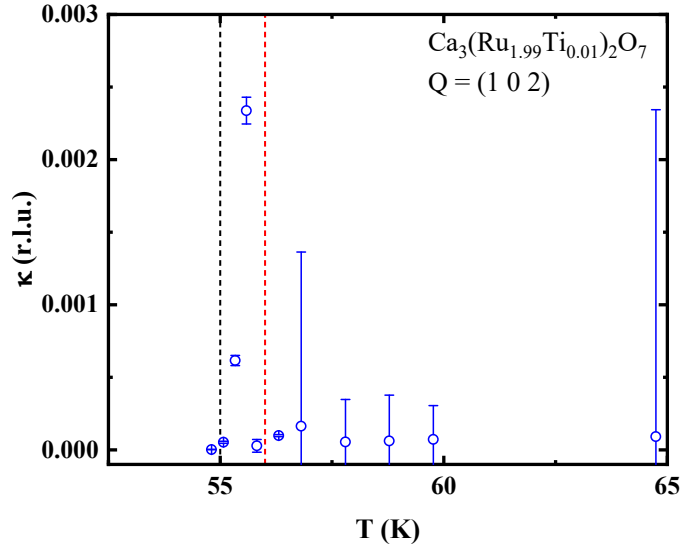


Fig. 6.37: Inverse correlation length $\kappa(T)$ of $\text{Ca}_3(\text{Ru}_{0.99}\text{Ti}_{0.01})_2\text{O}_7$. No critical behavior is observed in $\text{Ca}_3(\text{Ru}_{0.99}\text{Ti}_{0.01})_2\text{O}_7$. The enhanced Q -width at $T_{N,2} < T < T_{N,1}$ is assigned to a variance of lattice parameter prior to the structural transition at $T_{N,2}$. The vertical dashed lines show $T_{N,1}$ (red) and $T_{N,2}$ (black), respectively.

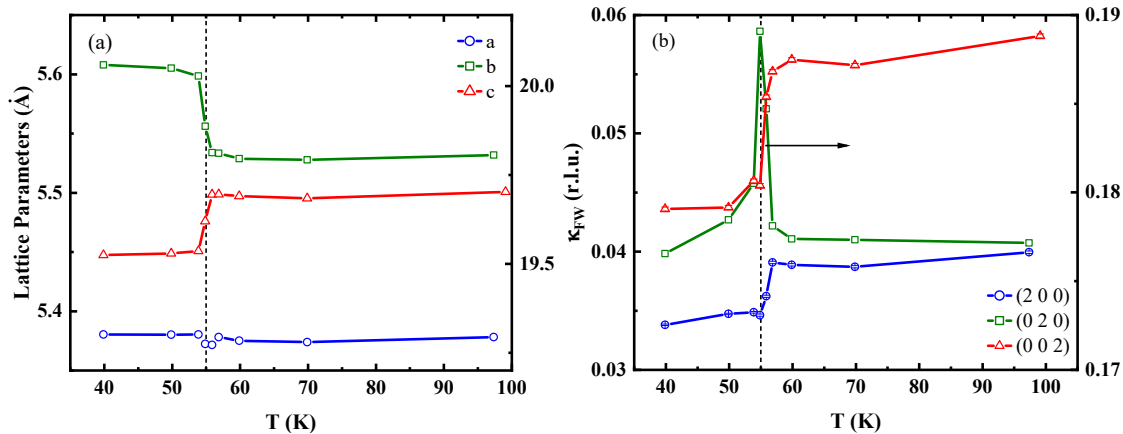


Fig. 6.38: (a) Lattice parameter *vs.* T extracted from the peak-position of Gaussian-fits on the nuclear (2 0 0), (0 2 0), and (0 0 2) peaks, respectively. (b) Corresponding Gaussian Q -widths (FWHM) of the nuclear peaks *vs.* T . The black dashed line, which indicates the first-order transition at $T_{N,2} = 55$ K, agrees with the jump in the lattice parameters and Q -widths.

6.4. Discussion and Conclusion

For Ca₂RuO₄, we revealed that the description of the static critical properties by PL scaling gave only partially satisfactory results, whereas application of the 2D-XY model provided a conclusive picture. In more detail, the obtained critical exponent $\beta = 0.158(6)$ is consistent with a 2D-XY model with fourfold crystal anisotropy (XY h_4) [262]. The inverse correlation length κ , in principle, could be fitted with different PLs and the 2D-XY model. Specifically, the observed saturation of κ in the range between T_N and $T_N + 4$ K was captured by a PL with Q_L -dependence, likely indicating the presence of 3D fluctuations close to T_N . Nevertheless, the employed PL fits, with and without κ offset, were not consistent with the 2D nature of Ca₂RuO₄ far above T_N and results from fits of the amplitudes of the critical scattering.

Instead, the 2D-XY model captured both, κ and the amplitude adequately. The resulting Kosterlitz-Thouless temperature $T_{KT} = 87(2)$ K was consistent with the ratio $J'/J = 0.002$ derived from the offset in $\kappa(T)$. Our attempt to describe the amplitude of the critical scattering by PL scaling showed that the functional form does not capture the data appropriately and the extracted critical exponent

$\gamma = 0.47(2)$ is not compatible with universal values. Yet, 2D-XY scaling captured the critical amplitudes in a broad T-range around T_N , in agreement with the Hamiltonian extracted from the magnon dispersion in the ordered phase [6].

The energy-width $\Gamma(T)$ derived from TAS was best captured by a PL fit with $z\nu = 1.1(1)$, which is compatible with 3D AFM Heisenberg scaling ($z\nu_{3DH} = 1.067$, [15, 93]). However, such a model for the dynamical critical scaling would be in stark contrast to the static critical behaviors, the magnon dispersion [6], and the quasi-2D character of Ca_2RuO_4 . Consequently, we fitted the data with the 2D-XY model and $z_{XY} = 2.0$ [117], which also captured the data reasonably well in a Γ vs. κ plot on double logarithmic scale.

In general, a crossover in the critical behavior from 2D-XY to Ising scaling close to T_N can be expected in Ca_2RuO_4 due to the orthorhombic terms in the spin Hamiltonian [6]. The observed saturation of $\kappa(T)$ close to T_N might be indicative for a dimensionality crossover to 3D scaling, whereas signatures of such a crossover were less clear in the analysis of the other critical exponents.

This apparent absence could be due to the limited instrumental resolution of our TAS measurements and called for a complementary high-resolution NSE study, focusing on the temperature range in close vicinity to T_N . The enhanced energy resolution of NSE previously helped to resolve controversies about the scaling behavior of heavy-fermion superconductors [53] and revealed scaling crossovers close to T_N in the classical AFMs MnF_2 and Rb_2MnF_4 [54]. We therefore conducted NSE experiments on Ca_2RuO_4 at $Q = (1\ 0\ 0)$ and $Q = (1\ 0\ 0.53)$. With the capability of separating in-plane and out-of-plane fluctuations [54], we could confirm that the critical scattering intensity results purely from longitudinal fluctuations. The temperature-scaling of $\Gamma(T)$ measured at $Q = (1\ 0\ 0)$ with the critical exponent $z\nu = 0.90(3)$ was close to the results from TAS ($z\nu = 1.1(1)$). We attribute the deviations to the broad energy-widths for NSE. In consequence, the dynamic scaling of $\Gamma(T)$ from TAS was corroborated by the NSE experiments. As our NSE data at $Q = (1\ 0\ 0.53)$ indicate a q -dependence of the energy-width we propose for a future study to alternatively determine z via $\Gamma \propto q^z$ at $T \sim T_N$. Apart from that, it will be interesting to probe the existence of possible vortex/antivortex-pairs with cryogenic microscopy techniques, such as Lorentz transmission electron microscopy [277], which might be particularly pronounced in thin films of Ca_2RuO_4 [278].

Overall, the distribution in T_N in our sample introduces some uncertainty in our analysis of the critical scattering in Ca_2RuO_4 . Nonetheless, we find that our determination of the critical exponents of the Q -width, critical amplitudes, and energy-width is relatively insensitive to the details of the variance of T_N . Along these lines, we performed fits (not shown here) assuming a difference of ± 0.5 K to our above value of $\Delta T_N = 4.84(1)$ K. The resulting values for ν and z are closely similar to the above ones (difference smaller than the error bars). This is plausible since we fit the data only for $T > T_N + 4$ K, where the impact of the T_N distribution is relatively small. For the critical amplitudes, where the impact of the T_N distribution on the critical exponent is expected to be strongest, as we fit in the range 110-140 K, we find a deviation of only four percent. Also in the case of the critical amplitudes, the change of the critical exponent is smaller than the error bars. This result suggests that even a putative uncertainty in our value of ΔT_N would not critically affect our determination of the critical exponents, corroborating the robustness of our analysis. A definitive determination of the critical behavior close to T_N will require the synthesis of large, monolithic Ca_2RuO_4 single crystals, which appears to be out of reach of the methodologies currently at hand.

Next, we like to compare our results on Ca_2RuO_4 with related **TMOs** and more established solid-state systems, that can be described within the **2D-XY** model. As already pointed out, critical scattering studies on $4d$ -electron **TMOs** are to date unexplored. Nevertheless, we can compare the critical behavior with structurally related, quasi-2D square-lattice $3d$ - and $5d$ -electron **TMOs**. In the $3d$ **AFMs** Rb_2MnF_4 [46], $\text{Sr}_2\text{CuO}_2\text{Cl}_2$, and $\text{Sr}_2\text{Cu}_3\text{O}_4\text{Cl}_2$ [47], as well as the **AFM** parent compounds of the cuprate superconductors [48], for instance, **2D-H** scaling properties above their Néel temperatures were observed. Whereas, in the single-layer $5d$ **AFM** Sr_2IrO_4 an admixture of easy-plane anisotropy to the **2D-H** behavior was observed [57, 58]. The isotropic scaling behavior in the $3d$ -electron systems is consistent with the suppression of the spin-orbit coupling [6], which likely is responsible for the admixture of **2D-XY** behavior to the critical scaling in Sr_2IrO_4 . For Ca_2RuO_4 , we propose that an interplay of the moderate spin-orbit coupling and the strong single-ion anisotropy [6, 7], which was not required to describe the spin-wave excitations in Sr_2IrO_4 [58, 279], reveals a more pronounced **2D-XY** behavior. In comparison with more established solid-state systems for the study

of the **2D-XY** model Rb_2CrCl_4 [30, 270, 280], K_2CuF_4 [29] (square-lattice **FMs**), as well as $\text{Ba}(\text{MXO}_4)_2$ with ($M = \text{Ni, Co, X} = \text{As, P, V}$ [28, 32]) and MnPS_3 [31] (honeycomb **AFMs**), it is striking that Ca_2RuO_4 is the only realization of the **2D-XY AFM** on a square lattice.

For the bilayer compound $\text{Ca}_3\text{Ru}_2\text{O}_7$, which exhibits strong intra-bilayer couplings, the critical scaling was only partly compatible with the **2D-XY** model. Although $\beta = 0.230(6)$ extracted from the temperature-dependence of the magnetic (0 0 1) peak matches the expected value for realistic **2D-XY** systems [91, 274], the result should be taken with caution, due to a relatively low point density around $T_{\text{N},1}$ and a possible overlap with the signal from the transition at $T_{\text{N},2}$. While the extracted β is seemingly far from the corresponding value of the **3D-I** model ($\beta_{\text{3DI}} = 0.327$, [18]), previous works in the context of $\text{Sr}_3\text{Ir}_2\text{O}_7$ pointed out that a significant underestimation of β can arise when the power law analysis is not narrowly focused around T_{N} [59], which provides a possible reconciliation between our small β and the proposed **3D-I** scaling. The critical scaling of the Q -width, amplitude, and energy-width above $T_{\text{N},1}$ showed deviations from the **2D-XY** theory (especially at low temperatures), whereas the **3D-I** model captured the data comprehensively. The Ising character of the magnetic correlations likely results from the orthorhombic anisotropy, which eventually drives the magnetic transition at $T_{\text{N},1}$. We remark, however, that in the Γ *vs.* κ plot, **3D-I** scaling and the **2D-XY** model were indistinguishable, due to identical dynamical critical exponents of the universality classes ($z = 2$). Consequently, the **3D-I** model provides the most conclusive description of the critical behaviors in $\text{Ca}_3\text{Ru}_2\text{O}_7$, although a partial **2D-XY** character can not be excluded. This ambiguity likely reflects the geometry of the exchange bonds in the bilayer structure of $\text{Ca}_3\text{Ru}_2\text{O}_7$, which is intermediate between 2D and 3D. The theoretical description of the resulting crossover phenomena and detailed comparison with the experimental data are important challenges for future research. In the 1% Ti-doped compound $\text{Ca}_3(\text{Ru}_{0.99}\text{Ti}_{0.01})_2\text{O}_7$, no evidence for critical magnetic fluctuations was found due to the first-order character of the G-type **AFM** transition.

In conclusion, our results imply that the layered ruthenates are potential solid-state platforms for research on the **2D-XY** model and the effects of 3D interactions and additional spin-space anisotropies on the magnetic fluctuations. Along with

Sr_2IrO_4 , which hosts a nearly ideal 2D Heisenberg AFM [57, 58], this work illustrates the power of 4*d*- and 5*d*-electron materials with strongly spin-orbit-entangled magnetic moments as a platform for fundamental research on quantum magnetism.

7. Critical magnetic fluctuations in $\text{CeCu}_{6-x}\text{Au}_x$ ($x = 0.1, 0.2$)

We present a **NSE** study on the critical magnetic fluctuations in the near quantum critical heavy-fermion system $\text{CeCu}_{5.8}\text{Au}_{0.2}$, and briefly compare it with measurements on the critically doped $\text{CeCu}_{5.9}\text{Au}_{0.1}$. We find a quantum-to-classical crossover in the dynamical scaling behavior of $\text{CeCu}_{5.8}\text{Au}_{0.2}$, whereas the **NSE** scans on $\text{CeCu}_{5.9}\text{Au}_{0.1}$ could not resolve critical scaling.

7.1. $\text{CeCu}_{5.8}\text{Au}_{0.2}$

Experimental details

The measurements were conducted at TRISP [232, 259] on a single-crystal of $\text{CeCu}_{5.8}\text{Au}_{0.2}$ (size $\approx 1 \text{ cm}^3$) [Fig. 7.1a], that was grown by the Czochralski-method by Stockert and previously used in other neutron scattering experiments [1, 220, 223, 281, 282]. The mosaicity of the crystal with lattice parameters $a = 8.105$, $b = 5.100$, and $c = 10.171$ was about 0.5° [Fig. 7.1c]. For the measurements, the sample was mounted on two small piezo-goniometer to provide an in-situ crystal alignment with neutrons Fig. 7.1a. We installed the sample holder in a closed-cycle dilution cryostat, and observed with a thermometer close to the sample a sample base temperature of $\sim 40 \text{ mK}$. The scattering plane was (H 0 L).

The TRISP spectrometer was operated in two-axis mode, *i. e.* only a polarization analyzer (Bender crystal) was implemented, with clockwise scattering sense at the monochromator and sample ($SM = -1$, $SS = -1$) at $k_i = 2.51 \text{ \AA}^{-1}$. The two-axis mode was chosen to increase the intensity at the detector by a factor of three.

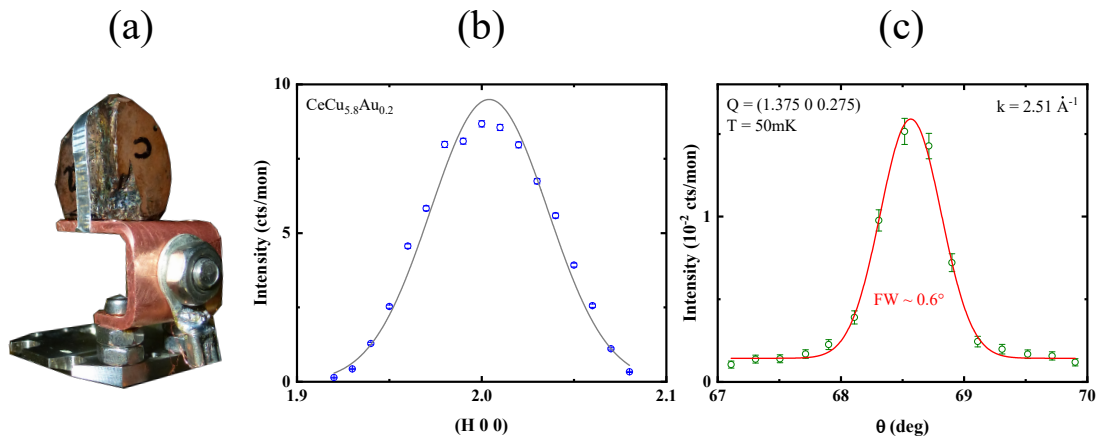


Fig. 7.1: (a) Picture of the $\text{CeCu}_{5.8}\text{Au}_{0.2}$ single crystal detached on a small piezoelectric goniometer. (b) $(H\ 0\ 0)$ scan. The grey solid line corresponds to a Gaussian fit ($\text{FWHM} \approx 0.07$ r.l.u.). (c) Rocking scan at the magnetic $(1.375\ 0\ 0.275)$ Bragg-peak and at 50 mK ($T < T_N$).

Critical scattering in $\text{CeCu}_{5.8}\text{Au}_{0.2}$

Prior to the discussion of the [NSE](#) results, we address the critical behavior of the magnetic order parameter derived from the temperature-dependence of the magnetic $(1.375\ 0\ 0.275)$ Bragg intensity [Fig. 7.2a]. On heating, the intensity indicates a second-order transition at $T_N \approx 0.25$ K in agreement with previous works [211, 223]. The Bragg-intensity drops sharply towards T_N , which indicates that no significant variance of T_N is present in our sample. After subtracting the BG, we assign the remaining intensity for $T > T_N$ mostly to the critical magnetic fluctuations, as was also suggested in [1]. In addition, we find a small bump in the scattering intensity at $T > T_N$ discussed below (see Fig. 7.3b), which likely results from small fractions of the crystal with higher Au-dopings and thus a higher transition temperature. To extract the critical exponent β and T_N , we fitted the peak intensity with a $\text{PL} \propto |t|^{2\beta}$ in the range $0.1\text{ K} < T < T_N$ ($0 < |t| < 0.6$) without a T_N variance [Fig. 7.2]. A fit of the intensity of the magnetic Bragg-peak yields $T_N = 0.254$ K in agreement with previous works [211, 223]. The resulting $\beta = 0.414(5)$ is between the universal values of the [3D-H](#) ($\beta_{3\text{DH}} = 0.369$, [93]) and the [MF](#)-model ($\beta_{\text{MF}} = 0.5$, [16]). The latter was similarly reported in previous neutron scattering studies on the same crystal [222, 283].

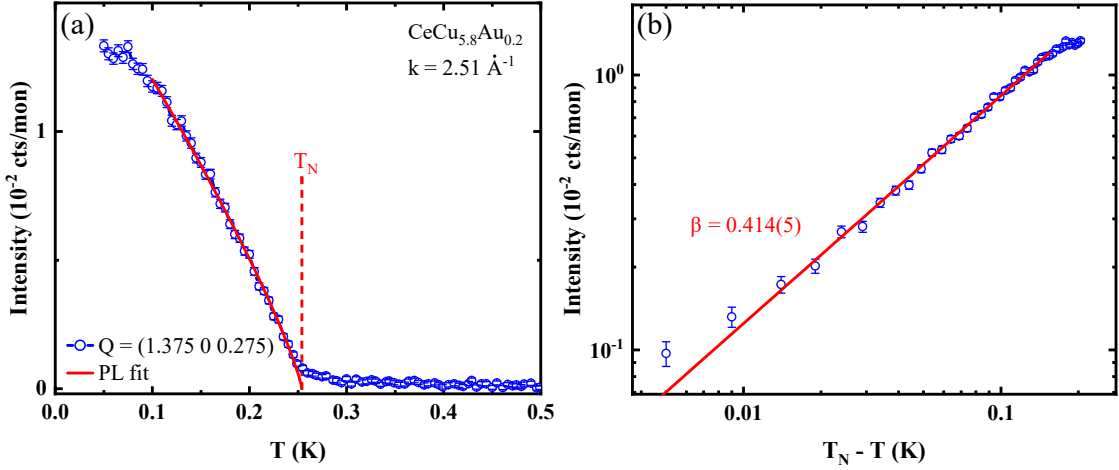


Fig. 7.2: (a) Intensity of the magnetic (1.375 0 0.275) peak measured *vs.* T . The red solid line is a PL fit $I \propto M^2 \propto |t|^{2\beta}$, with $\beta = 0.414(5)$ and $T_N = 0.254$ K. (b) Shows the same data as in (a) on a double-logarithmic scale.

Similarly, the temperature-dependence of the magnetic Bragg-intensity $I(T)$ can be obtained from the mean intensity of the NSE scans [Fig. 7.3a]. This approach benefits from the long measuring time used for the spin-echo scans, as it ensures good statistics and temperature stability. The latter is particularly important at the relatively low sample temperatures used in this experiment. $I(T)$ exhibits a small bump (0.5% of I_{max}) between 0.3-0.4 K ($T > T_N$), which was only faintly indicated in the T -dependence of the magnetic Bragg-intensity (grey line in Fig. 7.3a). The bump is reminiscent of an order parameter-like behavior with higher transition temperature $T_{N,\text{imp}} \sim 0.4$ K and is therefore assigned to an enhanced Au-doping in small fractions of the $\text{CeCu}_{5.8}\text{Au}_{0.2}$ crystal, as $T_N \propto |x - x_c|$ (see Fig. 4.1a). It turns out that the small bump has only negligible impact on the results and thus we ignore it in the following. To extract the corresponding β exponent of $I(T)$, we performed a PL fit $I(T) \propto |t|^{2\beta}$ [Fig. 7.3b] in the same range as for the T -scan ($0.1 \text{ K} < T < T_N$) [Fig. 7.2]. The data are described by the parameters $T_N = 0.259$ K and $\beta = 0.402(2)$. Both parameters are in good agreement with the values obtained from the T -scan: $\beta = 0.414(5)$, $T_N = 0.254$ K. The slightly reduced T_N likely results from temperature-drifts during the T -scan, which are averaged out in the long NSE scans. In consequence, we will use $T_N = 0.259$ K and $\beta = 0.402(2)$ in the following.

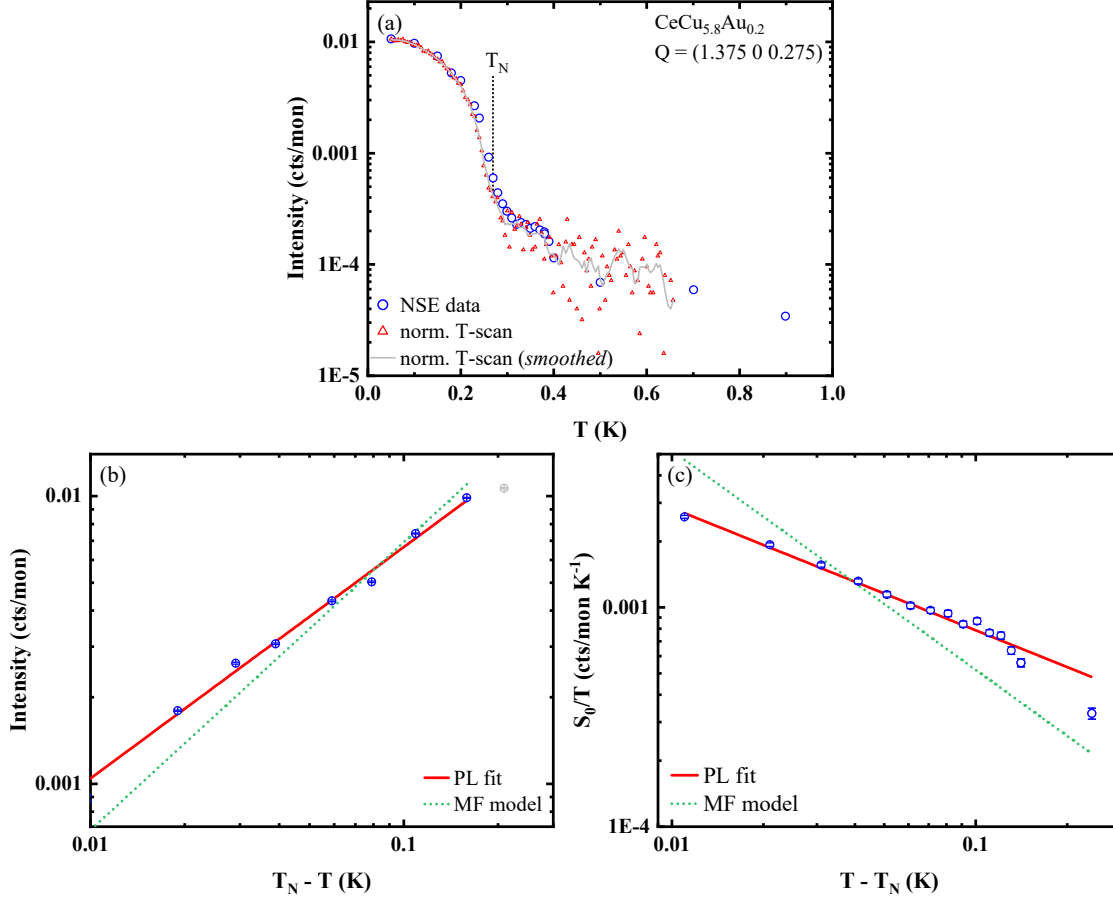


Fig. 7.3: (a) Mean intensity $I(T) = (I_0(T) - I_{0,\text{BG}}(0.9\text{K}))/2$ of the NSE scans *vs.* temperature on semi-logarithmic scaling. The data show a small bump at 0.3-0.4 K. For comparison, we also plot the data from the T -scan (red triangles) [Fig. 7.2] normalized on the 0.05 K point. The smoothed T -scan data (grey solid line) indicate also a small bump. The black dashed vertical line indicate T_N . (b,c) T -dependence of corresponding (b) (1.375 0 0.275) peak intensity and (c) diffuse scattering intensity S_0/T at $Q = (1.375 0 0.275)$ derived from the data in (a). (b) From a PL fit (red solid line) in the range $0.1\text{K} \leq T < T_N$ we extract the parameters $T_N = 0.259\text{K}$ and $\beta = 0.402(2)$. The grey data point was not considered in the fit. (c) From a PL fit (red solid line) in the range $0.27\text{K} \leq T < 0.5\text{K}$ we extract $\gamma = 0.557(8)$. For comparison, we also show fits according to the MF model (green dotted lines).

As the NSE intensity at $Q = (1.375 \ 0 \ 0.275)$ above T_N can be assigned to the critical scattering, we can also determine the critical exponent γ via the scaling relation $\chi_0 \propto S_0/T \propto |t|^{-\gamma}$. The corresponding linear fit in the double-logarithmic plot [Fig. 7.3c] in the range $0.27\text{K} \leq T < 0.5\text{K}$ reveals $\gamma = 0.557(8)$. This critical exponent is not related to any universality class. Here, additional Q -scans would be desirable, as they would allow the investigation of the scaling behavior of the correlation length κ^{-1} .

Now, we discuss the NSE results. At first, we address the NSE spin-flip model in CeCu_{5.8}Au_{0.2}. Depending on the alignment of the magnetic field \mathbf{B}_2 in the second PD ($\uparrow\uparrow$ or $\uparrow\downarrow$), either the in-plane (M_y) or out-of-plane (M_z) magnetic fluctuations fulfill the echo-condition, as described in the methods (see Chap. 5). To assign the measured polarization for the different operation modes ($\uparrow\uparrow$ or $\uparrow\downarrow$) to the corresponding fluctuations, we apply the general NSE spin-flip model [Fig. 5.9] on the scattering plane and Q -position used in CeCu_{5.8}Au_{0.2} [Fig. 7.4]. Due to the effective field inversion ($\varphi_{f,c} = \pi - \varphi_i$), neutrons scattered by the longitudinal fluctuations along the c -axis (M_y) fulfill the echo-condition for parallel fields ($\tau > 0$), while the echo-condition for scattering on the transverse fluctuations along the b -axis (M_z) is fulfilled for antiparallel fields ($\tau < 0$). The position of the magnetic Bragg-peak $Q = (1.375 \ 0 \ 0.275)$ is incommensurate and thus $M_y \perp Q$ is not exactly along the c -axis, but slightly tilted by 9° [Fig. 7.4]. However, the corresponding projection of $M_{\parallel,c}$ on M_y yields $M_y = 0.99M_c$ and we approximate $M_y \sim M_{\parallel,c}$ in the following.

In Fig. 7.5, we show exemplary raw spin-echo scans with corresponding fits for $\tau = 1$ ps (DC-coils) and $\tau = 23$ ps (RF-coils) in both operation modes at various temperatures. The background (BG) [Fig. 7.5a] was measured in distance to the magnetic Bragg position at $Q = (1.875 \ 0 \ 0.275)$ and $T = 0.9\text{K}$, and is indicated in the other panels by grey lines. To extract the polarization from the NSE scans, we fitted the data, analogous to Ca₂RuO₄, with the sinusoidal relation [Eqn. (5.19)]. From panel (e), we conclude that the small background polarization at higher τ obtained from the fit is likely a statistical artefact as the data show no clear evidence for a nonzero polarization.

Now, we consider the normalized spin-echo polarization *vs.* τ and temperature. The BG shows significant polarization at small τ [Fig. 7.6a], which requires a

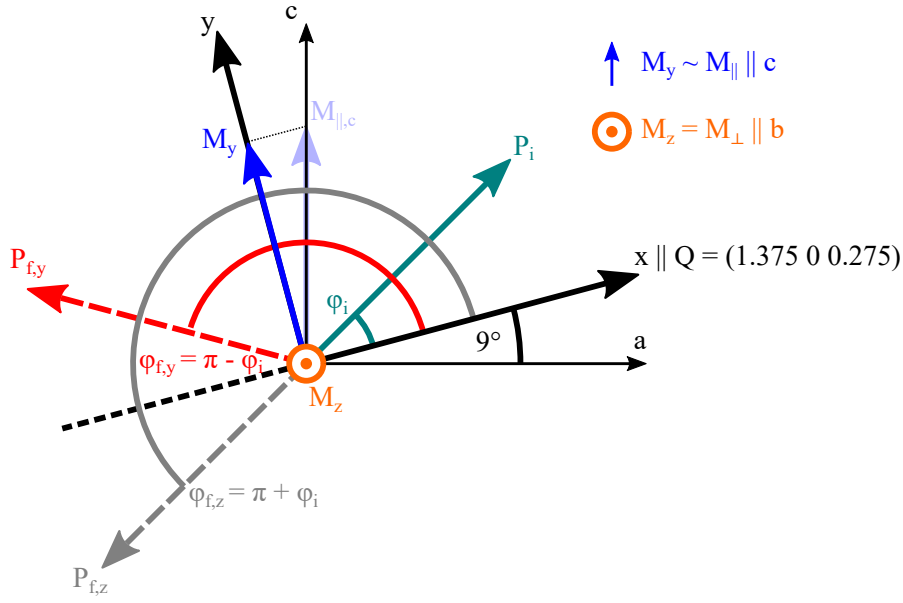


Fig. 7.4: Model of magnetic spin-flip scattering of Fig. 5.9 was adjusted according to the used scattering plane for our CeCu_{5.8}Au_{0.2} sample (H 0 L) such that $Q_{\text{AFM}} = (1.375 \ 0 \ 0.275)$ is parallel to the x -axis. The longitudinal and transverse fluctuations $M_{\parallel,c}$ and $M_{\perp,b}$ correspond to M_y and M_z of the model. Q is almost parallel to the a -axis ($\approx 9^\circ$ tilting) and thus the projection of $M_y \sim M_{\parallel,c}$.

polarized BG subtraction from the data. As we collected our data from different experimental runs, the phase relations between the data and the BG are not known and cannot be reproduced. In consequence, we used for CeCu_{5.8}Au_{0.2} a different BG treatment as for Ca₂RuO₄, where in the latter the BG scans were fitted by Eqn. (5.19) and subtracted from the raw data. Due to the unknown phase relations, such a procedure could artificially generate or extinct polarization. We therefore used a more general approach, where we first determined the BG components contributing to the polarization, which are then fixed in the RTS of the data. For this, we consider the polarization *vs.* τ obtained from the NSE scans at $Q = (1.875 \ 0 \ 0.275)$ in more detail [Fig. 7.6a]. The polarization of the BG shows fast oscillations at small τ signalling interference of different scattering processes. We fitted the BG with the RTS by including the following components: (i) A non-polarized BG ($P = 0$), that reduces the polarization. (ii) A spin-flip component ($\varphi_f = \pi + \varphi_i$) from incoherent scattering. (iii) An elastic non-spin-flip

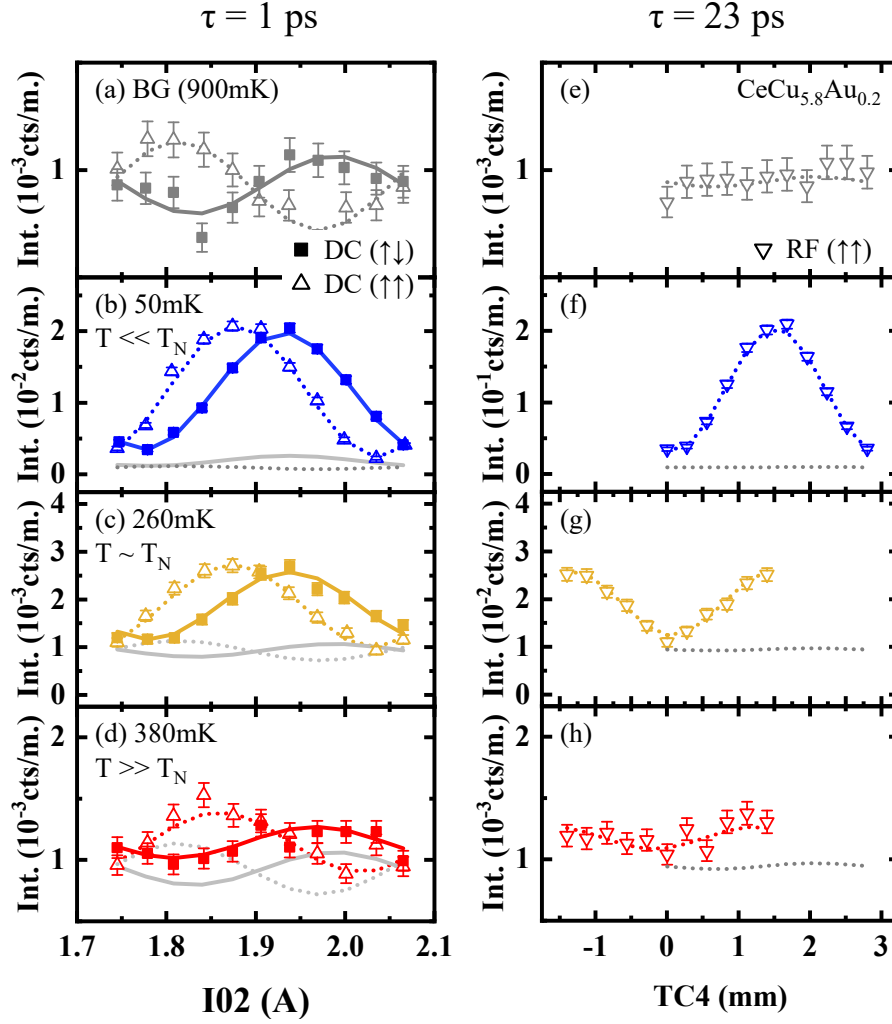


Fig. 7.5: NRSE scans with DC-coils (a-d) and RF-coils (e-h) in parallel and anti-parallel magnetic field configuration for selected temperatures and representative spin-echo times $\tau = 1$ ps and $\tau = 23$ ps, respectively. The polarized BG, measured in distance to the nominal magnetic Bragg-position at $Q = (1.875, 0, 0.275)$ and $T \gg T_N$, is shown in (a+e) and indicated as grey lines in the other panels. The corresponding fits on the data with Eqn. (5.19) including the BG are also drawn (solid and dotted lines).

component ($\varphi_f = \varphi_i$). (iv) A small inelastic magnetic spin-flip component M_y ($\varphi_f = \pi - \varphi_i$) as remainder of the critical scattering. We assign a fixed energy-width $\Gamma \sim 100 \mu\text{eV}$ for the fit of the BG, where the fit is very insensitive to this Γ value. With these components the BG polarization, in particular the fast oscillations, are well described [Fig. 7.6a].

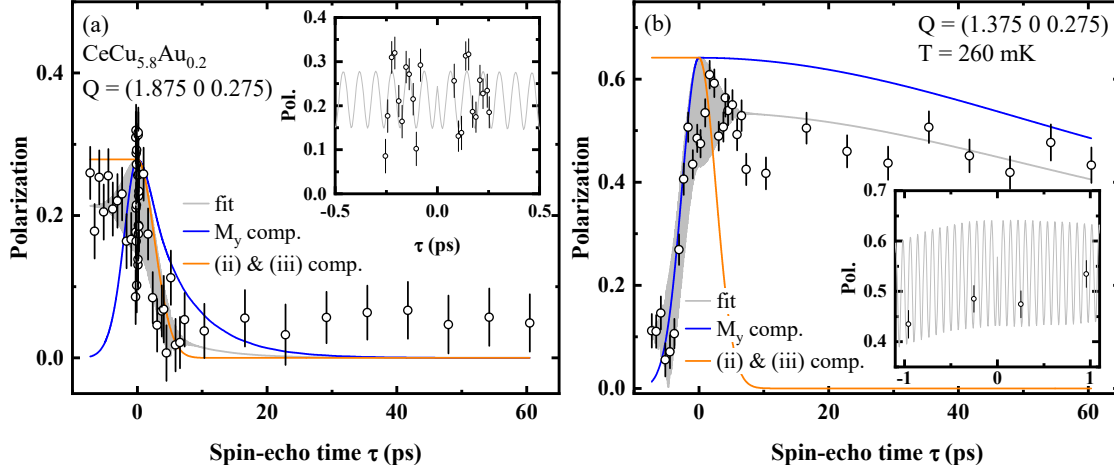


Fig. 7.6: NSE polarization *vs.* τ for (a) the background scans measured at 900 mK and $Q = (1.875 \ 0 \ 0.275)$ and (b) the 260 mK scans measured at $(1.375 \ 0 \ 0.275)$. Both data show fast oscillations of the polarization at small τ due to an interference of different scattering processes, as described in the text, where the orange lines include the components (ii) and (iii). The grey shaded region corresponds to the RTS fit and the blue and orange solid lines are attributed to the pure components as if the other would not be present. (b) The significant polarization at $\tau > 0$ results from in-plane magnetic scattering, whereas no evidence for an additional out-of-plane magnetic scattering for $\tau < 0$ was observed.

Having determined the BG components, we can now discuss the polarization associated with the critical scattering in vicinity of T_N . As exemplarily shown for the 260 mK data [Fig. 7.6b], the critical longitudinal scattering (M_y) reveals significant polarization at $\tau > 0$, whereas no evidence for transverse critical scattering (M_z) was observed at $\tau < 0$. Thus, we performed the RTS with the BG components previously determined [Fig. 7.6a] and an in-plane magnetic component (M_y) with intensity $I_{0,\text{crit}}(T) = I_{0,\text{sig}}(T) - I_{0,\text{BG}}$ and variable energy-width accounting for the critical scattering. An overview of the RTS for selected temperatures is shown

in Fig. 7.7a. Moreover, Figs. Fig. 7.7b-e show a zoom on the small τ region to illustrate the quality of the fits.

The extracted energy-width $\Gamma(T)$ is plotted in Fig. 7.8 on double logarithmic scaling ($T_N = 0.259$ K). The blue points indicate the NSE results from this work, while the green squares correspond to previous TAS measurements by Stockert *et al.* [1]. The NSE data are compatible with the TAS data, but show a better energy-resolution and a higher point-density in the range $T < T_N + 0.25$ K (~ 0.5 K). On heating, $\Gamma(T)$ shows a significant broadening at $T > T_N + 0.02$ K up to $\Gamma = 40$ μeV at $T = T_N + 0.1$ K (~ 0.4 K), which is compatible with a classical PL scaling $\Gamma \propto t^{z\nu}$, as indicated by the red solid line with slope $z\nu = 1.2(1)$. Although we would like to point out that the data are noisy likely due to the limited statistics, this critical exponent is close to the value predicted for the 3D-I model ($z\nu_{3\text{DI}} = 1.26$, [15, 118]), which is expected close to T_N due to the orthorhombic anisotropy and the 3D magnetic ordering. Above 0.4 K, $\Gamma(T)$ consists of a small plateau up to $T = T_N + 1$ K and increases again for higher temperatures broadly consistent with a quantum critical scaling $\propto k_B T$ (black dashed line). In consequence, our results suggest the expected quantum-to-classical crossover in the scaling behavior, which takes place almost exactly at $\Gamma = k_B T$. An additional dimensionality crossover from 3D to 2D scaling, that could be expected from the proposed 2D nature of the critical fluctuations in $\text{CeCu}_{6-x}\text{Au}_x$ (see Chap. 4), was not observed.

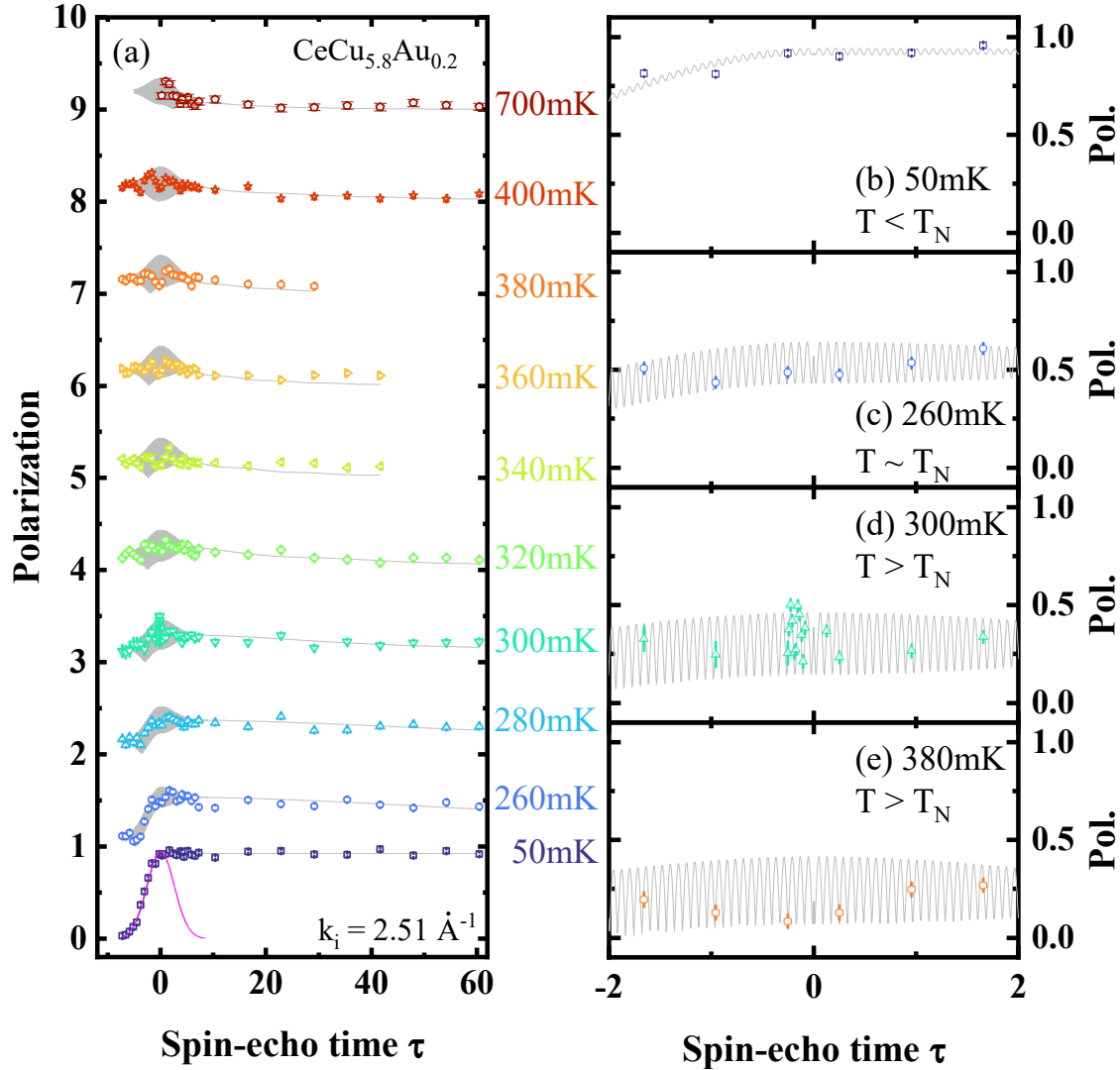


Fig. 7.7: (a) Overview of $P(\tau)$ curves for selected temperatures with corresponding fits from ray-tracing simulations (grey shaded region). The pink solid line indicates the depolarization of an elastic component not fulfilling the echo-condition. For clarity we plotted the curves with a constant offset. (b-e) Shows zooms on the small τ region for selected temperatures.

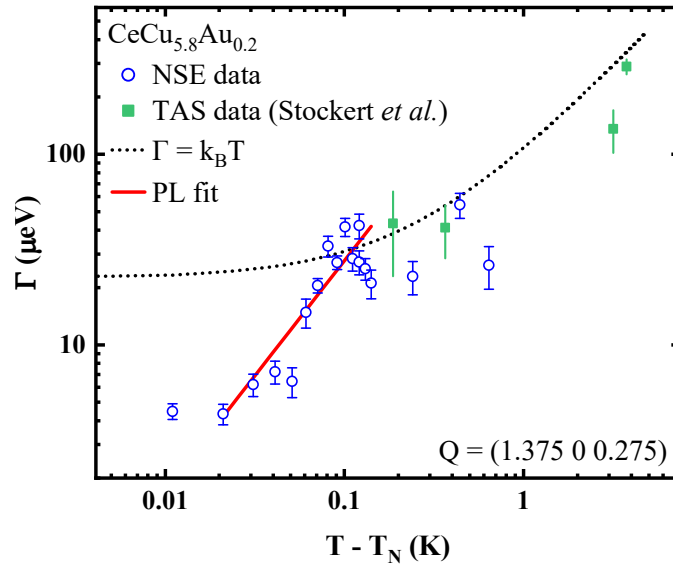


Fig. 7.8: Energy width $\Gamma(T)$ on double logarithmic scaling ($T_N = 0.259$ K). The blue points indicate the NSE results from this work, while the green squares correspond to previous TAS measurements by Stockert *et al.* [1]. Close to T_N , the energy-width can be described by a classical PL scaling $\Gamma \propto t^{z\nu}$, as indicated by the red solid line with slope $z\nu = 1.2(1)$. At higher temperatures ($T > 1$ K), the scaling behavior is broadly consistent with a quantum critical scaling $\propto k_B T$ (black dashed line) signalling a quantum-to-classical scaling crossover at $\Gamma \sim k_B T$.

7.2. CeCu_{5.9}Au_{0.1}

Complementary to the measurements on CeCu_{5.8}Au_{0.2}, we also examined the critically doped compound CeCu_{5.9}Au_{0.1} with $T_N \approx 0$ K on critical scaling behavior by using NSE. The measurements were conducted at TRISP [232, 259] on a high-quality single crystal of CeCu_{5.9}Au_{0.1} (size ≈ 1 cm³), that was similarly grown by the Czochralski-method and previously used in other neutron scattering studies [1, 220, 223]. The lattice parameters are $a = 8.049$, $b = 5.0835$, and $c = 10.11$. For the measurements, the sample was mounted on two small piezo-goniometers to provide an in-situ crystal alignment by neutrons just as for CeCu_{5.8}Au_{0.2} [Fig. 7.9a]. We further installed the sample holder in a closed-cycle dilution cryostat with a sample base temperature of ~ 40 mK. The scattering plane was (H 0 L). The TRISP spectrometer was operated in the configuration $SM = -1$, $SS = -1$, $SA = 1$ at $k_i = 2.51 \text{ \AA}^{-1}$.

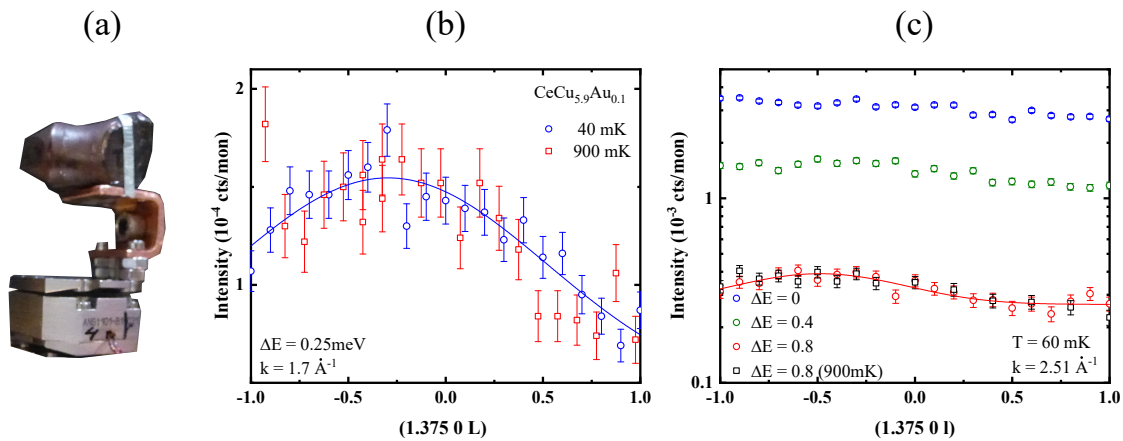


Fig. 7.9: (a) Photography of the CeCu_{5.9}Au_{0.1} single crystal detached on a small piezo-goniometer. (b,c) Display (1.375 0 Q_L) scans at 40 mK and 900 mK for various energy-transfers ΔE . The curves show an enhanced scattering intensity around $Q = (1.375 0 - 0.275)$, *i. e.* at the 3D magnetic Bragg position of CeCu_{5.8}Au_{0.2}. The blue and red solid lines are guides to the eye.

Analogous to previous works on the same crystal [1, 220], we found in Q_L -scans a slightly enhanced scattering intensity [Fig. 7.9b,c] at the 3D magnetic Bragg-position of CeCu_{5.8}Au_{0.2}, *i. e.* on top of the proposed 1D rods [Fig. 4.3a]. For nonzero energy-transfers the peaked structure becomes more prominent as the elastic

BG is more suppressed. Despite these indications for critical scattering, we were not able to separate it from the BG in our NSE measurements at $k_i = 2.51 \text{ \AA}^{-1}$ and with $\Delta E = 0.8 \text{ meV}$. This follows from the absence of a T -dependent depolarization of $P(\tau)$ [Fig. 7.10], which contradicts the previous results obtained from TAS experiments [1]. Potential reasons for this might be that the critical scattering is weak and/or very broad compared to the NSE resolution, or obscured by the BG. We therefore propose for a future NSE experiment rather to take the $\text{CeCu}_{5.8}\text{Au}_{0.2}$ compound, tune it gradually towards quantum criticality by hydrostatic pressure and examine how the critical behavior changes.

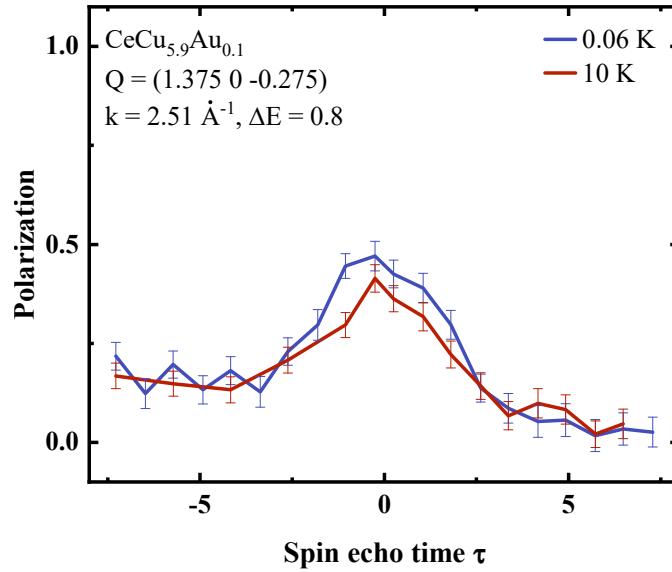


Fig. 7.10: Polarization of raw data vs. τ for $T = 0.06 \text{ K}$ and 10 K . No T -dependent change of the depolarization is observed indicating that the critical scattering cannot be separated from the BG in our experiment.

7.3. Discussion and Conclusion

We investigated the critical behavior of the magnetic fluctuations in the near quantum critical compound $\text{CeCu}_{5.8}\text{Au}_{0.2}$ with high-resolution NSE spectroscopy. From a PL fit on the magnetic $(1.375 \ 0 \ 0.275)$ Bragg-intensity vs. T [Fig. 7.3b] we derived the transition temperature $T_N = 0.259 \text{ K}$ and a critical exponent $\beta =$

0.402(2). The extracted β is between the values predicted for the **3D-H** model ($\beta_{3\text{DH}} = 0.369$) and the **MF**-model ($\beta_{\text{MF}} = 0.5$). The **3D-H** model is at odds with the orthorhombic anisotropy in $\text{CeCu}_{5.8}\text{Au}_{0.2}$, whereas a **MF** value was also reported in previous neutron studies on the same $\text{CeCu}_{5.8}\text{Au}_{0.2}$ crystal [222, 283]. A **MF** value generally indicates the presence of long-ranged couplings [16], which would be in line with the dominant **RKKY** interactions, as similarly proposed for metallic erbium [284]. Alternatively, a continuous change of the β exponent from a **3D-I** value ($\beta_{3\text{DI}} = 0.327$) to the **MF** value was observed in the 3D anisotropic antiferromagnet $\text{MnCl}_2 \cdot 4\text{H}_2\text{O}$ while the systems' **QCP** was approached [128–130]. This was attributed to a dimensionality crossover due to quantum fluctuations ($d_{\text{eff}} = d + z$, [33]). Although the picture of the long-ranged **RKKY** interactions is more consistent for $\text{CeCu}_{5.8}\text{Au}_{0.2}$ located in the classical ordered regime, it would be interesting to examine the temperature scaling of the order parameter for different pressures ($0 < p < p_c$) or Au-dopings ($x_c < x \neq 0.2$). In addition, we derived a critical exponent $\gamma = 0.557(8)$ from the temperature-dependence of the critical amplitudes S_0/T above T_N . This exponent is not related to any universality class.

For the study of the dynamical critical properties, we investigated the temperature scaling of the energy-width $\Gamma(T)$. Taking advantage of the higher energy resolution of **NSE**, we complemented previous **TAS** measurements [1] in close vicinity to T_N . On heating, we find a broadening of the critical scattering in energy that is consistent with a classical **PL** scaling $\Gamma \propto t^{z\nu}$ with $z\nu = 1.2(1)$. The critical exponent contains uncertainties due to the noise in our data. Nevertheless, it is close to the value predicted for the classical **3D-I** model ($z\nu_{3\text{DI}} = 1.26$, [15, 118]), which can be expected for $\text{CeCu}_{5.8}\text{Au}_{0.2}$ close to T_N because of the orthorhombic anisotropy and the 3D magnetic ordering. In combination with the proposed quantum critical scaling at higher temperatures $\Gamma \propto k_B T$ [1], our results indicate the expected quantum-to-classical scaling crossover. The crossover takes place at $\Gamma \sim k_B T$, *i. e.* where the condition $\Gamma > k_B T$ of the quantum critical regime is no longer valid. Although a quantum-to-classical crossover in the scaling behavior of systems close to **QCPs** is predicted by theory [33, 34, 131, 226, 285], there are only a few experimental studies reporting on such a crossover in solid-state systems [128–130, 286–288]. In this respect, our results signal that the $\text{CeCu}_{6-x}\text{Au}_x$ series

is a good platform to investigate the transition from classical to quantum critical behavior. To further establish this scaling crossover, we propose additional cold neutron **TAS** measurements with higher point-density around 0.5 K. By this, we can also address the question whether or not an additional dimensionality crossover from **3D-I** to **2D-I** scaling behavior occurs. Such a crossover was not observed in our **NSE** data but can be expected [226] from the previously proposed 2D nature of the magnetic fluctuations in $\text{CeCu}_{6-x}\text{Au}_x$ [219–224]. Moreover, the capability of **TAS** to measure high-resolution Q -scans would allow us to study the critical scaling of the correlation length and re-examine the temperature-dependence of the critical amplitudes.

In addition to the $\text{CeCu}_{5.8}\text{Au}_{0.2}$ compound, we also investigated the quantum critically doped compound $\text{CeCu}_{5.9}\text{Au}_{0.1}$. Despite an enhanced scattering intensity at the 3D magnetic Bragg-position of $\text{CeCu}_{5.8}\text{Au}_{0.2}$ in agreement with previous **TAS** experiments [1, 220], we did not observe a T -dependent depolarization of $P(\tau)$. This indicates that the critical scattering could not be separated from the BG in our **NSE** measurements. Possible reasons for this are that the critical scattering is relatively weak and/or that the linewidth is broad compared to energy-resolution of **NSE**. We therefore plan in a future experiment to rather put the $\text{CeCu}_{5.8}\text{Au}_{0.2}$ crystal in a pressure cell, gradually tune the system to quantum criticality by a hydrostatic pressure of $p \leq p_c \sim 5$ kbar [121] and examine with **NSE** how the dynamical critical behavior changes *vs.* p .

Appendix A.

1D and 2D spin-flip scattering

In the following, we discuss the spin-flip processes of polarized neutrons in 1D and 2D. Prior to this, we note that a more general expression of Eqns. (5.1) and (5.7) can be obtained by using *Fermi's Golden Rule*, which describes the excitation of a system from a ground state $|i\rangle$ into an excited state $\langle f|$ through an external perturbation. For the transition rate it follows [84]:

$$W_{i \rightarrow f} = \frac{2\pi}{\hbar} |\langle f|V|i\rangle|^2 \rho_f(E) \quad , \quad (\text{A.1})$$

where $\rho_f(E)$ and V denote the density of final scattering states and the interaction potential between the probe and the sample, respectively. For neutron scattering the change of the sample state λ from λ_i to λ_f is accompanied by a change of the neutron states from (\mathbf{k}_i, σ_i) to (\mathbf{k}_f, σ_f) , where $\sigma_{i,f}$ denote the neutron spin-polarization states. From Eqn. (A.1), the so-called master equation can be derived, which generally is the basis of the interpretation of all experimental neutron scattering data [39]:

$$\left(\frac{d^2\sigma}{d\Omega dE} \right)_{k_0 \rightarrow k_1} \propto \sum_{\lambda_i \sigma_i} P_{\lambda_i} P_{\sigma_i} \sum_{\lambda_f \sigma_f} |\langle \mathbf{k}_f \sigma_f \lambda_f | V(\mathbf{r}) | \mathbf{k}_i \sigma_i \lambda_i \rangle|^2 \delta(\hbar\omega + E_{\lambda_i} - E_{\lambda_f}) \quad . \quad (\text{A.2})$$

Equation (A.2) sums over all final states of the sample λ_f and final polarization states σ_f of the neutron, averaged over all initial states of the sample λ_i and initial polarization states σ_i of the neutron, which occur with the probability P_{λ_i} and P_{σ_i} [39]. The delta-function ensures energy conservation. By the assumption of various

interaction potentials $V(\mathbf{r})$, one can describe different scattering processes such as nuclear or magnetic scattering.

Now, by using the magnetic interaction potential $V(\mathbf{r}) = -\boldsymbol{\mu}_n \mathbf{M}_\perp$ [39] and calculating the matrix elements $\langle i|V(\mathbf{r})|f\rangle$, one can address the elastic magnetic SF scattering. As has been shown in [84, 230], for the 1D case this corresponds to $\langle +, -|\boldsymbol{\sigma} \mathbf{M}_\perp|+, -\rangle$, where spin-up $|+\rangle$ and spin-down states $|-\rangle$ of the neutron are defined as the eigenfunctions of σ_z (see Eqn. (5.6))

$$|+\rangle \equiv \begin{pmatrix} 1 \\ 0 \end{pmatrix} \quad |-\rangle \equiv \begin{pmatrix} 0 \\ 1 \end{pmatrix} . \quad (\text{A.3})$$

The matrix elements for the possible NSF and SF scattering channels are

$$\langle +|\boldsymbol{\sigma} \mathbf{M}_\perp|+\rangle = M_{\perp,z} , \quad (\text{A.4})$$

$$\langle -|\boldsymbol{\sigma} \mathbf{M}_\perp|-\rangle = -M_{\perp,z} , \quad (\text{A.5})$$

$$\langle -|\boldsymbol{\sigma} \mathbf{M}_\perp|+\rangle = M_{\perp,x} + iM_{\perp,y} , \quad (\text{A.6})$$

$$\langle +|\boldsymbol{\sigma} \mathbf{M}_\perp|-\rangle = M_{\perp,x} - iM_{\perp,y} . \quad (\text{A.7})$$

From (A.2) it also follows that the scattering cross section of polarized neutrons on magnetic fluctuations is proportional to the square of the above matrix elements.

For NSE spectroscopy (2D-case) the scattering process can be described as the following: We assume an incoming neutron with its spin making an angle of φ_i with the x -axis after the first PD [Fig. 5.9]. Further, we define the coordinate system such that the momentum transfer \mathbf{Q} is along x . Depending on φ_i , the initial spin-state $|\sigma_i\rangle$ (spinor) of the neutron reads [251]

$$|\sigma_i\rangle \equiv |s_i\rangle = \frac{1}{\sqrt{2}} \begin{pmatrix} \exp(-i\varphi_i/2) \\ \exp(i\varphi_i/2) \end{pmatrix} . \quad (\text{A.8})$$

The corresponding expectation value of the initial polarization P_i can be calculated by

$$P_i = \langle \boldsymbol{\sigma} \rangle_i = \begin{pmatrix} \langle s_i | \sigma_x | s_i \rangle \\ \langle s_i | \sigma_y | s_i \rangle \\ \langle s_i | \sigma_z | s_i \rangle \end{pmatrix} = \begin{pmatrix} \cos(\varphi_i) \\ \sin(\varphi_i) \\ 0 \end{pmatrix} . \quad (\text{A.9})$$

In the scattering process, the neutron spin can either interact with $M_{\perp,y}$ or with $M_{\perp,z}$ to reach the corresponding states $|s_{M_{y,z}}\rangle \equiv |s_{M_{y,z}}\rangle$

$$|s_{M_y}\rangle = \sigma_y M_{\perp,y} |s_i\rangle = \frac{M_{\perp,y}}{\sqrt{2}} \begin{pmatrix} -i \exp(i\varphi_i/2) \\ i \exp(-i\varphi_i/2) \end{pmatrix} , \quad (\text{A.10})$$

$$|s_{M_z}\rangle = \sigma_z M_{\perp,z} |s_i\rangle = \frac{M_{\perp,z}}{\sqrt{2}} \begin{pmatrix} \exp(-i\varphi_i/2) \\ -\exp(i\varphi_i/2) \end{pmatrix} . \quad (\text{A.11})$$

The expectation value for the final polarization $P_{M_{y,z}}$ is then

$$P_{f_y} = \langle \boldsymbol{\sigma} \rangle_{M,y} = \begin{pmatrix} \langle s_{M_y} | \sigma_x | s_{M_y} \rangle \\ \langle s_{M_y} | \sigma_y | s_{M_y} \rangle \\ \langle s_{M_y} | \sigma_z | s_{M_y} \rangle \end{pmatrix} = M_{\perp,y}^2 \begin{pmatrix} -\cos(\varphi_i) \\ \sin(\varphi_i) \\ 0 \end{pmatrix} , \quad (\text{A.12})$$

$$P_{f_z} = \langle \boldsymbol{\sigma} \rangle_{M,z} = \begin{pmatrix} \langle s_{M_z} | \sigma_x | s_{M_z} \rangle \\ \langle s_{M_z} | \sigma_y | s_{M_z} \rangle \\ \langle s_{M_z} | \sigma_z | s_{M_z} \rangle \end{pmatrix} = M_{\perp,z}^2 \begin{pmatrix} -\cos(\varphi_i) \\ -\sin(\varphi_i) \\ 0 \end{pmatrix} . \quad (\text{A.13})$$

Thus, the SF scattering on in-plane ($M_{\perp,y}$) and out-of-plane fluctuations ($M_{\perp,z}$) affect the following change of the precession angles $\varphi_{f_{y,z}}$

$$\varphi_{f_y} = \pi - \varphi_i \quad , \quad (\text{A.14})$$

$$\varphi_{f_z} = \pi + \varphi_i \quad . \quad (\text{A.15})$$

Deutsche Zusammenfassung

Kritische magnetische Fluktuationen in stark korrelierten Elektronensystemen

Aufgrund konkurrierender Energieskalen intra- und interionischer Wechselwirkungen, zeigen stark korrelierte Elektronensysteme oft eine Fülle von physikalischen Grundzuständen. Neben den umfassend untersuchten $3d$ -Elektronen Übergangsmetalloxiden (*Transition Metal Oxides (TMO)*) [2], haben in den letzten Jahren auch TMO der benachbarten $4d$ und $5d$ Perioden viel Aufmerksamkeit auf sich gezogen [3]. Insbesondere die Gruppe der geschichteten Ruthenate ($4d$ TMO) hat durch die Entdeckung der unkonventionellen Supraleitung in Sr_2RuO_4 [4] breites Interesse geweckt. Dabei stellte sich heraus, dass die Ruthenate ein komplexes Phasendiagramm und Spinanregungen aufweisen [5–7], was eine Untersuchung der kritischen magnetischen Fluktuationen in der Nähe der Phasenübergänge motiviert. Solche Fluktuationen sind mit dem Grundzustand des Systems gekoppelt und können daher wichtige Informationen liefern. Neben den TMO, zählen auch die schweren Fermionensysteme zu stark korrelierten Elektronensystemen. Hierbei ist häufig der magnetische Grundzustand durch konkurrierende Wechselwirkungen unterdrückt, was zur Ausbildung eines quantenkritischen Punkts (*quantum critical point (QCP)*) führt. In der Nähe eines QCP können exotische Phasen wie *z. B.* Supraleitung auftreten [8–11], weshalb die Untersuchung der kritischen Fluktuationen in diesen Systemen ebenfalls von großem Interesse ist.

Eine der ersten Studien zu kritischen Phänomenen bezog sich auf den Übergang zwischen der flüssigen und gasförmigen Phase von Kohlenstoffdioxid [12]. Hierbei konnte durch das Aufkommen von Dichtefluktuationen nahe des kritischen Punktes bei \tilde{T}_c eine verstärkte Lichtstreuung (kritische Opaleszenz) beobachtet werden

sobald die Korrelationslänge der Dichtefluktuationen mit der Wellenlänge des sichtbaren Lichts übereinstimmte.

Bei magnetischen Übergängen sind das Analogon der Dichtefluktuationen die Fluktuationen des magnetischen Ordnungsparameters, deren Korrelationslänge ξ und Relaxationszeit τ bei Annäherung an \tilde{T}_c (Curie- oder Néel-Temperatur) divergieren [13–16]. Weitere fundamentale physikalische Größen des Materials wie *z. B.* die magnetische Suszeptibilität und die Wärmekapazität zeigen auch ein kritisches Verhalten in der Nähe von \tilde{T}_c , welches oftmals durch ein Potenzgesetz $\propto |t|^\lambda$ mit den kritischen Exponenten λ und $t \equiv (T/\tilde{T}_c - 1)$ [14–18] beschrieben werden kann. Dabei sind die Skalierungsverhalten der statischen und dynamischen Eigenschaften eines Systems über das dynamische Skalierungsgesetz $\Gamma \propto \kappa^z \propto t^{z\nu}$ [15] miteinander verknüpft, wobei ν und z die kritischen Exponenten der inversen Korrelationslänge $\kappa = \xi^{-1}$ und der charakteristischen Energie der Fluktuationen $\Gamma \propto \tau^{-1}$ bezeichnen. Ein weiterer wichtiger Bestandteil der Skalentheorie ist das Konzept der Universalität [16, 19, 20], welches besagt, dass die kritischen Exponenten zwar unabhängig von mikroskopischen Details sind, jedoch universell von der Dimension des Ordnungsparameters bzw. des Systems, sowie der Reichweite der Wechselwirkungen abhängen. Dadurch können auch komplexe Systeme anhand der kritischen Exponenten einer Universalitätsklasse zugeordnet und vorhandene Anisotropien durch Veränderungen im Skalierungsverhalten aufgedeckt werden [16]. In diesem Zusammenhang weckte vor allem das zweidimensionale XY (2D-XY)-Modell breites wissenschaftliche Interesse, da es als Ausgangspunkt für die Beschreibung des von Berezinskii, Kosterlitz, and Thouless (BKT) [21–23] postulierten topologischen BKT-Phasenübergangs diente. Der BKT-Phasenübergang beschreibt die Bildung von magnetischen Wirbelpaaren unterhalb einer Temperatur T_{KT} , welche oberhalb von T_{KT} aufbrechen. In diesem Fall wurde für die Temperaturabhängigkeit der Korrelationslänge zwischen den Wirbelpaaren ein exponentielles Verhalten $\xi \propto \exp(b/\sqrt{t_{KT}})$ mit dem nicht-universellem Parameter b und $t_{KT} \equiv (T/T_{KT} - 1)$ postuliert. Übereinstimmungen mit den abgeleiteten Eigenschaften des BKT-Phasenübergangs konnten in superfluiden ^4He -Dünnschichten [24, 25] und *proximity-coupled Josephson junction arrays* [26, 27] beobachtet werden. Bisher sind jedoch Realisierungen des 2D-XY-Modells in Festkörpersystemen selten [28–32].

Neben den klassischen Phasenübergängen zweiter Ordnung bei endlichen Temperaturen, können auch Phasenübergänge bei $T = 0$ auftreten [33–36]. Die sogenannten Quantenphasenübergänge (*quantum phase transition* (QPT)) werden dann durch nicht-thermische *tuning-parameter* kontrolliert und von Quantenfluktuationen begleitet. In Analogie zum kritischen Punkt in klassischen Phasenübergängen, findet der QPT am quantenkritischen Punkt (QCP) statt. Dieser kann zwar experimentell nicht erreicht werden, aber seine Präsenz bei $T = 0$ kann das kritische Verhalten des Systems bei endlichen Temperaturen beeinflussen und so das Auftreten neuer physikalischer Phasen wie Supraleitung fördern [8, 9, 11, 37]. Damit ist die Untersuchung des kritischen Verhaltens von magnetischen Fluktuationen in der Nähe eines QCP von großer Bedeutung [10].

Prädestiniert für die experimentelle Untersuchung von kritischen magnetischen Phänomenen ist Neutronen Dreiachsen-Spektroskopie (*Triple-Axis Spectroscopy* (TAS)), welche eine direkte Messungen der dynamischen Streufunktion $S(\mathbf{Q}, \omega)$ ermöglicht. Diese beinhaltet κ and Γ [38–40], wobei Γ aus TAS Energie-Scans der kritischen magnetischen Streuung abgeleitet werden kann und κ der energieintegrierten Q -Breite im Impulsraum entspricht. Wegweisende Arbeiten in diesem Zusammenhang waren die Studien der kritischen magnetischen Fluktuationen in klassischen magnetischen Systemen wie dem 3D FM EuO [41–43] und dem 3D AFM RbMnF₃ [44, 45]. Im späteren Verlauf wurden auch TAS-Studien an Systemen mit quasi-2D magnetischen Wechselwirkungen durchgeführt, wie *z. B.* den isotropen (*square lattice*) AFM Rb₂MnF₄ [46], Sr₂CuO₂Cl₂, and Sr₂Cu₃O₄Cl₂ [47], sowie am AFM Ausgangsmaterial der Kupratsupraleiter [48], welche ein 2D-H-Skalierungsverhalten oberhalb ihrer Néel-Temperaturen zeigen. Ergänzend zu den TAS Experimenten, konnte die Neutronen Spin Echo (NSE) Spektroskopie [49–52] mit besserer Energieauflösung beispielsweise dazu beitragen Unstimmigkeiten im Skalierungsverhalten von schweren Fermionen Supraleitern aufzulösen [53] und einen Übergang von Heisenberg zur Ising Skalierung aufgrund von uniaxialer Anisotropie im klassischen 3D AFM MnF₂ nahe T_N aufzudecken [54].

Darüberhinaus wurden erste Studien zu den kritischen magnetischen Fluktuationen in $5d$ -Elektronen TMO mit Hilfe von Röntgenstreuung durchgeführt. Dabei wurde für das einfach geschichtete AFM Sr₂IrO₄, welches starke Spin-Bahn-Kopplung aufweist [55, 56], von einer 2D-H-Skalierung mit schwacher *easy-plane* Anisotropy

berichtet [57, 58]. Im Gegensatz dazu zeigt das Doppelschicht-System $\text{Sr}_3\text{Ir}_2\text{O}_7$ ein Skalierungsverhalten, welches unter der Berücksichtigung von kristallographischer Unordnung im System konsistent mit der 3D-I-Universalitätsklasse ist [59].

Das kritische Verhalten in den $4d$ -Elektronen TMO wurden bisher noch nicht untersucht. Diesbezüglich sind besonders die geschichteten Ruthenate interessant, da sie eine Fülle an elektronischen Grundzuständen zeigen [3, 60–63], wie zum Beispiel unkonventionelle Supraleitung in Sr_2RuO_4 [4] und exzitonische AFM Ordnung im Mott-Isolator Ca_2RuO_4 [64, 65]. Dies lässt sich auf die ähnlichen Energieskalen von Spin-Bahn-Kopplung, Kristallfeldaufspaltung, Hundscher Kopplung und interatomaren Austauschwechselwirkungen in $4d$ -Elektronen TMO zurückführen.

Im einfach geschichteten Ca_2RuO_4 , mit einer Néel-Temperatur von $T_N \sim 110\text{K}$ [66–68], sind die magnetischen Momente AFM entlang der b -Achse in quadratischen RuO_2 -Ebenen angeordnet und nach dem G -Typ Schema entlang der c -Achse gestapelt. Der exzitonische Charakter des Magnetismus soll von exzitonischen Übergängen zwischen nicht-magnetischen Singluett ($J_{\text{eff}}=0$) und magnetischen Triplet Zuständen ($J_{\text{eff}}=1$) resultieren [64, 65]. Dieses physikalische Bild wurde kürzlich durch die Detektion einer Soft-Amplituden-Mode im Spinwellenspektrum durch resonante inelastische Röntgenstreuung (RIXS) [69], Raman-Streuung [70], sowie inelastische Neutronenstreuung (INS) [6] bestätigt.

Darüberhinaus führt der nicht-unterdrückte Bahndrehimpuls der magnetischen Ru-Momente in Ca_2RuO_4 zu einem ungewöhnlichen Spektrum der transversalen Spinwellen im AFM Zustand [6]. Die aus der Analyse dieses Spektrums abgeleitete magnetische Hamilton-Funktion wird von einer XY *single-ion* Anisotropie dominiert, die viel größer ist als die Austauschwechselwirkung zwischen den nächsten Nachbarn, sowie von einer Ising *single-ion* Anisotropie, die auf eine orthorhombische Verzerrung der Kristallstruktur zurückzuführen ist. Gleichzeitig zeigten die INS-Experimente keine Dispersion der Magnonen senkrecht zu den RuO_2 -Schichten, was bedeutet, dass die Wechselwirkungen zwischen den Schichten viel schwächer sind als die Wechselwirkungen innerhalb der Schichten. Die Bestätigung einer Quasi-2D-XY Symmetrie der magnetischen Hamilton-Funktion, die aus der Analyse der Magnonendispersionen abgeleitet wurde, hat unter Anderem diese Arbeit motiviert.

Im Gegensatz zum Mott-Isolator Ca_2RuO_4 , ist das Doppelschichtsystem $\text{Ca}_3\text{Ru}_2\text{O}_7$ im paramagnetischen Zustand metallisch und behält unterhalb der Néel Tempe-

ratur $T_{N,1} \sim 56$ K eine signifikante elektrische Leitfähigkeit [71]. Die magnetische Struktur kann dem *A*-Typ AFM zugeordnet werden, *d. h.* FM Doppelschichten mit den magnetischen Momenten orientiert entlang der *a*-Achse sind alternierend gestapelt entlang der *c*-Achse [71, 72]. Bei einem zweiten magnetischen Übergang bei $T_{N,2} \sim 48$ K kommt es zu einer Umorientierung der Spins von der *a*- zur *b*-Achse in den RuO₂-Ebenen [73] und einer stärkeren Abnahme der elektrischen Leitfähigkeit [71]. Da die Kristallstruktur von Ca₃Ru₂O₇ aus zwei eng benachbarten RuO₂-Schichten innerhalb einer Einheitszelle besteht, existieren erhebliche Wechselwirkungen zwischen den Schichten innerhalb einer Doppelschicht-Einheit wie durch INS-Studien der Magnonendispersionen nachgewiesen wurde [7, 74]. Die Austauschwechselwirkungen zwischen den jeweiligen Doppelschicht-Einheiten sind dagegen schwach, weshalb die Dimensionalität des Austauschbindungsnetzwerks zwischen 2D und 3D liegt. Obwohl die INS-Daten auch eine Anregungslücke aufgrund der Anisotropie zeigten, reichten sie nicht aus, um die Art der vorherrschenden Anisotropie zu bestimmen (Ising oder XY). Es wurde zudem festgestellt, dass die Dotierung mit einer kleinen Menge an nicht-magnetischen Ti-Ionen im Doppelschicht-System Ca₃(Ru_{1-x}Ti_x)₂O₇ ausreichend ist, um den AFM *A*-Typ Zustand wieder in den *G*-Typ Zustand von Ca₂RuO₄ zu invertieren [75–78]. Der zweistufige Übergang in Ca₃Ru₂O₇ wird dann zu einem scharfen einstufigen Übergang erster Ordnung.

In dieser Arbeit benutzen wir TAS- und NSE-Spektroskopie zur Untersuchung der kritischen Streuung in Ca₂RuO₄, Ca₃Ru₂O₇ sowie Ca₃(Ru_{0.99}Ti_{0.01})₂O₇ in der Nähe und oberhalb von T_N . Wir bestimmen dabei statische und dynamische Exponenten und ordnen sie den Universalitätsklassen zu, um die Dimension des Ordnungsparameters sowie mögliche Anisotropien zu erhalten. Diese Ergebnisse vergleichen wir dann mit den Hamiltonoperatoren, die durch frühere INS- und RIXS-Experimente unterhalb von T_N abgeleitet wurden. Aus der Temperaturabhängigkeit der AFM (1 0 0) Bragg-Intensität [Fig. Ia] erhalten wir für Ca₂RuO₄ mit dem Potenzgesetz (rote Linie) $I \propto M^2 \propto |t|^{2\beta}$, welches zusätzlich mit einer intrinsischen Gaussverteilung an Néel-Temperaturen T_N mit einer Vollwertbreite von 4.84(1) K (graue Schattierung) gefaltet wurde, die Parameter $\beta = 0.158(6)$ und $T_N = 112.20(1)$ K. Die weiteren statischen kritischen Eigenschaften werden aus der *Q*-Breite (inverse Korrelationslänge κ) und der Amplitude (magnetische Suszeptibilität χ) der diffusen magnetischen Streuung bei (1 0 0.83) oberhalb

von T_N abgeleitet [Fig. Ib,c]. Der dynamisch kritische Exponent z wird aus der Temperaturabhängigkeit der Energiebreite der diffusen magnetischen Streuung bei $(1\ 0\ 0)$ bestimmt [Fig. Id]. Die Skalierungen der statischen kritischen Eigenschaften können gut durch das **2D-XY**-Modell beschrieben werden mit den Parametern $T_{KT} = 87(2)\text{K}$ und $b = 1.9$. Die dynamische Skalierung zeigt zwar Abweichungen vom theoretisch vorhergesagtem **2D-XY**-Verhalten [117], jedoch ist es verglichen mit den anderen Modellen das Geeignetste. Obwohl, das dynamische Verhalten von Ca_2RuO_4 sowohl durch **TAS**- als auch **NSE**-Messungen bestätigt wurde, wäre eine alternative Bestimmung von z durch die q -Abhängigkeit der Energiebreite über $\Gamma(T_N, q) \propto q^z$ wünschenswert. Desweiteren bieten Experimente mit Kryoelektronenmikroskopie [277] einen vielversprechenden Zugang zur Untersuchung magnetischer Wirbelstrukturen.

Für $\text{Ca}_3\text{Ru}_2\text{O}_7$ mit starker Kopplung zwischen den Doppelschichten bestimmen wir β aus Temperaturabhängigkeit der **AFM** $(0\ 0\ 1)$ Bragg-Intensität unterhalb von T_N [Fig. IIa], während ν , γ und z wiederum von der Q -Breite, Amplitude und Energiebreite der diffusen Streuung bei $(0\ 0\ 1)$ oberhalb von T_N abgeleitet werden Fig. IIb,c]. Die Skalierung des Ordnungsparameters $\beta = 0.230(6)$ stimmt zwar mit dem prognostizierten Wert des **2D-XY**-Modells überein [91, 274], jedoch werden die übrigen Skalierungsverhalten besser durch das **3D-I**-Modell eingefangen. Diese Zweideutigkeit spiegelt vermutlich die Geometrie der Austauschbindungen in der Doppelschichtstruktur von $\text{Ca}_3\text{Ru}_2\text{O}_7$ wider, die zwischen 2D und 3D liegt. Die theoretische Beschreibung der daraus resultierenden Crossover-Phänomene und ein detaillierter Vergleich mit den experimentellen Daten sind wichtige Aufgaben für die künftige Forschung. Für das 1% Ti-dotierte Doppelschichtsystem $\text{Ca}_3(\text{Ru}_{0.99}\text{Ti}_{0.01})_2\text{O}_7$ mit G -Typ **AFM** Grundzustand beobachten wir, dass der magnetische Übergang von erster Ordnung ist und daher die kritischen Fluktuationen unterdrückt sind.

Zusammenfassend veranschaulichen unsere Ergebnisse, dass die geschichteten Ruthenate vielversprechende Festkörperplattformen für die Erforschung des **2D-XY**-Modells und der Auswirkungen von 3D-Wechselwirkungen und zusätzlichen Spin-Raum-Anisotropien auf die magnetischen Fluktuationen sind. Damit konnten wir zeigen, dass der **2D-XY AFM** auf einem quadratischen Gitter realisiert werden kann. In Verbindung mit Sr_2IrO_4 , was einen nahezu idealen **2D-H AFM** [57, 58] abgibt,

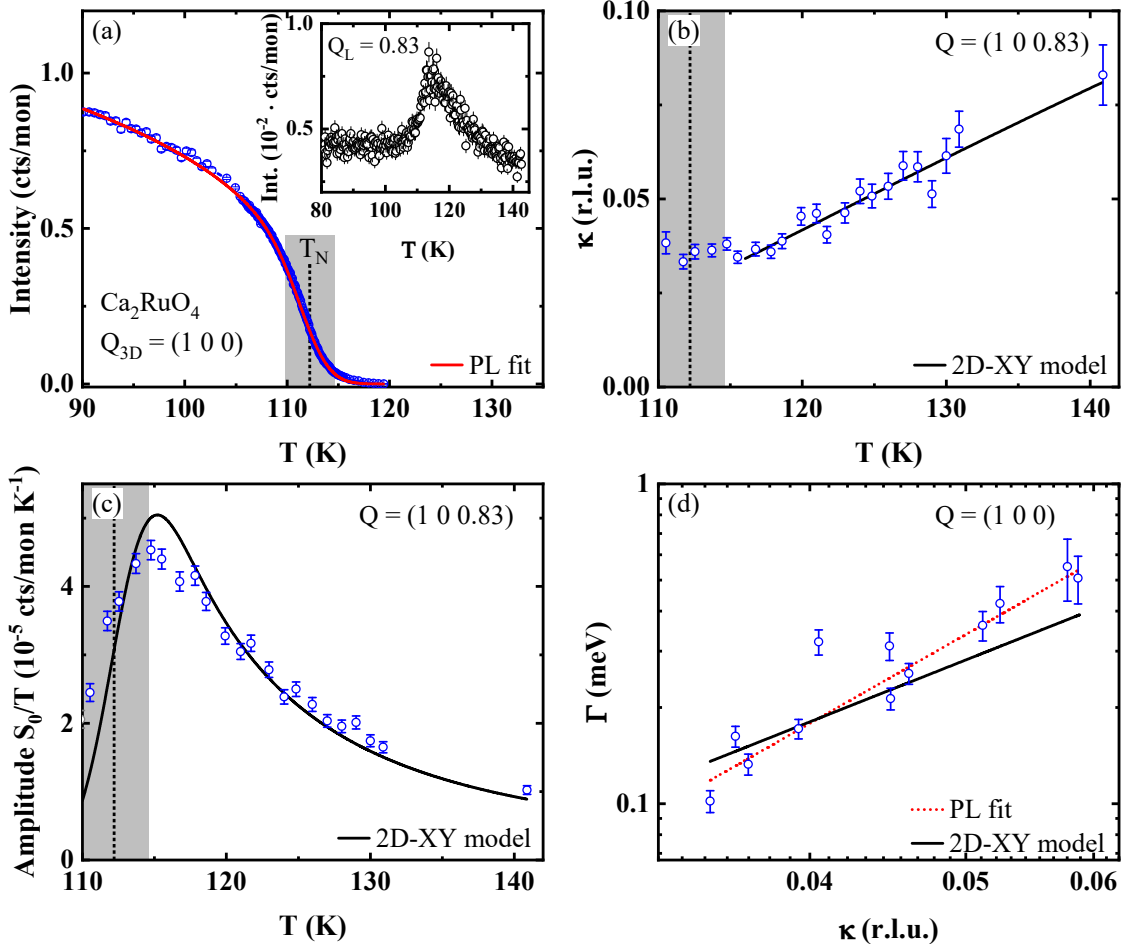


Fig. I: Ergebnisse der kritischen Streuung in Ca_2RuO_4 . (a) Temperaturabhängigkeit der Intensität des magnetischen $(1\ 0\ 0)$ Bragg-Peaks. Die durchgezogene rote Linie beschreibt einen Fit mit dem Potenzgesetz $I \propto M^2 \propto |t|^{2\beta}$, welches zusätzlich mit einer Gaussverteilung an T_N (graue Schattierung entspricht Vollwertsbreite) gefaltet wurde. Das Inset zeigt die gemessene Intensität bei $Q = (1\ 0\ 0.83)$. Der Anstieg der Intensität in der Nähe von T_N resultiert von der Streuung an kritischen magnetischen Fluktuationen. (b) Inverse Korrelationslänge $\kappa(T)$. Die durchgezogene schwarze Linie beschreibt einen 2D-XY-Fit. Die konstante Q -Breite bei $\kappa \sim 0.035$ r.l.u. für $T \leq 116$ K wird dem Aufkommen von 3D-Wechselwirkungen in der Nähe von T_N zugeschrieben. (c) Peak-Amplitude der kritischen Streuung $\chi \propto S_0(T)/T$. (d) Energiebreite der magnetischen Fluktuationen Γ aufgetragen gegen die inverse Korrelationslänge κ in einem doppelt-logarithmischen Plot ($\Gamma \propto \kappa^z$). Zum Vergleich ist eine Skalierung passend zum 2D-XY-Modell gezeigt mit $z_{XY} = 2.0$ [117] (schwarze Linie).

veranschaulicht diese Arbeit das Potenzial der $4d$ - und $5d$ -Elektronensystemen mit stark *spin-orbit entangled* magnetischen Momenten als Plattform für die Grundlagenforschung zum Quantenmagnetismus.

Ergänzend zu den geschichteten Ruthenaten, haben wir ebenfalls das Verhalten von kritischen magnetischen Fluktuationen in der Nähe eines QCP studiert. Besonders geeignet für die Untersuchung von QCPs ist die Gruppe der schweren-Fermionensysteme aufgrund der Konkurrenz zwischen Kondo-Abschirmung und den RKKY-Wechselwirkungen. In diesem Zusammenhang weckte die $\text{CeCu}_{6-x}\text{Au}_x$ Reihe mit einer quantenkritischen Dotierung von $x_c \simeq 0.1$ ($T_N \rightarrow 0$) und der Möglichkeit ausreichend große Kristalle für Neutronenstreuexperimente herzustellen breites wissenschaftliches Interesse. In Bezug auf das dynamisch kritische Verhalten wurde dabei für das undotierte ($x = 0$), das quantenkritische ($x = 0.1$) und das nahe-quantenkritische ($x = 0.2$) System eine Temperaturabhängigkeit der charakteristischen Energie Γ beobachtet, die bei höheren Temperaturen kompatibel mit einem quantenkritischen Verhalten ist ($\Gamma \propto k_B T$). Für $\text{CeCu}_{5.8}\text{Au}_{0.2}$ mit 3D AFM Ordnung unterhalb von $T_N \sim 0.25$ K, würde man jedoch einen Übergang zu einem klassischen Skalierungsverhalten nahe T_N erwarten [33]. Ein solcher Übergang konnte bisher möglicherweise aufgrund der begrenzten Energieauflösung des TAS Spektrometers nicht beobachtet werden.

Wir haben deshalb hochauflösende NSE-Messungen an $\text{CeCu}_{5.8}\text{Au}_{0.2}$ durchgeführt um das dynamisch kritische Verhalten nahe von T_N zu untersuchen und einen möglichen quanten-klassischen Übergang aufzudecken. Wie in Fig. IIIb gezeigt, vervollständigen unsere NSE-Messungen (blaue Punkte) dabei frühere TAS-Ergebnisse (grüne Quadrate) von Stockert *et al.* [1] im Bereich $T_N < T < 1$ K. Während unsere Daten bis etwa 0.5 K durch ein klassisches Skalierungsverhalten mit 3D Charakter beschrieben werden können, können die TAS-Daten bei höheren Temperaturen durch eine quanten-kritische Skalierung angenähert werden. Dadurch deuten unsere Ergebnisse einen erwarteten Übergang von quanten- zu klassisch-kritischer Skalierung an. Um diesen Übergang weiter zu charakterisieren, sind zusätzliche TAS-Messungen mit kalten Neutronen und erhöhter Punktdichte um $T = 1$ K geplant. Mit solchen TAS-Messungen könnte möglicherweise ein zusätzlicher Übergang in der Dimensionalität von 3D zu 2D Verhalten aufgedeckt werden, welcher aufgrund des postulierten 2D Charakters der kritischen Fluktuationen in $\text{CeCu}_{6-x}\text{Au}_x$

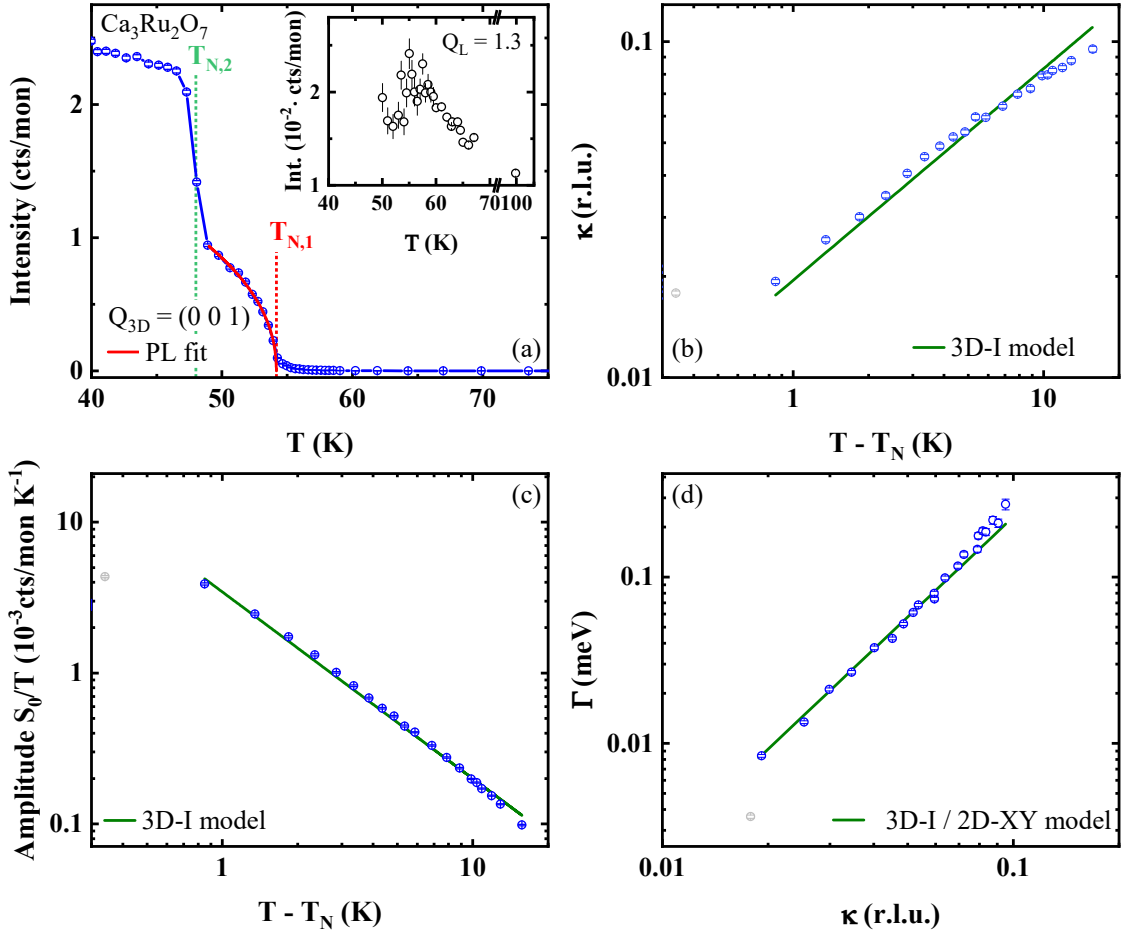


Fig. II: Ergebnisse der kritischen Streuung in $\text{Ca}_3\text{Ru}_2\text{O}_7$. (a) Temperaturabhängigkeit der Intensität des magnetischen $(0\ 0\ 1)$ Bragg-Peaks. Die durchgezogene rote Linie beschreibt einen Fit mit dem Potenzgesetz (*power law* (PL)) $I \propto M^2 \propto |t|^{2\beta}$ mit $\beta = 0.230(6)$ und $T_{N,1} = 54.16(2)$ K. Der kritische Exponent ist in guter Übereinstimmung mit dem 2D-XY Wert. Die zweite übergangstemperatur $T_{N,2}$ indiziert den strukturellen Übergang erster Ordnung. Das Inset zeigt die gemessene Intensität bei $Q = (0\ 0\ 1.3)$. Der Anstieg der Intensität in der Nähe von T_N resultiert von der Streuung an kritischen magnetischen Fluktuationen. (b-d) Zeigen doppelt-logarithmische Plots der (b) inverse Korrelationslänge $\kappa(T)$, (c) der kritischen Amplitude $S_0(T)/T$ und (d) der Energiebreite Γ der kritischen Fluktuationen. Die Skalierungsverhalten sind konsistent mit dem 3D-I Modell (durchgezogene grüne Linie). Die grauen Datenpunkte wurden in den Fits nicht berücksichtigt.

zu erwarten wäre. Desweiteren haben wir die statisch kritischen Exponenten β und γ des magnetischen Ordnungsparameters unterhalb von T_N sowie der kritischen Amplitude oberhalb von T_N aus der Temperaturabhängigkeit des magnetischen (1.375 0 0.275) Bragg-Peaks bzw. der diffusen Streuung bestimmt [Fig. IIIa]. Der resultierende kritische Exponent β befindet sich in der Nähe des 'mean-field' Wertes, was auf den Einfluss der langreichweitigen RKKY-Wechselwirkungen zurückgeführt wird [16, 284]. Die Temperaturabhängigkeit der kritischen Amplitude folgt einem nicht-universellem Verhalten, was durch zusätzliche TAS-Messungen (Q -Scans) bestätigt werden könnte. In Ergänzung zu den Messungen an $\text{CeCu}_{5.8}\text{Au}_{0.2}$, haben wir auch das quantenkritische System $\text{CeCu}_{5.9}\text{Au}_{0.1}$ mit NSE untersucht. Hierbei wurde jedoch im Gegensatz zu früheren TAS-Experimenten [1] kein kritisches Verhalten beobachtet. Dies kann damit erklärt werden, dass die kritische Streuung in $\text{CeCu}_{5.9}\text{Au}_{0.1}$ entweder schwach oder besonders breit in der Energie ist. Aus diesem Grund soll in einem zukünftigen Experiment die Veränderung des Skalierungsverhaltens von $\text{CeCu}_{5.8}\text{Au}_{0.2}$ bei Annäherung an den QCP untersucht werden. Praktisch kann das *z. B.* durch die Verwendung einer Druckzelle umgesetzt werden.

Insgesamt tragen die Ergebnisse der Arbeit zum besseren Verständnis des kritischen Verhaltens in stark korrelierten Elektronensystemen bei.

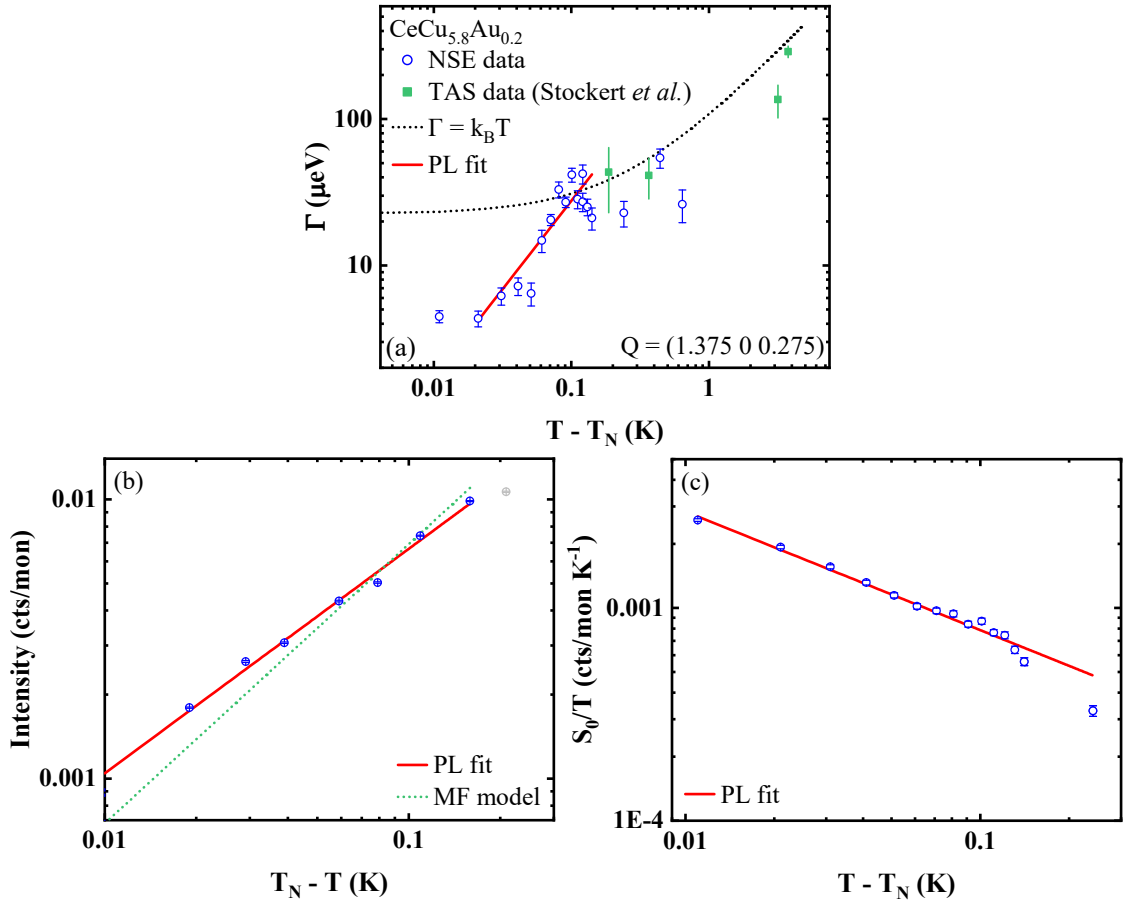


Fig. III: Ergebnisse der kritischen Streuung in $\text{CeCu}_{5.8}\text{Au}_{0.2}$. Temperaturabhängigkeit der (a) Energiebreite, (b) des Ordnungsparameters und (c) der kritischen Amplitude der kritischen magnetischen Fluktuationen in doppelt-logarithmischer Auftragung. (a) Die NSE-Messungen dieser Arbeit (blaue Punkte) vervollständigen die Ergebnisse aus früheren TAS-Studien (grüne Quadrate) von Stockert *et al.* [1] nahe T_N . Das Skalierungsverhalten (rote Linie) kann durch ein klassisches Potenzgesetz (*power law* (PL)) $\Gamma \propto t^{z\nu}$ mit kritischem Exponenten $z\nu = 1.2(1)$ beschrieben werden. Bei höheren Temperaturen sind die TAS-Daten dagegen mit einem quantenkritischen Skalierungsverhalten kompatibel (gepunktete schwarze Linie). (b) Die rote Linie beschreibt einen PL Fit $I \propto M^2 \propto |t|^{2\beta}$ mit dem kritischen Exponenten $\beta = 0.402(2)$ und $T_N = 0.259$ K. Dieser Exponent ist nahe des MF Wertes, wie durch die gepunktete grüne Linie angedeutet ist. (c) Das Skalierungsverhalten der kritischen Amplitude kann durch einen PL fit $S_0/T \propto t^{-\gamma}$ mit einem nicht-universellem $\gamma = 0.557(8)$ beschrieben werden. Die grauen Punkte wurden nicht im Fit berücksichtigt.

Bibliography

- [1] O. Stockert, H. von Löhneysen, W. Schmidt, M. Enderle, and M. Loewenhaupt, Quantum Criticality and Scaling of the Magnetic Response in $\text{CeCu}_{6-x}\text{Au}_x$. *J. Low. Temp. Phys.* **161** (2010), 55–66.
- [2] S. Maekawa, T. Tohyama, S. E. Barnes, S. Ishihara, W. Koshibae, and G. Khaliullin, Physics of Transition Metal Oxides, vol. 144 of Springer Series in Solid-State Sciences, Springer, Berlin and Heidelberg. (2004).
- [3] G. Cao and L. de Long, editors, Frontiers of 4d- and 5d-Transition Metal Oxides, World Scientific Publishing Company, Singapore. (2013).
- [4] Y. Maeno, H. Hashimoto, K. Yoshida, S. Nishizaki, T. Fujita, J. G. Bednorz, and F. Lichtenberg, Superconductivity in a layered perovskite without copper. *Nat.* **372** (1994), 532–534.
- [5] G. Cao, C. Alexander, S. McCall, J. Crow, and R. Guertin, From antiferromagnetic insulator to ferromagnetic metal: a brief review of the layered ruthenates. *Mater. Sci. Eng. B: Solid-State Mater. Adv. Technol.* **63** (1999), 76–82.
- [6] A. Jain, M. Krautloher, J. Porras, G. H. Ryu, D. P. Chen, D. L. Abernathy, J. T. Park, A. Ivanov, J. Chaloupka, G. Khaliullin, B. Keimer, and B. J. Kim, Higgs mode and its decay in a two-dimensional antiferromagnet: and supplementary informations. *Nat. Phys.* **13** (2017), 633–637.
- [7] J. Bertinshaw, M. Krautloher, H. Suzuki, H. Takahashi, A. Ivanov, H. Yavaş, B. J. Kim, H. Gretarsson, and B. Keimer, Spin and charge excitations in the correlated multiband metal $\text{Ca}_3\text{Ru}_2\text{O}_7$. *Phys. Rev. B* **103** (2021), 085108.
- [8] O. Stockert, J. Arndt, E. Faulhaber, C. Geibel, H. S. Jeevan, S. Kirchner, M. Loewenhaupt, K. Schmalzl, W. Schmidt, Q. Si, and F. Steglich, Magnetically driven superconductivity in CeCu_2Si_2 . *Nat. Phys.* **7** (2011), 119–124.
- [9] N. D. Mathur, F. M. Grosche, S. R. Julian, I. R. Walker, D. M. Freye, R. K. W. Haselwimmer, and G. G. Lonzarich, Magnetically mediated superconductivity in heavy fermion compounds. *Nat.* **394** (1998), 39–43.

- [10] O. Stockert and F. Steglich, Unconventional Quantum Criticality in Heavy-Fermion Compounds. *Annu. Rev. Condens. Matter Phys.* **2** (2011), 79–99.
- [11] B. Keimer, S. A. Kivelson, M. R. Norman, S. Uchida, and J. Zaanen, From quantum matter to high-temperature superconductivity in copper oxides. *Nat.* **518** (2015), 179–186.
- [12] T. Andrews, XVIII. The Bakerian Lecture .—On the continuity of the gaseous and liquid states of matter. *Phil. Trans. R. Soc.* **159** (1869), 575–590.
- [13] M. E. Fisher and R. J. Burford, Theory of Critical-Point Scattering and Correlations. I. The Ising Model. *Phys. Rev.* **156** (1967), 583–622.
- [14] H. E. Stanley, Introduction to phase transitions and critical phenomena, International series of monographs on physics, Oxford University Press, Oxford. (1971).
- [15] P. C. Hohenberg and B. I. Halperin, Theory of dynamic critical phenomena. *Rev. Mod. Phys.* **49** (1977), 435–479.
- [16] M. F. Collins, Magnetic critical scattering, Oxford series on neutron scattering in condensed matter, Oxford University Press, New York. (1989).
- [17] B. I. Halperin and P. C. Hohenberg, Scaling Laws for Dynamic Critical Phenomena. *Phys. Rev.* **177** (1969), 952–971.
- [18] A. Pelissetto and E. Vicari, Critical phenomena and renormalization-group theory. *Phys. Rep.* **368** (2002), 549–727.
- [19] R. B. Griffiths, Dependence of Critical Indices on a Parameter. *Phys. Rev. Lett.* **24** (1970), 1479–1482.
- [20] L. P. Kadanoff, Critical Behavior. Universality and Scaling, in From Order to Chaos, L. P. Kadanoff, ed., vol. 1 of World Scientific Series on Nonlinear Science Series A, World Scientific, (1993), 222–239.
- [21] V. L. Beresinskii, Destruction of Long-range Order in One-dimensional and Two-dimensional Systems Possessing a Continuous Symmetry Group. II. Quantum Systems. *Sov. Phys. JETP* **34** (1972), 610.
- [22] J. M. Kosterlitz and D. J. Thouless, Ordering, metastability and phase transitions in two-dimensional systems. *J. Phys. C: Solid State Phys.* **6** (1973), 1181–1203.

-
- [23] J. M. Kosterlitz, The critical properties of the two-dimensional xy model. *J. Phys. C: Solid State Phys.* **7** (1974), 1046–1060.
- [24] D. J. Bishop and J. D. Reppy, Study of the Superfluid Transition in Two-Dimensional He⁴ Films. *Phys. Rev. Lett.* **40** (1978), 1727–1730.
- [25] J. M. Kosterlitz, Superfluidity in Thin Films of ⁴He. *J. Low. Temp. Phys.* **201** (2020), 541–584.
- [26] D. J. Resnick, J. C. Garland, J. T. Boyd, S. Shoemaker, and R. S. Newrock, Kosterlitz-Thouless Transition in Proximity-Coupled Superconducting Arrays. *Phys. Rev. Lett.* **47** (1981), 1542–1545.
- [27] C. Leemann, P. Lerch, G. Racine, and P. Martinoli, Vortex dynamics and phase transitions in a two-dimensional array of Josephson junctions. *Phys. Rev. Lett.* **56** (1986), 1291–1294.
- [28] L. P. Regnault and J. Rossat-Mignod, Phase Transitions in Quasi Two-Dimensional Planar Magnets, in *Magnetic Properties of Layered Transition Metal Compounds*, L. J. Jongh, ed., Physics and Chemistry of Materials with Low-Dimensional Structures, Springer International Publishing, Cham, (1990).
- [29] K. Hirakawa, H. Yoshizawa, and K. Ubukoshi, Neutron Scattering Study of the Phase Transition in Two-Dimensional Planar Ferromagnet K₂CuF₄. *J. Phys. Soc. Jpn.* **51** (1982), 2151–2158.
- [30] S. T. Bramwell, P. C. W. Holdsworth, and M. T. Hutchings, Static and Dynamic Magnetic Properties of Rb₂CrCl₄: Ideal 2D-XY Behaviour in a Layered Magnet. *J. Phys. Soc. Jpn.* **64** (1995), 3066–3071.
- [31] H. M. Rønnow, A. R. Wildes, and S. T. Bramwell, Magnetic correlations in the 2D honeycomb antiferromagnet MnPS₃. *Phys. B* **276-278** (2000), 676–677.
- [32] E. S. Klyushina, J. Reuther, L. Weber, A. T. M. N. Islam, J. S. Lord, B. Klemke, M. Månsson, S. Wessel, and B. Lake, Signatures for Berezinskii-Kosterlitz-Thouless critical behavior in the planar antiferromagnet BaNi₂V₂O₈. *Phys. Rev. B* **104** (2021), 064402.
- [33] M. Vojta, Quantum phase transitions. *Rep. Prog. Phys.* **66** (2003), 2069–2110.
- [34] H. von Löhneysen, A. Rosch, M. Vojta, and P. Wölfle, Fermi-liquid instabilities at magnetic quantum phase transitions. *J. Phys. Soc. Jpn.* **79** (2007), 1015–1075.

- [35] S. Sachdev, Quantum phase transitions, Cambridge Univ. Press, Cambridge. 2. ed., (2011).
- [36] S. Haravifard, Z. Yamani, and B. D. Gaulin, Quantum Phase Transitions, in Neutron Scattering - Magnetic and Quantum Phenomena, D. L. Price and F. Fernandez-Alonso, eds., vol. 48 of Experimental Methods in the Physical Sciences, Elsevier Science, Saint Louis, (2015), 43–144.
- [37] B. Keimer and J. E. Moore, The physics of quantum materials. *Nat. Phys.* **13** (2017), 1045–1055.
- [38] G. Shirane, J. M. Tranquada, and S. M. Shapiro, Neutron scattering with a triple-axis spectrometer: Basic techniques, Cambridge University Press, Cambridge. (2002).
- [39] T. Chatterji, Neutron scattering from magnetic materials, Elsevier, Amsterdam. 1. ed., (2006).
- [40] G. L. Squires, Introduction to the theory of thermal neutron scattering, Dover books on physics, Dover, Mineola, NY. (1996).
- [41] J. Als-Nielsen, Neutron Scattering and Spatial Correlation near the Critical Point, in Phase transitions and critical phenomena, C. Domb and M. S. Green, eds., Academic Press, London, (1976).
- [42] O. W. Dietrich, J. Als-Nielsen, and L. Passell, Neutron scattering from the Heisenberg ferromagnets EuO and EuS. III. Spin dynamics of EuO. *Phys. Rev. B* **14** (1976), 4923–4945.
- [43] P. Böni and G. Shirane, Paramagnetic neutron scattering from the Heisenberg ferromagnet EuO. *Phys. Rev. B* **33** (1986), 3012–3019.
- [44] A. Tucciarone, H. Y. Lau, L. M. Corliss, A. Delapalme, and J. M. Hastings, Quantitative Analysis of Inelastic Scattering in Two-Crystal and Three-Crystal Neutron Spectrometry; Critical Scattering from RbMnF₃. *Phys. Rev. B* **4** (1971), 3206–3245.
- [45] R. Coldea, R. A. Cowley, T. G. Perring, D. F. McMorrow, and B. Roessli, Critical behavior of the three-dimensional Heisenberg antiferromagnet RbMnF₃. *Phys. Rev. B* **57** (1998), 5281–5290.
- [46] R. J. Christianson, R. L. Leheny, R. J. Birgeneau, and R. W. Erwin, Critical dynamics of a spin-5/2 two-dimensional isotropic antiferromagnet. *Phys. Rev. B* **63** (2001), 140401(R).

-
- [47] Y. J. Kim, R. J. Birgeneau, F. C. Chou, R. W. Erwin, and M. A. Kastner, Critical spin dynamics of the 2D quantum Heisenberg antiferromagnets $\text{Sr}_2\text{CuO}_2\text{Cl}_2$ and $\text{Sr}_2\text{Cu}_3\text{O}_4\text{Cl}_2$. *Phys. Rev. Lett.* **86** (2001), 3144–3147.
- [48] B. Keimer, N. Belk, R. J. Birgeneau, A. Cassanho, C. Y. Chen, M. Greven, M. A. Kastner, A. Aharony, Y. Endoh, R. W. Erwin, and G. Shirane, Magnetic excitations in pure, lightly doped, and weakly metallic La_2CuO_4 . *Phys. Rev. B* **46** (1992), 14034–14053.
- [49] F. Mezei, Neutron Spin Echo: Proceedings of a Laue-Langevin Institut Workshop Grenoble, October 15-16, 1979, vol. 128 of Lecture Notes in Physics, Springer, Berlin and Heidelberg. (1980).
- [50] T. J. Keller, H. Trepka, K. Habicht, and B. Keimer, Neutron Spin-Echo Instrumentation for Magnetic Scattering. *Phys. Status Solidi B* (2021), 2100164.
- [51] F. Mezei, Role of Spin-Nonconserving Forces in the Critical Dynamics of Fe at the Curie Point. *Phys. Rev. Lett.* **49** (1982), 1096–1099.
- [52] F. Mezei, Critical dynamics in isotropic ferromagnets. *J. Magn. Magn. Mater.* **45** (1984), 67–73.
- [53] F. Haslbeck, S. Säubert, M. Seifert, C. Franz, M. Schulz, A. Heinemann, T. Keller, P. Das, J. D. Thompson, E. D. Bauer, C. Pfleiderer, and M. Janoschek, Ultrahigh-resolution neutron spectroscopy of low-energy spin dynamics in UGe_2 . *Phys. Rev. B* **99** (2019), 014429.
- [54] K. F. Tseng, T. Keller, A. C. Walters, R. J. Birgeneau, and B. Keimer, Neutron spin-echo study of the critical dynamics of spin-5/2 antiferromagnets in two and three dimensions. *Phys. Rev. B* **94** (2016), 014424.
- [55] B. J. Kim, H. Jin, S. J. Moon, J.-Y. Kim, B.-G. Park, C. S. Leem, J. Yu, T. W. Noh, C. Kim, S.-J. Oh, J.-H. Park, V. Durairaj, G. Cao, and E. Rotenberg, Novel $J_{\text{eff}}=1/2$ Mott state induced by relativistic spin-orbit coupling in Sr_2IrO_4 . *Phys. Rev. Lett.* **101** (2008), 076402.
- [56] B. J. Kim, H. Ohsumi, T. Komesu, S. Sakai, T. Morita, H. Takagi, and T. Arima, Phase-sensitive observation of a spin-orbital Mott state in Sr_2IrO_4 . *Science* **323** (2009), 1329–1332.
- [57] S. Fujiyama, H. Ohsumi, T. Komesu, J. Matsuno, B. J. Kim, M. Takata, T. Arima, and H. Takagi, Two-dimensional Heisenberg behavior of $J(\text{eff})=1/2$ isospins in the paramagnetic state of the spin-orbital Mott insulator Sr_2IrO_4 . *Phys. Rev. Lett.* **108** (2012), 247212.

- [58] J. G. Vale, S. Boseggia, H. C. Walker, R. Springell, Z. Feng, E. C. Hunter, R. S. Perry, D. Prabhakaran, A. T. Boothroyd, S. P. Collins, H. M. Rønnow, and D. F. McMorrow, Importance of XY anisotropy in Sr_2IrO_4 revealed by magnetic critical scattering experiments. *Phys. Rev. B* **92** (2015), 020406.
- [59] J. G. Vale, S. Boseggia, H. C. Walker, R. S. Springell, E. C. Hunter, R. S. Perry, S. P. Collins, and D. F. McMorrow, Critical fluctuations in the spin-orbit Mott insulator $\text{Sr}_3\text{Ir}_2\text{O}_7$. *J. Phys.: Condens. Matter* **31** (2019), 185803.
- [60] I. Marković, M. D. Watson, O. J. Clark, F. Mazzola, E. Abarca Morales, C. A. Hooley, H. Rosner, C. M. Polley, T. Balasubramanian, S. Mukherjee, N. Kikugawa, D. A. Sokolov, A. P. Mackenzie, and P. D. C. King, Electronically driven spin-reorientation transition of the correlated polar metal $\text{Ca}_3\text{Ru}_2\text{O}_7$. *PNAS USA* **117** (2020), 15524–15529.
- [61] S. A. Grigera, R. S. Perry, A. J. Schofield, M. Chiao, S. R. Julian, G. G. Lonzarich, S. I. Ikeda, Y. Maeno, A. J. Millis, and A. P. Mackenzie, Magnetic field-tuned quantum criticality in the metallic ruthenate $\text{Sr}_3\text{Ru}_2\text{O}_7$. *Science* **294** (2001), 329–332.
- [62] M. Horio, Q. Wang, V. Granata, K. P. Kramer, Y. Sassa, S. Jöhr, D. Sutter, A. Bold, L. Das, Y. Xu, R. Frison, R. Fittipaldi, T. K. Kim, C. Cacho, J. E. Rault, P. Le Fèvre, F. Bertran, N. C. Plumb, M. Shi, A. Vecchione, M. H. Fischer, and J. Chang, Electronic reconstruction forming a C_2 -symmetric Dirac semimetal in $\text{Ca}_3\text{Ru}_2\text{O}_7$. *npj Quantum Mater.* **6** (2021), 1–7.
- [63] Y. Sidis, M. Braden, P. Bourges, B. Hennion, S. Nishizaki, Y. Maeno, and Y. Mori, Evidence for Incommensurate Spin Fluctuations in Sr_2RuO_4 . *Phys. Rev. Lett.* **83** (1999), 3320–3323.
- [64] G. Khaliullin, Excitonic magnetism in Van Vleck-type d^4 Mott insulators. *Phys. Rev. Lett.* **111** (2013), 197201.
- [65] A. Akbari and G. Khaliullin, Magnetic excitations in a spin-orbit-coupled d^4 Mott insulator on the square lattice. *Phys. Rev. B* **90** (2014), 035137.
- [66] M. Braden, G. André, S. Nakatsuji, and Y. Maeno, Crystal and magnetic structure of Ca_2RuO_4 : Magnetoelastic coupling and the metal-insulator transition. *Phys. Rev. B* **58** (1998), 847–861.
- [67] C. S. Alexander, G. Cao, V. Dobrosavljevic, S. McCall, J. E. Crow, E. Lochner, and R. P. Guertin, Destruction of the Mott insulating ground state of Ca_2RuO_4 by a structural transition. *Phys. Rev. B* **60** (1999), R8422–R8425.

-
- [68] S. Nakatsuji and Y. Maeno, Synthesis and Single-Crystal Growth of $\text{Ca}_{2-x}\text{Sr}_x\text{RuO}_4$. *J. Solid State Chem.* **156** (2001), 26–31.
- [69] H. Gretarsson, H. Suzuki, H. Kim, K. Ueda, M. Krautloher, B. J. Kim, H. Yavaş, G. Khaliullin, and B. Keimer, Observation of spin-orbit excitations and Hund’s multiplets in Ca_2RuO_4 . *Phys. Rev. B* **100** (2019), 045123.
- [70] S.-M. Souliou, J. Chaloupka, G. Khaliullin, G. Ryu, A. Jain, B. J. Kim, M. Le Tacon, and B. Keimer, Raman Scattering from Higgs Mode Oscillations in the Two-Dimensional Antiferromagnet Ca_2RuO_4 . *Phys. Rev. Lett.* **119** (2017), 067201.
- [71] S. McCall, G. Cao, and J. E. Crow, Impact of magnetic fields on anisotropy in $\text{Ca}_3\text{Ru}_2\text{O}_7$. *Phys. Rev. B* **67** (2003), 094427.
- [72] Y. Yoshida, S.-i. Ikeda, H. Matsuhata, N. Shirakawa, C. H. Lee, and S. Katano, Crystal and magnetic structure of $\text{Ca}_3\text{Ru}_2\text{O}_7$. *Phys. Rev. B* **72** (2005), 054412.
- [73] B. Bohnenbuck, I. Zegkinoglou, J. Stremper, C. Schüßler-Langeheine, C. S. Nelson, P. Leininger, H.-H. Wu, E. Schierle, J. C. Lang, G. Srajer, S. I. Ikeda, Y. Yoshida, K. Iwata, S. Katano, N. Kikugawa, and B. Keimer, Magnetic structure and orbital state of $\text{Ca}_3\text{Ru}_2\text{O}_7$ investigated by resonant x-ray diffraction. *Phys. Rev. B* **77** (2008), 224412.
- [74] X. Ke, T. Hong, J. Peng, S. E. Nagler, G. E. Granroth, M. D. Lumsden, and Z. Q. Mao, Spin-wave excitation in the antiferromagnetic bilayer ruthenate $\text{Ca}_3\text{Ru}_2\text{O}_7$. *Phys. Rev. B* **84** (2011), 014422.
- [75] X. Ke, J. Peng, D. J. Singh, T. Hong, W. Tian, C. R. Dela Cruz, and Z. Q. Mao, Emergent electronic and magnetic state in $\text{Ca}_3\text{Ru}_2\text{O}_7$ induced by Ti-doping. *Phys. Rev. B* **84** (2011), 201102.
- [76] S. Tsuda, N. Kikugawa, K. Sugii, S. Uji, S. Ueda, M. Nishio, and Y. Maeno, Mott transition extremely sensitive to impurities in $\text{Ca}_3\text{Ru}_2\text{O}_7$ revealed by hard x-ray photoemission studies. *Phys. Rev. B* **87** (2013), 241107.
- [77] J. Peng, X. Ke, G. Wang, J. E. Ortmann, D. Fobes, T. Hong, W. Tian, X. Wu, and Z. Q. Mao, From quasi-two-dimensional metal with ferromagnetic bilayers to Mott insulator with G-type antiferromagnetic order in $\text{Ca}_3(\text{Ru}_{1-x}\text{Ti}_x)_2\text{O}_7$. *Phys. Rev. B* **87** (2013), 085125.
- [78] J. Peng, J. Y. Liu, J. Hu, Z. Q. Mao, F. M. Zhang, and X. S. Wu, Magnetic phase separation in double layer ruthenates $\text{Ca}_3(\text{Ru}_{1-x}\text{Ti}_x)_2\text{O}_7$. *Sci. Rep.* **6** (2016), 19462.

- [79] M. J. Krautloher, J. Bertinshaw, J. Porras, D. G. Joshi, G. Khaliullin, H. Trepka, M. Hepting, D. Adroja, H. C. Walker, A. Ivanov, M. Enderle, U. Stuhr, B. J. Kim, and B. Keimer, Impurity-induced transformation of spin-orbit entanglement in a layered ruthenate: (submitted to *Phys. Rev. X*).
- [80] C. Domb and M. S. Green, editors, *Phase transitions and critical phenomena*, Academic Press, London. (1976).
- [81] M. E. Fisher, Scaling, universality and renormalization group theory, in *Critical Phenomena*, F. J. W. Hahne, ed., vol. 186 of *Lecture Notes in Physics*, Springer Berlin Heidelberg, Berlin, Heidelberg, (1983), 1–139.
- [82] C. Hohenemser, N. Rosov, and A. Kleinhammes, Critical phenomena studied via nuclear techniques. *Hyperfine Interact* **49** (1989), 267–323.
- [83] S.-K. Ma, *Modern Theory of Critical Phenomena*, Advanced Books Classics, Routledge, Boulder. (2018).
- [84] A. Boothroyd, *Principles of neutron scattering from condensed matter*, Oxford University Press, Oxford. (2020).
- [85] M. E. Fisher, Correlation Functions and the Critical Region of Simple Fluids. *J. Math. Phys.* **5** (1964), 944–962.
- [86] L. P. Kadanoff, W. Götze, D. Hamblen, R. Hecht, E. A. S. Lewis, V. V. Palciauskas, M. Rayl, J. Swift, D. Aspnes, and J. Kane, Static Phenomena Near Critical Points: Theory and Experiment. *Rev. Mod. Phys.* **39** (1967), 395–431.
- [87] R. B. Griffiths, Ferromagnets and Simple Fluids near the Critical Point: Some Thermodynamic Inequalities. *J. Chem. Phys.* **43** (1965), 1958–1968.
- [88] L. Onsager, Crystal Statistics. I. A Two-Dimensional Model with an Order-Disorder Transition. *Phys. Rev.* **65** (1944), 117–149.
- [89] M. E. Fisher, The renormalization group in the theory of critical behavior. *Rev. Mod. Phys.* **46** (1974), 597–616.
- [90] K. Wilson, The renormalization group and the ϵ expansion. *Phys. Rep.* **12** (1974), 75–199.
- [91] S. T. Bramwell and P. C. W. Holdsworth, Magnetization and universal sub-critical behaviour in two-dimensional XY magnets. *J. Phys.: Condens. Matter* **5** (1993), L53–L59.

-
- [92] G. A. Baker, B. G. Nickel, and D. I. Meiron, Critical indices from perturbation analysis of the Callan-Symanzik equation. *Phys. Rev. B* **17** (1978), 1365–1374.
- [93] M. Campostrini, M. Hasenbusch, A. Pelissetto, P. Rossi, and E. Vicari, Critical exponents and equation of state of the three-dimensional Heisenberg universality class. *Phys. Rev. B* **65** (2002), 144520.
- [94] L. J. de Jongh, Introduction to low-dimensional magnetic systems, in *Magnetic Properties of Layered Transition Metal Compounds*, L. J. Jongh, ed., Physics and Chemistry of Materials with Low-Dimensional Structures, Springer International Publishing, Cham, (1990).
- [95] M. Greven, R. J. Birgeneau, Y. Endoh, M. A. Kastner, B. Keimer, M. Matsuda, G. Shirane, and T. R. Thurston, Spin correlations in the 2D Heisenberg antiferromagnet $\text{Sr}_2\text{CuO}_2\text{Cl}_2$: Neutron scattering, Monte Carlo simulation, and theory. *Phys. Rev. Lett.* **72** (1994), 1096–1099.
- [96] T. J. Williams, A. A. Aczel, M. D. Lumsden, S. E. Nagler, M. B. Stone, J.-Q. Yan, and D. Mandrus, Magnetic correlations in the quasi-two-dimensional semiconducting ferromagnet CrSiTe_3 . *Phys. Rev. B* **92** (2015), 144404.
- [97] S. Chakravarty, B. I. Halperin, and D. R. Nelson, Low-temperature behavior of two-dimensional quantum antiferromagnets. *Phys. Rev. Lett.* **60** (1988), 1057–1060.
- [98] S. Chakravarty, B. I. Halperin, and D. R. Nelson, Two-dimensional quantum Heisenberg antiferromagnet at low temperatures. *Phys. Rev. B* **39** (1989), 2344–2371.
- [99] P. Hasenfratz and F. Niedermayer, The exact correlation length of the antiferromagnetic $d=2+1$ Heisenberg model at low temperatures. *Phys. Lett. B* **268** (1991), 231–235.
- [100] J.-i. Igarashi, $1/S$ expansion for thermodynamic quantities in a two-dimensional Heisenberg antiferromagnet at zero temperature. *Phys. Rev. B* **46** (1992), 10763–10771.
- [101] K. Nakajima, K. Yamada, S. Hosoya, Y. Endoh, M. Greven, and R. J. Birgeneau, Spin dynamics and spin correlations in the spin $S=1$ two-dimensional square-lattice Heisenberg antiferromagnet La_2NiO_4 . *Z. Physik B: Condens. Matter* **96** (1995), 479–489.
- [102] J. Als-Nielsen, S. T. Bramwell, M. T. Hutchings, G. J. McIntyre, and D. Visser, Neutron scattering investigation of the static critical properties of Rb_2CrCl_4 . *J. Phys.: Condens. Matter* **5** (1993), 7871–7892.

- [103] U. Tutsch, B. Wolf, S. Wessel, L. Postulka, Y. Tsui, H. O. Jeschke, I. Opahle, T. Saha-Dasgupta, R. Valentí, A. Brühl, K. Remović-Langer, T. Kretz, H.-W. Lerner, M. Wagner, and M. Lang, Evidence of a field-induced Berezinskii-Kosterlitz-Thouless scenario in a two-dimensional spin-dimer system. *Nat. Commun.* **5** (2014), 5169.
- [104] M. Heinrich, H.-A. Krug von Nidda, A. Loidl, N. Rogado, and R. J. Cava, Potential signature of a Kosterlitz-Thouless transition in $\text{BaNi}_2\text{V}_2\text{O}_8$. *Phys. Rev. Lett.* **91** (2003), 137601.
- [105] T. Roscilde, A. Cuccoli, and P. Verrucchi, Phase transitions in anisotropic two-dimensional quantum antiferromagnets. *Phys. Status Solidi B* **236** (2003), 433–436.
- [106] A. Cuccoli, T. Roscilde, R. Vaia, and P. Verrucchi, Detection of XY behavior in weakly anisotropic quantum antiferromagnets on the square lattice. *Phys. Rev. Lett.* **90** (2003), 167205.
- [107] A. Cuccoli, T. Roscilde, V. Tognetti, R. Vaia, and P. Verrucchi, Quantum Monte Carlo study of $S=1/2$ weakly anisotropic antiferromagnets on the square lattice. *Phys. Rev. B* **67** (2003), 104414.
- [108] L. P. Regnault, J. Rossat-Mignod, J. Y. Henry, and L. J. de Jongh, Magnetic properties of the quasi-2d easy plane antiferromagnet $\text{BaNi}_2(\text{PO}_4)_2$. *J. Magn. Mater.* **31-34** (1983), 1205–1206.
- [109] P. Gaveau, J. P. Boucher, L. P. Regnault, and Y. Henry, Magnetic-field dependence of the phosphorus nuclear spin-relaxation rate in the quasi-two-dimensional XY antiferromagnet $\text{BaNi}_2(\text{PO}_4)_2$. *J. Appl. Phys.* **69** (1991), 6228–6230.
- [110] R. Gross and A. Marx, *Festkörperphysik*, De Gruyter Studium Ser, De Gruyter Inc, Berlin/Boston. 3rd ed., (2018).
- [111] P. Pfeuty, D. Jasnow, and M. E. Fisher, Crossover scaling functions for exchange anisotropy. *Phys. Rev. B* **10** (1974), 2088–2112.
- [112] R. J. Birgeneau, J. Skalyo, and G. Shirane, Critical Magnetic Scattering in K_2NiF_4 . *Phys. Rev. B* **3** (1971), 1736–1749.
- [113] M. T. Hutchings, H. Ikeda, and E. Janke, Dynamic Critical Neutron Scattering from a Two-Dimensional Ising System Rb_2CoF_4 . *Phys. Rev. Lett.* **49** (1982), 386–390.

-
- [114] B. I. Halperin, P. C. Hohenberg, and S.-K. Ma, Calculation of Dynamic Critical Properties Using Wilson's Expansion Methods. *Phys. Rev. Lett.* **29** (1972), 1548–1551.
- [115] B. I. Halperin, P. C. Hohenberg, and S.-K. Ma, Renormalization-group methods for critical dynamics: I. Recursion relations and effects of energy conservation. *Phys. Rev. B* **10** (1974), 139–153.
- [116] G. F. Mazenko and O. T. Valls, Dynamic critical exponent z in some two-dimensional models. *Phys. Rev. B* **24** (1981), 1419–1428.
- [117] L. M. Jensen, B. J. Kim, and P. Minnhagen, Dynamic critical exponent of two-, three-, and four-dimensional XY models with relaxational and resistively shunted junction dynamics. *Phys. Rev. B* **61** (2000), 15412–15428.
- [118] M. Hasenbusch, Dynamic critical exponent z of the three-dimensional Ising universality class: Monte Carlo simulations of the improved Blume-Capel model. *Phys. Rev. E* **101** (2020), 022126.
- [119] O. Stockert, M. Nicklas, P. Thalmeier, P. Gegenwart, and F. Steglich, Magnetism and Quantum Criticality in Heavy-Fermion Compounds: Interplay with Superconductivity, in Handbook of magnetism and advanced magnetic materials, H. Kronmüller, S. Parkin, and S. S. P. Parkin, eds., Wiley, Chichester, (2007).
- [120] H. G. Schlager, A. Schröder, M. Welsch, and H. von Löhneysen, Magnetic ordering in $\text{CeCu}_{6-x}\text{Au}_x$ single crystals: Thermodynamic and transport properties. *J. Low. Temp. Phys.* **90** (1993), 181–204.
- [121] O. Stockert, F. Huster, A. Neubert, C. Pfleiderer, T. Pietrus, B. Will, and H. Löhneysen, Pressure versus magnetic-field tuning of a magnetic quantum phase transition. *Phys. B* **312-313** (2002), 458–460.
- [122] G. Fraunberger, B. Andraka, J. S. Kim, U. Ahlheim, and G. R. Stewart, Magnetic behavior of $\text{Ce}(\text{Cu}_{1-x}\text{Ag}_x)_6$. *Phys. Rev. B* **40** (1989), 4735–4739.
- [123] K. Heuser, J. S. Kim, E. W. Scheidt, T. Schreiner, and G. R. Stewart, Inducement of non-Fermi-liquid behavior with magnetic field in heavy-fermion antiferromagnets. *Phys. B* **259-261** (1999), 392–394.
- [124] A. Oosawa, M. Ishii, and H. Tanaka, Field-induced three-dimensional magnetic ordering in the spin-gap system. *J. Phys.: Condens. Matter* **11** (1999), 265–271.

- [125] C. Rüegg, N. Cavadini, A. Furrer, H.-U. Güdel, K. Krämer, H. Mutka, A. Wildes, K. Habicht, and P. Vorderwisch, Bose-Einstein condensation of the triplet states in the magnetic insulator TlCuCl_3 . *Nat.* **423** (2003), 62–65.
- [126] W. Shiramura, K.-i. Takatsu, H. Tanaka, K. Kamishima, M. Takahashi, H. Mitamura, and T. Goto, High-Field Magnetization Processes of Double Spin Chain Systems KCuCl_3 and TlCuCl_3 . *J. Phys. Soc. Jpn.* **66** (1997), 1900–1903.
- [127] S. Acharya, D. Dey, T. Maitra, and A. Taraphder, Quantum criticality associated with dimensional crossover in the iso-electronic series $\text{Ca}_{2-x}\text{Sr}_x\text{RuO}_4$. *J. Phys. Commun.* **2** (2018), 075004.
- [128] J. Steijger, E. Frikkee, L. J. de Jongh, and W. J. Huiskamp, Crossover in the critical behaviour of the Ising antiferromagnet $\text{MnCl}_2 \cdot 4 \text{H}_2\text{O}$ in transverse field. *J. Magn. Magn. Mater.* **31-34** (1983), 1091–1092.
- [129] W. A. C. Erkelens, L. P. Regnault, J. Rossat-Mignod, J. E. Moore, R. A. Butera, and L. J. de Jongh, Observation of Crossover to 4-Dimensional Critical Behaviour. *Europhys. Lett.* **1** (1986), 37–44.
- [130] M. Vasin, V. Ryzhov, and V. M. Vinokur, Quantum-to-classical crossover near quantum critical point. *Sci. Rep.* **5** (2015), 18600.
- [131] S. Sachdev, Theory of finite-temperature crossovers near quantum critical points close to, or above, their upper-critical dimension. *Phys. Rev. B* **55** (1997), 142–163.
- [132] M. Nič, J. Jiráť, B. Košata, A. Jenkins, and A. McNaught, editors, IUPAC Compendium of Chemical Terminology, IUPAC, Research Triangle Park, NC. (2009).
- [133] J. G. Bednorz and K. A. Müller, Possible high- T_c superconductivity in the Ba-La-Cu-O system. *Z. Physik B: Condens. Matter* **64** (1986), 189–193.
- [134] K. Held, G. Keller, V. Eyert, D. Vollhardt, and V. I. Anisimov, Mott-hubbard metal-insulator transition in paramagnetic V_2O_3 : an LDA+DMFT(QMC) study. *Phys. Rev. Lett.* **86** (2001), 5345–5348.
- [135] Tokura, Taguchi, Okada, Fujishima, Arima, Kumagai, and Iye, Filling dependence of electronic properties on the verge of metal-Mott-insulator transition in $\text{Sr}_{1-x}\text{La}_x\text{TiO}_3$. *Phys. Rev. Lett.* **70** (1993), 2126–2129.
- [136] A. P. Ramirez, Colossal magnetoresistance. *J. Phys.: Condens. Matter* **9** (1997), 8171–8199.

-
- [137] T. Kimura, S. Kawamoto, I. Yamada, M. Azuma, M. Takano, and Y. Tokura, Magnetocapacitance effect in multiferroic BiMnO₃. *Phys. Rev. B* **67** (2003), 180401.
- [138] T. Takayama, J. Chaloupka, A. Smerald, G. Khaliullin, and H. Takagi, Spin–Orbit-Entangled Electronic Phases in 4d and 5d Transition-Metal Compounds. *J. Phys. Soc. Jpn.* **90** (2021), 062001.
- [139] A. P. Mackenzie and Y. Maeno, The superconductivity of Sr₂RuO₄ and the physics of spin-triplet pairing. *Rev. Mod. Phys.* **75** (2003), 657–712.
- [140] M. Moretti Sala, M. Rossi, A. Al-Zein, S. Boseggia, E. C. Hunter, R. S. Perry, D. Prabhakaran, A. T. Boothroyd, N. B. Brookes, D. F. McMorrow, G. Monaco, and M. Krisch, Crystal field splitting in Sr_{n+1}Ir_nO_{3n+1} (n=1,2) iridates probed by x-ray Raman spectroscopy. *Phys. Rev. B* **90** (2014), 085126.
- [141] Y. Tokura and N. Nagaosa, Orbital physics in transition-metal oxides. *Science* **288** (2000), 462–468.
- [142] A. Earnshaw, B. N. Figgis, J. Lewis, and R. D. Peacock, The magnetic properties of some d⁴-complexes. *J. Chem. Soc.* (1961), 3132.
- [143] J. Bendix, M. Brorson, and C. E. Schaffer, Accurate empirical spin-orbit coupling parameters ζ_{nd} for gaseous nd^q transition metal ions. The parametrical multiplet term model. *Inorg. Chem.* **32** (1993), 2838–2849.
- [144] M. Zhu, J. Peng, T. Zou, K. Prokes, S. D. Mahanti, T. Hong, Z. Q. Mao, G. Q. Liu, and X. Ke, Colossal Magnetoresistance in a Mott Insulator via Magnetic Field-Driven Insulator-Metal Transition. *Phys. Rev. Lett.* **116** (2016), 216401.
- [145] A. J. Freeman and R. E. Watson, Theory of Direct Exchange in Ferromagnetism. *Phys. Rev.* **124** (1961), 1439–1454.
- [146] J. B. Goodenough, Theory of the Role of Covalence in the Perovskite-Type Manganites [La, M(II)]MnO₃. *Phys. Rev.* **100** (1955), 564–573.
- [147] P. W. Anderson, New Approach to the Theory of Superexchange Interactions. *Phys. Rev.* **115** (1959), 2–13.
- [148] J. Hubbard, Electron correlations in narrow energy bands. *Proc. R. Soc. Lond. A* **276** (1963), 238–257.
- [149] J. Hubbard, Electron correlations in narrow energy bands III. An improved solution. *Proc. R. Soc. Lond. A* **281** (1964), 401–419.

- [150] J. Hubbard, Electron correlations in narrow energy bands. II. The degenerate band case. *Proc. R. Soc. Lond. A* **277** (1964), 237–259.
- [151] N. F. Mott, Metal-insulator transitions, Taylor & Francis, London. 2. ed., (1990).
- [152] M. Imada, A. Fujimori, and Y. Tokura, Metal-insulator transitions. *Rev. Mod. Phys.* **70** (1998), 1039–1263.
- [153] J. B. Goodenough, An interpretation of the magnetic properties of the perovskite-type mixed crystals $\text{La}_{1-x}\text{Sr}_x\text{CoO}_{3-l}$. *J. Phys. Chem. Solids* **6** (1958), 287–297.
- [154] J. Kanamori, Superexchange interaction and symmetry properties of electron orbitals. *J. Phys. Chem. Solids* **10** (1959), 87–98.
- [155] C. Zener, Interaction between the d -Shells in the Transition Metals. II. Ferromagnetic Compounds of Manganese with Perovskite Structure. *Phys. Rev.* **82** (1951), 403–405.
- [156] S. N. Ruddlesden and P. Popper, New compounds of the K_2NiF_4 type. *Acta Cryst* **10** (1957), 538–539.
- [157] G. Cao, S. McCall, and J. E. Crow, Observation of itinerant ferromagnetism in layered $\text{Sr}_3\text{Ru}_2\text{O}_7$ single crystals. *Phys. Rev. B* **55** (1997), R672–R675.
- [158] G. Cao, S. K. McCall, J. E. Crow, and R. P. Guertin, Ferromagnetism in $\text{Sr}_4\text{Ru}_3\text{O}_{10}$: Relationship to other layered metallic oxides. *Phys. Rev. B* **56** (1997), R5740–R5743.
- [159] G. Cao, S. McCall, M. Shepard, J. E. Crow, and R. P. Guertin, Magnetic and transport properties of single-crystal Ca_2RuO_4 : Relationship to superconducting Sr_2RuO_4 . *Phys. Rev. B* **56** (1997), R2916–R2919.
- [160] A. Kanbayasi, Magnetic properties of SrRuO_3 Single Crystal. *J. Phys. Soc. Jpn.* **41** (1976), 1876–1878.
- [161] C. Kittel, Introduction to solid state physics, Wiley, New York, NY. 7. ed., (1996).
- [162] R. D. Shannon, Revised effective ionic radii and systematic studies of interatomic distances in halides and chalcogenides. *Acta Cryst A* **32** (1976), 751–767.

-
- [163] Y. Maeno, S. Kittaka, T. Nomura, S. Yonezawa, and K. Ishida, Evaluation of Spin-Triplet Superconductivity in Sr_2RuO_4 . *J. Phys. Soc. Jpn.* **81** (2012), 011009.
- [164] V. J. Emery and S. A. Kivelson, Superconductivity in bad metals. *Phys. Rev. Lett.* **74** (1995), 3253–3256.
- [165] Y. Ando, A. N. Lavrov, S. Komiya, K. Segawa, and X. F. Sun, Mobility of the doped holes and the antiferromagnetic correlations in underdoped high-Tc cuprates. *Phys. Rev. Lett.* **87** (2001), 017001.
- [166] S. Benhabib, C. Lupien, I. Paul, L. Berges, M. Dion, M. Nardone, A. Zitouni, Z. Q. Mao, Y. Maeno, A. Georges, L. Taillefer, and C. Proust, Ultrasound evidence for a two-component superconducting order parameter in Sr_2RuO_4 . *Nat. Phys.* **17** (2021), 194–198.
- [167] A. J. Leggett and Y. Liu, Symmetry Properties of Superconducting Order Parameter in Sr_2RuO_4 . *J Supercond Nov Magn* **34** (2021), 1647–1673.
- [168] O. Friedt, M. Braden, G. André, P. Adelman, S. Nakatsuji, and Y. Maeno, Structural and magnetic aspects of the metal-insulator transition in $\text{Ca}_{2-x}\text{Sr}_x\text{RuO}_4$. *Phys. Rev. B* **63** (2001), 174432.
- [169] Z. Fang and K. Terakura, Magnetic phase diagram of $\text{Ca}_{2-x}\text{Sr}_x\text{RuO}_4$ governed by structural distortions. *Phys. Rev. B* **64** (2001), 020509.
- [170] Z. Fang, N. Nagaosa, and K. Terakura, Orbital-dependent phase control in $\text{Ca}_{2-x}\text{Sr}_x\text{RuO}_4$ ($0 \leq x \leq 0.5$). *Phys. Rev. B* **69** (2004), 045116.
- [171] S. Mohapatra and A. Singh, Magnetic reorientation transition in a three orbital model for Ca_2RuO_4 — Interplay of spin-orbit coupling, tetragonal distortion, and Coulomb interactions. *J. Condens. Matter Phys.* **32** (2020), 485805.
- [172] J. P. Carlo, T. Goko, I. M. Gat-Malureanu, P. L. Russo, A. T. Savici, A. A. Aczel, G. J. MacDougall, J. A. Rodriguez, T. J. Williams, G. M. Luke, C. R. Wiebe, Y. Yoshida, S. Nakatsuji, Y. Maeno, T. Taniguchi, and Y. J. Uemura, New magnetic phase diagram of $(\text{Sr,Ca})_2\text{RuO}_4$. *Nat. Mater.* **11** (2012), 323–328.
- [173] S. Nakatsuji and Y. Maeno, Quasi-two-dimensional mott transition system $\text{Ca}_{2-x}\text{Sr}_x\text{RuO}_4$. *Phys. Rev. Lett.* **84** (2000), 2666–2669.

- [174] S. Nakatsuji and Y. Maeno, Switching of magnetic coupling by a structural symmetry change near the Mott transition in $\text{Ca}_{2-x}\text{Sr}_x\text{RuO}_4$. *Phys. Rev. B* **62** (2000), 6458–6466.
- [175] S. Nakatsuji, D. Hall, L. Balicas, Z. Fisk, K. Sugahara, M. Yoshioka, and Y. Maeno, Heavy-mass fermi liquid near a ferromagnetic instability in layered ruthenates. *Phys. Rev. Lett.* **90** (2003), 137202.
- [176] S. Nakatsuji, S.-i. Ikeda, and Y. Maeno, Ca_2RuO_4 : New Mott Insulators of Layered Ruthenate. *J. Phys. Soc. Jpn.* **66** (1997), 1868–1871.
- [177] D. G. Porter, V. Granata, F. Forte, S. Di Matteo, M. Cuoco, R. Fittipaldi, A. Vecchione, and A. Bombardi, Magnetic anisotropy and orbital ordering in Ca_2RuO_4 . *Phys. Rev. B* **98** (2018), 125142.
- [178] A. Abragam and B. Bleaney, Electron paramagnetic resonance of transition ions, Oxford classic texts in the physical sciences, Clarendon Press, Oxford. reprinted. ed., (2013).
- [179] V. I. Anisimov, I. A. Nekrasov, D. E. Kondakov, T. M. Rice, and M. Sigrist, Orbital-selective Mott-insulator transition in $\text{Ca}_{2-x}\text{Sr}_x\text{RuO}_4$. *Eur. Phys. J. B* **25** (2002), 191–201.
- [180] S. Kunkemöller, D. Khomskii, P. Steffens, A. Piovano, A. A. Nugroho, and M. Braden, Highly Anisotropic Magnon Dispersion in Ca_2RuO_4 : Evidence for Strong Spin Orbit Coupling. *Phys. Rev. Lett.* **115** (2015), 247201.
- [181] I. Zegkinoglou, J. Strempler, C. S. Nelson, J. P. Hill, J. Chakhalian, C. Bernhard, J. C. Lang, G. Srajer, H. Fukazawa, S. Nakatsuji, Y. Maeno, and B. Keimer, Orbital ordering transition in Ca_2RuO_4 observed with resonant X-ray diffraction. *Phys. Rev. Lett.* **95** (2005), 136401.
- [182] I. Zegkinoglou and B. Keimer, X-ray Scattering Studies of 4D- and 5D-Electron Transition Metal Oxides, in *Frontiers of 4d- and 5d-Transition Metal Oxides*, G. Cao and L. de Long, eds., World Scientific Publishing Company, Singapore, (2013).
- [183] J. Lotze and M. Daghofer, Suppression of effective spin-orbit coupling by thermal fluctuations in spin-orbit coupled antiferromagnets. *Phys. Rev. B* **104** (2021), 045125.
- [184] H. Liu and G. Khaliullin, Pseudo-Jahn-Teller Effect and Magnetoelastic Coupling in Spin-Orbit Mott Insulators. *Phys. Rev. Lett.* **122** (2019), 057203.

-
- [185] F. Nakamura, T. Goko, M. Ito, T. Fujita, S. Nakatsuji, H. Fukazawa, Y. Maeno, P. Alireza, D. Forsythe, and S. R. Julian, From Mott insulator to ferromagnetic metal: A pressure study of Ca_2RuO_4 . *Phys. Rev. B* **65** (2002), 220402.
- [186] P. Steffens, O. Friedt, P. Alireza, W. G. Marshall, W. Schmidt, F. Nakamura, S. Nakatsuji, Y. Maeno, R. Lengsdorf, M. M. Abd-Elmeguid, and M. Braden, High-pressure diffraction studies on Ca_2RuO_4 . *Phys. Rev. B* **72** (2005), 094104.
- [187] P. L. Alireza, F. Nakamura, S. K. Goh, Y. Maeno, S. Nakatsuji, Y. T. C. Ko, M. Sutherland, S. Julian, and G. G. Lonzarich, Evidence of superconductivity on the border of quasi-2D ferromagnetism in Ca_2RuO_4 at high pressure. *J. Condens. Matter Phys.* **22** (2010), 052202.
- [188] H. Nobukane, K. Yanagihara, Y. Kunisada, Y. Ogasawara, K. Isono, K. Nomura, K. Tanahashi, T. Nomura, T. Akiyama, and S. Tanda, Co-appearance of superconductivity and ferromagnetism in a Ca_2RuO_4 nanofilm crystal. *Sci. Rep.* **10** (2020), 3462.
- [189] F. Nakamura, M. Sakaki, Y. Yamanaka, S. Tamaru, T. Suzuki, and Y. Maeno, Electric-field-induced metal maintained by current of the Mott insulator Ca_2RuO_4 . *Sci Rep* **3** (2013), 2536.
- [190] C. Sow, S. Yonezawa, S. Kitamura, T. Oka, K. Kuroki, F. Nakamura, and Y. Maeno, Current-induced strong diamagnetism in the Mott insulator Ca_2RuO_4 . *Science* **358** (2017), 1084–1087.
- [191] J. Bertinshaw, N. Gurung, P. Jorba, H. Liu, M. Schmid, D. T. Mantadakis, M. Daghofer, M. Krautloher, A. Jain, G. H. Ryu, O. Fabelo, P. Hansmann, G. Khaliullin, C. Pfleiderer, B. Keimer, and B. J. Kim, Unique Crystal Structure of Ca_2RuO_4 in the Current Stabilized Semimetallic State. *Phys. Rev. Lett.* **123** (2019), 137204.
- [192] Y. Yoshida, I. Nagai, S.-i. Ikeda, N. Shirakawa, M. Kosaka, and N. Mōri, Quasi-two-dimensional metallic ground state of $\text{Ca}_3\text{Ru}_2\text{O}_7$. *Phys. Rev. B* **69** (2004), 220411.
- [193] W. J. Duncan, O. P. Welzel, D. Moroni-Klementowicz, C. Albrecht, P. G. Niklowitz, D. Grüner, M. Brando, A. Neubauer, C. Pfleiderer, N. Kikugawa, A. P. Mackenzie, and F. M. Grosche, Quantum phase transitions in NbFe_2 and $\text{Ca}_3\text{Ru}_2\text{O}_7$. *Phys. Status Solidi B* **247** (2010), 544–548.

- [194] F. Baumberger, N. J. C. Ingle, N. Kikugawa, M. A. Hossain, W. Meevasana, R. S. Perry, K. M. Shen, D. H. Lu, A. Damascelli, A. Rost, A. P. Mackenzie, Z. Hussain, and Z.-X. Shen, Nested fermi surface and electronic instability in $\text{Ca}_3\text{Ru}_2\text{O}_7$. *Phys. Rev. Lett.* **96** (2006), 107601.
- [195] G. Cao, S. McCall, J. E. Crow, and R. P. Guertin, Observation of a Metallic Antiferromagnetic Phase and Metal to Nonmetal Transition in $\text{Ca}_3\text{Ru}_2\text{O}_7$. *Phys. Rev. Lett.* **78** (1997), 1751–1754.
- [196] C. D. Dashwood, L. S. I. Veiga, Q. Faure, J. G. Vale, D. G. Porter, S. P. Collins, P. Manuel, D. D. Khalyavin, F. Orlandi, R. S. Perry, R. D. Johnson, and D. F. McMorrow, Spontaneous cycloidal order mediating a spin-reorientation transition in a polar metal. *Phys. Rev. B* **102** (2020), 180410.
- [197] G. Cao, L. Balicas, Y. Xin, E. Dagotto, J. E. Crow, C. S. Nelson, and D. F. Agterberg, Tunneling magnetoresistance and quantum oscillations in bilayered $\text{Ca}_3\text{Ru}_2\text{O}_7$. *Phys. Rev. B* **67** (2003), 060406.
- [198] E. Ohmichi, Y. Yoshida, S. I. Ikeda, N. Shirakawa, and T. Osada, Colossal magnetoresistance accompanying a structural transition in a highly two-dimensional metallic state of $\text{Ca}_3\text{Ru}_2\text{O}_7$. *Phys. Rev. B* **70** (2004), 104414.
- [199] X. N. Lin, Z. X. Zhou, V. Durairaj, P. Schlottmann, and G. Cao, Colossal magnetoresistance by avoiding a ferromagnetic state in the Mott system $\text{Ca}_3\text{Ru}_2\text{O}_7$. *Phys. Rev. Lett.* **95** (2005), 017203.
- [200] W. Bao, Z. Q. Mao, Z. Qu, and J. W. Lynn, Spin valve effect and magnetoresistivity in single crystalline $\text{Ca}_3\text{Ru}_2\text{O}_7$. *Phys. Rev. Lett.* **100** (2008), 247203.
- [201] M. Krautloher, Neutron scattering studies on layered ruthenates: PhD Thesis, Universität Stuttgart (2018).
- [202] Y. Ōnuki, Physics of heavy fermions: Heavy fermions and strongly correlated electrons systems, World Scientific, New Jersey and London and Singapore. (2018).
- [203] H. Q. Yuan, F. M. Grosche, M. Deppe, C. Geibel, G. Sparn, and F. Steglich, Observation of two distinct superconducting phases in CeCu_2Si_2 . *Science* **302** (2003), 2104–2107.
- [204] S. Quezel, P. Bulet, J. L. Jacoud, L. P. Regnault, J. Rossat-Mignod, C. Vettier, P. Lejay, and J. Flouquet, Magnetic ordering in $\text{Ce}_x\text{La}_{1-x}\text{Ru}_2\text{Si}_2$ solid solutions. *J. Magn. Magn. Mater.* **76-77** (1988), 403–404.

-
- [205] M. Nakashima, Y. Haga, F. Honda, T. Eto, G. Oomi, T. Kagayama, N. Takeshita, T. Nakanishi, N. Mōri, D. Aoki, R. Settai, and Y. Onuki, Non-Fermi-liquid behaviour around the magnetic quantum critical point in UGa_3 . *J. Phys.: Condens. Matter* **13** (2001), L569–L576.
- [206] J. Kondo, Resistance Minimum in Dilute Magnetic Alloys **32** (1964), 37–49.
- [207] S. Doniach, The Kondo lattice and weak antiferromagnetism. *Phys. B+C* **91** (1977), 231–234.
- [208] R. A. Robinson, D. J. Goossens, M. S. Torikachvili, K. Kakurai, and H. Okumura, A quantum multi-critical point in $\text{CeCu}_{6-x}\text{Au}_x$. *Phys. B* **385-386** (2006), 38–40.
- [209] A. Amato, D. Jaccard, J. Flouquet, F. Lapiere, J. L. Tholence, R. A. Fisher, S. E. Lacy, J. A. Olsen, and N. E. Phillips, Thermodynamic and transport properties of CeCu_6 . *J. Low. Temp. Phys.* **68** (1987), 371–397.
- [210] H. von Löhneysen, T. Pietrus, G. Portisch, H. G. Schlager, A. Schröder, M. Sieck, and T. Trappmann, Non-Fermi-liquid behavior in a heavy-fermion alloy at a magnetic instability. *Phys. Rev. Lett.* **72** (1994), 3262–3265.
- [211] H. von Löhneysen, M. Sieck, O. Stockert, and M. Waffenschmidt, Investigation of non-Fermi-liquid behavior in $\text{CeCu}_{6-x}\text{Au}_x$. *Phys. B* **223-224** (1996), 471–474.
- [212] H. von Löhneysen, S. Mock, A. Neubert, T. Pietrus, A. Rosch, A. Schröder, O. Stockert, and U. Tutsch, Heavy-fermion systems at the magnetic-nonmagnetic quantum phase transition. *J. Magn. Magn. Mater.* **177-181** (1998), 12–17.
- [213] H. Tsujii, E. Tanaka, Y. Ode, T. Katoh, T. Mamiya, S. Araki, R. Settai, and Y. Onuki, Magnetic order in the heavy fermion compound CeCu_6 at mK temperatures. *Phys. Rev. Lett.* **84** (2000), 5407–5410.
- [214] M. Ruck, G. Portisch, H. G. Schlager, M. Sieck, and H. von Löhneysen, Structure and electrical resistivity of the heavy fermion compound CeCu_5Au . *Acta Crystallogr B Struct Sci* **49** (1993), 936–941.
- [215] T. Pietrus, B. Bogenberger, S. Mock, M. Sieck, and H. v. Löhneysen, Pressure dependence of the Néel temperature in antiferromagnetic $\text{CeCu}_{6-x}\text{Au}_x$ for $0.3 \leq x \leq 1.3$. *Phys. B* **206-207** (1995), 317–319.

- [216] A. Hamann, O. Stockert, V. Fritsch, K. Grube, A. Schneidewind, and H. von Löhneysen, Evolution of the magnetic structure in $\text{CeCu}_{5.5}\text{Au}_{0.5}$ under pressure towards quantum criticality. *Phys. Rev. Lett.* **110** (2013), 096404.
- [217] M. L. Vrtis, J. D. Jorgensen, and D. G. Hinks, The structural phase transition in the RECu_6 compounds ($\text{RE} = \text{La}, \text{Ce}, \text{Pr}, \text{Nd}$). *J. Solid State Chem.* **84** (1990), 93–101.
- [218] H. von Löhneysen, Non-Fermi-liquid behaviour in the heavy-fermion system $\text{CeCu}_{6-x}\text{Au}_x$. *J. Phys.: Condens. Matter* **8** (1996), 9689–9706.
- [219] A. Rosch, A. Schröder, O. Stockert, and H. von Löhneysen, Mechanism for the Non-Fermi-Liquid Behavior in $\text{CeCu}_{6-x}\text{Au}_x$. *Phys. Rev. Lett.* **79** (1997), 159–162.
- [220] O. Stockert, H. von Löhneysen, A. Rosch, N. Pyka, and M. Loewenhaupt, Two-Dimensional Fluctuations at the Quantum-Critical Point of $\text{CeCu}_{6-x}\text{Au}_x$. *Phys. Rev. Lett.* **80** (1998), 5627–5630.
- [221] O. Stockert, H. Löhneysen, A. Rosch, N. Pyka, and M. Loewenhaupt, Spin dynamics at the magnetic instability in $\text{CeCu}_{6-x}\text{Au}_x$. *Phys. B* **259-261** (1999), 376–377.
- [222] O. Stockert, Spindynamik und magnetische Ordnung in $\text{CeCu}_{6-x}\text{Au}_x$: PhD Thesis, Universität Karlsruhe, Cuvillier, Göttingen. 1. Aufl. ed., (1999).
- [223] O. Stockert, H. Löhneysen, A. Schröder, M. Loewenhaupt, N. Pyka, P. L. Gammel, and U. Yaron, Incommensurate antiferromagnetism and magnetic correlations in $\text{CeCu}_{6-x}\text{Au}_x$. *Phys. B* **230-232** (1997), 247–249.
- [224] H. von Löhneysen, A. Neubert, T. Pietrus, A. Schröder, O. Stockert, U. Tutsch, M. Loewenhaupt, A. Rosch, and P. Wölfle, Magnetic order and transport in the heavy-fermion system CeCuAu . *Eur. Phys. J. B* **5** (1998), 447–455.
- [225] A. Schröder, J. W. Lynn, R. W. Erwin, M. Loewenhaupt, and H. Löhneysen, Magnetic structure of the heavy fermion alloy $\text{CeCu}_{5.5}\text{Au}_{0.5}$. *Phys. B* **199-200** (1994), 47–48.
- [226] M. Garst, L. Fritz, A. Rosch, and M. Vojta, Dimensional crossover in quantum critical metallic magnets. *Phys. Rev. B* **78** (2008), 235118.
- [227] V. F. Sears, Neutron scattering lengths and cross sections. *Neutron News* **3** (1992), 26–37.

-
- [228] L. van Hove, Correlations in Space and Time and Born Approximation Scattering in Systems of Interacting Particles. *Phys. Rev.* **95** (1954), 249–262.
- [229] W. Marshall and R. D. Lowde, Magnetic correlations and neutron scattering. *Rep. Prog. Phys.* **31** (1968), 705–775.
- [230] R. M. Moon, T. Riste, and W. C. Koehler, Polarization Analysis of Thermal-Neutron Scattering. *Phys. Rev.* **181** (1969), 920–931.
- [231] B. N. Brockhouse, Scattering of Neutrons by Spin Waves in Magnetite. *Phys. Rev.* **106** (1957), 859–864.
- [232] T. Keller and B. Keimer, TRISP: Three axes spin echo spectrometer. *JLSRF* **1** (2015), A37.
- [233] M. J. Cooper and R. Nathans, The resolution function in neutron diffractometry. I. The resolution function of a neutron diffractometer and its application to phonon measurements. *Acta Cryst* **23** (1967), 357–367.
- [234] M. Popovici, On the resolution of slow-neutron spectrometers. IV. The triple-axis spectrometer resolution function, spatial effects included. *Acta Cryst A* **31** (1975), 507–513.
- [235] A. Zheludev, ResLib 3.4 (2009).
- [236] T. Weber, R. Georgii, and P. Böni, Takin: An open-source software for experiment planning, visualisation, and data analysis. *SoftwareX* **5** (2016), 121–126.
- [237] K. Schmalzl, W. Schmidt, S. Raymond, H. Feilbach, C. Mounier, B. Vettard, and T. Brückel, The upgrade of the cold neutron three-axis spectrometer IN12 at the ILL. *Nucl. Instrum. Methods. Phys. Res. B* **819** (2016), 89–98.
- [238] B. Farago, P. Falus, I. Hoffmann, M. Gradzielski, F. Thomas, and C. Gomez, The IN15 upgrade. *Neutron News* **26** (2015), 15–17.
- [239] M. P. Schulhof, P. Heller, R. Nathans, and A. Linz, Critical Magnetic Scattering in Manganese Fluoride. *Phys. Rev. B* **1** (1970), 2304–2311.
- [240] P. Steffens, O. Friedt, Y. Sidis, P. Link, J. Kulda, K. Schmalzl, S. Nakatsuji, and M. Braden, Magnetic excitations in the metallic single-layer ruthenates $\text{Ca}_{2-x}\text{Sr}_x\text{RuO}_4$ studied by inelastic neutron scattering. *Phys. Rev. B* **83** (2011), 054429.
- [241] F. Mezei, Neutron spin echo: A new concept in polarized thermal neutron techniques. *Z. Physik* **255** (1972), 146–160.

- [242] F. Mezei, Fundamentals of Neutron Spin Echo Spectroscopy, in Neutron Spin Echo Spectroscopy, F. Mezei, C. Pappas, and T. Gutberlet, eds., Lecture Notes in Physics, Springer, Berlin and Heidelberg, (2003).
- [243] R. Golub and R. Gähler, A neutron resonance spin echo spectrometer for quasi-elastic and inelastic scattering. *Phys. Lett. A* **123** (1987), 43–48.
- [244] R. Gähler and R. Golub, A high resolution neutron spectrometer for quasielastic scattering on the basis of spin-echo and magnetic resonance. *Z. Physik B: Condens. Matter* **65** (1987), 269–273.
- [245] R. Gähler and R. Golub, Neutron resonance spin echo, bootstrap method for increasing the effective magnetic field. *J. Phys. France* **49** (1988), 1195–1202.
- [246] D. Dubbers, P. El-Muzeini, M. Kessler, and J. Last, Prototype of a zero-field neutron spin-echo spectrometer. *Nucl. Instrum. Methods. Phys. Res. B* **275** (1989), 294–300.
- [247] R. Gähler, R. Golub, and T. Keller, Neutron resonance spin echo—a new tool for high resolution spectroscopy. *Phys. B* **180-181** (1992), 899–902.
- [248] M. T. Rekveldt, High-resolution diffraction using Larmor precession and multiple narrow beams defined by multislits. *J. Appl. Phys.* **84** (1998), 31–37.
- [249] M. T. H. Rekveldt and W. H. Kraan, High-resolution neutron diffraction using larmor precession for angular and wavelength labelling. *JNR* **8** (1999), 53–70.
- [250] T. Keller, R. Golub, and R. Gähler, Neutron Spin Echo—A Technique for High-Resolution Neutron Scattering, in Scattering, R. Pike, ed., Acad. Press, San Diego Calif. u.a., (2002), 1264–1286.
- [251] K. F. Tseng, Critical dynamics in classical antiferromagnets: PhD Thesis, Universität Stuttgart (2016).
- [252] M. P. Schulhof, R. Nathans, P. Heller, and A. Linz, Inelastic Neutron Scattering from MnF_2 in the Critical Region. *Phys. Rev. B* **4** (1971), 2254–2276.
- [253] T. Keller, M. Rekveldt, and K. Habicht, Neutron Larmor diffraction measurement of the lattice-spacing spread of pyrolytic graphite. *Appl. Phys. A* **74** (2002), s127–s129.
- [254] M. T. Rekveldt, W. Kraan, and T. Keller, High-resolution diffraction using Larmor precession of polarized neutrons. *J Appl Crystallogr* **35** (2002), 28–33.

-
- [255] J. Repper, T. Keller, M. Hofmann, C. Kremaszky, W. Petry, and E. Werner, Neutron Larmor diffraction measurements for materials science **58** (2010), 3459–3467.
- [256] X. Lu, K.-F. Tseng, T. Keller, W. Zhang, D. Hu, Y. Song, H. Man, J. T. Park, H. Luo, S. Li, A. H. Nevidomskyy, and P. Dai, Impact of uniaxial pressure on structural and magnetic phase transitions in electron-doped iron pnictides. *Phys. Rev. B* **93** (2016), 134519.
- [257] A. Lupascu, J. P. Clancy, H. Gretarsson, Z. Nie, J. Nichols, J. Terzic, G. Cao, S. S. A. Seo, Z. Islam, M. H. Upton, J. Kim, D. Casa, T. Gog, A. H. Said, V. M. Katukuri, H. Stoll, L. Hozoi, J. van den Brink, and Y.-J. Kim, Tuning magnetic coupling in Sr₂IrO₄ thin films with epitaxial strain. *Phys. Rev. Lett.* **112** (2014), 147201.
- [258] J. Porras, J. Bertinshaw, H. Liu, G. Khaliullin, N. H. Sung, J.-W. Kim, S. Francoual, P. Steffens, G. Deng, M. M. Sala, A. Efimenko, A. Said, D. Casa, X. Huang, T. Gog, J. Kim, B. Keimer, and B. J. Kim, Pseudospin-lattice coupling in the spin-orbit Mott insulator Sr₂IrO₄. *Phys. Rev. B* **99** (2019), 085125.
- [259] T. Keller, K. Habicht, H. Klann, M. Ohl, H. Schneider, and B. Keimer, The NRSE-TAS spectrometer at the FRM-2. *Appl. Phys. A* **74** (2002), s332–s335.
- [260] M. D. Le, D. L. Quintero-Castro, R. Toft-Petersen, F. Groitl, M. Skoulatos, K. C. Rule, and K. Habicht, Gains from the upgrade of the cold neutron triple-axis spectrometer FLEXX at the BER-II reactor. *Nucl. Instrum. Methods. Phys. Res. B* **729** (2013), 220–226.
- [261] O. W. Dietrich, Critical magnetic fluctuations in MnF₂. *J. Phys. C: Solid State Phys.* **2** (1969), 2022–2036.
- [262] A. Taroni, S. T. Bramwell, and P. C. W. Holdsworth, Universal window for two-dimensional critical exponents. *J. Phys.: Condens. Matter* **20** (2008), 275233.
- [263] R. J. Birgeneau, R. A. Cowley, G. Shirane, J. A. Tarvin, and H. J. Guggenheim, Spin fluctuations in random magnetic-nonmagnetic two-dimensional antiferromagnets. II. Heisenberg percolation. *Phys. Rev. B* **21** (1980), 317–332.
- [264] R. A. Cowley, R. J. Birgeneau, G. Shirane, H. J. Guggenheim, and H. Ikeda, Spin fluctuations in random magnetic-nonmagnetic two-dimensional antiferromagnets. III. An Ising system. *Phys. Rev. B* **21** (1980), 4038–4048.

- [265] F. G. Mertens, A. R. Bishop, G. M. Wysin, and C. Kawabata, Dynamical correlations from mobile vortices in two-dimensional easy-plane ferromagnets. *Phys. Rev. B* **39** (1989), 591–602.
- [266] M. Papoular, M. D. Núñez-Regueiro, and M. Altarelli, Two-length-scale problem in critical scattering: Narrow-component line shape. *Phys. Rev. B* **56** (1997), 166–169.
- [267] R. A. Cowley and S. M. Shapiro, Structural Phase Transitions. *J. Phys. Soc. Jpn.* **75** (2006), 111001.
- [268] D. L. Huber, Dynamics of spin vortices in two-dimensional planar magnets. *Phys. Rev. B* **26** (1982), 3758–3765.
- [269] F. G. Mertens, A. R. Bishop, G. M. Wysin, and C. Kawabata, Vortex signatures in dynamic structure factors for two-dimensional easy-plane ferromagnets. *Phys. Rev. Lett.* **59** (1987), 117–120.
- [270] M. T. Hutchings, P. Day, E. Janke, and R. Pynn, Critical spin dynamics in Rb_2CrCl_4 : A nearly two-dimensional easy-plane ferromagnet. *J. Magn. Magn. Mater.* **54-57** (1986), 673–674.
- [271] L. P. Regnault, J. P. Boucher, J. Rossat-Mignod, J. Bouillot, R. Pynn, J. Y. Henry, and J. P. Renard, Nonlinear excitations in 1d and 2d magnetic systems. *Phys. B+C* **136** (1986), 329–334.
- [272] H. Trepka, M. Boehm, M. Hepting, M. J. Krautloher, and J. Porras, Complex magnetic fluctuations in Ca_2RuO_4 above the Néel temperature: (data cite, doi: 10.5291/ILL-DATA.4-03-1738).
- [273] M. Boehm, S. Roux, A. Hiess, and J. Kulda, ThALES—towards the next generation cold neutron three-axis spectrometer. *J. Magn. Magn. Mater.* **310** (2007), e965–e967.
- [274] S. T. Bramwell and P. C. W. Holdsworth, Universality in two-dimensional magnetic systems. *J. Appl. Phys.* **73** (1993), 6096–6098.
- [275] M. Hemmida, H.-A. Krug von Nidda, N. Büttgen, A. Loidl, L. K. Alexander, R. Nath, A. V. Mahajan, R. F. Berger, R. J. Cava, Y. Singh, and D. C. Johnston, Vortex dynamics and frustration in two-dimensional triangular chromium lattices. *Phys. Rev. B* **80** (2009), 054406.
- [276] H. Trepka, M. Hepting, T. Keller, Maximilian J. Krautloher, J. Porras, Schmalzl, Karin, and Schmidt Wolfgang F, Critical magnetic fluctuations in Ti-doped $\text{Ca}_3\text{Ru}_2\text{O}_7$: (data cite, doi: 10.5291/ILL-DATA.CRG-2756).

-
- [277] Y. Togawa, T. Akashi, H. Kasai, G. W. Paterson, S. McVitie, Y. Kousaka, H. Shinada, J.-i. Kishine, and J. Akimitsu, Formations of Narrow Stripes and Vortex–Antivortex Pairs in a Quasi-Two-Dimensional Ferromagnet K_2CuF_4 . *J. Phys. Soc. Jpn.* **90** (2021), 014702.
- [278] C. Dietl, S. K. Sinha, G. Christiani, Y. Khaydukov, T. Keller, D. Putzky, S. Ibrahimkuty, P. Wochner, G. Logvenov, P. A. van Aken, B. J. Kim, and B. Keimer, Tailoring the electronic properties of Ca_2RuO_4 via epitaxial strain. *Appl. Phys. Lett.* **112** (2018), 031902.
- [279] J. Kim, M. Daghofer, A. H. Said, T. Gog, J. van den Brink, G. Khaliullin, and B. J. Kim, Excitonic quasiparticles in a spin-orbit Mott insulator. *Nat. Commun.* **5** (2014), 4453.
- [280] M. T. Hutchings, J. Als-Nielsen, P. A. Lindgard, and P. J. Walker, Neutron scattering investigation of the temperature dependence of long-wavelength spin waves in ferromagnetic Rb_2CrCl_4 . *J. Phys. C: Solid State Phys.* **14** (1981), 5327–5345.
- [281] H. von Löhneysen, C. Pfleiderer, T. Pietrus, O. Stockert, and B. Will, Pressure versus magnetic-field tuning of a magnetic quantum phase transition. *Phys. Rev. B* **63** (2001), 8330.
- [282] O. Stockert, M. Enderle, and H. von Löhneysen, Magnetic fluctuations at a field-induced quantum phase transition. *Phys. Rev. Lett.* **99** (2007), 237203.
- [283] O. Stockert, A. Schröder, H. Löhneysen, N. Pyka, E. Garcia-Matres, R. Kamp, S. Welzel, and M. Loewenhaupt, Evolution of the magnetic order in $\text{CeCu}_{6-x}\text{Au}_x$. *Phys. B* **259-261** (1999), 383–384.
- [284] H. Lin, M. F. Collins, and T. M. Holden, Critical scattering from erbium. *J. Appl. Phys.* **73** (1993), 5341–5343.
- [285] P. Pfeuty, The quantum-classical crossover critical behaviour of the Ising model in a transverse field. *J. Phys. C: Solid State Phys.* **9** (1976), 3993–4001.
- [286] P. Merchant, B. Normand, K. W. Krämer, M. Boehm, D. F. McMorrow, and C. Rüegg, Quantum and classical criticality in a dimerized quantum antiferromagnet. *Nat. Phys.* **10** (2014), 373–379.
- [287] W. Knafo, S. Raymond, P. Lejay, and J. Flouquet, Antiferromagnetic criticality at a heavy-fermion quantum phase transition. *Nat. Phys.* **5** (2009), 753–757.

- [288] R. Jaramillo, Y. Feng, J. Wang, and T. F. Rosenbaum, Signatures of quantum criticality in pure Cr at high pressure. *PNAS USA* **107** (2010), 13631–13635.

Acknowledgements

The research work presented in this thesis would not have been possible without the help of my supervisors, co-workers, friends, and family. My sincere gratitude to everyone who helped me realizing this work:

- Prof. Dr. **Bernhard Keimer** for giving me the opportunity to join his department at the Max-Planck-Institut für Festkörperforschung (MPI-FKF) and providing me with this fascinating PhD project. Undoubtedly, this work would not have been as successful and of high quality as without the helpful and encouraging discussions with him.
- Dr. **Thomas Keller** for his support as the instrument scientist at TRISP and his continued guidance, patience, and help to realize this work.
- Dr. **Matthias Hepting** for his support as the head of the neutron scattering group and countless helpful discussions.
- Prof. Dr. **Maria Daghofer**, Prof. Dr. **Sebastian Loth**, and Prof. Dr. **Dirk Manske** for participating my thesis committee
- My colleagues Dr. **Yury Kaydukov**, **Laura Guasco**, and **Franz Tralmer** from the outstation of the Max-Planck-Society at the Heinz Maier-Leibnitz Zentrum (Munich)
- My colleagues Dr. **Katrin Fürsich**, Dr. **Pascal Puphal**, **Valentin Zimmermann**, **Lee Hangoo**, **Vignesh Sundaramurthy**, **Pablo Lizama** for helpful discussions during our weekly neutron scattering group-meetings
- Dr. **Maximilian Krautloher** for providing me with high-quality Ca_2RuO_4 , $\text{Ca}_3\text{Ru}_2\text{O}_7$, and $\text{Ca}_3(\text{Ru}_{0.99}\text{Ti}_{0.01})_2\text{O}_7$ single-crystals and his support during various neutron experiments, as well as Dr. **Joel Bertinshaw**, and **Juan Porras** for fruitful discussions.
- Priv.-Doz. Dr. **Hans-Albrecht Krug von Nidda** for supporting me with his expertise since my master's thesis in his group at the Augsburg University.

Acknowledgements

- Priv.-Doz. Dr. **Oliver Stockert** for providing me with high-quality $\text{CeCu}_{5.8}\text{Au}_{0.2}$ and $\text{CeCu}_{5.9}\text{Au}_{0.1}$ single-crystals.
- The **beamline scientists** of the FLEXX, ThALES, IN12 at other neutron facilities for their help during the experiments.
- **Adrian Heiler**, **Benjamin Krugmann**, and **Tobias Köhler** for scientific discussions during our coffee-breaks
- **Sonja Balkema** for her help with all non-scientific issues.
- All other colleagues of the **MPI-FKF** and the colleagues at the **MLZ**.
- My **family**, in particular, my parents **Karin & Günter Trepka**
- My beloved **Martina Ziegler**

Heiko Trepka

Curriculum Vitae

Fields of Interest

- Critical magnetic phenomena of strongly correlated materials
- Unconventional superconductors

Education

2018 - 2022 **Ph.D. in Physics**

MPI for Solid State Research Stuttgart, Germany
Advisor: Prof. Dr. Bernhard Keimer

2015 - 2017 **M.Sc Physics**

University of Augsburg, Germany
Advisor: Priv.-Doz. Dr. Hans-Albrecht Krug von Nidda

2012 - 2015 **B.Sc Physics**

University of Augsburg, Germany
Advisor: Prof. Dr. Achim Wixforth

2012 **Abitur**

Bernhard-Strigel-Gymnasium Memmingen, Germany

Publication list

- **H. Trepka**, *et al.*, Critical magnetic fluctuations in the layered ruthenates Ca_2RuO_4 and $\text{Ca}_3\text{Ru}_2\text{O}_7$ (Phys. Rev. Res. 4, 023181 (2022))
- R. A. Ortiz, P. Puphal, **H. Trepka**, *et al.*, Magnetic correlations in infinite-layer nickelates: an experimental and theoretical multi-method study (Phys. Rev. Res. 4, 023093 (2022))
- T. Keller, **H. Trepka**, *et al.*, Neutron Spin-Echo Instrumentation for Magnetic Scattering (Phys. Status Solidi B, 2100164 (2021)).
- M. J. Krautloher, **H. Trepka**, *et al.*, Impurity-induced transformation of spin-orbit entanglement in a layered ruthenate (*submitted to Phys. Rev. X*)

Experimental Techniques

- Neutron Spin-Echo and Triple-Axis Spectroscopy
- Neutron (Larmor-)Diffraction